Ref: RAF/00/G32 BCLME

BCLME Project EV/LS/02/06

Diagnosis of Large Scale South Atlantic Modes that Impact on the Transboundary Benguela Current Large Marine Ecosystem: Investigating the Potential for Improved Predictability and Sustainable Management

Final Report

Dr F. Colberg, and Prof C. J. C. Reason

January 2007

Centre for Marine Studies **University of Cape Town**	**Oceanography** **University of Cape Town**

Executive summary

This report discusses the variability of the South Atlantic climate. In order to account for both large and regional scales, two ocean models are applied. An ocean general circulation model, forced with the National Centre for Environmental Prediction/ National Centre for Atmospheric Research reanalysis is used to investigate the South Atlantic leading modes and also to investigate the South Atlantic response to El Niño-Southern Oscillation induced climate variability. A regional ocean model is used to investigate variability in the South East Atlantic, especially in the Angola Benguela Frontal Zone.

A rotated Empirical Orthogonal Function analysis of the mixed layer temperature suggests a breakdown of the South Atlantic into four subdomains, with characteristic spatial and temporal scales: (a) the tropical Atlantic, with mainly interannual fluctuations, (b) the northeastern subtropics, with variability on an interannual to decadal scale, (c) the midlatitudes, with interannual and multi-decadal variability and (d) the southwestern subtropics/ midlatitudes with a mixture of interannual and decadal variability. These modes are closely connected to anomalous atmospheric circulation patterns, which induce typical forcing mechanisms for each region.

Temperature changes in the western to central tropics are found to be driven by changes in surface heat fluxes and horizontal advection of heat, while in the central to eastern tropics and the northern Benguela, temperature changes are connected to reduced vertical entrainment, altering the depth of the mixed layer and leading to reduced upwelling.

In the western and eastern subtropics, changes in the net surface fluxes drive the upper ocean temperature anomalies, and wind induced vertical mixing dissipate them, inducing changes in the depth of the mixed layer. Anomalous heat and volume transports are found to be related to anomalous Ekman and geostrophic currents in the eastern subtropics. A wind driven mechanism is suggested, whereby changes in Ekman related heat and volume transport lead to modulations of the subtropical gyre and thus to changes in the geostrophic related heat and volume transport.

The midlatitudes experience temperature changes resulting mainly from horizontal advection and wind induced vertical mixing, whereby geostrophic advection of heat dominates in the western to central area, and Ekman induced heat transports are confined to the eastern midlatitudes.

Seasonal El Niño-Southern Oscillation composites suggest that the El Niño-Southern Oscillation induced wind anomalies play a major role in driving upper ocean temperatures by altering the net surface heat fluxes, the meridional Ekman heat transport and Ekman pumping. Model diagnostics indicate that the Ekman heat transport changes are in better agreement with the upper ocean temperature anomalies during the first half of the El Niño-Southern Oscillation event whereas, in the latter half, the surface heat flux anomalies agree better. In general, the atmospheric forcing tends to lead to a coherent ocean response with a time lag of about one season. Subsurface temperatures evolve more slowly in response to El Niño-Southern Oscillation forcing than the upper ocean. They receive time filtered ENSO signals from mainly Ekman pumping (suction) and variations in thermocline depth that result in the poleward and equatorward margins of the subtropical gyre exhibiting temperature anomalies of the same sign but opposite to those in the central regions of the gyre.

A regional ocean model is used to further investigate variability in the South East Atlantic. Several experiments are conducted in order to assess the sensitivity of the Angola Benguela Frontal Zone towards changes in windstress. The results suggest that the position of the Angola Benguela Frontal Zone is mainly determined by opposing northward and southward flow near the coast. The windstress *curl* plays a major role in altering the position of the Angola Benguela Frontal Zone, as it controls the southeastward flow of the South Equatorial Counter Current. The opposing northward flow is mainly the result of geostrophic adjustment to coastal upwelling enforced by apparent alongshore windstress. The strength of the frontal zone is related to the strength of the alongshore windstress that controls the coastal upwelling.

The internal variability of the Angola Benguela Front is investigated. It appears

that anomalous northward (southward) positions of the Angola Benguela Frontal Zone are connected to anomalous intensities of the front. A mechanism is suggested whereby anomalous northward shifts of the Angola Benguela Frontal Zone are associated with an anticyclonic circulation pattern in the area that shifts the frontal system towards the north. This anomalous circulation also forces changes in coastal upwelling that in turn drive anomalous upper ocean temperatures, which act to enhance the meridional temperature gradient. This mechanism appears to be most efficient during austral spring and summer.

Interannual variability within the front is investigated and is found to be connected to periodic westward propagating anomalies of the large scale sea surface height. It is suggested that oceanic instability processes are mainly responsible for this wave-like motion.

A comparison between internal variability near the Angola Benguela Frontal Zone and other modes of variability suggests that internal variability could at times account for the same amount of variability induced by El Niño-Southern Oscillation, and for up to 20% of the variability apparent during major warm events in the South East Atlantic such as Benguela Niños.

Contents

List of Figures

List of Tables

1 Introduction

Over the last decade an increasing number of studies have been devoted to investigating South Atlantic climate variability. The importance of the South Atlantic Ocean is thought to be twofold. On the global scale the South Atlantic Ocean is unique, as it is the only ocean that transports heat from higher latitudes towards (and over) the equator. This behaviour marks an important part of the global thermohaline circulation (*Schmitz*, 1995; *Gordon*, 1986), and is required in order to maintain the global heat balance. The reason for this self stabilising and convenient feedback mechanism, is due to numerous factors (*Berger and Wefer*, 1996). These factors imply the position of the Inter Tropical Convergence Zone (ITCZ), which lies generally somewhat northward of the equator and the extent of the North Atlantic to high latitudes, where deep water production can occur. *Gordon* (1996) noted that the salty North Atlantic is needed in order to precondition the region for the production of North Atlantic Deep Water (NADW). But why is the North Atlantic Ocean so salty ? Here, one has to consider the distributions of the landmasses in the Southern Hemisphere. The differences in the southward extension of the South American and African continents, allow for a net outflow of fresh water into the Indian Ocean. In addition, the South Atlantic Ocean is fed with warm saline water from the Agulhas Current via ring shedding (*Gordon*, 1985). Since the evaporation of subtropical waters is more or less equal to the precipitation rate in the midlatitudes, a net increase in salinity is the result, which is then transported towards the North Atlantic. Hence, allowing for the production of the relative warm and saline NADW, which is important in driving the global "conveyor belt". Thus, variability within the South Atlantic may substantially affect the thermohaline circulation and the global climate system.

On a regional scale, changes in sea surface temperature (SST) anomalies are found to impact on the atmospheric circulation and may lead to significant changes in rainfall variability over the adjacent land masses, as has been investigated by for example *Reason et al.* (2002); *Rouault et al.* (2003); *Robertson et al.* (2003). As

well as climate effects, the existence of warm events in the South East Atlantic has been shown to cause dramatic changes in fish stocks along the western African coast (*Binet et al.*, 2001; *Gammelsrod et al.*, 1998), often with devastating consequences for local fisheries.

In addition, the South Atlantic contains one of the four eastern boundary currents of the world ocean (the Benguela Current). Although all four upwelling systems account for less than 1% of the total surface area of the world ocean, these regions account for almost 30% of the world's total fish catches (*Dengler*, 1985). The Benguela upwelling system is unique, as it is bounded by warm waters at both its northern and southern system boundaries. The northern boundary is the confluence zone between the northward flowing Benguela Current and the southward flowing Angola Current, otherwise known as the Angola Benguela Frontal Zone (ABFZ). The southern boundary is the Agulhas retroflection area. Both system boundaries are known to vary on different time scales, affecting the upwelling regime and the heat transport within the South Atlantic.

Figure 1 displays the upper ocean circulation of the South Atlantic Ocean (from *Berger and Wefer*, 1996), which is reviewed completely in a series of papers (*Stramma*, 1989; *Stramma and Peterson*, 1989; *Stramma et al.*, 1990; *Stramma and Peterson*, 1990; *Peterson and Stramma*, 1991; *Stramma*, 1991). The South Atlantic Gyre is like all subtropical gyres in that, to a first approximation, it is in geostrophic balance and the wind-driven circulation is dominated by the semi-permanent subtropical anticyclone or the South Atlantic Anticyclone (SAA). The SAA and its associated trade and westerly wind systems experience seasonal variations, in which the SAA varies in strength and position. The annual meridional migration of the SAA is about 5-6°, comparable to that of the Azores High and the South Indian Ocean Anticyclone. The zonal migration is larger, about 12°, but only half as much than those observed for the Azores High and South Indian Ocean Anticyclone (*McGee and Hastenrath*, 1966; *Preston-Whyte and Tyson*, 1988; *Davis et al.*, 1997).

The SAA attains its southern most position during austral summer. During this time the land-sea pressure gradient is strongest, since solar heating over the

southern African and American subcontinents reaches its peak. This favours the development of thermal low pressure system over the subtropical landmasses and results in strong alongshore winds off the west coast. These in turn maximize the offshore Ekman drift, resulting in stronger upwelling in the southern Benguela. During austral winter, the SAA moves northwestwards, intensifying the southeasterly trades and leading to strong northward directed heat transport, in conjunction with the northern most position of the ITCZ at about 15°N. Strong midlatitude westerlies are associated with the SAA, due to the strong pressure gradient between the SAA and the circumpolar trough of the Southern Hemisphere. The associated eastward moving frontal systems influence the weather pattern over southern Africa. Evidence exists that these are at times preconditioned by SSTs in the South Atlantic (*Reason and Jagadheesha*, 2005). Superimposed onto the annual cycle is a semi-annual variation of the position and strength of the SAA and midlatitude westerlies, that becomes more pronounced towards the south and is at times greater than that of the yearly cycle. This semi-annual oscillation is thought to be driven by the annual march of the tropospheric temperature differences between the Southern Oceans and the Antarctic continent (e.g. *van Loon and Jenne*, 1972).

This work seeks to provide a better understanding of intra-annual to decadal variability in the South Atlantic region on a basin wide and on a regional scale. In order to achieve this, the output of two ocean models is examined. Firstly, a global ocean general circulation model (OGCM), forced with interannual varying windstress and heat fluxes is used to investigate basin wide variability and possible remote forcing. Secondly, a higher resolution regional ocean model, forced at the surface with monthly climatological windstress and heat fluxes is used to explore variability in the South East Atlantic, particularly at the northern system boundary of the Benguela upwelling system, the ABFZ.

With this in mind the structure of this report is as follows: Section 2 reviews the appropriate literature that is concerned with South Atlantic variability. This includes the leading modes of the South Atlantic, El Niño-Southern Oscillation (ENSO) related variability and variability in the South East Atlantic. Models, data

and methods used in this thesis are discussed in Section 3. Section 4 investigates the leading modes of upper South Atlantic Ocean temperatures, their variability and associated mechanisms. Section 5 explores the South Atlantic response to ENSO induced variability in the OGCM, while Section 6 investigates the sensitivity of the position and strength of the ABFZ towards changes in windstress and also investigates intra-annual to interannual variability within the ABFZ. Each section ends with a discussion of the main findings and Section 7 summarises the main results of the work.

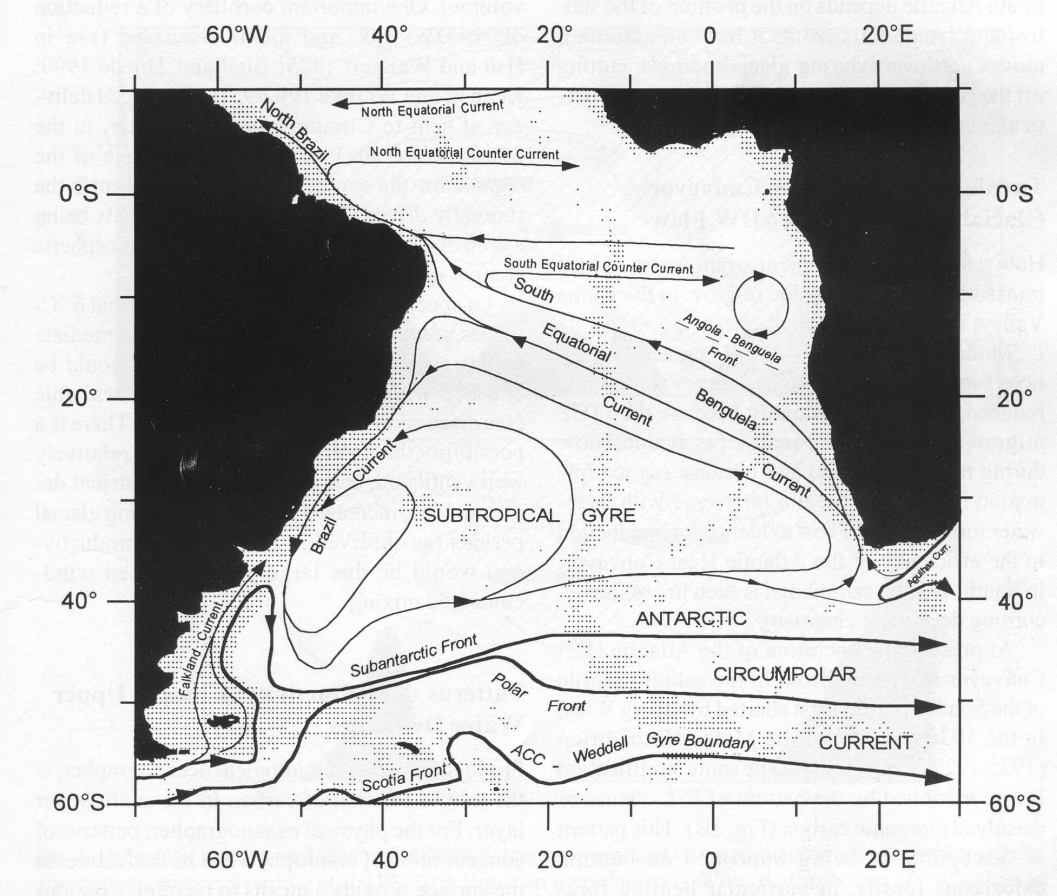

Figure 1: Schematic picture of the upper ocean geostrophic currents in the South Atlantic Ocean (from *Berger and Wefer*, 1996).

2 Literature Review

In this section the appropriate literature concerning South Atlantic variability will be reviewed. The larger scale variability within the South Atlantic is discussed first. This includes the South Atlantic leading modes, multi-decadal variability and relationships with ENSO. Then the focus is shifted towards the tropical Atlantic, highlighting the dynamical modes present there, after which variability in the South East Atlantic is discussed. As it is important for this thesis, the distinct circulation features within the South East Atlantic, i.e. the Angola Benguela Frontal Zone (ABFZ) and the Benguela upwelling system, are highlighted and where possible their variations on different time scales are pointed out. This section ends with a summary which leads to the formulation of some important key questions that will be addressed during the course of this thesis.

2.1 Variability in the South Atlantic

Previous work on variability in the South Atlantic has focused on interannual to multi-decadal time scales (e.g. *Venegas et al.*, 1996, 1997, 1998; *Reason*, 2000; *Reason et al.*, 2000, 2002; *Wainer and Venegas*, 2001; *Palastanga et al.*, 2002, 2005; *Colberg et al.*, 2004). *Venegas et al.* (1997) were one of the first to investigate the leading modes of the South Atlantic Ocean and their connection to the atmospheric circulation. They performed an empirical orthogonal function (EOF) analysis on 40 years of SST from the Comprehensive Ocean Atmosphere Dataset (COADS) and found that the first three leading modes account for about 48% of the total variance displayed. The first mode appeared to be a monopole in SST, which fluctuates on an interannual to decadal time scale. The second mode was a north-southward oriented dipole with variability also ranging from interannual to inter-decadal time scales, while the third mode exhibited three latitudinal bands of centres of action with alternating signs. This pattern was associated with mainly interannual variability.

These findings were only broadly consistent with those of *Sterl and Hazeleger* (2003), who analysed 52 years of SSTs obtained from the National Centre for Environmental Prediction/ National Centre for Atmospheric Research (NCEP/ NCAR) reanalysis. Their EOF analysis suggested that the dominant mode in the South Atlantic consists of a north-southward oriented dipole, while the second leading mode displays a monopole signal centred in the southwestern South Atlantic. The authors suggested that these differences are likely due to the use of different datasets and due to the fact that *Venegas et al.* (1997) did not detrend their data prior to performing the EOF analysis, hence favouring the evolution of a monopole like signal.

Other factors that affect the spatial and temporal shape of the South Atlantic leading modes are the statistical methods that are used in determining them, as pointed out by *Palastanga et al.* (2002, 2005). These authors examined SSTs from the NCEP/ NCAR reanalysis and found that the resulting leading modes were different prior to 1982, but agreed after that time period. It appears that this sensitivity is subject to an EOF analysis performed in sample or time space and it was suggested that fewer observations in the pre-satellite era and thus the lack of data coverage caused this sensitivity. It appears that the South Atlantic monopole is questionable as it is affected by the distribution of observations and their density. By contrast, the dipole mode in SST is a very consistent and robust feature.

Evidence for a possible connection between the leading modes and atmospheric circulation pattern has been put forward by *Venegas et al.* (1997), who showed that significant correlations exist between certain modes of the principal components resulting from the EOF analysis of SST and SLP. The correlations reach maximum values when the atmospheric modes lead the oceanic ones by 1 to 3 months, hence suggesting an atmosphere to ocean forcing. Further analysis of the coupled ocean-atmosphere variability using a singular value decomposition (SVD) analysis between SST and sea level pressure (SLP) confirmed these correlations. It was found by *Venegas et al.* (1997) that the leading joint SVD consists of an inter-decadal oscillation of the subtropical anticyclone that is accompanied by a north-south dipole structure in SST on the same time scale. The second mode involved an east-west shift of the

anticyclone with fluctuations of 6-7 years in SST, while the third mode is associated with a north-south fluctuation of the subtropical high and SST anomalies in a latitudinal band in the central South Atlantic. *Sterl and Hazeleger* (2003) found a similar leading coupled mode. They furthermore examined possible mechanisms associated with the leading modes using NCEP/ NCAR reanalysis fluxes and winds. An analysis of the temperature tendency equation suggests that wind induced changes in latent heat flux are mainly responsible in driving the upper ocean temperatures for the first coupled mode. The second joint SVD found by *Sterl and Hazeleger* (2003) displays major centres of variability in the midlatitudes. It appears that in the area of the roaring forties, changes in windstress with associated anomalous mixed layer deepening were increasingly important in altering SSTs. These findings were confirmed by *Haarsma et al.* (2005), who investigated the dominant leading modes of the South Atlantic with a hierarchy of coupled ocean-atmosphere models.

Further evidence for climate variability in the South Atlantic region has been put forward by *Venegas et al.* (1998); *Reason* (2000); *Wainer and Venegas* (2001). *Venegas et al.* (1998) used a SVD analysis to detect multi-decadal variability between SST from the Global Ice and Sea Surface Temperature (GISST) dataset and sea level pressure taken from the 80 years long Gridded Monthly Sea Level Pressure dataset (GMSLP). They discovered a coupled climate cycle in the South Atlantic that oscillates with an approximate period of 20 years. SST anomalies propagate anticlockwise around the South Atlantic basin, following roughly the subtropical gyre. It is thought that the anomalous atmospheric circulation provides a positive feedback mechanism, which involves changes in the heat fluxes and the SSTs. A negative feedback is subject to horizontal advection of heat by the ocean currents.

Variability on a similar time scale has been investigated by *Wainer and Venegas* (2001). They detected South Atlantic multi-decadal variability in the NCAR Climate System model in a 300 year integration model run and found significant oscillations of a 25-30 year period. This oscillation is associated with changes in the atmospheric circulation, that in turn affects the position of the Malvinas/ Falkland Brazil Current Confluence Zone (MFBCZ), leading to changes in upper ocean tem-

peratures there. The findings are in agreement with observational data, indicating that models can provide some useful information for the detection of climate signals in the South Atlantic region.

Reason (2000) analysed output from an OGCM to investigate mechanisms associated with multi-decadal climate variability in the subtropics/ midlatitudes of the Southern Hemisphere oceans. Analyses of the low frequency variability of SST using observational data (GISST), suggested that during 1900-1920 the South Atlantic was abnormally cool in the midlatitudes and eastern subtropics to tropics and warm over the western subtropics and tropics. The midlatitude cooling generally strengthened in the next epoch (1921-1941), and warming over the tropics to subtropics became apparent, suggesting a dipole like structure. This structure was roughly reversed between 1942 and 1962. The last epoch (1963-1983) showed SST anomalies that are roughly opposite to those for 1900-1921.

The model results of *Reason* (2000) suggested that the dynamic effect of windstress is significant mostly near the western boundary currents and in the equatorial upwelling zones. The mechanisms involve modulation of the intensity of the subtropical gyre. Over most of the subtropics and midlatitudes, changes in net surface heat flux, mainly in latent heat, appear to be more important for SST variability than dynamic effects.

Most of the studies mentioned above suggest that South Atlantic Ocean variability is mainly driven by the atmosphere. However, *Robertson et al.* (2003) provide evidence for an atmospheric response to SSTs using an Atmosphere General Circulation Model (AGCM). They conducted two experiments in which they prescribe different SST anomalies. The first one was associated with a strengthening of the South Atlantic Convergence Zone (SACZ) and consists of a cold SST anomaly over the subtropics, while the other one is the leading seasonally varying EOF of SST. Although the atmospheric response was sensitive to the SSTs in both experiments, only for the second one do the modelled results resemble observations. *Robertson et al.* (2003) thus concluded that the interannual variability in the SACZ is predominantly independent of the underlying SST in agreement with *Barreiro et al.*

(2000).

Further evidence for an atmospheric response to upper ocean temperatures has been provided by *Reason and Jagadheesha* (2005). The authors used an AGCM to explore the relationship between South Atlantic SST variability and the atmospheric circulation over the South African region during austral winter. Several idealised experiments were conducted. The results suggested that the atmosphere is sensitive to subtropical-midlatitude SST anomalies in the South Atlantic during winter and hence may lead to changes in regional circulation and rainfall over South Africa. An anomalous large scale response in the midlatitudes is also evident in the atmospheric model, which consisted of Southern Annual Mode and wavenumber-3 changes that are similar to those observed during anomalous winters in this region.

2.1.1 ENSO induced variability in the South Atlantic

Some of the studies mentioned above present evidence for a possible connection of the South Atlantic variability with ENSO. *Venegas et al.* (1996, 1997) found that the third mode of the EOF analysis of SST was highly correlated with the Southern Oscillation Index (SOI), as is the third mode of the combined variability between SST and SLP. The analysis suggested that warming in the central South Atlantic occurs one month prior to maximum warming in the equatorial Pacific. The anomalous pattern of SLP suggests southeasterly wind anomalies in the trades during ENSO phases. This result is in agreement with *Enfield and Mayer* (1997) who suggested that the ENSO impact in the tropical Atlantic consists of a north-southward shift in the ITCZ. A possible connection to the Pacific North American (PNA) pattern was also found, which is consistent with the correlation between the positive phase of the PNA pattern and the equatorial Pacific warming (*Horel and Wallace*, 1981). *Sterl and Hazeleger* (2003) found that South Atlantic variability is rather independent of that elsewhere. However, weak correlations between ENSO and the second coupled ocean-atmosphere modes are evident and in agreement with *Venegas et al.* (1997).

Further evidence of an ENSO impact on the South Atlantic region has been given by *Reason et al.* (2000), who investigated 100 years of GISST SST and UKMO/ CSIRO GMSLP, version 2.1f, for mean sea level pressure (MLSP). Although the main focus of this study lies in the investigation of ENSO and climatic signals across the Indian Ocean basin, global composites of SLP and SST anomalies for ENSO years in this study revealed a coherent response in the South Atlantic region that manifests itself in surface pressure and temperature anomalies there. It seems that during El Niño years, a general warming is apparent in the southern Benguela which extends across the basin, negative SST anomalies occur off the Angolan coast and the tropics. The corresponding SLP pressure fields show a general weakening of the subtropical high pressure system. These features are roughly the reverse for the La Niña year composites. Furthermore, analyses of SST anomalies in the western South Atlantic (*Lentini et al.*, 2000) show that warm (cold) phases of ENSO are connected to northward (southward) extensions of cold (warm) water a year later in that region. Other studies such as *Melice and Servain* (2003) find correlations between the tropical Atlantic meridional SST gradient (TAMG) and the SOI, again suggesting connections between ENSO and the South Atlantic region.

2.2 Tropical Atlantic variability

While relatively little research has been done on South Atlantic variability, the tropical Atlantic variability has been subject to numerous studies. There are two major modes of variability in the tropical Atlantic, (i) the meridional gradient mode, and (ii) the eastern cold tongue mode and Atlantic Niños. The first mode describes a pattern of variability with opposing sign on either side of the equator. Early observations (e.g. *Hastenrath and Heller*, 1977; *Moura and Shukla*, 1981) suggest a relationship between SST variability in the western tropical Atlantic and rainfall variability over the northern Nordeste region of Brazil. It was shown that dry spells in that region are often associated with an anomalous northward shift of the ITCZ, in conjunction with an anomalous northward gradient of SST. Somewhat weaker correlation with the northward gradient of SST and rainfall variability over the

African subcontinent were found (*Folland et al.*, 1986; *Hastenrath*, 1990; *Lamb and Peppler*, 1992).

The meridional gradient mode or Atlantic dipole and the associated structure of SST anomalies is controversial. Principal component analyses performed by *Weare* (1977) and *Servain* (1991) suggest a stationary cross equatorial pattern of SST, with variability on decadal time scales. This result is in agreement with *Carton et al.* (1996), who noted that the inter-hemispheric pattern of anomalous SST results from low frequency changes in the surface evaporation and are de-coupled from thermocline variations, implying that this mechanism will be most effective at low frequencies. However, other studies find that when the assumption of orthogonality has been relaxed the northern and southern hemispheres tend to act independently of each other (*Enfield and Mayer*, 1997; *Mehta*, 1998; *Rajagopalan et al.*, 1998).

Ruiz-Barradas et al. (2000) suggested that confusion about this mode arises as most authors did not take into account the coupled ocean-atmosphere variability when deriving this mode. They calculated the combined atmosphere-ocean variability using rotated SVD analyses and again confirm the existence of a cross equatorial dipole in agreement with *Nobre and Shukla* (1996). This mode fluctuates on a decadal time scale and is connected to a dipole pattern of atmospheric heating and is strongest in austral autumn. Fluctuations in SST seem larger in the northern hemisphere than south of the equator and the anomalous winds indicate a response to the SST gradient that consists of strong meridional cross-equatorial flow.

The second mode of variability is often seen as the Atlantic counterpart of the ENSO phenomenon, centred in the tropical Indo-Pacific. This mode has been shown to fluctuate mainly on interannual time scales (e.g. *Carton et al.*, 1996; *Ruiz-Barradas et al.*, 2000). Model studies from *Zebiak* (1993) suggested that this mode is more tightly focused on the equator and is positioned farther to the west then the Pacific counterpart. The mechanisms that generate this mode of variability involve coupled air-sea interaction following the principles of the Bjerknes feedback. Hence, ocean temperature anomalies lead to changes in the atmospheric meridional temperature gradient, and thus provide a positive feedback process. However, the

Atlantic coupled-mode signal is less robust than the corresponding Pacific ENSO signal and is not self-sustained (*Zebiak*, 1993). Thermocline variations are caused by variations in the zonal windstress at the equator, with weaker windstress to the west of the anomalous warm water (*Picaut*, 1985; *Carton et al.*, 1996; *Ruiz-Barradas et al.*, 2000). During warm events, the excess of warm water seems to originate either from the northwestern or southwestern basin. This mode is associated with anomalous heat content in the eastern equatorial basin and is strongly linked to the annual cycle, with maximum amplitudes in austral winter in conjunction with the development of the equatorial cold tongue.

Carton and Huang (1994) examined two warm events associated with the Atlantic Niño mode that occurred in 1984 and 1988 using an OGCM. Their results suggest that the 1984 warm event was closely connected to the El Niño event in 1983, whereby changes in the tropical Atlantic pressure system led to an early onset of the trades in late 1983. These stronger and longer lasting trade winds increased the heat content in the western tropical Atlantic, and deepened the thermocline in the west. The sudden relaxation of the trades in late 1983 led to an eastward propagating pulse of the heat stored in the western tropics, which resulted in the warming in 1984. By contrast, the warm event in 1988 resulted from changes in the equatorial winds during spring of the same year. However, both of these warm events were characterised by anomalous deepening of the thermocline in the east.

The tropical Atlantic is subject to strong forcing by external modes such as ENSO (*Enfield and Mayer*, 1997; *Roy and Reason*, 2001; *Melice and Servain*, 2003). The ENSO impact on the tropical Atlantic is found to be almost simultaneous with the establishment of anomalous SSTs in the central and eastern equatorial Pacific (*Giannini et al.*, 2001). During a warm ENSO event, the SLP is higher over the tropical Atlantic due to anomalous Walker circulation induced subsidence. This subsidence consequently leads to a weakening of the meridional SLP gradient and is consistent with reduced trades over both hemispheres. The PNA teleconnection pattern of ENSO then acts to reinforce the weakening of meridional SLP gradient thus leading to a warming in the tropical North Atlantic Ocean, peaking in austral

autumn.

The North Atlantic Oscillation (NAO) has been found to impact mainly on the northern tropical Atlantic variability, as it modulates the strength of the northeasterly trades and hence upper ocean temperature in the subtropical North Atlantic (*Xie and Tanimoto*, 1998). However, decadal extra-tropical forcing has been shown to force a dipole pattern that links both the northern and southern tropical Atlantic (*Xie and Tanimoto*, 1998; *Tanimoto and Xie*, 1999).

A possible NAO influence on rainfall variability over Central Equatorial Africa was investigated by *Todd and Washington* (2004). It appeared that the large scale circulation structure associated with rainfall in this area is similar at interannual and multi-annual time scales and showed the typical NAO signature. A possible link between the TNA and rainfall variability was found on multi-decadal time scales.

2.3 Variability in the South East Atlantic

Although some of the studies mentioned above do not explicitly focus on the South East Atlantic, they provide evidence for significant variability in this region. For an example the second, ENSO related mode of the coupled ocean-atmosphere system presented by *Sterl and Hazeleger* (2003) displays major amounts of variability of opposing signs in the Angolan and Benguela Current regions, with the zero line approximately running along the ABFZ. This suggests possible large scale influences on a regional scale and is in agreement with *Reason* (2000), who also provides evidence of ENSO related variability in the area.

Generally, few reliable long-term data series are available for the South East Atlantic (*Shannon and Nelson*, 1996). The longest dataset exists for SST and dates back from the early part of this century. However, it is fragmented both in time and space. Subsequently, most of the understanding of low frequency variability in the South East Atlantic has been deduced from case studies of extreme events (*Shannon and Agenbag*, 1990).

Walker (1987) performed a principal component analysis in order to investigate interannual SST variability and associated atmospheric forcing within the Benguela

system. The analysis suggested a coherency of SST events in tropical and subtropical areas of the South East Atlantic, with the sustained cool event from 1981 - 1983 being a remarkable exception of the nearshore/ offshore coherency. In general, SST trends in the southern Benguela differ markedly from those farther north due to the Agulhas Current influence and different seasonality in the upwelling seasons. Warm (cold) SST events in the subtropics were found to correlate fairly well with reduced (enhanced) equatorward windstress.

Taunton-Clark and Shannon (1988) highlighted some of the key aspects of interannual to decadal variability in the South East Atlantic during the last 80 years (1906-1984) using data obtained from the South African Data Centre for Oceanography (SADCO). They examined SST and pseudo-windstress in six areas, which they find representative for the shelf and oceanic regimes, respectively. Although the dataset is scattered in time and space, they were able to draw a general picture of the variability present in the area. A principal component analysis of SST revealed an increasing trend in SST this century, with the post World War II era being typically 0.8°C warmer than earlier periods. This trend was accompanied by stronger equatorward winds during the last few decades. Furthermore, the existence of a weak 8-10 year cycle has been found that coincides with the mean period of the Benguela Niños (as discussed below).

In a more recent study, *Rouault et al.* (2003) present composite patterns of SST, moisture flux and precipitation rates of 4 events in which anomalous warming occurred off the Angolan Coast (1984, 1986, 1995, 2001) and found that these warm events are generally associated with enhanced precipitation over Angola/ Namibia. However, the strength of the upper ocean warming and the anomalous precipitation rate is not necessarily linear, suggesting that the associated mechanisms producing the rainfall anomalies differ between the events. In fact, moisture flux anomalies indicate that during the warm events of 1984 and 1986 an anticyclonic pattern existed over the sub-continent. This pattern reduces the southeasterly climatological export of moisture along the southwestern African coast, and at the same time enhances the moisture flux from the South West Indian Ocean, leading to the strongest rainfall

anomalies. On the other hand, during the warm events of 1995 and 2001 a cyclonic pattern in moisture flux was apparent. Thus, the moisture transport from the South West Indian Ocean is reduced. The stronger than average precipitation rate here is rather the result of entrainment of moisture favoured by local SST anomalies, which act to augment the moisture transport from the South West Indian Ocean.

2.3.1 Benguela Niños

The El Niño phenomena in the Pacific has a less well known counterpart in the South East Atlantic, which has been termed "Benguela Niño" (after *Shannon et al.*, 1986). Benguela Niños are less frequent and intense than the Pacific events, and reflect the smaller South Atlantic scales. They express themselves as extreme warm events in the tropical South East Atlantic and are accompanied by intrusions of warm saline tropical surface waters along the Angolan and Namibian coast (*Shannon et al.*, 1986; *Boyd et al.*, 1987). These events have been documented by various authors (e.g. *Stander and De Decker*, 1969; *Gammelsrod et al.*, 1998; *Rouault et al.*, 2003) and have been recorded in 1934, 1963, 1984, 1995, 1999 and 2001. Benguela Niños tend to occur in late austral summer to early autumn, and are thus manifested in a different season than the Atlantic Niños (discussed above) which are dominant in austral winter.

Shannon et al. (1986) provided the first detailed discussion of the Benguela Niños occurring in 1934, 1963 and 1984. It appeared that these events coincided with periods of low or reduced zonal windstress in the western tropical Atlantic and were associated with anomalous flow in the equatorial current system, suggesting that large scale forcing rather than local changes in windstress were responsible for driving these events. However, *Horel et al.* (1986) suggested that the sudden changes in the wind patterns over the western equatorial region are more important than the absolute values. This is in agreement with *Carton and Huang* (1994) who modelled the warm event in 1984. Their results indicated that the Benguela Niño during that year was associated with a relaxation of the stronger than normal trade winds. Furthermore, variations in the trade winds over the western tropical Atlantic appear to

trigger equatorial Kelvin wave-like disturbances. These disturbances are transported eastward via the equatorial wave guide and may be reflected south and northwards along the western African coast as coastal trapped waves (*Carton and Huang*, 1994; *Carton et al.*, 1996; *Florenchie et al.*, 2003). However, the eastward propagation of these disturbances is typically too slow when compared with theoretical calculations, suggesting that coastal shelf, slope bottom or bottom friction modify the phase speed of the propagating wave (*Clark and Van Gorder*, 1994; *Pizarro et al.*, 2001).

Florenchie et al. (2003, 2004) investigated the sources of the Benguela Niños using model and altimeter data and found that most of these events are correlated with windstress anomalies over the western tropical Atlantic, thus confirming the results of *Carton and Huang* (1994). Furthermore, they provided evidence that warm temperature anomalies travel southward, beneath the surface layer, and eventually outcrop off Angola when they meet the northern Benguela upwelling system.

2.3.2 The Benguela upwelling system

The Benguela is one of the four major eastern boundary current regions of the world ocean but is unique in that it is exposed to a warm water region at both its equatorward and poleward margins. The oceanography is dominated by a coastal upwelling system that is strongly controlled by the pressure gradient between the South Atlantic Anticyclone and the pressure system over adjacent subtropical southern Africa. In simplistic terms, the latter is dominated by a winter anticyclone and, in summer, by heat lows that develop most strongly over the western interior. The associated winds over the northern (southern) Benguela Current large marine ecosystem (BCLME) region are therefore mainly southerly throughout the year (southerly or southeasterly in summer but more westerly in winter). The prevailing southerly winds induce Ekman transports that, in turn, drive the upwelling cells (*Peterson and Stramma*, 1991) that are strongest in winter along the Namibian coast and in summer along the south-western South African coast. Clearly, seasonal variations of the subtropical high pressure system strongly affect the upwelling region - allowing

westerly winds and frontal disturbances to become more dominant in the south in winter and weakening the southerly winds in the northern Benguela in summer.

On synoptic and intra-seasonal scales, sources of variability in the coastal winds result from the occurrence of cold fronts, berg wind events or mesoscale offshore flow events (*Tyson and Preston-Whyte*, 2000), coastal lows (*Reason and Jury*, 1990), west coast troughs and cut-off lows (*Singleton and Reason*, 2006) over the southern Benguela. Over the northern Benguela easterly waves and pulses in tropical convection are important. The latter may occur either over Angola and Congo in the summer half of the year, or over West Africa in austral winter (*Risien et al.*, 2004). Analysis of QuikSCAT wind data by these authors showed that most parts of the Benguela upwelling system are characterised by significant intra-seasonal variations in alongshore windstress.

The northern and southern boundaries of the Benguela upwelling system are the Angolan Current, with the associated Angola Benguela Front and to the south the Agulhas Current and its retroflection zone. The Agulhas ring shedding that occurs at the retroflection zone is known to play a role in affecting the global overturning circulation (*Gordon et al.*, 1992; *Lutjeharms*, 1996; *de Ruijter et al.*, 1999; *Sloyan and Rintoul*, 2001). The Agulhas rings influence water mass properties in the Benguela Current region and thus, via this current transport warmer and saltier water to the northwest South Atlantic. Model simulations (e.g. *Reason et al.*, 2003) suggest that heat and volume fluxes between the South Atlantic and South Indian Oceans in the Agulhas Region are highly variable, having significant implications for South Atlantic climate variability.

2.3.3 The Angola Benguela Frontal Zone (ABFZ)

A sharp thermal front situated at approximately 16°S was first reported by *Hart and Currie* (1960). While sailing southward along the coast from Lobito in Angola on the R.R.S *William Scoresby*, these authors registered a decrease in temperature from 27°C to 20.5°C within only one hour. Although the thermal gradient may have been anomalously strong (*Shannon et al.*, 1986), the reported position of the front is

in good agreement with observations thereafter (e.g. *Shannon et al.*, 1987; *Meeuwis and Lutjeharms*, 1990; *Shannon and Nelson*, 1996; *Kostianoy et al.*, 1999).

Large scale characteristics of the ABFZ as described by *Shannon et al.* (1987) reveal a zonally orientated front, separating the waters of the opposing Benguela and Angola Currents with typical temperature gradients of 4°C per 1° of latitude. The front is particularly marked in the upper $50m$, but may extend to a depth of $200m$ as suggested by salinity data. Persistent tongue like features of warm water between 12°S and 16°S exist due to the combined effect of poleward flow and coastal upwelling over a steeply shelving bottom. On the mesoscale there is evidence of two existing fronts in the area between 14°S and 18°S. While the southern most front may be associated with the Benguela upwelling system and hence marks the northern boundary of the Benguela system, the northern front relates to the Angola tongue, as its position coincides with the penetration of tropical and equatorial surface waters. The current system in the ABFZ is rather complex, as intense stratification occurs, particularly north of 16°S, and strong vertical shear in the currents is likely. *Shannon et al.* (1987) noted that the upper ocean currents will depend to a certain degree on the winds, but the dominant flow is determined by the interaction between the Benguela and Angola Currents. Variability in the ABFZ occurs in time and space. There is a general seasonal shift of the front of about 2° of latitude. On time scales of days, migrations of $150km$ or more have been observed.

Shannon et al. (1987) suggested that the front is maintained around 16°S due to a combination of factors. These include the coastline orientation, bathymetry, stratification and windstress. The coast changes its direction at Cape Frio and Porto Alexander, which has consequences for the upwelling. Also a dramatic change in the width of the shelf and the steepness of the continental slope is apparent between 15°S and 20°S. Changes in stratification and upwelling-favourable winds also exist between these latitudes.

Meeuwis and Lutjeharms (1990) investigated the ABFZ using satellite derived weekly maps of SST for the period of 1982 to 1985. They concluded that the ABFZ is a permanent feature at the sea surface between 14°S and 16°S. The front is most

clearly defined in austral summer, when it reaches its southern most position, while it is less intense and positioned farthest north in winter. The frontal zone consists at times of double fronts, most commonly during summer. In contrast to *Shannon et al.* (1987), *Meeuwis and Lutjeharms* (1990) concluded that the position of the front is almost exclusively controlled by the opposing Angola and Benguela Currents. Strongest southward flow in summer is therefore accompanied by maximum temperature gradients within the front, which is also widest and extents farthest offshore during that season.

Short term variability of the ABFZ has been investigated by *Kostianoy et al.* (1999). They examined 72 days of thermal infra-red observations for the period April 1 to June 13, 1988. During that period, they observed the typical seasonally related northward propagation of both northern and southern borders of the front. The positions of the southern (northern) border changes from 18°S to 16.5°S (16°S to 15°S), with short term changes of about 1.5° superimposed. Short term movements of the front were best correlated with the pressure gradient associated with the South Atlantic Anticyclone (SAA). High SAA gradients were associated with a northward movement of the southern border of the ABFZ a day later and an increase in temperature.

Lass et al. (2000) examined hydrographic and current measurements in the area of the ABFZ from 20 April to 13 May 1997. They observed the position of the front at 16.5°S, separating a $40m$ thick layer of, warm and saline Angola Current water in the north from the cold and less saline water of the Benguela in the south. A poleward current was found to enter the study area through the northern boundary at 13.5°S. Furthermore, an eastward directed geostrophic current driven by the windstress *curl* entered the region from the northwest in the upper $400m$ bending southward at 15°S. *Lass et al.* (2000) suggested that this current is an important link between the cyclonic gyre in the Angola Dome area and the source region of the Benguela Current.

Variability on interannual to decadal time scales within the ABFZ has been observed by *Veitch et al.* (2005) who examined observational data for SST. It appears

that anomalous southward positions of the ABFZ occur in conjunction with warm events such as Benguela Niños and may be the result of coastally trapped waves, generated by wind anomalies in the tropical Atlantic.

Kim et al. (2003) indirectly showed that the thermal gradient associated with the front may vary on time scales of up to millennia. The authors reconstructed the associated trade wind intensity under the assumption that any changes in the winds may alter the strength of the front. The basic idea behind their study was that the southeast tradewinds influence heat transport from the South Atlantic subtropical zone into the western equatorial Atlantic by affecting the intensity of the South Equatorial Current (SEC, *Johns et al.*, 1998). During stronger tradewinds the SEC is enhanced, hence leading to increased heat transport into the region north of the ABFZ. At the same time enhanced upwelling is also favoured by the stronger trade winds and thus leads to cooler temperatures towards the south of the ABFZ. Therefore, increased tradewinds trigger both cooling south of the ABFZ and warming to the north of it and thereby effectively enhancing the temperature gradient across the ABFZ.

2.4 Summary and motivation

This review has highlighted previous research on South Atlantic climate variability on interannual to inter-decadal time scales. Furthermore, it appears that most of the South Atlantic variability is derived from regional atmospheric forcing. Changes in upper ocean temperatures within the subtropics are found to be connected to changes mainly in latent heat flux (e.g. *Reason*, 2000; *Sterl and Hazeleger*, 2003), while in the midlatitudes wind induced mixing becomes more important (*Sterl and Hazeleger*, 2003; *Haarsma et al.*, 2005), the role of advection appears to be important in the dynamical active areas, such as the MFBCZ, and the western boundary currents (*Reason*, 2000).

In the tropical Atlantic, variability on interannual and decadal time scales is associated with two different modes, whose dynamics vary substantially. It appears that wave-like disturbances may be associated with interannual variability, manifest

at the zonal mode or Atlantic Niño (*Picaut*, 1985; *Carton et al.*, 1996; *Ruiz-Barradas et al.*, 2000; *Florenchie et al.*, 2003), while variability on interannual to inter-decadal time scales is associated with the cross-equatorial mode (*Weare*, 1977; *Servain*, 1991) . This mode has been under debate but seems to be firmly established when considering the combined ocean-atmosphere variability (*Ruiz-Barradas et al.*, 2000).

The Benguela Niños seem to arise from similar mechanisms to the Atlantic Niños but peak in a different season. These events extend towards the South East Atlantic and are the dominate mode of variability there. Problematic in this region is the lack of observational data and its inhomogeneous distribution in time and space. Hence, most of the knowledge of South East Atlantic variability has been deduced from case studies (*Shannon and Nelson*, 1996).

The ABFZ has been shown to vary on different time scales. Since the ABFZ separates the cold nutrient rich Benguela upwelling system from the warm nutrient poor Angolan Current, any anomalous shifts in the position or strength may have substantial socio-economic effects on the southern African region via changes in fisheries and rainfall. On longer time scales, variability in the ABFZ may even be considered as a proxy for climate changes (*Kim et al.*, 2003).

Relatively few analyses on South Atlantic variability have been done using OGCMs, coupled GCMs or regional models. The advantage of using model derived data is obvious: Models offer a more complete picture of what is happening in the oceans since they supply not only information about the surface but also allow insights into the ocean dynamics within sub-surface levels. Furthermore, the data supplied by ocean models is homogeneous in both time and space. On the downside, ocean models strongly depend on the given boundary conditions, which according to *He et al.* (2004) may limit the quality of ocean model output. Due to the various time scales that exist within the oceanic circulation, long spinup times are needed to reveal an oceanic mean state. When considering the deep water flow, equilibria are only established after centuries. Hence, a careful approach is necessary when using ocean models. With this in mind an OGCM and a regional ocean model are used in this thesis in an attempt to fill some gaps in knowledge about variability in

the South Atlantic. The following key questions are posed:

- **What are the dominant mechanisms of low frequency variability within the South Atlantic ?**

  The South Atlantic leading modes have shown to be closely connected to the overlying atmospheric circulation. However, there is still some debate about the spatial and temporal structure of these modes. Furthermore, associated mechanisms, heat and volume fluxes need to be firmly established. In order to go beyond previous work, the leading modes diagnosed from model output will be investigated. Only OGCMs can provide additional information on advective processes and baroclinic structures of the upper ocean. This information is vital in order to further understand the role of South Atlantic ocean variability in a global and regional climate context.

- **How does ENSO project onto the South Atlantic region ?**

  Several authors provide evidence for significant ENSO related variability in the South Atlantic. A dedicated study for the South Atlantic examining the evolution, impact and possible mechanisms of ENSO related variability is still missing, but will be addressed in this thesis.

- **How sensitive is the position and strength of the Angola Benguela Frontal Zone towards changes in windstress ?**

  The ABFZ has been shown to be an important system boundary between the Benguela ecosystem and the tropics. It is thought that the position and intensity of the ABFZ depends on several factors, as the coastline orientation, windstress and topography. However, so far, no study exists that examines the possible influence of these factors. Several experiments with a regional ocean model forced with anomalous windstress have been designed in order to address the above question.

- **What are the preferred time scales of variability in the ABFZ ?**

  It is necessary to understand the natural variability within the ABFZ in order to distinguish it from other, remotely forced variability. A regional ocean

model, applied to the South East Atlantic region, is applied in order to investigate the intra-annual to interannual variability in the frontal area.

3 Data and Methods

In this study, an ocean general circulation model (OGCM) and a regional ocean model are used to investigate South Atlantic Ocean variability. Details of the model physics and configurations will be given in the first part of this section. The datasets used in this thesis are discussed thereafter, followed by a description of the statistical methods employed. Finally, some important variables analysed in this thesis are introduced.

3.1 Ocean models

3.1.1 Ocean General Circulation Model (OGCM)

The OGCM used is the ORCA2 model, which is the global version of the Ocean Parallelise (*Madec et al.*, 1998). The global domain extends from 78°S to 90°N. The bottom topography and coastlines are derived from *Smith and Sandwell* (1997) data complemented by values from the 5'× 5' ETOPO 5 data set at the northernmost latitudes. Lateral mixing is oriented isopycnically, and the eddy parametrisation scheme of *Gent and McWilliams* (1990) is applied poleward of 10 degrees in both hemispheres. Vertical mixing is achieved using the TKE scheme of *Blanke and Delecluse* (1993). The zonal resolution is 2 degrees, the meridional resolution decreases from 0.5° at the equator to $2 \times cos(latitude)$ poleward of 20 degrees in either hemisphere. The model grid is tripolar, with two poles in the Northern Hemisphere (over North America and Siberia) and one centred over Antarctica. In the vertical, the model consists of 30 layers with 20 of these layers in the upper $500m$. Thus, the model has appropriate resolution to represent both the equatorial circulation and upper ocean processes. A sea ice model representing both thermodynamic and dynamic processes is coupled to the OGCM (*Fichefet and Morales*, 1997). The OGCM model is initialised with *Levitus* (1998) temperature and salinity values.

The surface boundary condition is a bulk mixed layer that is given the air temperature, air humidity, total cloudiness, surface pressure and surface windspeed (from the NCEP/ NCAR reanalysis) from which surface heat fluxes are calculated. Since

the NCEP/ NCAR reanalysis uses observed SST as a lower boundary condition and observations in the South Atlantic are relatively sparse before 1958, the quality of these reanalysis could be questioned. However, *Sterl and Hazeleger* (2003) have discussed this problem in detail and conclude that using the reanalysis in the South Atlantic is reasonable. A 200 year spin up with a restoring boundary condition on surface salinity (2 month time scale) and climatological wind and heat flux forcing has been performed (*Madec et al.*, 1998). A salinity flux correction for the 1948-1999 run has been made by applying the annual mean fluxes from the last 50 years to the interannually varying NCEP runs. Salinity variability may affect the ocean circulation due to density changes, which may then lead to pressure gradient changes and anomalous currents. Given the relatively poor quality of available freshwater flux data, this approach is necessary and is also frequently used by other modellers (e.g. POCM, *Stammer et al.*, 1996). The model output analysed in this study consists of a 24.33 day average (i.e. 15 outputs per year) for each variable for the 1948-1999 period.

3.1.2 Regional Ocean Modelling System (ROMS)

Model Description

The regional ocean modelling system (ROMS) solves the incompressible, hydrostatic, primitive equations of fluid dynamics with a free surface. The coordinates in the horizontal are curvilinear, while they are terrain following in the vertical. The prognostic variables are the surface elevation and the barotropic and baroclinic horizontal velocity components as well as the material properties temperature and salinity.

The open boundary conditions are a combination of outward radiation and flow-adaptive nudging towards prescribed external conditions (*Marchesiello et al.*, 2001). The advection operator is third order, upstream biased, and designed to reduce dispersive errors. Excessive dissipation rates are needed to maintain smoothness, thereby effectively enhancing the resolution on a given grid (*Shchepetkin and McWilliams*, 1998).

The interior vertical mixing is calculated using the non-local K-Profile parametrisation scheme (*Large et al.*, 1994). A mode splitting technique separates the barotropic and baroclinic components. The time stepping scheme is a leapfrog/ Adams-Moulton predictor-corrector scheme, which is third order accurate in time.

Model Configuration

In this thesis the ROMS model is applied to the South East Atlantic region, with the aim of investigating the intra-annual to interannual variability within the Angola Benguela Frontal Zone. Possible mechanisms that are important in altering the frontal position and its intensity are also established. Thus, the model domain extends meridionally from 30°S to 7°N, including equatorial dynamics, and zonally from 5°W to 20°E. The horizontal grid spacing is 1/3°, which is high enough to sufficiently resolve the ABFZ, but at the same time allows for longer integrations at reasonable computational costs. The model has 32 vertical levels. The explicit lateral viscosity (diffusivity) is zero inside the model domain and increases within $200\,km$ (i.e. the sponge layer width) of an open boundary and attains a maximum value of $2000\,m^2/s$ (see also *Penven et al.*, 2005a). The bottom topography is derived from a 2' resolution database (*Smith and Sandwell*, 1997). The model is nested within the ORCA2 model (as described above), which provided temperature and salinity for initialisation and the monthly climatology of temperature, salinity and velocities, as well as fresh water fluxes for the open boundaries and upper ocean forcing. Heat fluxes are taken from the NCEP/ NCAR reanalysis (*Kalnay et al.*, 1996).

For the windstress a monthly mean climatology is computed from QuikSCAT satellite scatterometer data (*Liu et al.*, 1998), covering the period from October 1999 till March 2003. The reference run is then integrated for 32 years and serves to investigate the intra-annual to interannual variability within the ABFZ.

A series of experiments have been conducted in order to investigate the response of the ABFZ towards changes in windstress. These experiments were each integrated for 10 years, and will be described in more detail in Section 6.

3.2 Datasets

3.2.1 Global Ice and Sea Surface Temperature 2.3 (GISST2.3)

The GISST dataset version 3.0 (*Rayner et al.*, 1996), has a zonal and meridional resolution of 1 degree and is available from 1856 to present. The derived SSTs are based on the in-situ data set of the UK Meteorological Office Historical Sea Surface Temperature Anomalies (MOHSST). Gaps in the data are filled using Empirical Orthogonal Function (EOF) interpolation. GISST sea-ice fractions are based on a mixture of charts, satellite observations and statistical interpolations. The GISST2.3 data set is thought to be suitable for monthly and seasonal comparisons with the ORCA2 data.

3.2.2 National Centre for Environmental Prediction/ National Centre for Atmospheric Research (NCEP/ NCAR reanalysis)

The NCEP/ NCAR reanalysis (*Kalnay et al.*, 1996) is a global reanalysis for atmospheric fields. Data from land surface, ship, rawinsonde, pibal, aircraft, satellite and others are assimilated. The global resolution is 2.5° and the reanalysis starts from the year 1948. The sparse data coverage over the Southern Ocean may potentially have consequences for the quality of reanalysis, as well as inhomogeneities due to the availability of satellite data after 1982. Several authors have addressed this issue. *Mulenga et al.* (2003) find the NCEP/ NCAR reanalysis reasonable for analysing large scale circulation anomalies over the South Atlantic, while *Tennant* (2004) concluded that the NCEP/ NCAR reanalysis is best suited to analyse seasonal to interannual time scales. *Sterl and Hazeleger* (2003) noted, that since the reanalysis data are derived from model output, they are internally consistent, which is important for studies that deal with the coupled variability of the ocean and atmosphere. Furthermore, validity of the reanalysis is provided by the relationships between the latent heat flux and the upper ocean temperature. These quantities are thought to be strongly positively correlated in the extra-tropics. *Sterl* (2001) showed that this correlation is present in the reanalysis.

3.2.3 QuikSCAT

The Seawind scatterometer, QuickSCAT was launched in June 1999. Its orbit is about $110km$ and its swath is $1800km$. Spaceborne scatterometers transmit microwave pulses to the ocean surface and measure the electromagnetic backscatter received at the instrument. An indirect technique is used to measure the wind velocity over the ocean. Windstress generates ripples and small waves and roughens the sea surface. The roughness of the sea surface modifies the radar cross section (sigma-0) of the ocean surface and hence the magnitude of the backscattered power. The relationship between sigma-0 and the near surface winds is known as the geophysical model function (*Dunbar*, 2000). The QuikSCAT model function has a tendency to underestimate high winds. There is also insufficient information in its behaviour in calm situations. The level 3 data used here is given on a global grid with 1440 grid points in the longitudinal direction and 720 grid points in the latitudinal. Hence, the resolution is 0.25° in each direction.

Measurements of the ocean roughness become contaminated in the presence of rain as some of the transmitted energy is backscattered by the rain before it reaches the ocean surface. This part of the backscattered energy may contribute towards a significant, but unknown, part of the measured energy. Some of the transmitted energy is scattered or absorbed by the rain and hence is therefore never measured by the scatterometer. In addition the rain alters the ocean's roughness and changes its radar cross section (*Huddleston and Stiles*, 2000).

3.3 Statistical tools

To analyse data from model output and the different datasets described above, various statistical tools are used in this thesis. In the following two of them will be described in more detail. They are Empirical Orthogonal Function analysis and Wavelet analysis. Other well known, statistical methods employed in this thesis, which are not described in full detail here, are: Correlation and regression analyses and statistical significant tests.

3.3.1 Empirical Orthogonal Functions (EOFs)

Variability of the global climate system is the result of complex linear and non linear interactions with its subsystems (e.g. the ocean and atmosphere). Since these systems inherit a very large amount of degrees of freedom, one major challenge to date is to recognise and define the important modes of variability in a given subsystem. EOF analysis is known to be an excellent tool for reducing the variables and therefore the degrees of freedom in a given system, while at the same time keeping most of its variance. Since the analytical derivation of EOFs is fairly simple (see below), it has become a widely used instrument in analysing geophysical data sets. Two limitations of EOF analyses should be mentioned (*Richman*, 1986),

(a) due to its mathematical formulation, the resulting spatial pattern and time series are orthogonal in space and time and

(b) the spatial patterns are often sensitive to the given domain under investigation.

Both points make physical interpretation of EOFs often very difficult or even impossible, as there is, for example, no *a priori* reason for physical modes to be orthogonal. To overcome these shortcomings, the EOFs are typically *rotated*. The basic idea behind rotated EOFs is to maximize the variability in a certain region. This leads to more localized structures whilst at the same time compromising some of the EOFs properties such as orthogonality (*Hannachi*, 2004). Usually the rotation is done by defining a new basis for the already derived EOFs. This basis is found by defining a rotation matrix that fulfils a given minimisation criterion. The most widely used is the *varimax* criteria formulated by *Kaiser* (1958).

In this thesis the EOFs are rotated using the varimax rotation in sample space (also known as dual space rotation). This results in a new set of orthogonal expansion coefficients, while the associated eigenvectors are no longer orthogonal. A short description of the formalism is given here. A more detailed discussion is given in *Richman* (1986); *von Storch* (1995); *Björnsson and Venegas* (1997); *Hannachi* (2004) and references therein.

Derivation of EOFs

Given a centred data matrix X, the covariance matrix R may be defined as:

$$R = \frac{1}{n-1} X^t X, \tag{1}$$

with n being the number of observations. The aim of the EOF analysis is to find linear combinations of the grid points that explain maximum variance. This is equivalent to finding a vector $\mathbf{a}$ so that $X\mathbf{a}$ has maximum variability. Assuming $\mathbf{a}$ to be unitary, this problem can be defined as:

$$max(\mathbf{a}^t R \mathbf{a}). \tag{2}$$

The solution of Equation 2 is the eigenvalue problem,

$$R\mathbf{a} = \lambda \mathbf{a}, \tag{3}$$

with λ being the eigenvalue corresponding to the eigenvector $\mathbf{a}$. There will be as many eigenvalues as original variables. However, many of them will not be significantly different from zero. The eigenvalue λ_k corresponding to the k^{th} EOF gives a measure of the explained variance by $\mathbf{a_k}$. It is given as:

$$\frac{\lambda_k}{\sum_{k=1}^{p} \lambda_k}, \tag{4}$$

where p is the number of gridpoints (*Hannachi*, 2004).

Varimax rotation

As stated above the intention of rotating EOFs is to maximize the variability in a certain region. Given a rotation matrix Q, the rotated EOFs are given as:

$$U = LQ, \tag{5}$$

where L is the matrix containing the number of leading EOFs to rotate. The choice of the matrix Q constitutes the rotation algorithm. The most widely used criterion is the varimax criterion (*Kaiser*, 1958):

$$\max \left(\sum_{k=1}^{m} \left[p \sum_{j=1}^{p} u_{ij}^4 - \left(\sum_{j=1}^{p} u_{ik}^2 \right)^2 \right] \right), \tag{6}$$

where $U = (u_{ij})$ are the rotated EOFs and m is the number of EOFs chosen for rotation. The quantity inside the square brackets is proportional to the spatial variance of the square of the rotated vector $\mathbf{u_k}$. The varimax rotation thus tends to simplify patterns by maximizing the variance, tending the coefficients towards 0 or 1 (*Hannachi*, 2004).

3.3.2 Wavelet analysis

Wavelet analysis is well suited to study multi-scale, non-stationary processes that occur over a finite spatial and temporal domain (*Lau and Weng*, 1996; *Emery and Thomson*, 1998). The Wavelet transform decomposes a time series into time frequency space, producing a localised , 'instantaneous' estimate for the amplitude and phase of each spectral component. From this it is possible to determine both, the dominant modes of variability and how these modes vary in time. Wavelets are widely used in meteorology and oceanography, including turbulence, surface gravity waves and variation in ENSO (e.g. *Emery and Thomson*, 1998; *Torrence and Compo*, 1998; *Risien et al.*, 2004).

The continuous wavelet transform (CWT) decomposes a signal $x(t)$ into elementary contributions of both space and time. The mathematical tools allowing for this transformation are called wavelets. They are derived from a single function ψ, which is modified by dilatation and translation, hence

$$\psi_{b,a} = \frac{1}{a}\psi\left(\frac{t-b}{a}\right), \tag{7}$$

with $a > 0$ and b being the dilatation and time translation parameters, respectively.

The CWT of the signal $x(t)$ with the analysing wavelet ψ is the convolution of $x(t)$ with a set of dilated and translated wavelets The CWT expands a time series $x(t)$ into a two-dimensional parameter space (b,a) and yields a measure of the relative amplitude of local activity at scale a and time b (*Melice et al.*, 2001). The choice of the wavelet ψ depends on the signal to be analysed. In this thesis the Morlet *Morlet* (1983) wavelet is chosen. It is a complex cosine wave modulated by

a Gaussian function

$$\psi(t) = \pi^{-1/4} e^{-t^2/2} e^{i\omega_0 t}, \tag{8}$$

with $i = (-1)^{1/2}$ and where $\omega_0 = \pi(2/ln2)^{1/2}$ (*Daubechies*, 1992) is chosen large enough to ensure that $\psi(t)$ satisfies the admissibility condition which is equivalent to

$$\int_{-\infty}^{\infty} \psi(t)dt = 0. \tag{9}$$

When inverting the scale of the Morlet wavelet the CWT becomes a time frequency analysis, in which the dilatation parameter a corresponds to the period and the translation parameter b to the time. In Equation 7, the normalisation $1/a$ is used instead of the usual $1/a^{1/2}$. This allows for a direct comparison of the CWT and the Morlet wavelet can be interpreted as a bandpass filter of weight $1/a$ centred around $\omega = \omega_0/a$. The filter thus allows for the extraction of the different local components of the signal (local value, amplitude and phase), for each point of the time frequency space (*Melice et al.*, 2001).

3.4 Variables analysed

In this section, an overview is given of some of the fundamental equations of geophysical fluid dynamics relevant to this thesis. In addition, the meridional and zonal ocean heat transport and the heat budget of the ocean's mixed layer are discussed. This section ends with a description of a variable called the "Combined Windstress Anomaly and Climatology Pattern", which will be used in Section 5.

3.4.1 Oceanic velocity

Horizontal velocity

The horizontal component of the velocity $\mathbf{v}$ can be split up into a geostrophic and an Ekman part, so that $\mathbf{v} = \mathbf{v_g} + \mathbf{v_e}$. The geostrophic velocity is due to existing pressure gradients, which depend on the sea surface height h_{ssh}:

$$\mathbf{v_g} = -\mathbf{k} \times \frac{g}{f} h_{ssh}, \tag{10}$$

where f is the Coriolis parameter, g the gravitational acceleration and $\mathbf{k}$ a unit vertical vector. Alternatively, when the horizontal density distribution is known, the geostrophic velocity can be derived by integrating the thermal wind equation, hence solving

$$\frac{\partial \mathbf{v}}{\partial z} = -\frac{g}{\rho f}\mathbf{k} \times (\nabla \rho), \tag{11}$$

with ρ being the density. An assumption has to be made about a level of no motion, which is required in order to fulfil the necessary boundary condition for the integration. This level clearly depends on the region of interest. Depths of below $500m$ are often found to be adequate.

Ekman velocities are entirely due to the presence of frictional forces. For the upper ocean the friction is proportional to the wind. The bulk formula is often used to estimate the windstress from the wind direction and speed. It is given as:

$$\tau = \rho_a C_d |\mathbf{v}| \mathbf{v}, \tag{12}$$

where τ is the resulting windstress vector, ρ_a the density of air and C_d the non-dimensional drag coefficient, which is a function of the windspeed $|\mathbf{v}|$. Typical values for the drag coefficient are between $C_d = 1.2 \times 10^{-3}$ and $C_d = 0.5 \times 10^{-3}$.

The total mass flux per unit area in the Ekman layer $\mathbf{M_E}$ is perpendicular and to the left (Southern Hemisphere) of the frictional stress acting upon the fluid. It is given as:

$$\mathbf{M_E} = \frac{\tau \times \mathbf{k}}{\rho f} \tag{13}$$

Since,

$$\mathbf{M_E} = \int_0^\infty \mathbf{v} dz, \tag{14}$$

it follows that the horizontal Ekman velocities can be calculated from the derivative of Equation 13. Assuming that the depth of the Ekman layer can be approximated by the depth of the mixed layer z_h the horizontal velocities are derived from Equation 13 by dividing it by z_h.

Vertical velocity

Vertical velocity can be obtained from horizontal velocities due to mass conservation, which simply requires that the net flow in and out of an arbitrary sized

volume is zero. This fundamental law is expressed by the equation of continuity, which, when density changes are taken into account can be written as:

$$\frac{d\rho}{dt}\frac{1}{\rho} = \frac{\partial u}{\partial x} + \frac{\partial v}{\partial y} + \frac{\partial w}{\partial z} \tag{15}$$

From here it follows that if the density and the horizontal velocities are known, the vertical velocity component can be found by integrating the above equation. The necessary boundary condition is fulfilled when assuming zero vertical motion at the top of the layer.

The same applies for the vertical Ekman velocity, which is given as the divergence of the horizontal Ekman mass transport. Since Ekman velocities are purely caused by frictional forces, they can be expressed as a function of the applied stress. For the upper Ekman layer this readily yields,

$$w_e = \frac{1}{\rho f}\left(\frac{\partial \tau_y}{\partial x} - \frac{\partial \tau_x}{\partial y}\right), \tag{16}$$

where w_e is the vertical Ekman velocity. The upward (downward) vertical velocities due to the applied windstress are usually referred to as *Ekman pumping (suction)* velocities.

3.4.2 The Sverdrup balance

One of the most important relationship between windstress and oceanic mass transport is expressed by the Sverdrup relation, which states that the total meridional mass transport M_y is given by the *curl* of the windstress,

$$\beta M_y = \mathbf{k}\, curl \frac{\tau}{\rho}, \tag{17}$$

where $\beta = \partial f/\partial y$ and is the variation of the Coriolis frequency with latitude. The assumptions leading to the Sverdrup relation are flat bottom, negligible accelerations and friction from horizontal gradients of velocity. The zonal mass transport can be derived by integrating the equation of continuity for mass transport in the westward direction. This requires an eastern boundary, where $M_x = 0$.

3.4.3 Oceanic heat transport

The meridional heat transport Q (the zonal heat transport can be calculated accordingly) across a section of width L and thickness h is to good approximation given as

$$Q = \int_0^L \int_{-h}^0 \rho C_p \theta \, v \, dxdz, \tag{18}$$

where ρ is the density, θ the potential temperature, C_p the specific heat capacity and v the absolute meridional velocity of the water across the latitude circle (e.g *Bryan*, 1962). Equation 18 is only well defined for sections across closed basins, requiring a net zero volume flux due to mass conservation. This transport can be split up into a geostrophic heat transport Q_g,

$$Q_g = \int_0^L \int_{-h}^0 \rho C_p \theta \, v_g \, dxdz, \tag{19}$$

with v_g being the meridional geostrophic velocity, and an Ekman heat transport Q_e,

$$Q_e = \int_0^L \int_{-h}^0 \rho C_p (\theta_e - \overline{\theta}) v_e dxdz, \tag{20}$$

with θ_e, v_e being the potential temperature in the Ekman layer and the Ekman velocity, respectively.

The average potential temperature of the section $\overline{\theta}$ is included in Equation 20, since the total heat flux through a section is the result of northward flowing water at a certain temperature and returning southward flow at a different temperature. It is the net heat flux due to the opposing flows that is here referred to as the Ekman heat flux (see also *Levitus*, 1987).

Assuming the average temperature within the Ekman layer can be approximated by the sea surface temperature, then the meridional Ekman heat flux can be written as,

$$Q_{me} = -\frac{C_p (T - \overline{\theta}) \tau_x}{f}, \tag{21}$$

where C_p is the specific heat capacity, T the surface temperature, $\overline{\theta}$ the annual vertical mean potential temperature, τ_x the zonal windstress component and f the Coriolis parameter (see e.g. *Levitus*, 1987).

3.4.4 The ocean mixed layer heat budget

The temperature tendency equation for the mixed layer temperature (see also *Seager et al.*, 2003) is useful to investigate the forcing mechanisms of ocean temperature variability. It is given as:

$$\begin{aligned}\frac{\partial T_a}{\partial t} &= -\left[\left(u_a\frac{\partial T_a}{\partial x}+v_a\frac{\partial T_a}{\partial y}\right)-\left(\frac{T_a-T_h}{h}\right)\left(u_a\frac{\partial h}{\partial x}+v_a\frac{\partial h}{\partial y}\right)\right] \\ &\quad -\left[\left(\frac{T_a-T_h}{h}\right)\left(\frac{\partial h}{\partial t}+w_h\right)+\left(\frac{\overline{w'T'}}{h}\right)_h\right]+\frac{Q_{sfc}^{net}-Q_h^{pen}}{\rho c_p h} \qquad (22)\end{aligned}$$

Here, T_a, u_a, v_a are the temperature and horizontal velocities vertically averaged over the depth h of the mixed layer. T_h is the temperature just below the mixed layer and w_h is the vertical velocity at the base of the mixed layer. w', T' are deviations from the mean, thus, the term describes the turbulent or Reynolds flux. Q_{scf}^{net} is the net surface heat flux, while Q_h^{pen} is the amount of short wave radiation that penetrates through the base of the mixed layer. c_p is the specific heat capacity of ocean water, and ρ is the density of sea water. The terms in the first square brackets describe temperature changes due to horizontal processes. The terms in the second square bracket describe temperature changes due to vertical processes, that are associated with (a) mixing due to wind stirring, buoyancy loss and vertical shear ($\partial h/\partial t$), (b) vertical entrainment (w_h) and (c) turbulent mixing ($w'T'$).

The penetration depth of the solar radiation strongly depends on its wavelength (spectral dependence). Wavelengths in the red to infra-red (IR) spectrum are absorbed in the upper $5m$ of the ocean, while shorter wavelengths in the visible and ultra visible (UV) range penetrate into deeper depths. The attenuation depths depend on the water properties. *Jerlov* (1968) defined a scheme for classifying oceanic waters according to its clarity. The penetration depth of the short wave radiation can be deduced using the *Paulson and Simpson* (1977) solar irradiance parametrization. Two exponential functions are used to describe the solar penetration in the visible and infra-red wavebands,

$$Q_h^{pen} = Q_0\left(Re^{(-z/\zeta_1)}+(1-R)e^{(-z/\zeta_2)}\right) \qquad (23)$$

with

$$Q_0 = (1 - \alpha) Q_{sw}$$

where $\alpha = 0.05$ is the oceanic albedo and Q_{sw} the short-wave radiation. The first exponential term characterizes the rapid attenuation in the upper 5 to 10m of the IR light. The second exponential describes the decay of the visible and UV light.

3.4.5 Combined Windstress Anomaly and Climatology Pattern (CWP)

Any changes in windstress over the ocean may lead to changes in evaporation and associated latent heat flux. To a first approximation enhanced (reduced) windstress may cause upper ocean cooling (warming) due to thermodynamic effects. Since it is not necessarily obvious whether a windstress anomaly acts to enhance or reduce the climatological values, it is necessary to define any anomalous windstresses relative to their climatology. In an attempt to quantify this relationship a "Combined Windstress Anomaly and Climatology Pattern (CWP)" has been defined as follows:

Let

$$x = \bar{\tau}\, \tau',$$

with $\bar{\tau}$ denoting the windstress climatology and τ' the windstress anomaly. Thus, positive (neagtive) values of x indicate that the climatology and anomaly possess the same (different) sign. By defining,

$$\begin{aligned} y(x) &= -1, \quad \text{for} \quad x > 0 \\ y(x) &= 1, \quad \text{for} \quad x < 0, \end{aligned}$$

positive and negative values are set to 1 and -1. y thus provides a mask, that is applied towards the absolute values of the windstress anomaly,

$$cwp = -|\tau'| y, \tag{24}$$

with *cwp* being the combined windstress anomaly and climatology pattern. Therefore, the resulting field possesses the same absolute value as the original windstress anomaly τ. Areas with positive (negative) values of CWP correspond to reduced

(enhanced) winds and therefore may lead to positive (negative) surface temperature anomalies via thermodynamic effects such as changes in the net surface heat fluxes.

4 OGCM Diagnosis of Low Frequency Climate Variability in the South Atlantic Region

This section investigates low frequency climate variability in the South Atlantic region by means of an OGCM (ORCA2). A better understanding of interannual to decadal climate variability within the South Atlantic is important, due to its vital role in the global climate system. As discussed in the Introduction, changes in heat flux within the South Atlantic may significantly alter the thermohaline circulation (*Schmitz*, 1995; *Gordon*, 1986) and thus potentially affect climate as far afield as northern Europe. Locally, South Atlantic climate variability may induce changes in ocean temperatures that are known to alter fish stocks (*Binet et al.*, 2001) and are related to rainfall variability (*Rouault et al.*, 2003; *Robertson et al.*, 2003; *Reason et al.*, 2002) over the adjacent countries and thus potentially affect the lives of many.

Model studies are necessary as only OGCMs can provide additional information on advective processes and baroclinic structures of the ocean. This information is vital in order to further understand the role of South Atlantic ocean variability in a global and regional climate context. Thus, in an attempt to better understand South Atlantic variability the leading modes of the South Atlantic upper ocean temperatures are derived and the physical processes, atmospheric forcing, heat and volume transports associated with these modes are investigated.

The section begins with a general description of the chosen model domain, the variables and statistical tools used. The leading modes of the upper ocean temperature are then derived and compared to observations, followed by a discussion of the associated atmospheric forcing fields. Possible mechanisms leading to upper ocean temperature changes are discussed thereafter. The heat and volume transports are discussed where appropriate in the following section. The section ends with a summary and discussion.

4.1 South Atlantic Ocean variability

In this section ORCA2 temperature, salinity, horizontal velocities, net heat flux and short wave flux are diagnosed. All oceanic variables analysed are integrated over the depth of the mixed layer z_h, which is given as the level where the density increases by $0.01\,kg\,m^{-3}$ from the surface. The reason for doing so is that a useful application of the temperature tendency equation defined in Section 3, Section 3.4.4, requires mixed layer temperatures and velocities. Equation 22 will be used to explore the possible forcing mechanisms of upper ocean variability. It should be noted at this stage that the applied upper ocean boundary condition in form of the bulk mixed layer implies a nudging of SST towards observed near surface air temperatures. This may bias the model mixed layer depth to some extent (see e.g. *Seager et al.*, 1995).

Monthly anomalies are derived by subtracting the monthly climatological mean values (52 years) from the original values. All derived anomalies are detrended, by subtracting the linear trend from the anomalies, and smoothed with a 3 month running mean. The detrending of the data is necessary, because there is an overall warming trend present in the NCEP/ NCAR reanalysis and the ORCA2 model output, which significantly affects the rotated EOF analysis. The purpose of the detrending is to help isolate the natural interannual to decadal signals in the time series under investigation, which is the main interest of this study.

The South Atlantic leading modes of the mixed layer temperature are derived using the rotated EOF analysis described in Section 3, Section 3.3.1. The region of study ranges from the equator to 50°S and from 70°W to 20°E. It is important to note that an extension of the analysed domain into the Northern Hemisphere does not significantly alter the results of the rotated EOF analysis as long as the northern boundary is equatorward of 10°N. A further northward extension leads to a subsequent pronunciation of the tropical modes (see e.g. *Ruiz-Barradas et al.*, 2000), and to a reduction of the South Atlantic midlatitude modes. Since the South Atlantic is the prime target of investigation here, the domain is chosen as stated above and is thus confined to the Southern Hemisphere.

The robustness of the eigenvector rotation has been tested by systematically increasing the number of rotated eigenvectors (starting from 1). The first four rotated EOFs explain the maximum amount of variance. They are stable and preserve their pattern and order of occurrence as long as more than five EOFs are rotated. Rotating less than five eigenvectors leads to a change in pattern mainly for the last two modes, which is likely due to instabilities caused by *underfactoring* (*Richman*, 1986). The same robustness tests have been applied to the rotated EOFs of NCEP/ NCAR reanalysis SST and GISST SST.

In the following section, the resulting ORCA2 modes are compared to the NCEP/ NCAR modes and GISST modes in order to validate the ability of ORCA2 to represent upper ocean variability in the South Atlantic. Evidence that the ORCA2 model is satisfactory in its representation of the upper ocean variability in the South Atlantic Ocean has been given by e.g. *Hermes and Reason* (2005). However, for this study it is also necessary to check that the mixed layer depth is modelled in a realistic fashion. This is especially important in the tropics, where the east-west gradient of the thermocline is essential for the equatorial dynamics. Figure 2a shows the annual mean of the thermocline depth in the tropical channel, which compares reasonably well with the one shown in e.g. *Hazeleger et al.* (2002). Hence, the east-west gradient in the model appears adequate, allowing for a realistic representation of the equatorial dynamics.

Since, the net heat flux may significantly contribute towards the heat balance (Equation 22), the modelled heat fluxes are compared with those from the NCEP/ NCAR reanalysis (Figure 2b and 2c). The modelled fluxes agree well with the NCEP fluxes in terms of magnitude and spatial distribution. However, the modelled fluxes are generally weaker in the tropics to subtropics and near the Agulhas retroflection/ Southern Benguela, but seem to overestimate the magnitude in the area near the Angola Benguela Frontal Zone (ABFZ).

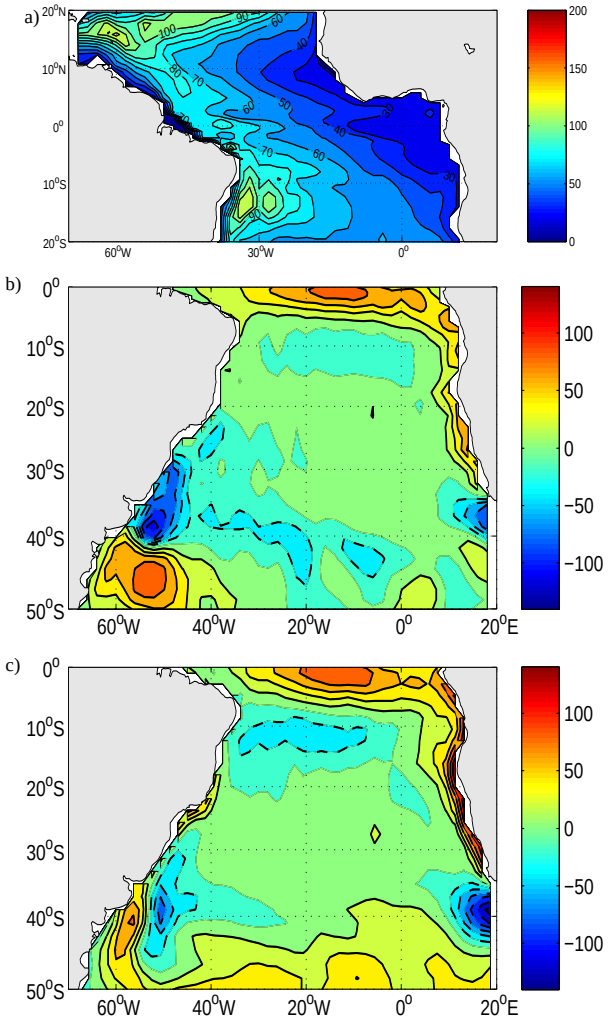

Figure 2: Annual mean of (a) ORCA2 thermocline depth, (b) ORCA2 net heat flux and (c) NCEP/ NCAR reanalysis net heat flux. Positive (negative) contour lines are solid (dashed). The zero contour line is omitted. The contour interval is 10 m for (a) and 20 Wm^{-2} for (b) and (c).

4.1.1 Spatial pattern and temporal variability

In the following a qualitative description of the first four REOFs of mixed layer temperature are given, and are compared to NCEP/ NCAR reynolds reconstructed SST (*Reynolds and Smith*, 1994) and UKMO GISST3.0 SST (*Rayner et al.*, 1996) and differences to previous work are shown.

The spatial pattern and corresponding expansion coefficients of the first four rotated EOFs for the mixed layer temperature (REOF(MLT)) are shown in Figure 3. They are presented as correlation maps in which the expansion coefficients of each time series is cross correlated with the grid points of the mixed layer temperature anomaly. Only correlations that exceed the 95% confidence interval are discussed, unless mentioned otherwise. The confidence interval is calculated using a standard t-test, which has been applied after reducing the degrees of freedoms for each time series, respectively (see also *Bretherton et al.*, 1999).

The displayed modes account for 28%, 17%, 13% and 11% of the total variance, respectively. The first pattern is a southwest/ northeast oriented dipole. The strongest variability is concentrated in the tropical region with a connection to the western African coast. A wavelet analysis (Figure 4a) of the corresponding time series (also Figure 3), reveals strongest power on interannual time scales.

Most of the variability of the second spatial pattern (Figure 3) is located in the subtropical region, stretching from the South African/ Namibian coast westwards to Brazil. The wavelet analysis (Figure 4b) of the corresponding time series exhibits a strong signal at the 5 year period, which is most pronounced during 1950 to 1960 and from 1970 to 1980. This mode is significantly correlated to ENSO. Maximum correlations occur when the SOI-index leads the MLT anomaly by about one season, in agreement with *Sterl and Hazeleger* (2003).

The third REOF (Figure 3) displays strong variability centred in the midlatitudes between 20°W and 5°E. The corresponding time series fluctuates on interannual (less than 3 years) and decadal to inter-decadal time scales (10 to 40 years). Between 1948 and 1999, this mode is negative until 1960, then becomes positive until the

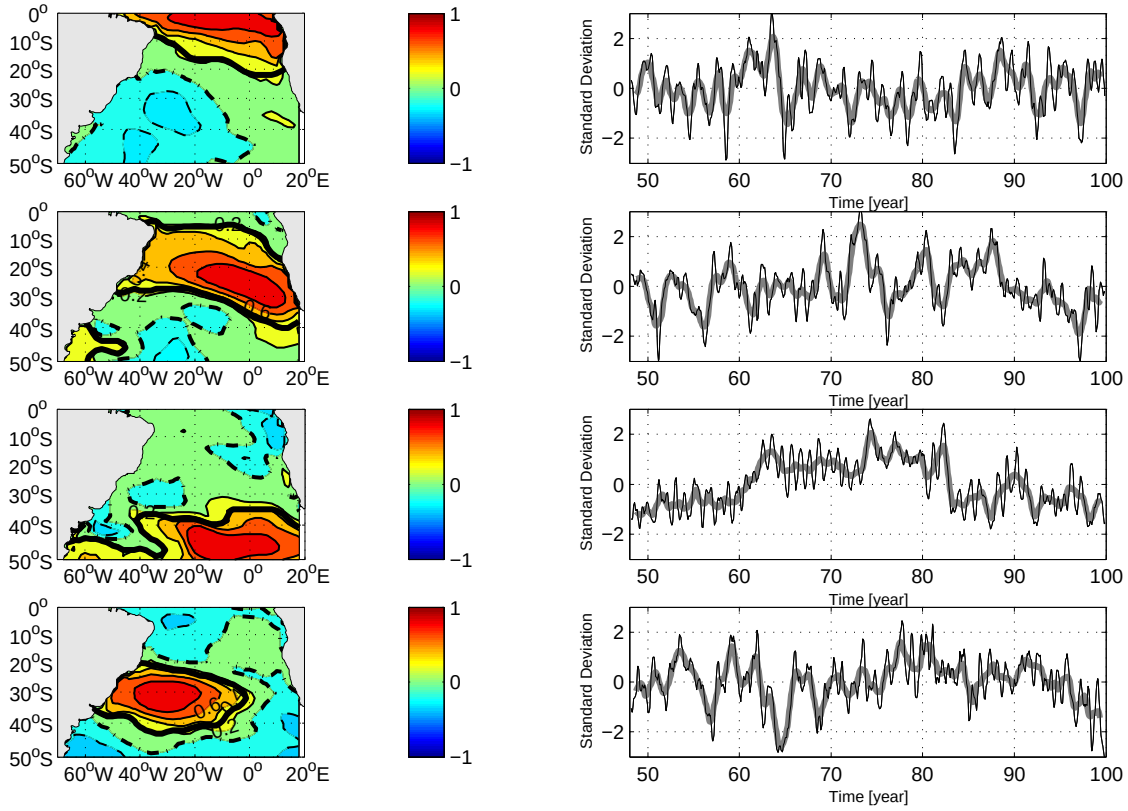

Figure 3: From top to bottom: First four rotated EOFs of ORCA2 MLT. Left: Spatial pattern as correlation maps. Positive (negative) contour lines are solid (dashed). The zero contour line is dashed - dotted. The contour interval is 0.2. The regions of significant correlation at the 95% level are within the thick lines. Right: Corresponding time series normalized by their standard deviation. The raw time series is shown black. The grey line represent the time series smoothed with a one year running mean.

beginning of 1980, when another negative phase starts. This inter-decadal signal is not very well seen in the wavelet transform (Figure 4c), due to the large period. Also evident is a weakening of the interannual signal during 1960 to 1970.

The fourth REOF (Figure 3) shows maximum variability in the western subtropics, centred near the South Atlantic Convergence Zone (SACZ). The displayed variability (Figure 4d) ranges from interannual to decadal time scales. There is a preference for lower interannual frequencies with periods of 5 and 8 years to occur in the first half of the analysed period, while higher frequencies with periods between 1 and 2 years are apparent thereafter.

The analysis is repeated with NCEP/ NCAR reynolds reconstructed SST (*Reynolds and Smith*, 1994) and the variance explained by the modes (Figure 5) is 21%, 18%, 15% and 9%, respectively. There is a good agreement in both spatial pattern and temporal variability between the first two modes obtained from the ORCA2 MLT and those of NCEP/ NCAR SST. The cross correlation between the time series of the first two modes is maximum at zero lag with correlation values of 0.81 and 0.84. However, the first mode of ORCA2 MLT is constricted closer to the equator, and the second mode is centred farther to the east. This may be due to the higher resolution of the ORCA2 model at low latitudes. The good agreement between modelled upper ocean temperature variability and observations may partly reflect the applied upper ocean boundary conditions. Although the bulk mixed layer attempts to represent what is actually being forced from the atmospheric boundary layer without providing SST information, by prescribing atmospheric temperature values, the upper ocean level is nudged towards observed temperatures.

Larger differences occur for the latter two modes. Although both the NCEP/ NCAR and ORCA2 modes display the majority variability in the southwestern subtropics and mid to eastern midlatitudes, it is apparent that the order of occurrence between the modes of NCEP/ NCAR SST and ORCA2 MLT is swapped. The corresponding time series show lower correlation values with the NCEP ones (0.34 and 0.35). These values increase significantly (0.64 and 0.57) when only the second half of the 52 year time frame is considered. It has been shown by *Sterl and*

Hazeleger (2003) that variability within the NCEP/ NCAR reanalysis is somewhat underestimated in regions with low data coverage such as the southern midlatitudes, especially before 1982. It is therefore possible that differences between the modes derived from the ORCA2 model and NCEP ones arise as a result of underestimated variability in this region by NCEP. On the other hand, it is possible, that, since the model resolution increases towards the poles, the variability in the midlatitudes may be overestimated by ORCA2 due to enhanced spatial correlation.

The same comparison has also been made with the GISST3.0 SST (Appendix 65) and the results are found to be similar. Thus a good comparison is apparent between the first two modes, while the third and fourth modes appear to be in different order.

Differences between the ORCA2 modes and those of *Sterl and Hazeleger* (2003), who analyse NCEP/ NCAR reanalysis SSTs, are most likely due to the applied rotation procedure, which leads to more localized structures of variability in our analyses. Thus, the first (second) mode of *Sterl and Hazeleger* (2003) shows a mixture of the first two (last two) modes discovered here.

The resulting ORCA2 modes show larger differences with those found by *Venegas et al.* (1997), which is expected as *Venegas et al.* (1997) use a different dataset with a different grid density, do not rotate the EOFs and do not detrend the SSTs prior to the analysis. Not detrending the data clearly favours the evolution of a monopole like signal in the South Atlantic. Hence, the second and third mode of *Venegas et al.* (1997) show, like those of *Sterl and Hazeleger* (2003) a mixture of the four modes shown here.

From the comparison above it is evident that the ORCA2 model adequately resolves the major modes of variability in the South Atlantic, and thus may be used to further investigate the relationships with the atmosphere and associated mechanisms.

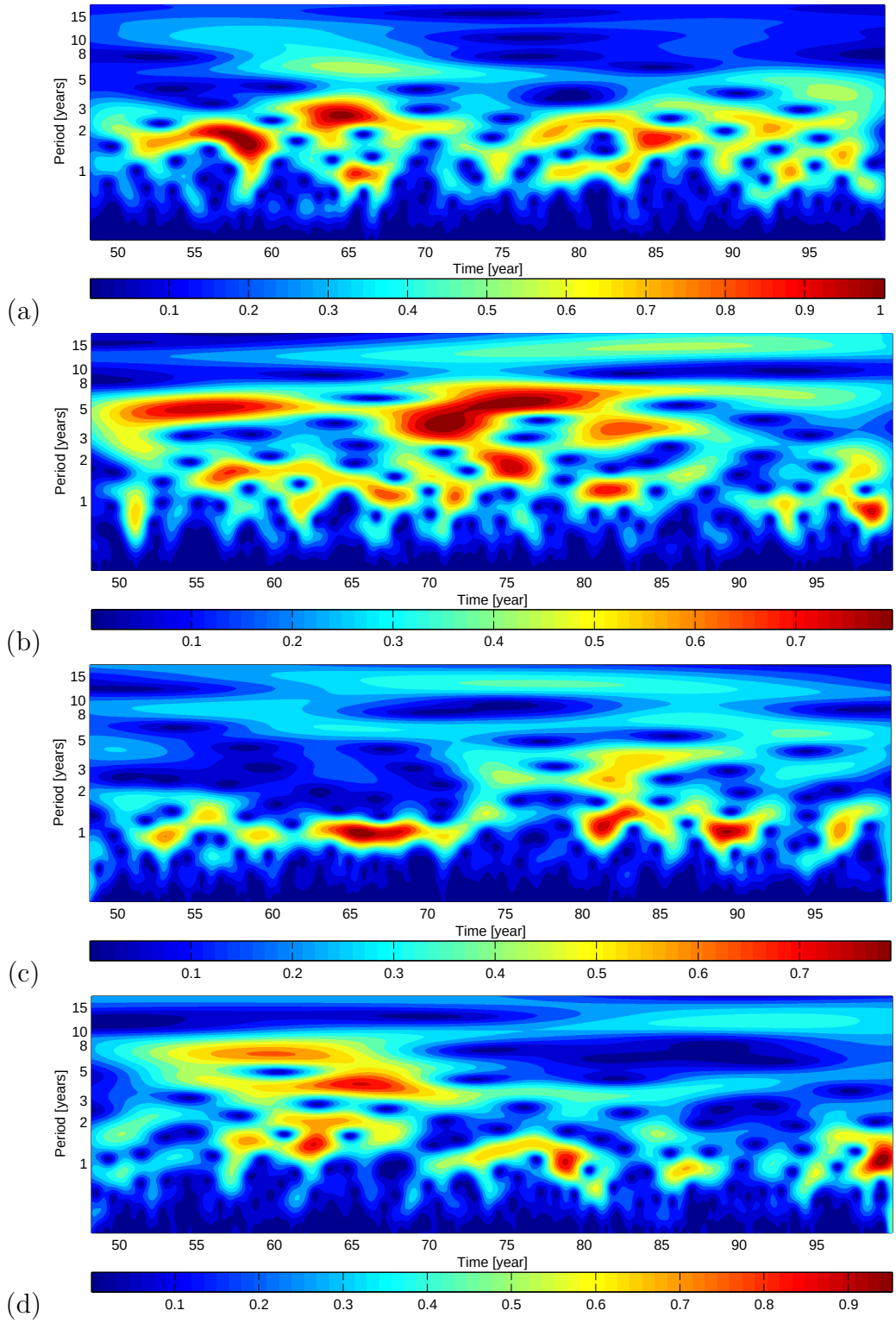

Figure 4: Morlet wavelet for the four rotated EOFs in Figure 3.

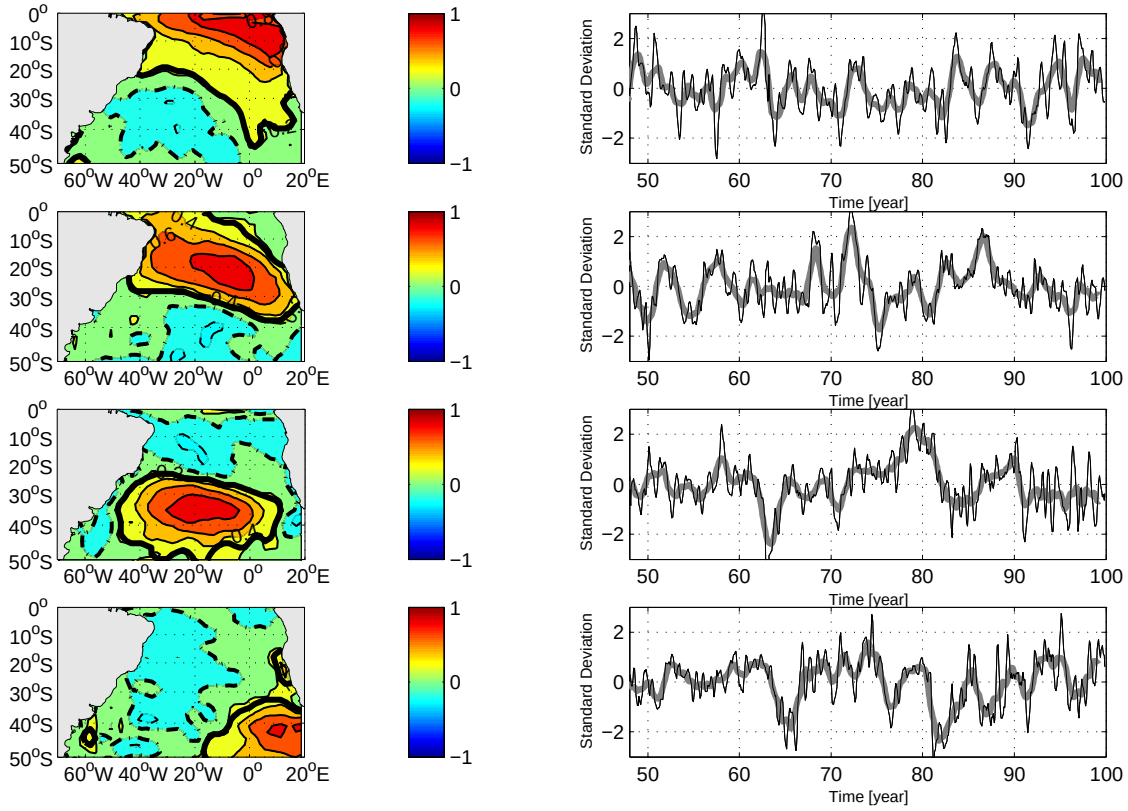

Figure 5: From top to bottom: First four rotated EOFs of NCEP/ NCAR SST. Left: Spatial pattern as correlation maps. Positive (negative) contour lines are solid (dashed). The zero contour line is dashed - dotted, the contour interval is 0.2. The regions of significant correlation at the 95% level are within the thick lines. Right: Corresponding time series normalized by their standard deviation. The raw time series is shown in black. The grey line represent the time series smoothed with a one year running mean.

4.1.2 Atmospheric linkages - windstress anomalies

In order to investigate possible atmospheric influences on the derived leading modes in the South Atlantic, lagged correlation analyses between windstress anomalies and the four expansion coefficients are performed. The correlation sequences are shown in Figures 6 and 7. Each sequence consists of three correlation maps, with firstly (Figures a and d), windstress leading the MLT by 3 months, secondly (Figures b and e) zero lag between windstress and MLT and finally (Figures e and f) windstress lagging the MLT by 3 months.

The correlation sequence for the first REOF (Figures 6a to 6c) suggests positive correlations in the central to western equatorial region peaking at zero lag. The windstress anomalies are from the west/ northwest and therefore tend to reduce the tropical trades. These wind anomalies are consistent with the observed ocean mixed layer warming (Figure 3) due to reduced vertical mixing, Ekman heat transport and reduced latent heat flux. However, the area of weaker trades does not cover the eastern tropics and the northern Benguela, which are strongly affected by the warming, suggesting other processes are responsible for the observed temperature changes there. The correlation analysis of the mixed layer depth anomaly (Figures 8a to 8c) reveals a deepened mixed layer in the eastern tropics, consistent with the observed warming. In the western tropics, the mixed layer depth tends to be shallower than average, since the southeasterly trades are reduced.

The lagged correlation analyses between the windstress anomalies and the second mode (Figures 6d to 6f) reveals highest correlations in the eastern subtropics, where the windstress anomalies tend to reduce the trades. Strongest correlations occur one season before and at zero lag, suggesting that ocean temperatures are mainly driven by wind induced changes in latent heat flux. This assumption is further supported by the mixed layer depth (Figures 8d to 8f), which is generally decreased over the regions of strongest warming, suggesting a stronger vertical stratification due to reduced wind stirring and increased heat flux into the ocean.

Correlations between the windstress anomalies and the third REOF(MLT) (Fig-

ures 7a to 7c) are smaller compared to the other two modes, implying that the windstress is less important in driving upper ocean temperatures here. Strongest correlations occur in the midlatitudes at zero lag. The windstress acts to reduce the prevailing westerlies and supports ocean warming due to reduced vertical mixing, wind driven Ekman heat transport and reduced latent heat flux. Due to reduced (enhanced) entrainment, the mixed layer depth (Figure 9a to 9c) is deeper (shallower) in regions that correspond to ocean warming (cooling) and thus is decoupled from reduced (enhanced) wind stirring.

Weak correlation between the windstress anomalies and the fourth REOF(MLT) (Figures 7d to 7f) is apparent. The anomalous windstress tends to enhance (reduce) the subtropical anticyclone, for warm (cool) phases of MLT, suggesting that MLTs are altered due to advection and wind stirring. The mixed layer depth (Figure 9d to 9f) is anomalously deep due to the stronger winds and enhanced wind stirring.

4.1.3 Forcing fields

To further investigate the forcing mechanisms behind the four modes, lagged field-index regressions, using least squares, are performed between all terms arising in the temperature tendency equation 22 and the expansion coefficients of the rotated EOF of the MLT (the lagged regression analyses allow for a direct comparison of the forcing terms). Typical values for the four modes are calculated by taking averages over positive and negative values of the resulting regression fields respectively. A significant region is defined as an area of significant cross correlations between the REOFs and the mixed layer temperature anomalies. The bar diagrams for each REOF are displayed in Figure 10. The numbers 1 to 6 indicate the different forcing terms in Equation 22. Positive (negative) values indicate a forcing term that acts to enhance (reduce) the temperature tendency and therefore favours mixed layer warming (cooling).

In the following, sequences of correlation maps between the dominant forcing terms and the expansion coefficients are presented. Each sequence consists of three correlation maps, with firstly (Figures a and d) the forcing field leading the MLT

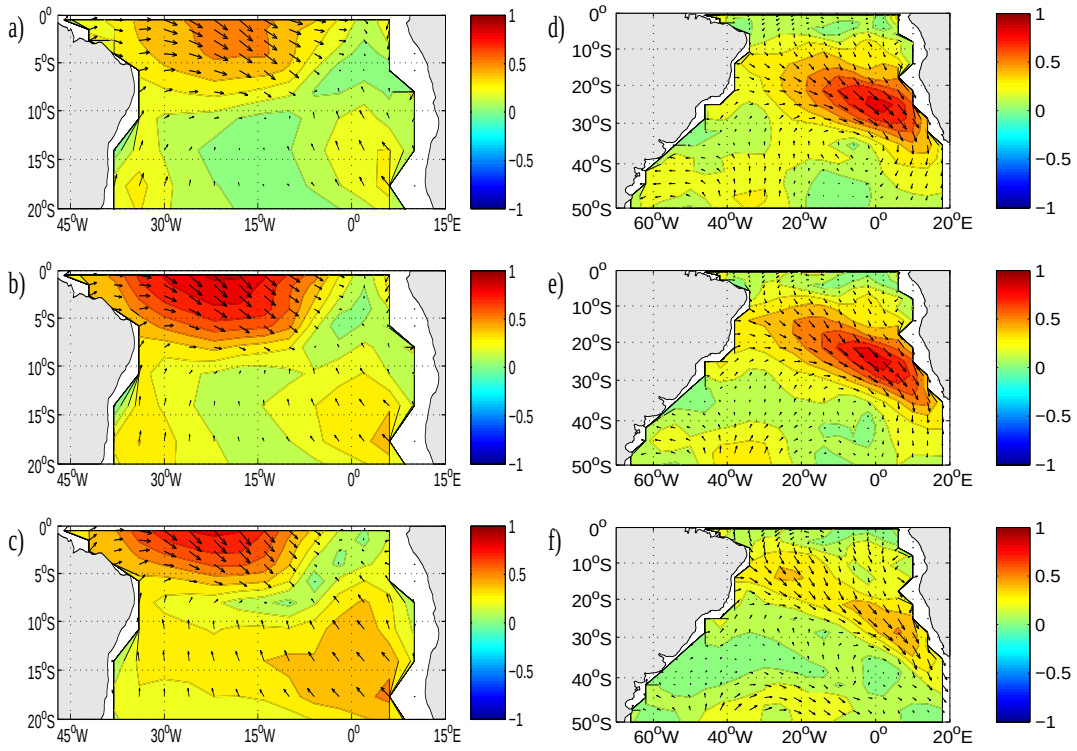

Figure 6: Sequences of lagged correlation between windstress (arrows) and the first (left) and second (right) REOF(MLT). With $lag = -3$ (upper), $lag = 0$ (middle) and $lag = 3$ (lower). Lag in *months*. The contour interval is 0.2.

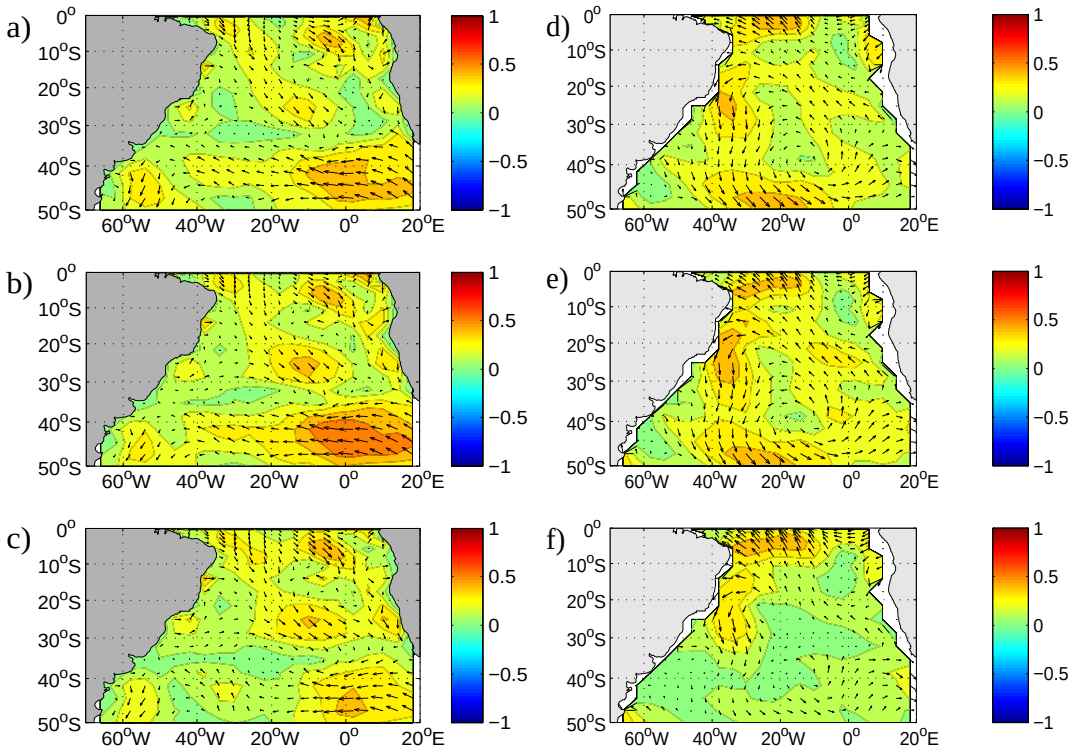

Figure 7: Sequence of lagged correlation between windstress (arrows) and the third (left) and fourth (right) REOF(MLT). With $lag = -3$ (upper), $lag = 0$ (middle) and $lag = 3$ (lower). Lag in *months*. The contour interval is 0.2.

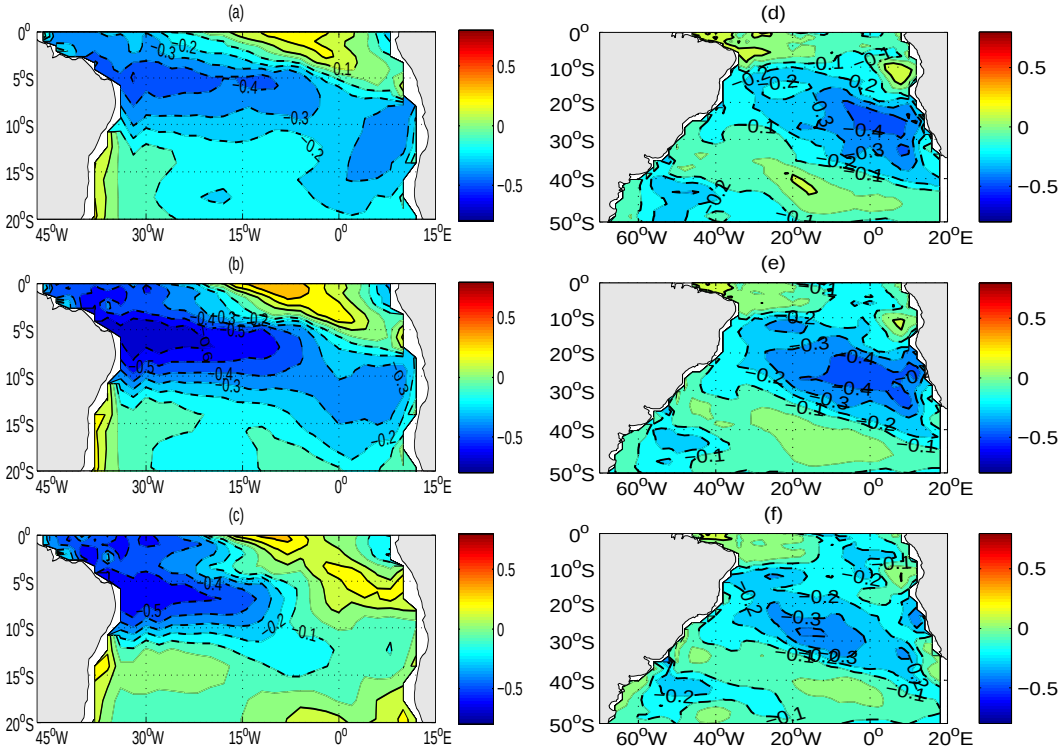

Figure 8: Sequences of lagged correlation between the mixed layer depth and the first (left) second (right) REOF(MLT). With $lag = -3$ (upper), $lag = 0$ (middle) and $lag = 3$ (lower). Lag in *months*. Negative (positive) lag means leading (lagging) forcing field. Positive (negative) contour lines are solid (dashed). The zero contour line is omitted. The contour interval is 0.1.

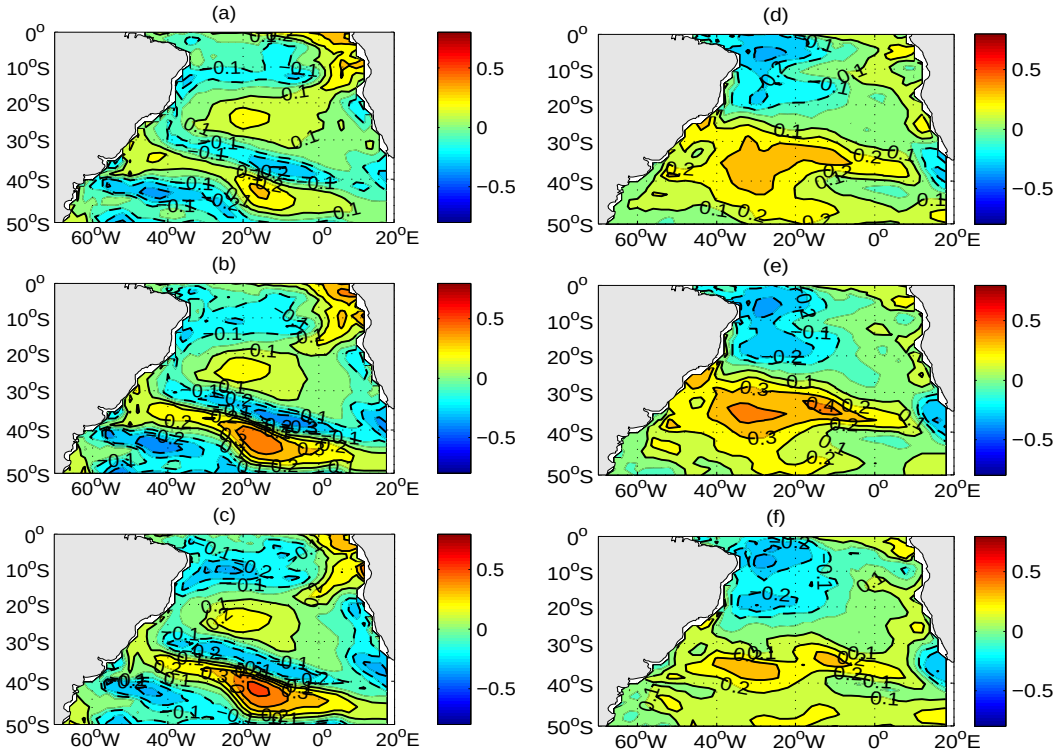

Figure 9: Sequences of lagged correlation between the mixed layer depth and the third (left) and fourth (right) REOF(MLT). With $lag = -3$ (upper), $lag = 0$ (middle) and $lag = 3$ (lower). Lag in *months*. Negative (positive) lag means leading (lagging) forcing field. Positive (negative) contour lines are solid (dashed). The zero contour line is omitted. The contour interval is 0.1.

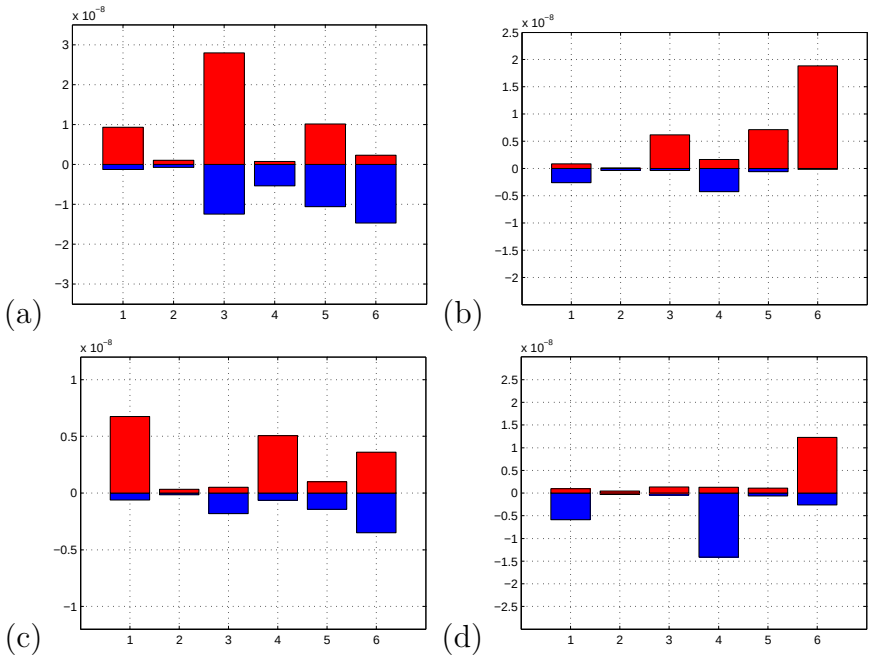

Figure 10: Bar diagram of the lagged regression analyses between the forcing terms in the temperature tendency equation 22 and the first four REOF(MLT). Bars correspond from left to right: (1) $-v\nabla T$, (2) $\frac{\Delta T}{h}v\nabla h$, (3) $-\frac{\Delta T}{h}w_h$, (4) $-\frac{\Delta T}{h}\frac{\partial h}{\partial t}$, (5) $-\frac{\overline{w'T'}}{h}$, and (6) $\frac{Q_{sfc}^{net}}{\rho c_p h}$. See text for details.

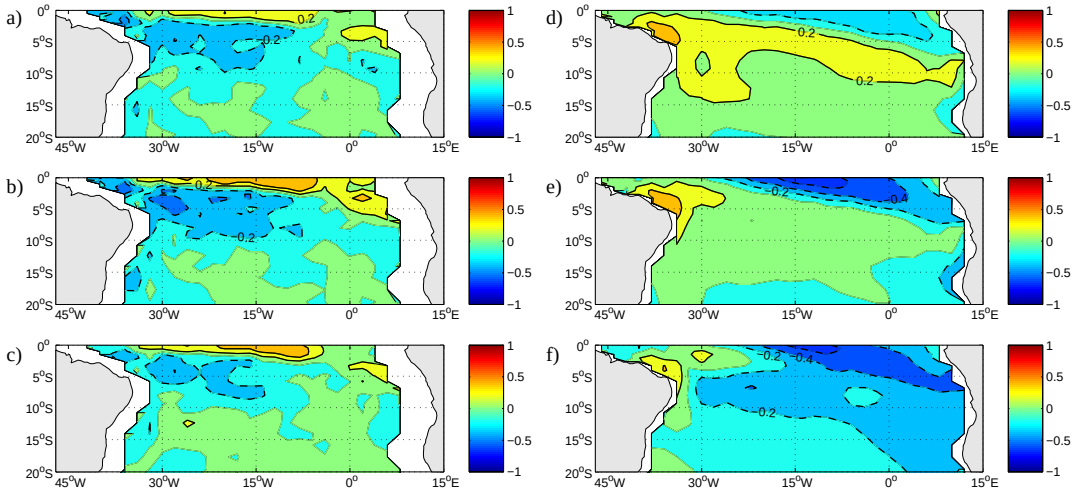

Figure 11: Sequence of the lagged correlation between the first REOF(MLT) and $-\frac{T_a - T_h}{h} w_h$, (left) and $\frac{Q_{sfc}^{net}}{\rho c_p h}$ (right). With $lag = -3$ (upper), $lag = 0$ (middle) and $lag = 3$ (lower). Lag in *months*. Negative (positive) lag means leading (lagging) forcing field. Positive (negative) contour lines are solid (dashed). The zero contour line is dashed - dotted. The contour interval is 0.2.

by 3 months, secondly (Figures b and e) zero lag between the forcing field and MLT and finally (Figures c and f) the forcing field lagging the MLT by 3 months.

First REOF(MLT)

From Figure 10 it is apparent that the dominant forcing term for the first REOF is vertical entrainment. It is positively correlated with the time series of the first REOF(MLT) in the eastern to central tropics (see Figures 11a to 11c), with maximum correlation at zero lag (Figure 11b). Since vertical entrainment only acts to cool the mixed layer, as colder water is entrained from deeper ocean levels, positive values translate into reduced mixing and therefore reduced upwelling, which favours ocean warming. The seasonal cycle of the vertical entrainment term (Appendix 66) reveals enhanced advection during the austral winter months, consistent with the annual cooling. Therefore, reduced vertical entrainment of cold water into the mixed layer is plausible in explaining the observed warming.

Net surface heat flux (Figure 11d to 11f), is the second largest term in magnitude

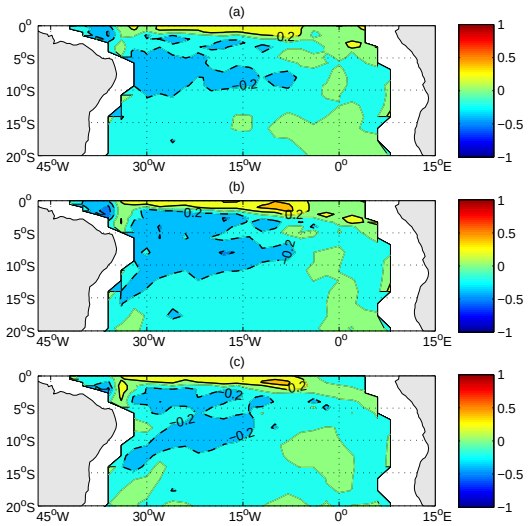

Figure 12: Sequence of the lagged correlation between the first REOF(MLT) and $-\frac{\overline{w'T'}}{h}$. With $lag = -3$ (upper), $lag = 0$ (middle) and $lag = 3$ (lower). Lag in *months*. Negative (positive) lag means leading (lagging) forcing field. Positive (negative) contour lines are solid (dashed). The zero contour line is omitted. The contour interval is 0.2.

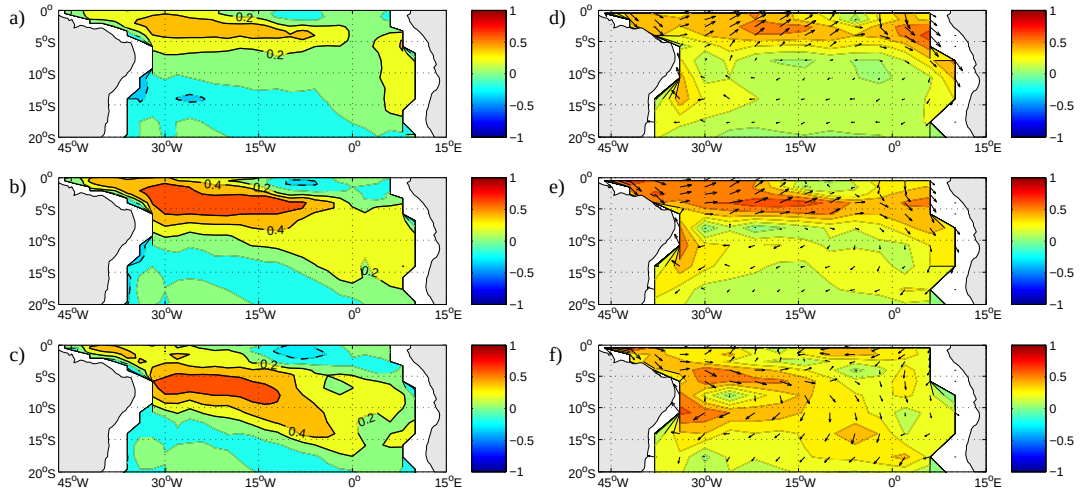

Figure 13: Sequence of the lagged correlation between the first REOF(MLT) and $-v\nabla T$ (left) and v (right). With $lag = -3$ (upper), $lag = 0$ (middle) and $lag = 3$ (lower). Lag in *months*. Negative (positive) lag means leading (lagging) forcing field. Positive (negative) contour lines are solid (dashed). The zero contour line is omitted. The contour interval is 0.2.

(Figure 10a), and is negatively correlated with the first REOF(MLT) in the central to eastern tropical region. The negative correlation suggests that net surface heat flux acts as to dampen the prevailing upper ocean temperature anomalies. The net heat flux term reaches strongest negative correlations 3 month after maximum upper ocean temperature anomalies occur, indicating that increased turbulent heat fluxes due to the observed upper ocean warming may become important in the heat flux balance and thereby counteracting the anomalous ocean temperatures.

Ocean warming is also supported by the net surface heat flux mainly in the western tropics between 40°W and 30°W, as positive correlations are evident there, and are strongest a season before the warmest temperature anomalies occur. However, the regression analysis (Figure 10a) suggest that warming due to the net heat flux is rather small compared to advection and turbulent mixing.

The correlation sequence for the turbulent mixing (Figure 12a to 12c) reveals strongest positive correlations near the equator at zero lag, favouring warming there.

Cooling is supported southward of that, due to increased mixing. The horizontal advection sequence (Figures 13a to 13c) suggests warming over most of the tropical Atlantic region, with the exception of the far northeast, which is the region where vertical entrainment dominates. Highest correlation is found in the western tropics, peaking at zero lag (Figure 13b). Dividing the advection term into the mean field multiplied by the anomaly field suggests that upper ocean warming is mainly caused by advection of anomalous temperature by the mean currents. However, the anomalous oceanic currents also contribute towards the observed warming (shown in Figures 13d to 13f), as they act to reduce the southwestward directed mean currents. Hence, less cool water is transported towards to the western tropics, favouring the observed warming there.

Second REOF(MLT)

Figure 10b, shows that the dominant forcing term for the second REOF is the net surface heat flux. The corresponding correlation sequence is shown in Figures 14a to 14c. The correlation is positive in the subtropics with greatest values at 3 months lead and is positive at zero lag (Figures 14a and 14b, respectively). Latent heat flux has shown to be the dominant term in driving SST anomalies in the South Atlantic *Sterl and Hazeleger* (2003), and *Colberg et al.* (2004), therefore changes in temperatures are likely to be caused by reduced (enhanced) evaporation driven by anomalous winds (Figure 6). Turbulent mixing, and vertical entrainment (Appendix 67) are reduced due to the weaker trades, hence contributing towards the observed warming. The first vertical mixing term (Figure 14d to 14f) favours ocean cooling, due to increased heat loss as the mixed layer depth is reduced.

Third REOF(MLT)

The significant forcing terms for the third mode are horizontal advection, the first vertical mixing term and the net heat flux term (Figure 10c). The correlation sequence for the horizontal advection is shown in Figures 15a to 15c. The positive areas in the central to eastern midlatitudes match well with the observed warming shown in Figure 3. Two centres of strong correlations occur at around 20°W, 40°S-50°S and between 0° and 10°E, 40°S-50°S. These correlations are strongest at

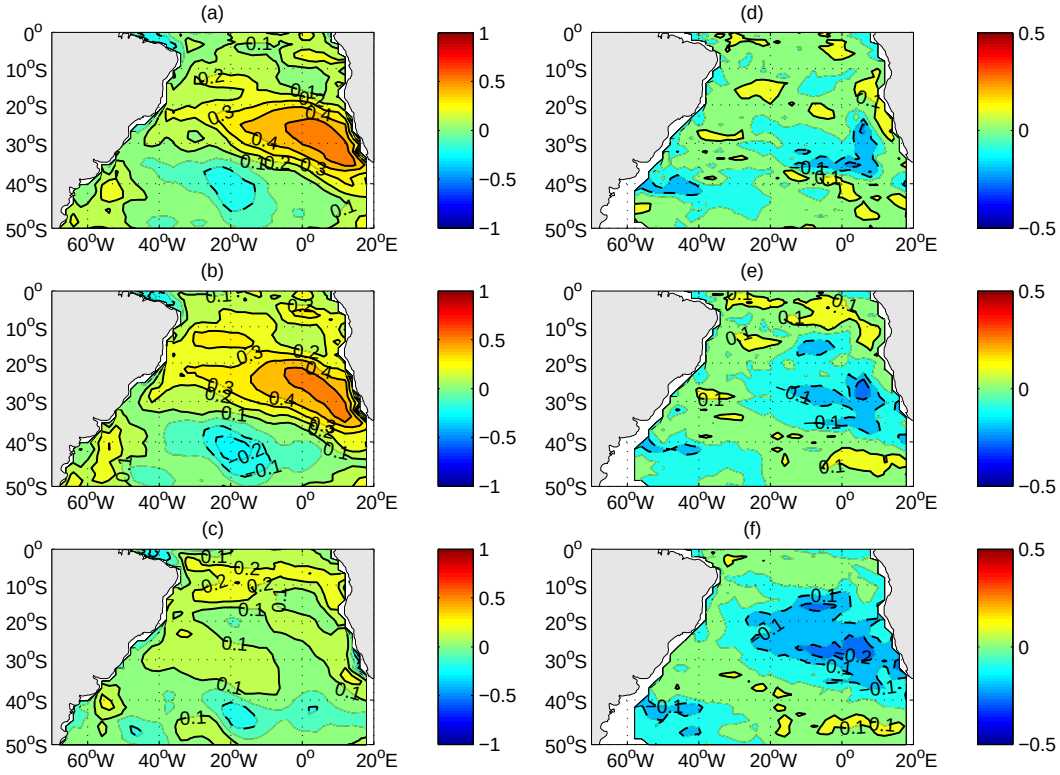

Figure 14: Sequence of the lagged correlation between the second REOF(MLT) and $\frac{Q_{sfc}^{net}}{\rho c_p h}$ (left) and $-\frac{\Delta T}{h}\partial h/\partial t$ (right). With $lag = -3$ (upper), $lag = 0$ (middle) and $lag = 3$ (lower). Lag in *months*. Negative (positive) lag means leading (lagging) forcing field. Positive (negative) contour lines are solid (dashed). The zero contour line is omitted. The contour interval is 0.1.

3 month lead and at zero lag (Figures 15a and 15b). The corresponding anomalous ocean currents (Figures 15d to 15f), reveal strongest correlations in the midlatitudes near 20°W, where they are southward, suggesting a reduced northward Ekman transport of cold water into the area, thus contributing to the observed warming there. To some extent, the same is true for the region near 0°E.

To further investigate the nature of the upper ocean currents, the velocities are split up into an Ekman and a geostrophic part. Ekman velocities are derived using Equation 13 whilst geostrophic velocities are calculated by integrating the thermal wind equation (Equation 11). Their respective correlation sequences are shown in Figure 16. It appears that the area between 15°W and 20°E is dominated by anomalous southward Ekman flow (Figures 16a to 16c), consistent with the windstress anomalies discussed in Section 4.1.2. Hence warming there is possibly related to a reduced northward meridional Ekman heat transport (Appendix 68). The area west of 15°W on the other hand is strongly correlated with the geostrophic velocities (Figures 16d to 16f). Also evident are strong correlations in the far western midlatitudes, implying that changes in the opposing Falklands/ Malvinas and Brazil currents may be important in driving upper ocean temperatures there. However, although the correlation coefficients are much higher compared to the ones seen for the Ekman velocities, they are just below the 95% confidence interval. This may indicate that two different mechanisms associated with two different time scales (and certainly different degrees of freedom) are present here.

The possibility of different mechanisms being associated with different time scales is further investigated by taking the averages over the regions of highest correlations of meridional geostrophic (30°W-10°W, 40°S-50°S) and Ekman velocities (10°W-10°E, 40°S-50°S), respectively. The two resulting time series are cross correlated with the third expansion coefficient of the rotated EOF analysis. The correlation values and their corresponding wavelet analysis are shown in Figure 17. The wavelet analysis for the geostrophic time series reveals highest energy between 10 and 20 years. This signal is related to the decadal to inter-decadal variability described in section 4.1.1. This peak is also visible for the Ekman time series (Figure 17b). A

strong signal at 5 years is also present in the Ekman time series and is significantly correlated with the SOI, suggesting possible connections to ENSO, in agreement with *Colberg et al.* (2004). *Colberg et al.* (2004) showed that, during ENSO, significant temperature changes in the midlatitude South Atlantic Ocean occur and are associated with changes in the strength of the South Atlantic Anticyclone, which favours anomalous Ekman heat transport in the eastern midlatitudes.

This analysis suggests that the western midlatitudes are characterized by inter-decadal variability related to changes in the geostrophic currents (significant just below the 95% confidence interval). Due to the limited length of the available data, it is not clear whether the inter-decadal variability describes a real physical mode or not. However, timing, region of variability and the baroclinic nature of this mode are similar to that found by *Wainer and Venegas* (2001).

The second largest term in the temperature tendency equation is the first vertical mixing term (Figure 10 and 18a to 18c). Reduced westerlies lead to reduced entrainment and thus upper ocean warming. Positive (negative) correlations match well with areas of observed warming (cooling), being strongest 3 months after zero lag, and agree with a generally deeper (shallower) mixed layer there.

According to the bar diagram (Figure 10) net surface heat flux (Figure 18d 18f) is the third dominant term in the temperature tendency. It favours upper ocean warming between 45°S-50°S and 60°W-40°W with strongest correlation values 3 month before and at zero lag and counteracts the observed warming between 40°S-50°S and 20°W-10°E with maximum correlation values 3 month after zero lag.

Fourth REOF(MLT)

The bar diagram for the last REOF (Figure 10d) of the mixed layer temperature suggests that net heat flux is the most important term in creating the anomalous temperatures. Its sequence is shown in Figures 19a to 19c. This term shows maximum correlation at one season lead and at zero lag. Unlike the second REOF(MLT), increased heat flux into the ocean is accompanied with enhanced windstress (see Section 4.1.2), which suggests latent heat flux counteracts the observed temperatures

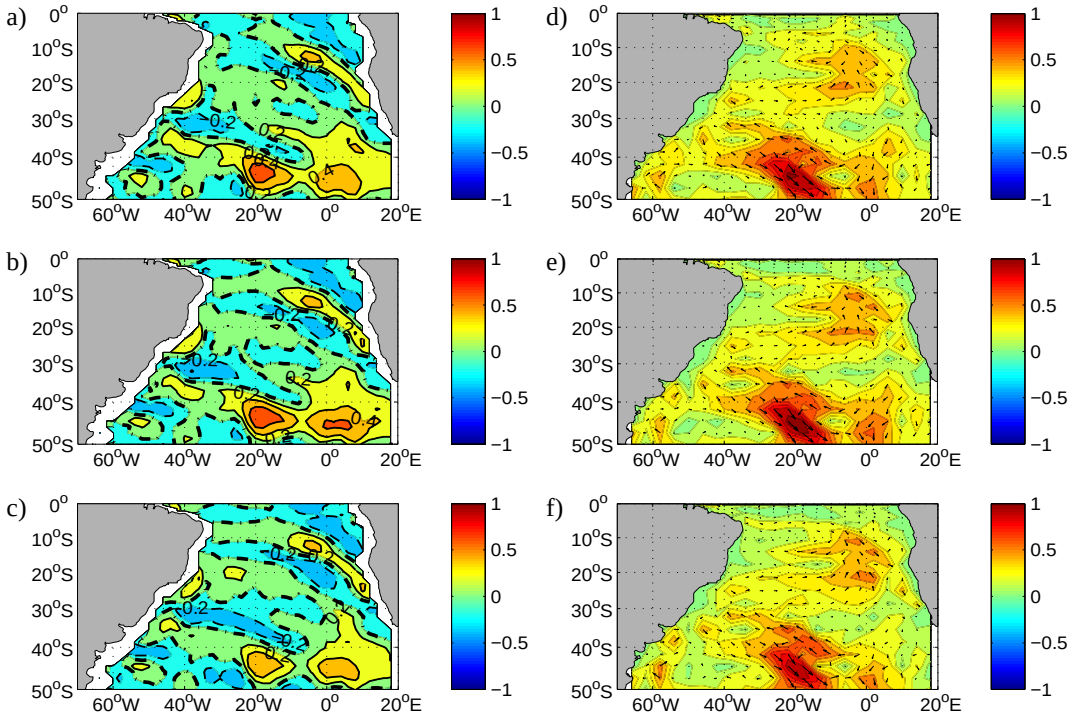

Figure 15: Sequence of the lagged correlation between the third REOF(MLT) and $-v\nabla T$ (left), and v (right). With $lag = -3$ (upper), $lag = 0$ (middle) and $lag = 3$ (lower). Lag in *months*. Negative (positive) lag means leading (lagging) forcing field. Positive (negative) contour lines are solid (dashed). The zero contour line is dashed - dotted. The contour interval is 0.2.

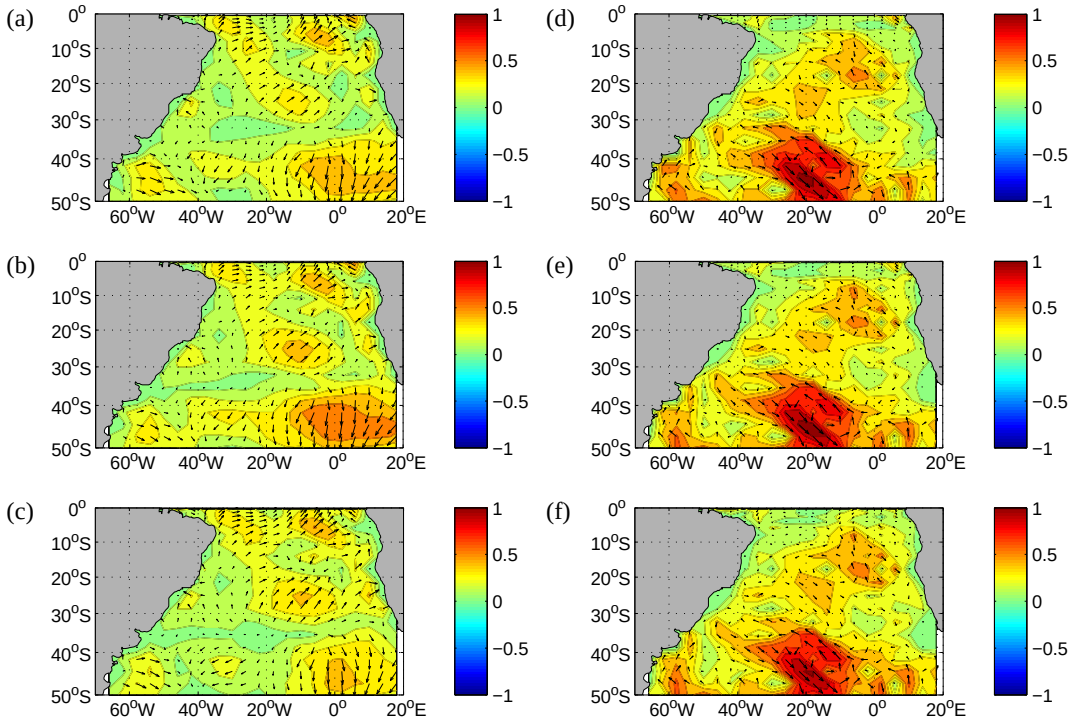

Figure 16: Sequence of the lagged correlation between the third REOF(MLT) and Ekman velocity (left) and geostrophic velocity (right). With $lag = -3$ (upper), $lag = 0$ (middle) and $lag = 3$ (lower). Lag in *months*. Positive (negative) contour lines are solid (dashed). The zero contour line is omitted. Negative (positive) lag means leading (lagging) forcing field. The contour interval is 0.2.

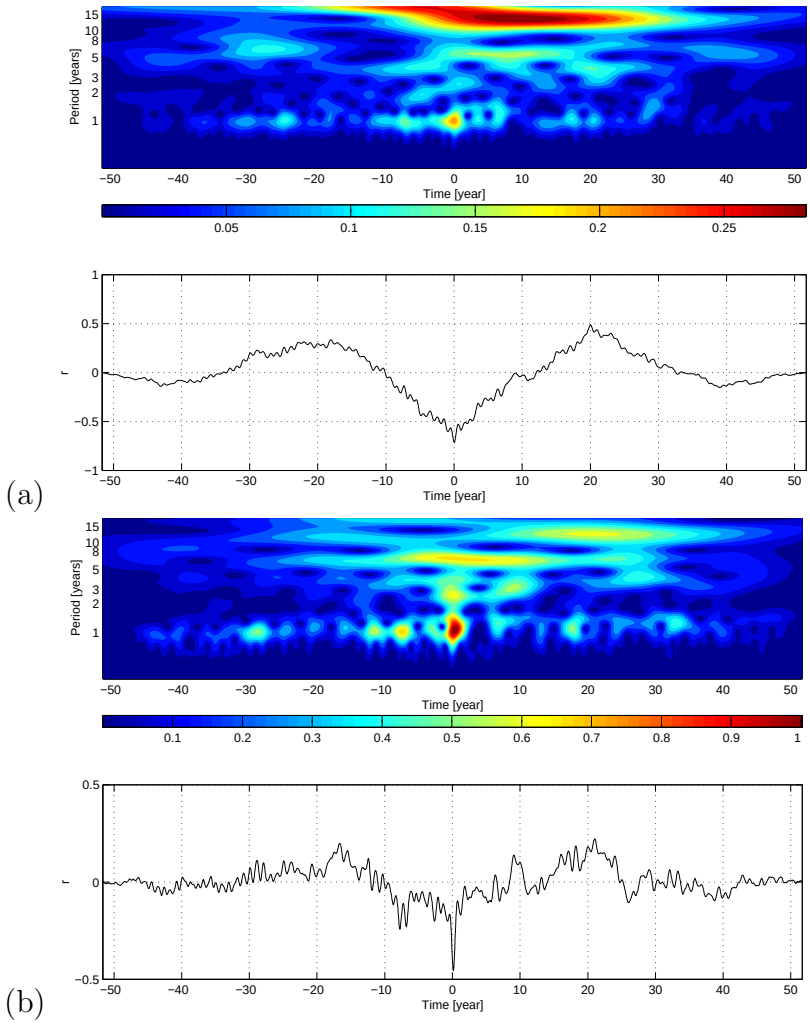

Figure 17: Wavelet analyses of the correlation between the third REOF(MLT) and (a) meridional geostrophic, (b) meridional Ekman velocity in an index region. See text for details.

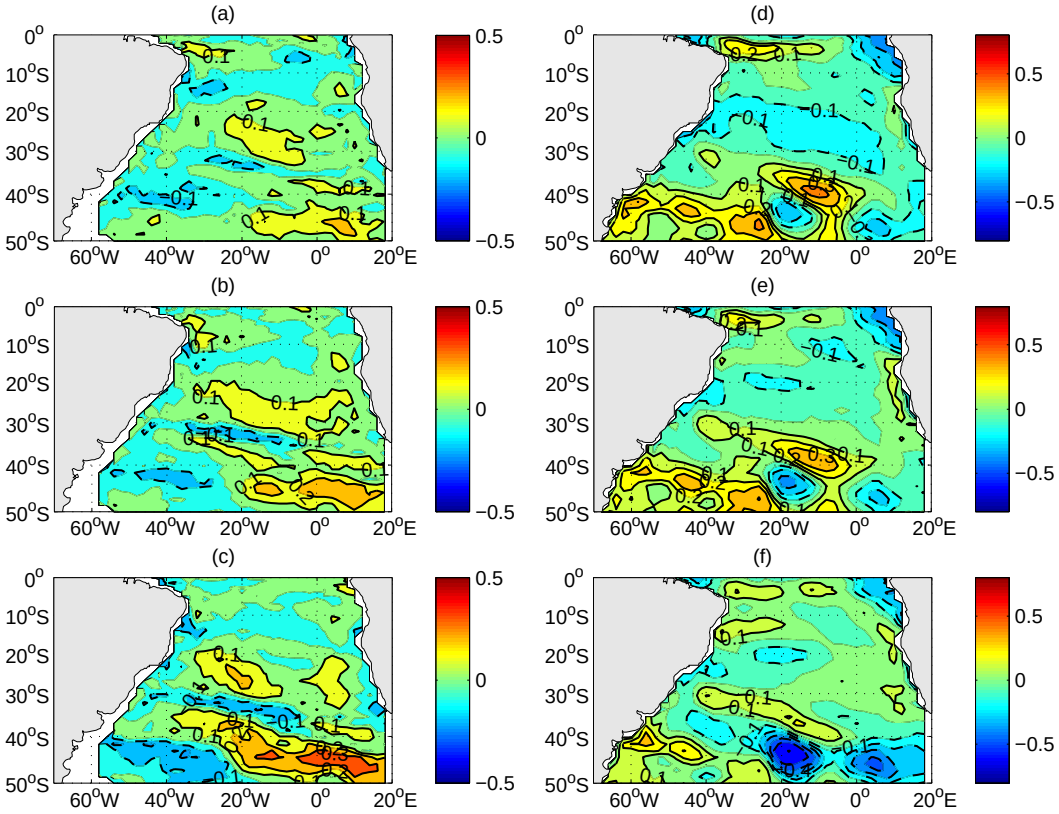

Figure 18: Sequence of the lagged correlation between the third REOF(MLT) and $-\frac{\Delta T}{h}\partial h/\partial t$ (left) and $\frac{Q_{sfc}^{net}}{\rho c_p h}$ (right). With $lag = -3$ (upper), $lag = 0$ (middle) and $lag = 3$ (lower). Lag in *months*. Positive (negative) contour lines are solid (dashed). The zero contour line is omitted. Negative (positive) lag means leading (lagging) forcing field. The contour interval is 0.1.

as it is increased. The regression and correlation analysis has been repeated with the modelled short wave flux (Appendix 69). It appears that short wave flux favours warming between 20°S-30°S and 30°W-10°W. Partly covering the region of anomalous MLT, but counteracting the observed temperatures elsewhere. Reduced short wave flux may also be indicative of enhanced cloud cover and thus increased reflected long wave radiation, which could account for the observed warming. Since only the modelled net heat and short wave flux were available examination of the ORCA2 long wave flux was not possible. However, since the MLT anomaly is centred near the SACZ, a region associated with convection and strong cloud cover, long wave radiation may become important and substantially affect upper ocean temperatures here.

The first vertical mixing term (Figures 19d to 19f) counteracts the temperature anomalies and shows strongest correlations at zero and at 3 month lag. The enhanced windstress leads to mixed layer cooling as more cold water is entrained. The bar diagram also suggests some influence of the advection term, which tends to counteract the observed SST anomalies. This term shows strongest correlation between 20°S and 30°S at 3 month lag (Appendix 69). The corresponding velocity fields (Appendix 70) are partly directed northwards and northwestwards, thus suggesting an enhanced northward transport of colder midlatitudinal watermasses into the area.

4.1.4 Heat and volume transport at 30°S

In the following, changes in heat and volume transport that are associated with the second leading mode are examined. It is shown below that transports associated with this mode reveal a rather complex behaviour compared to the other leading modes and furthermore are associated with gyre modifications. The analysis focusses on the meridional component of the heat and volume transport and defines an east-west section that lies within the area of highest variability displayed by this mode. As before, correlation analyses are used to investigate possible linkages between the REOF and the transports. Heat and volume transports are derived using (a) total

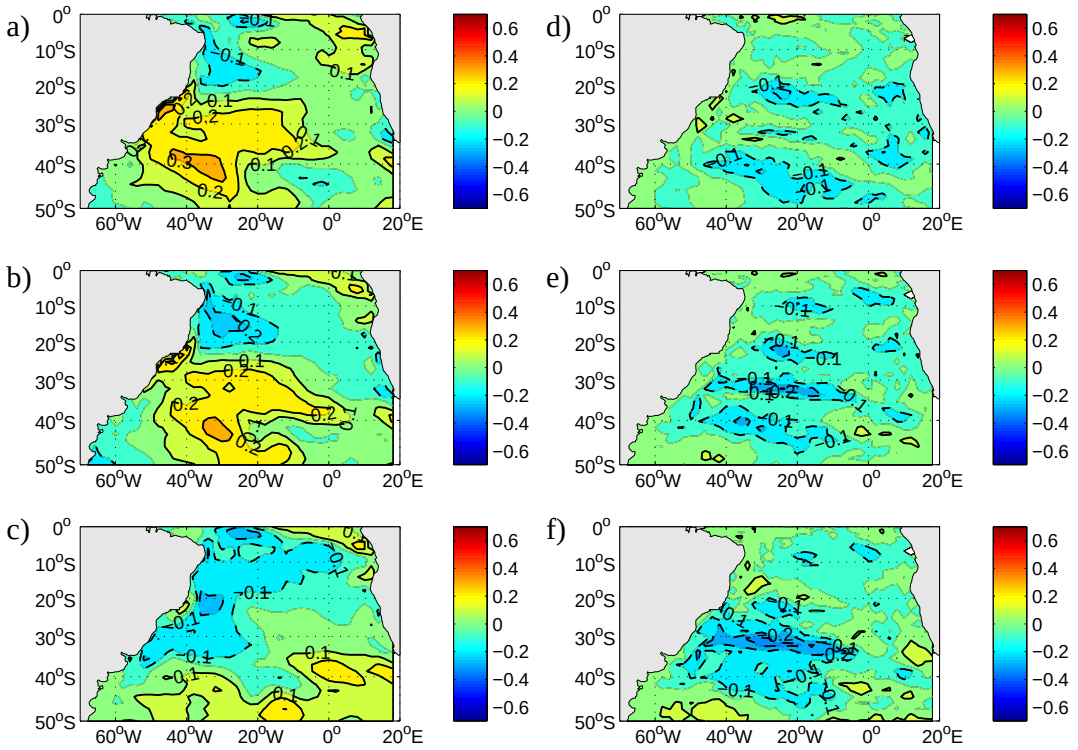

Figure 19: Sequence of the lagged correlation between the fourth REOF(MLT) and $\frac{Q_{sfc}^{net}}{\rho c_p h}$ (left), and $\frac{\Delta T}{h}\ \frac{\partial h}{\partial t}$ (right). With $lag = -3$ (upper), $lag = 0$ (middle) and $lag = 3$ (lower). Lag in *months*. Negative (positive) lag means leading (lagging) forcing field. Positive (negative) contour lines are solid (dashed), zero contour line is omitted, the contour interval is 0.2.

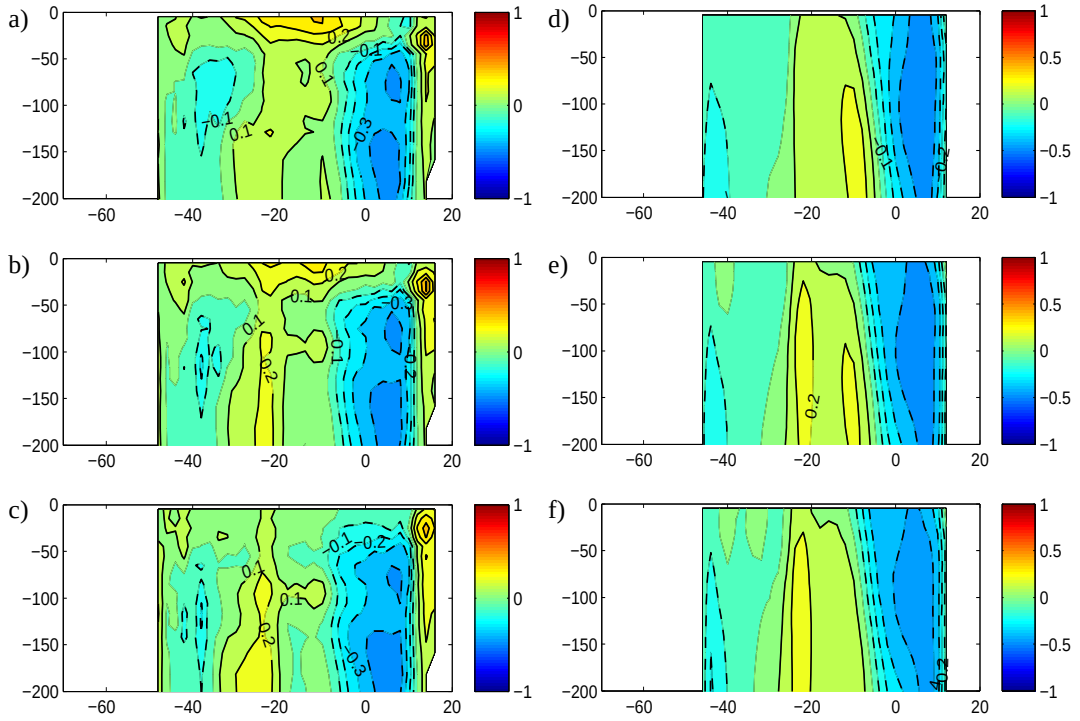

Figure 20: Sequence of vertical section of correlation between the second REOF(MLT) and heat transport anomalies through 30°S. The transport has been calculated using total model velocities (left), geostrophic velocities (right). With $lag = -3$ (upper), $lag = 0$ (middle) and $lag = 3$ (lower). Lag in *months*. Negative (positive) lag means leading (lagging) transport field. Positive (negative) contour lines are solid (dashed). The zero contour line is omitted. The contour interval is 0.1.

model velocities, and (b) geostrophic velocities (Equations 18 and 19, respectively)

.

The east-west section of correlation between the second REOF(MLT) and the heat transport anomalies through 30°S are shown in Figures 20a to 20c. Three regions of significant correlation are apparent. The first one is located in the upper ocean to about $30m$, stretching from 30°W to 0°. The correlation is positive and indicates an enhanced northward or reduced southward heat transport, during phases of positive MLT anomalies. The second region shows negative correlation

and is significant at depths of $50m$ to $200m$, it is centred between 0°E to 10°E. The negative correlation thus indicates a reduced northward or enhanced southward heat transport. The third region is smaller than the first two. Significant positive correlation is centred at $z = 25m$ near 15°E, thus indicating enhanced northward or reduced southward heat transport there.

To further investigate the nature of the anomalous transports, anomalies corresponding to (a) transport of temperature due to anomalous volume transport, (i.e. $v'T$) and (b) advection of anomalous temperature by the mean volume transport (i.e. vT') are calculated (both shown in Appendix 71). These correlation plots indicate that the positive and negative anomalies of the first two described areas are mainly due to anomalous volume transport, as they are significantly correlated with the $v'T$ term. The anomaly of the third region although visible is not exceeding the 95% confidence interval and is therefore likely to be related to the vT' term, which shows strong positive correlations centred between 0-16°S in the upper $100m$.

The vertical section resulting from the correlation analyses including only geostrophic velocities is shown in Figures 20d to 20f. The negative anomaly between 0°E and 10°E, apparent from the surface to at least $200m$ depth, resembles the one seen in Figures 20a to 20c and it is concluded that the anomalous heat transport there is mainly due to anomalous geostrophic currents. The eastern located positive anomaly near 15°E in Figures 20a to 20c does not appear in Figures 20d to 20f, but becomes apparent when calculating the heat transport due to anomalous temperatures (i.e. $v_g T'$, Appendix 71). However, there is no evidence of the western positive anomaly near 0-30°W in Figures 20a to 20c in any geostrophic related correlation analyses, therefore indicating indirectly that it may be related to anomalous meridional Ekman heat transports. This assumption is further supported as the correlation analysis between the second REOF and meridional Ekman heat transport anomalies (Equation 21, Figures 21a to 21c) is positive in an area stretching from the Benguela Current region northwestwards along the South Equatorial Current, therefore matching with the area seen in the vertical section of Figures 20a to 20c.

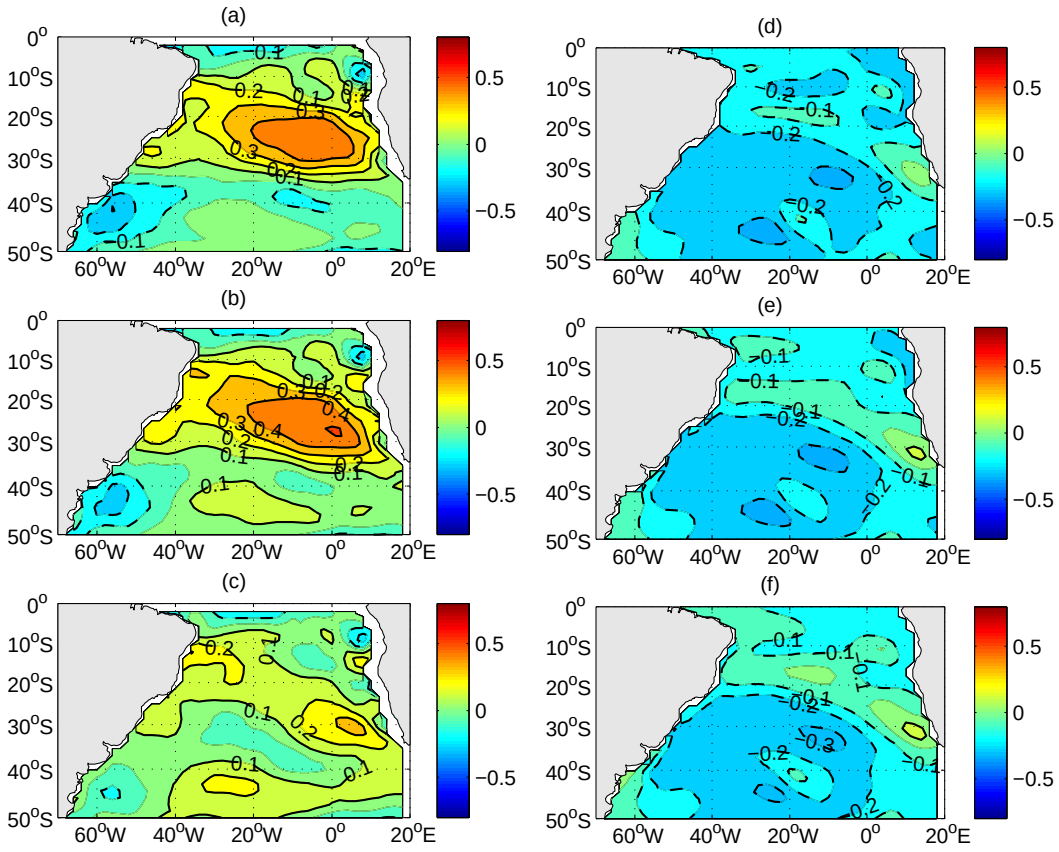

Figure 21: Sequence of the lagged correlation between the second REOF(MLT) and the meridional Ekman heat transport (left) and SSH anomaly (right). With $lag = -3$ (upper), $lag = 0$ (middle) and $lag = 3$ (lower). Lag in *months*. Negative (positive) lag means leading (lagging) forcing field. Positive (negative) contour lines are solid (dashed). The zero contour line is omitted. The contour interval is 0.1.

These results suggest that changes in the heat transport associated with the second mode are mostly induced by changes in volume transport, which are related to anomalous currents. The Benguela Ocean Current is reduced (enhanced) at 30°S during positive (negative) phases of the second REOF, and thus transports less (more) cold water northwards, which subsequently leads to warming (cooling) in the region of the second REOF. The induced anomalous heat transport is primarily caused by anomalous geostrophic currents and reaches depths of $200m$. On the other hand, anomalous meridional Ekman heat transport dominates the region westward of 0°W and is confined to the upper $50m$.

It is clear that the second mode is associated with gyre modifications, leading to anomalous volume fluxes and thus anomalous heat fluxes at the eastern margin of the subtropical gyre. A possible wind induced mechanism, could explain this: The reduced windstress (Figures 6d to 6f) associated with positive phases of the second REOF(MLT), leads to a reduction of the southwestward directed Ekman volume transport. This in turn affects the sea surface height in the centre of the subtropical gyre and thus weakens the outward directed pressure gradient, thereby weakening the geostrophic balanced gyre circulation. One therefore would expect changes in the sea surface height to be associated with this mode. Correlation analyses between the SSH anomalies and this mode (Figures 21d to 21f) indicate a lower (higher) centre of the subtropical gyre, thereby supporting this theory. However, the correlation analyses are not significant at the 95% confidence interval.

4.2 Summary and discussion

In this section, the variability of the South Atlantic Ocean has been examined by means of a global OGCM (ORCA2) forced with 52 years of NCEP/ NCAR reanalysis. A rotated EOF analysis of MLT has been applied and the four leading modes have been investigated. These modes divide the South Atlantic into four subdomains, each with typical time and spatial scales. These modes are (a) the tropical mode, with primarily interannual variability mainly located in the tropics and northern Benguela, (b) the northeastern subtropical mode, with variability between

interannual and decadal time scales, (c) the midlatitude mode, with variability on both interannual and inter-decadal time scales, forming an east-west oriented dipole in the midlatitudes and (d) the southwestern subtropical/ midlatitude mode, that fluctuates on an interannual and decadal time scale. Correlation analyses between these modes and windstress suggest that all modes are primarily driven by the atmospheric circulation.

Table 1 provides an overview of the leading modes, their associated regions and most important forcing terms. The first mode is connected with anomalous northwesterly windstresses that reduce the prevailing trades in the central to western tropical region. Hence, surface latent heat fluxes are reduced leading to warming there. Furthermore, these anomalous winds tend to reduce the zonal component of the southwestward directed upper ocean mean currents. Thus less cold water is transported towards the western tropics, favouring warming there.

The windstress anomalies do not favour warming over the eastern tropics and northern Benguela, suggesting non-local atmospheric influences such as equatorial Kelvin wave propagation being responsible in creating these temperature anomalies (as suggested by *Carton and Huang*, 1994; *Florenchie et al.*, 2003, 2004). In fact, strongest warming associated with this mode occurs during 1963, which was a 'Benguela-Niño' year (*Shannon et al.*, 1986), suggesting a possible connection between this mode and these events. However, although other strong warm events such as the one in 1984 are captured by the time series of this mode, they are not as extreme as the one in 1963. Nevertheless, the above model results suggest that warming in the central to eastern tropics is connected to reduced upwelling mainly due to reduced vertical entrainment and, to a less extent, reduced turbulent mixing. The mode investigated in this study shows strong similarities with the Atlantic Zonal Gradient Mode (also Equatorial Mode), described by *Zebiak* (1993); *Enfield and Mayer* (1997); *Carton et al.* (1996); *Ruiz-Barradas et al.* (2000).

The second mode is connected to reduced trade winds over the subtropics. These lead to changes in the latent heat flux, that in turn alter upper ocean temperatures. Changes in horizontal advection and vertical mixing processes make smaller

contributions to the observed ocean temperature changes. The timing and spatial structure of this mode suggests a connection to ENSO, which is in agreement with *Reason et al.* (2000), *Sterl and Hazeleger* (2003), *Colberg et al.* (2004). In addition, trade wind modulations appear to significantly alter the Ekman related meridional volume and heat transport, which in turn lead to changes in the gyre circulation and thus geostrophic related volume and heat transports. These anomalous transports are strongest in the Benguela Ocean Current region and reach depths of up to $200m$.

For the third mode, the midlatitude westerlies are weakened and result in a reduced northward directed Ekman heat transport, which leads to warming in the central to eastern midlatitudes. Vertical mixing here becomes increasingly important, in agreement with *Sterl and Hazeleger* (2003); *Haarsma et al.* (2005). However, inter-decadal variability is associated with changes in the geostrophic currents that alter the northward (southward) flowing Falklands/ Malvinas (Brazil) current, bringing cooler (warmer) water into the area. This mode may be connected to the inter-decadal SST signal found by *Wainer and Venegas* (2001).

Upper ocean temperature anomalies for the fourth mode respond to changes in the net heat flux, which is increased (reduced) during warm (cold) phases. Associated with this mode are changes in the strength of the South Atlantic anticyclone, which mainly acts to enhance (reduce) entrainment during positive (negative) phases and thus dissipates the observed temperature anomalies.

REOF	REGION	$dT/dt > 0$	$dT/dt < 0$
1	Western tropics	Horizontal advection	Net heat flux
	Eastern tropics	Vertical entrainment	Net heat flux
2	Eastern subtropics	Net heat flux	Vertical mixing
3	Western midlatitudes	Geostrophic advection	Net heat flux
	Eastern midlatitudes	Ekman advection	Net heat flux
4	Western subtropics	Net heat flux	Vertical mixing

Table 1: The four leading modes derived for the mixed layer temperature, associated regions and most important forcing terms.

5 South Atlantic Response to ENSO Induced Climate Variability

This section focuses on the South Atlantic response to ENSO induced climate variability. Despite the fact that ENSO is a major contributor towards global climate variability, few attempts have been made to investigate ENSO related variability in the South Atlantic region. Evidence suggests that ENSO significantly affects South Atlantic upper ocean temperatures and modifies the strength of the South Atlantic Anticyclone (e.g. *Venegas et al.*, 1997; *Reason et al.*, 2000). This potentially affects rainfall variability over southern Africa and South America, due to modulations of the South Atlantic Convergence Zone, the Pacific South American pattern (*Mo and Paegle*, 2001) and the midlatitudinal westerlies (*Reason and Jagadheesha*, 2005).

In the previous section, significant correlations between the second and third South Atlantic leading modes and ENSO were found. The regions associated with these correlations are the central to eastern subtropics and eastern midlatitudes. The important forcing term for the first region is the net surface heat flux, which is increased for positive phases of the second mode. For the second region the meridional Ekman heat flux drives changes in upper ocean temperatures. It is reduced for positive phases of the third mode. Both forcings are found to be related to anomalous atmospheric circulation pattern, that acts to reduce the southeasterly trades and the westerlies for positive phases of these modes. To further understand the evolution of the ENSO signal over the South Atlantic and the associated mechanisms in this basin, composites of ENSO years will be presented. In particular the ORCA2 model will be used to investigate potential linkages between subsurface ocean processes and the evolution of SST anomalies over the South Atlantic during ENSO.

The structure of this section is as follows: First, the calculated variables, model domain and the relevant ENSO years are discussed and composites of ENSO years are compared to observations. Following this, a detailed description of the evolution of the ENSO signal in the South Atlantic, for both, El Niño and La Niña events will

be given. The section ends with a summary and discussion of the main findings.

5.1 ENSO events and data validation

In this section, ORCA2 data for the sea surface temperature (SST), temperature at $55m$ (ST55) and temperature at $215m$ detph (ST215) are analysed. In addition SLP and SST taken from the NCEP/ NCAR reanalysis and GISST SST have been examined. The region of study ranges from 20°N to 50°S and from 70°W to 20°E and thus covers the tropical North Atlantic.

A simplified form of the temperature tendency equation 22 is used in this section. It takes the form

$$\frac{\mathrm{d}T}{\mathrm{d}t} = \frac{Q_{sfc}^{net}}{C_p\,\rho\,z}, \tag{25}$$

where Q_{sfc}^{net} is the net downward heat flux ($W\,m^{-2}$), z the depth of the mixed layer, calculated as the level where the density increases by $0.01\,kg\,m^{-3}$ from the surface, C_p the specific heat capacity ($4187\,J\,kg^{-1}K^{-1}$) and ρ the density of sea water (an average value of $1025\,kg\,m^{-3}$ has been taken).

Hence, it is assumed in Equation 25 that (a) the temperature of the mixed layer depth can be approximated by the sea surface temperature, and (b) the total change of T is given by the net surface heat flux. The analysis of the second rotated EOF in Section 4 implies that this may be a reasonable approach for the eastern subtropical South Atlantic. In addition Ekman heat transport (*Levitus*, 1987) and Ekman pumping (Equations 21 and 16, respectively) and the "Combined Windstress Anomaly and Climatology Pattern (CWP)" (Section 3, Section 3.4.5) are derived.

In order to identify individual ENSO events, the Niño 3.4 Index is applied to both the ORCA2 model SST anomalies and the GISST 3.0 SST anomalies. El Niño (La Niña) events are identified if the 5-month running average of the Niño 3.4 index exceeds 0.4°C (-0.4°C) for at least 6 consecutive months. Figure 22 displays the resulting indices for the ORCA2 and GISST3.0 SST. Generally, the two indices compare well during 1948-1999. However, it appears that at times that ORCA2 overestimates positive or negative temperature anomalies, which results in slightly

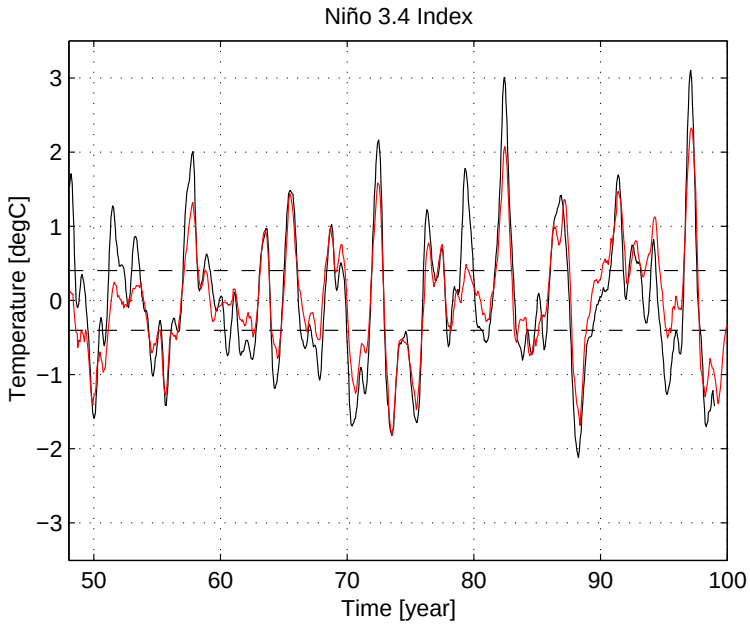

Figure 22: The Niño 3.4 Index derived from ORCA2 model SST (black), and GISST3.0 SST (red).

different ENSO years (best seen for the year 1960). Due to this difference, only those ENSO years are chosen for the composite analysis that are detected by both time series. Table 2 lists the events that result from this selection method as El Niño (La Niña) and El Niño +1 (La Niña+1) years. The former refers to years when the Niño 3.4 SST anomaly first appears while the +1 years refer to the following years (i.e. the mature phase years).

A simple t-test has been applied to all seasonal fields shown in this section. No t-test has been applied to the fields showing yearly means because, due to averaging, there are only small areas that are significant at the 90% confidence level.

The previous section demonstrated the capability of the ORCA2 model in representing variability in the South Atlantic. However, it must be shown that ENSO signals are captured in a reasonable manner by ORCA2. To validate the ORCA2 model output, seasonal composites of SST anomalies (shown in the second column of Figure 25 for El Niño and Figure 28 for La Niña years) were compared to the GISST3.0 SSTA (Figure 23) and to the NCEP surface air temperature (not shown).

El Niño	La Niña
1957 / 58	1949 / 50
1963 / 64	1954 / 55
1965 / 66	1955 / 56
1972 / 73	1970 / 71
1982 / 83	1973 / 74
1986 / 87	1975 / 76
1997 / 98	1988 / 89
	1995 / 96
	1998 / 99

Table 2: El Niño and La Niña years chosen such that the 5-month running average of the Niño 3.4 Index exceeds 0.4°C (-0.4°C) for at least 6 consecutive months.

There is generally good agreement between the GISST SST anomalies (Figure 23) and the ORCA2 SST anomalies (Figures 25 and 28 second column) for each of the composite years in terms of spatial pattern although smaller features displayed by the GISST SST anomalies are not always captured by ORCA2. This may partly reflect the higher resolution of the GISST dataset (apart from the equatorial region) compared to ORCA2. The similarity of the ORCA2 SST anomalies to the NCEP surface air temperature anomalies (not shown) is expected and reflects the nature of the model forcing using NCEP surface air temperature in the surface heat flux forcing, which implies a nudging of SST anomalies towards observed air temperatures. However, there are differences in the spatial patterns as well as in the magnitudes. Generally the NCEP surface air temperatures are somewhat stronger than the ORCA2 SST anomalies. When assessing the accuracy of the ORCA2 SST, two points should be emphasized. Firstly, the spatial distribution as well as the magnitudes of ORCA2 SST anomalies seem to be able to capture the seasonal evolution of the large scale interannual anomalies such as El Niño or La Niña patterns. Secondly, the upper model level is not optimal for showing the ability of ORCA2 to

represent temperature variations due to the manner in which the heat flux boundary condition is applied. Although the bulk mixed layer attempts to represent what is actually being forced from the atmospheric boundary layer without providing SST information, by prescribing atmospheric temperature values the upper ocean level is nudged towards observed temperatures. It is therefore appropriate to use subsurface temperatures and, in the following, anomalies at the surface, at $55m$ (near mixed layer base) and at $215m$ (near thermocline) levels are presented

5.2 South Atlantic response to ENSO events

In the following section, the response of the South Atlantic to ENSO events will be discussed by looking at seasonal composites of ENSO. Upper ocean temperature anomalies are examined from JAS of the ENSO year to AMJ following the mature phase (ENSO+1 year). Sea level pressure, windstress and variables that are a function of these (CWP, meridional Ekman heat flux) and net surface heat fluxes are examined from AMJ of the ENSO year to JFM of the following year (i.e., the mature phase). The reason for so doing is that it is found that upper ocean temperature anomalies during ENSO are mainly the result of the atmospheric forcing and respond to them with a time lag of roughly one season. Unfortunately, latent heat fluxes from ORCA2 are not available; hence, NCEP values area examined instead (Figure 24). These fluxes are generally consistent with the model upper ocean temperatures with the latter lagging the flux by one season similar to what is shown below for the wind and net surface heat flux. Furthermore, the NCEP latent heat fluxes agree well with the net downward heat flux anomalies shown below, suggesting that the latent heat flux is the dominant factor in the surface heat budget. During El Niño, the upper ocean temperature anomalies in the South Atlantic generally start off negative (weakly positive) in the tropics (midlatitudes) and warm (cool) by the mature phase and then weaken or, in some areas, take the opposite sign during the following austral autumn. The La Niña anomalies are roughly the reverse. Evidence is presented below that these changes in temperature are caused by anomalous windstresses, that lead to changes in net surface heat fluxes and Ekman

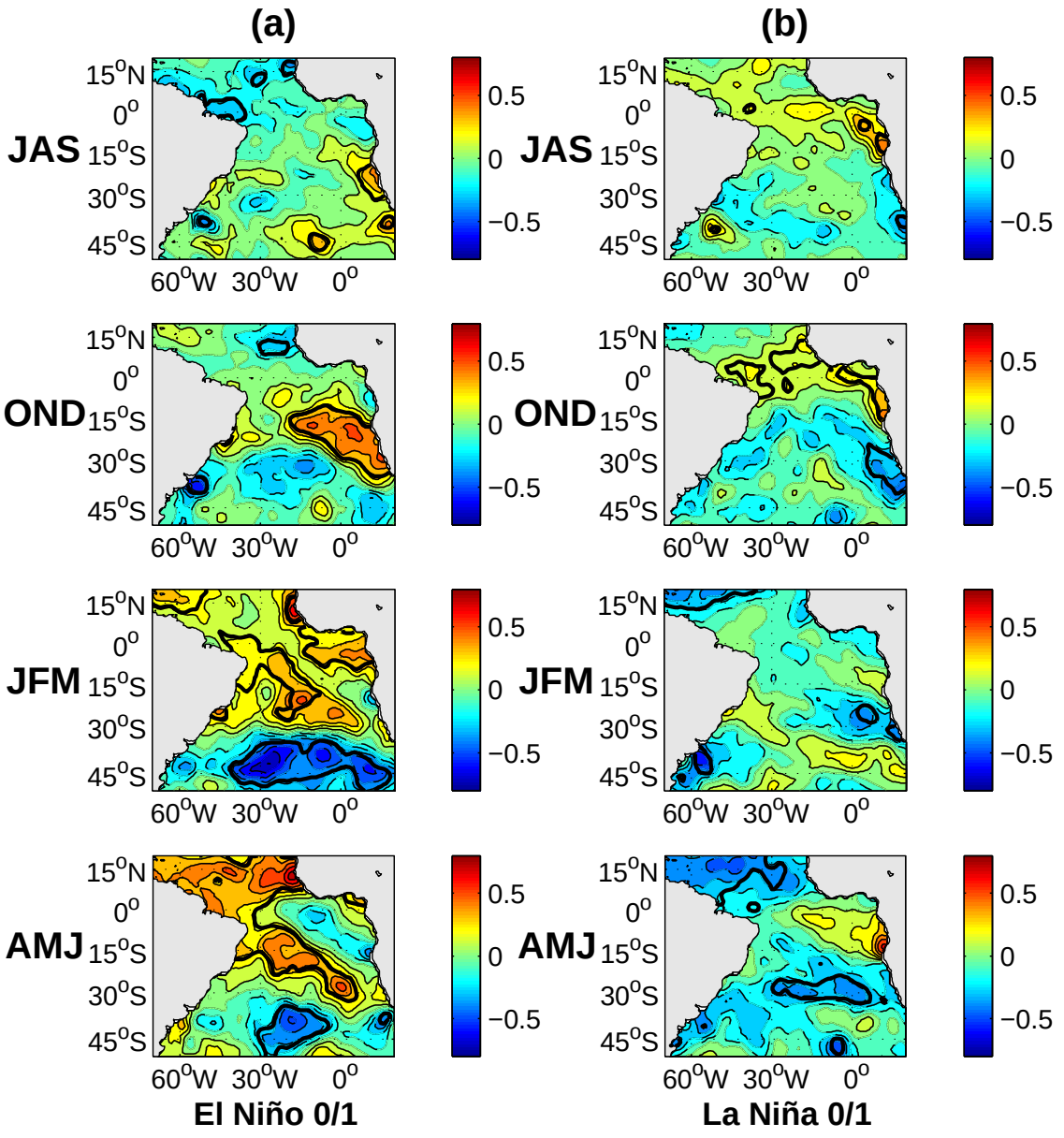

Figure 23: Seasonal composites of UKMO GISST 3.0 SSTA for the (a) El Niño phase (b) La Niña phase from austral winter of the onset year through to austral autumn of the following year. Dashed (solid) contours denote negative (positive) values. Significant t-test areas at the 90% level are within the thick line. The contour interval is 0.1°C. The zero contour line is omitted.

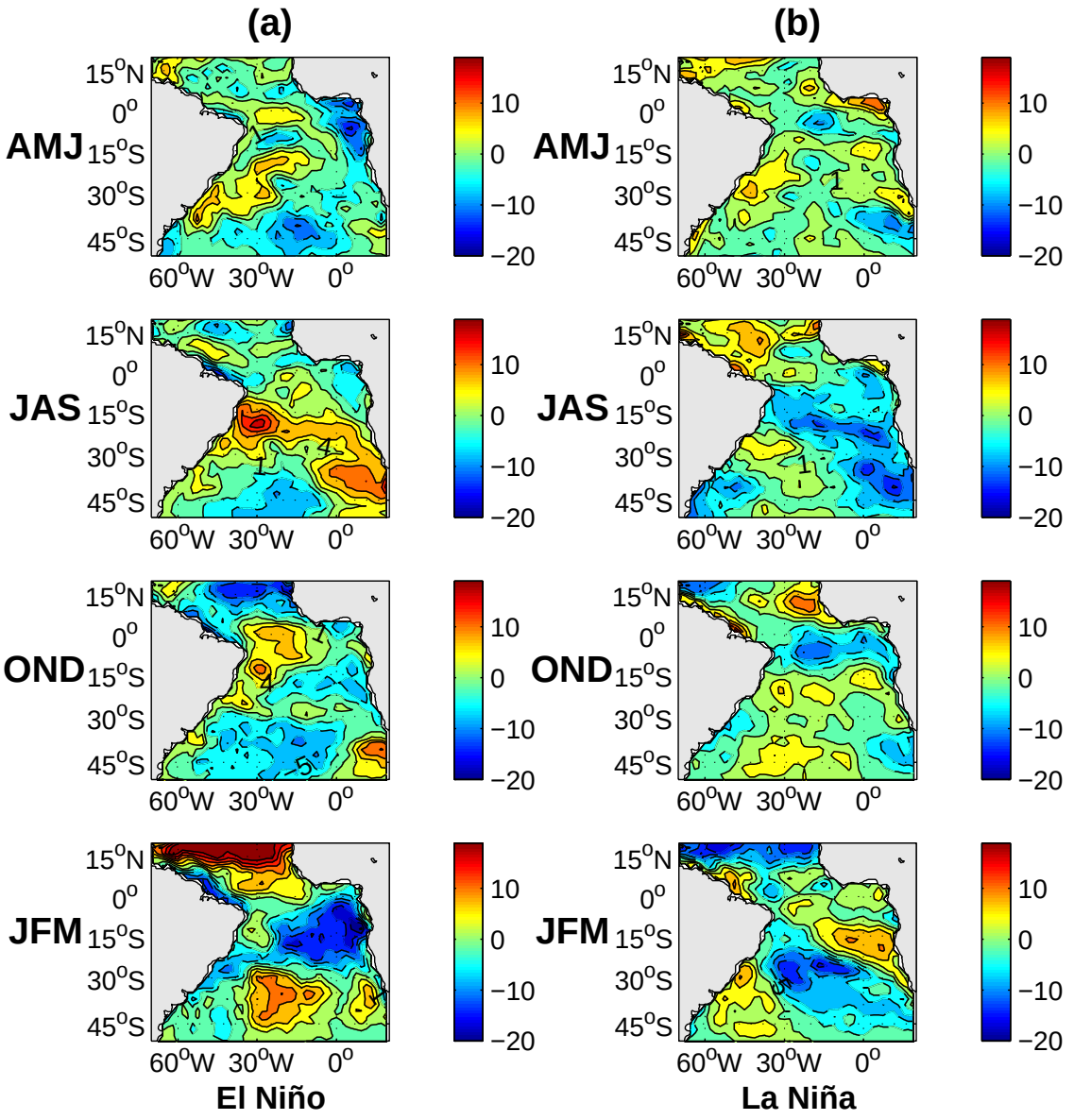

Figure 24: Seasonal composites of NCEP/ NCAR latent heat flux for (a) El Niño and (b) La Niña phase. Positive (negative) contour lines are solid (dashed). The zero contour line is omitted. The contour interval is $3\,Wm^{-2}$.

heat transports. For the El Niño phase, a reduced tropical southward and enhanced midlatitude northward heat transport is apparent, consistent with the warming in the tropics and parts of the subtropics and the cooling in the midlatitudes. For the La Niña phase, the reverse seems to occur, again consistent with the temperature anomalies.

5.2.1 Detailed analysis of the El Niño-induced anomalies

Upper ocean temperatures (SST and ST55)

Figure 25b and 25c show the model surface (SST) and 55m depth (ST55) temperature anomalies. During JAS, significant warming at the 90% level is apparent in the Benguela current region and this extends northwestwards and peaks during the following season (OND). By OND, areas of the western subtropics/ midlatitudes show cold anomalies, and this northeast/ southwest pattern evolves to a more north/ south oriented warm/ cool anomaly by JFM. A larger tropical North Atlantic area shows warm anomalies in the following AMJ with a band of subtropical warming also apparent across the South Atlantic. The South Atlantic central midlatitudes remain cool, but weaker than JFM, and the eastern equatorial and tropical South Atlantic has evolved towards cool anomalies.

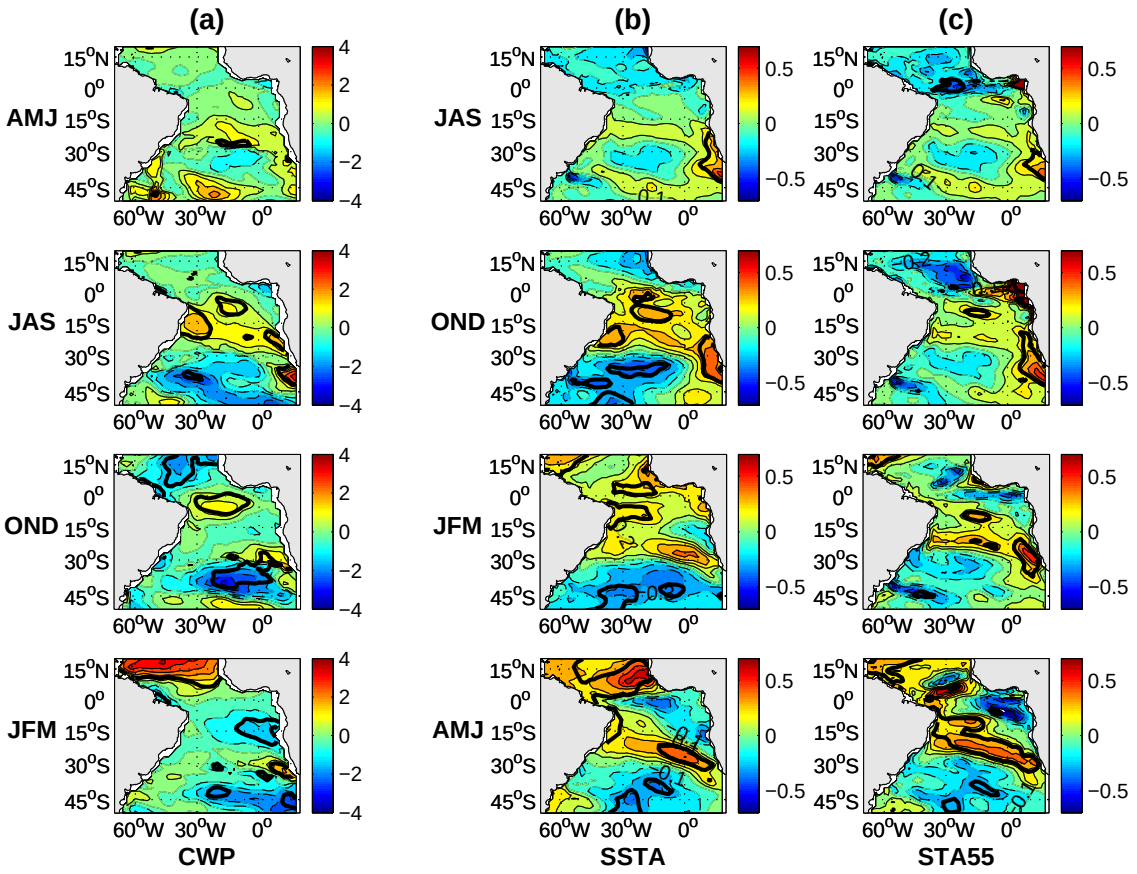

Figure 25: Seasonal composites of ORCA2 (a) CWP, (b) SSTA and (c) STA55 for the El Niño phase. Positive (negative) CWP indicate areas where the windstress anomalies and the windstress climatology have the opposite (same) sign, thus favouring warm (cold) SSTA and STA55. Dashed (solid) contours denote negative (positive) values. Significant t-test areas at the 90% level are within the thick line. The contour intervals are (a) $0.5 \times 10^{-4} N\, m^2$, (b) and (c) $0.1°C$. The zero contour line is omitted.

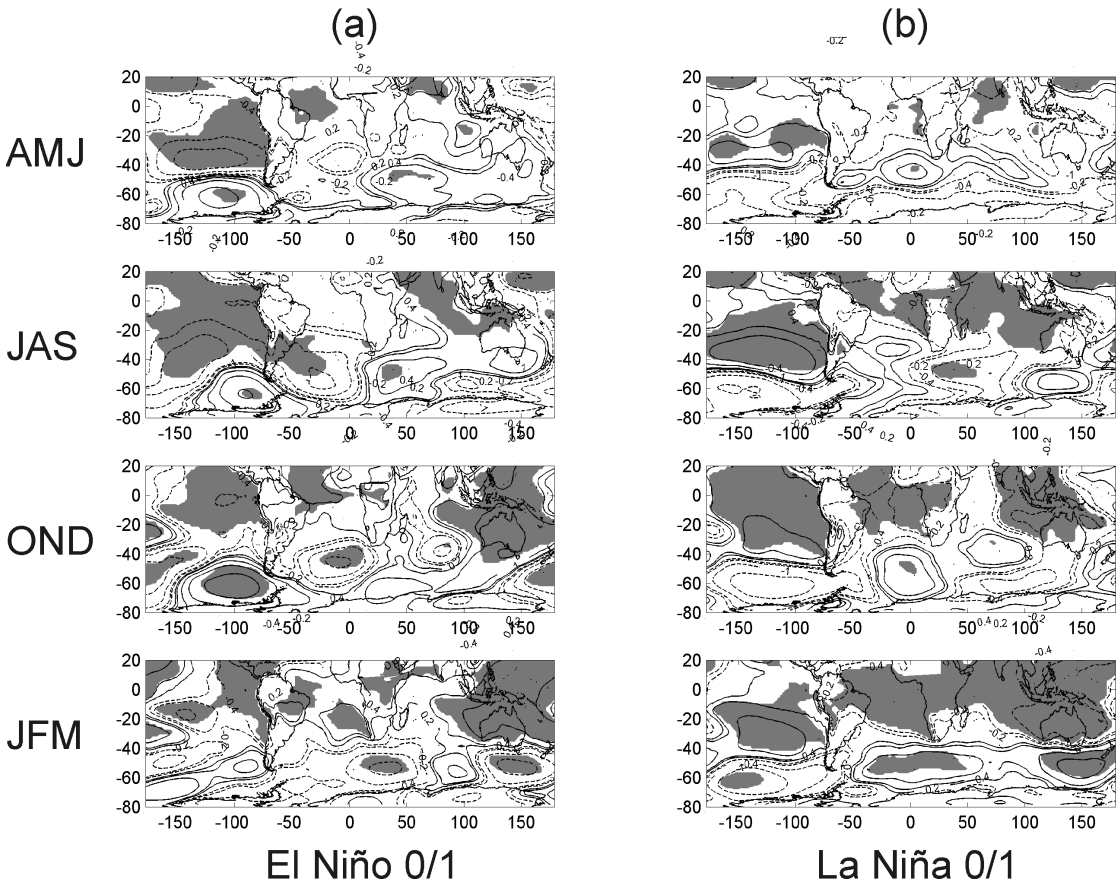

Figure 26: Seasonal composites of ORCA2 SLPA, for (a) the El Niño phase and (b) the for La Niña phase. Dashed (solid) contours denote negative (positive) values. Significant t-test areas at the 90% level are shaded grey. The given contour lines in $h\,Pa$ are 4, 2, 1, 0.4 and 0.2 for positive and negative values respectively.

Sea level pressure (SLP) and Combined Windstress Anomaly and Climatology Pattern (CWP)

Figure 26a shows global SLP anomalies for the El Niño composite episode with the well-known ENSO patterns over the tropical Indo-Pacific evident. Over the South Atlantic, a negative anomaly is apparent in the subtropics/ midlatitudes which strengthens in JAS, and weakens by JFM. These anomalies therefore modulate the subtropical anticyclone and the midlatitude westerlies. This pattern is likely part of the Pacific South American wavetrain pattern caused by atmospheric Rossby waves emanating from ENSO-modulated atmospheric convection in the Indo-Pacific region (*Mo and Paegle*, 2001).

During AMJ, the reduced South Atlantic subtropical anticyclone leads to a weakening of the trades and the westerlies over the basin. The corresponding CWP plot (Figure 25a) shows the resulting enhanced and reduced windstress anomalies. These areas more or less correspond to those of cooling (warming) seen one season later (JAS) in the upper ocean temperature fields (Figures 25b, 25c). During JAS, the negative SLP anomaly strengthens and moves further to the southwest and is now significant at the 90% level (Figure 26). As a result, the westerlies are enhanced, but the trades are still reduced (Figure 25a), and the temperature anomalies (Figures 25b, 25c) essentially reflect this a season later.

The negative SLP anomaly weakens and moves northeast in OND, as the positive pressure anomalies west of the Drake Passage and the neighbouring Southern Ocean strengthen, and positive anomalies become apparent in the tropical South Atlantic. As a result, the westerlies are still enhanced over the South Atlantic and the trades immediately south of the equator are reduced (Figure 25a). Consistent with these CWP anomalies, large areas of tropical warming (midlatitude cooling) are apparent in Figure 25b. The temperature anomalies do not correspond exactly, and, as shown below, other factors are also significant. During the mature phase (JFM), the cyclonic anomaly now south of Africa and the weak positive anomaly in the central to eastern South Atlantic (Figure 26a) lead to enhanced tradewinds and westerlies (Figure 25a). As a result, negative temperature anomalies become

apparent (Figures 25b, 25c) except for a band of warming extending northwest from the southern Benguela region where the winds tend to be weaker than average.

In general, the results of this section indicate that there is a one season lag between the ocean temperature anomalies and the wind (CWP) forcing. This finding suggests that wind-driven surface flux changes in the South Atlantic may play a significant role in the evolution of upper ocean temperatures during El Niño.

Meridional Ekman heat transport(MEHT)

The calculated MEHT anomalies are shown in Figure 27a. In AMJ, a positive MEHT anomaly is apparent from the subtropics (40°S) to the equatorial South Atlantic. With respect to climatology, this anomaly weakens the generally negative (i.e. southward) net transport that is apparent from the equator to about 25°S, but strengthens the climatologically (i.e. northward) positive Ekman heat transport southward of 25°S. Hence, there is a decrease in Ekman heat transport away from the subtropics, consistent with the relative warming there. This is apparent in the warm band at 15°S-25°S a season later in JAS (Figure 25b). This reduction of Ekman heat transport into the midlatitudes contributes towards the cold temperature apparent from 25°S to 40°S, in JAS (Figure 25b). The cold anomaly is enhanced by the increase in northward Ekman heat transport away from the region.

During JAS, the positive MEHT anomaly in the tropical South Atlantic remains, thus supporting warming there in OND due to a reduced southward heat transport. In the southwestern South Atlantic, a positive anomaly evolves (Figure 27), enhancing the climatologically northward heat transport, and is thus consistent with the observed cold anomalies there in OND (Figure 25b). In the southern Benguela current region, the Ekman heat transport anomaly is negative reducing heat transport out of the region, and supporting the strong warming seen there in OND (Figure 25b). There is a less obvious agreement between the OND MEHT anomalies and the observed temperature anomalies a season later than was the case for the previous two seasons. A significant positive anomaly exists south of 25°S in OND and acts to enhance the northward heat transport, and thus supports midlatitude cooling in JFM (Figure 25b). The cold temperature anomaly that evolved in the north-

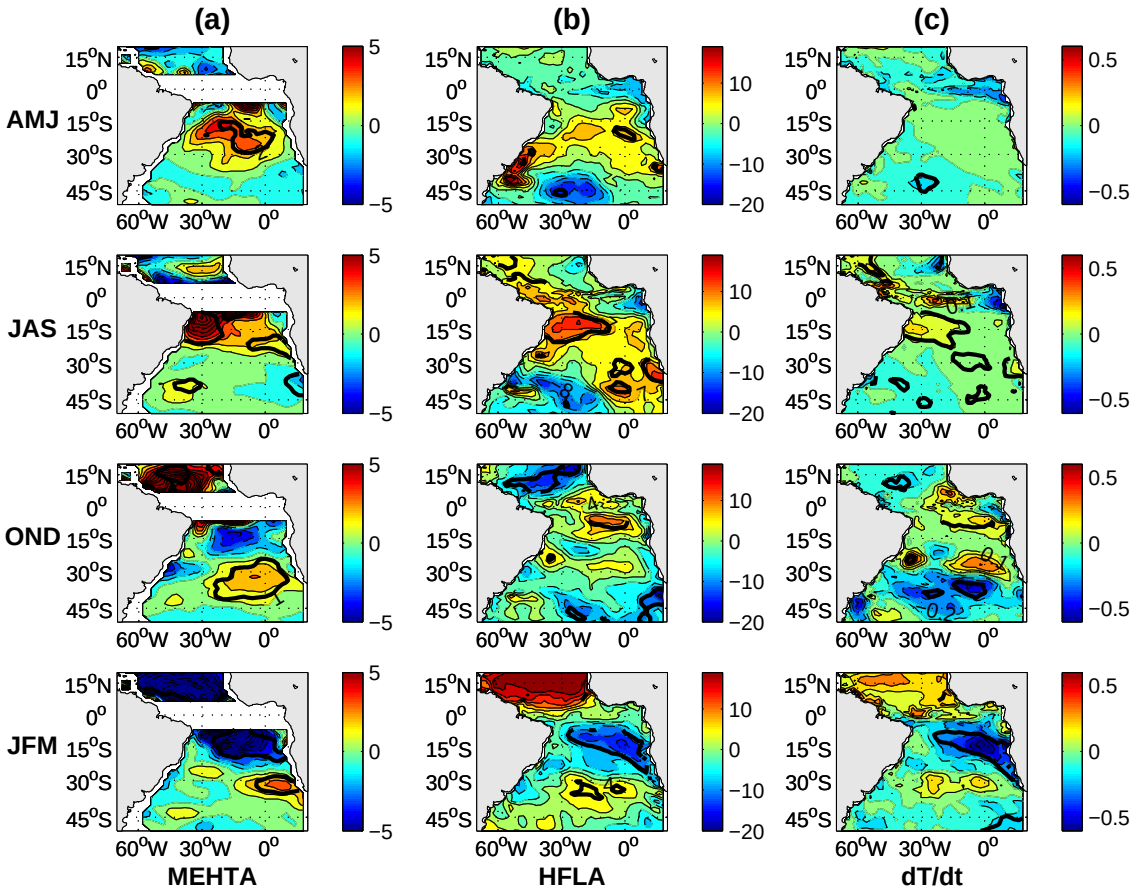

Figure 27: Seasonal composites of ORCA2 (a) meridional Ekman heat transport anomalies, negative (positive) values indicate anomalous southward (northward) heat transport, (b) net surface heat flux where negative (positive) values indicate flux out of (into) the ocean and (c) expected temperature change. Dashed (solid) contours denote negative (positive) values. Significant t-test areas at the 90% level are within the thick line. The contour intervals are (a) $1 \times 10^6\, W\, m^2$, (b) $4\, W\, m^2$ and (c) $0.1\ ^\circ C$. The zero contour line is omitted.

ern Benguela region during JFM is consistent with the enhanced southward heat transport that is apparent in the subtropical South Atlantic.

During JFM, the negative MEHT anomaly extends from the equator to near 20°S (Figure 27a), strengthening the cold anomalies that extend northwestwards from the northern Benguela region in AMJ (Figure 25b). Over, and west of, the southern Benguela, positive MEHT anomalies are apparent which contribute towards the warm anomalies seen here in AMJ (Figure 27a).

Net downward surface heat flux (HFL) and the temperature tendency

During AMJ, the HFL anomalies shown in Figure 27b are positive in the central South Atlantic and negative in the midlatitudes and the equatorial region. Thus, they mainly support the observed upper ocean temperatures occurring a season later in JAS (Figure 25b). The expected temperature changes due to these surface flux anomalies (Figure 27c) imply a weak warming over the tropics to subtropics, but underestimate the observed magnitude by about a factor of 10. The predicted temperatures in the equatorial region (Figure 27c) match much more closely with the observed ones (Figure 25b) as do those in the tropical North Atlantic. This result is consistent with the Ekman heat transport anomalies being important for the South Atlantic during JAS, as discussed above. Both the HFL anomalies in JAS and the expected temperature changes (Figures 27b,c) compare better to the observed OND ocean temperatures (Figure 25b). However, the magnitudes are still too low when compared to the actual temperature anomalies. Improved agreement occurs during the next OND and JFM season, especially in the southern subtropics/ midlatitudes where cooling is apparent (Figure 25b).

Summary

The El Niño phase is characterized by warmer upper ocean temperatures in the tropics and subtropics of the South Atlantic that reach their peak during OND of the composite El Niño year. Warming in the tropical North Atlantic occurs about one season later compared to the southern tropics. This delayed warming may partly be due to the remote ENSO pre-conditioning role of tropical Atlantic variability recently discussed by *Giannini et al.* (2004). Since the meridional gradient mode

mainly projects onto the tropical Atlantic in MAM or AMJ, positive phases (warm tropical North Atlantic, cool tropical South Atlantic) of the meridional gradient mode could effectively alter the warm ENSO signal in the tropical Atlantic and may partly be responsible for the delayed warming observed here.

The midlatitude South Atlantic becomes significantly colder during OND of the El Niño year and JFM of the following year (mature phase) after which the negative anomalies begin to weaken. The South Atlantic subtropical anticyclone is generally weaker than usual during all of the El Niño year and the following mature phase, leading to a reduction in the southeasterly trades. As the negative SLP anomaly moves further to the south, it tends to strengthen the midlatitude westerlies, thus inducing anomalous winds that affect the meridional Ekman heat fluxes. The southward tropical Ekman heat transport is reduced during AMJ to OND, favouring the observed warming in the tropics and parts of the subtropics. On the other hand, the northward midlatitude Ekman heat transport is enhanced, consistent with the observed cooling in the midlatitudes. Surface heat flux anomalies contribute to the evolution of the upper ocean temperature anomalies. This can be seen most clearly in OND and JFM, when the calculated temperature changes match reasonably well with the model temperature anomalies one season later. There is an increased heat flux into the ocean mainly over the tropics, subtropics and the Benguela current region in AMJ, JAS, and to lesser extent, OND. Reduced heat fluxes are apparent over parts of the midlatitudes consistent with cool temperatures there.

5.2.2 Detailed analysis of the La Niña-induced anomalies

Upper ocean temperatures

Figure 28b and 28c show the model SST and ST55 anomalies for the La Niña phase. In JAS, a centre of cold anomalies lies in the southern Benguela current region. It becomes significant at the 90% level and moves northward during the following OND, JFM and AMJ. In JFM, these cool anomalies peak in the central and eastern subtropics with weaker cooling apparent over most of eastern tropics. The midlatitudes are cold in JAS but these cool anomalies disappear in the mature

phase (JFM) and AMJ. The eastern equatorial South Atlantic is warm in JAS, with the anomalies weakening in OND and becoming mainly negative by JFM. In AMJ, a reversal to mainly warm anomalies is apparent in the equatorial region and southeastern tropics.

Sea level pressure (SLP) and CWP

Figure 26b shows the global SLP anomalies during La Niña. Over the South Atlantic, a positive SLP anomaly is apparent in AMJ in the subtropics/ midlatitudes. This feature weakens during JAS but becomes stronger and significant again during OND and JFM as the well-known cyclonic anomalies become more established over the tropical Indo-Pacific. The SLP evolution is more or less opposite to that shown in Figure 26a for the El Niño composite and, essentially shows the reverse phase Pacific South American pattern over the South Pacific/ South Atlantic region. It should be noted that the positive anomalies are further south than the corresponding cyclonic anomalies during El Niño (Figure 26a) so they correspond more to a weakening of the midlatitude westerly belt in the South Atlantic rather than a strengthening of the anticyclone. The evolution in CWP and upper ocean temperatures (Figure 28) is again more or less the reverse in pattern to that seen for the El Niño so a detailed discussion is not provided. Thus, there is a one season lag between the wind changes and the upper ocean temperature response. However, the magnitudes of the anomalies are not always the same as those seen in Figure 25 for the El Niño, suggesting that the relationship between the ENSO forcing and the South Atlantic response is not necessarily linear. In general, agreements between the CWP fields and the observed upper ocean temperature fields is not as clear during La Niña as it is during El Niño. Nevertheless, the significant temperature anomalies (mainly in, and northwest of, the southern Benguela current region) are supported by the anomalous winds.

Meridional Ekman heat transport (MEHT), net downward surface heat flux (HFL) and temperature tendency

With the exception of AMJ, the MEHT anomalies (Figure 29a) are roughly the reverse of the El Niño ones (Figure 27a). The anomalies tend to be negative

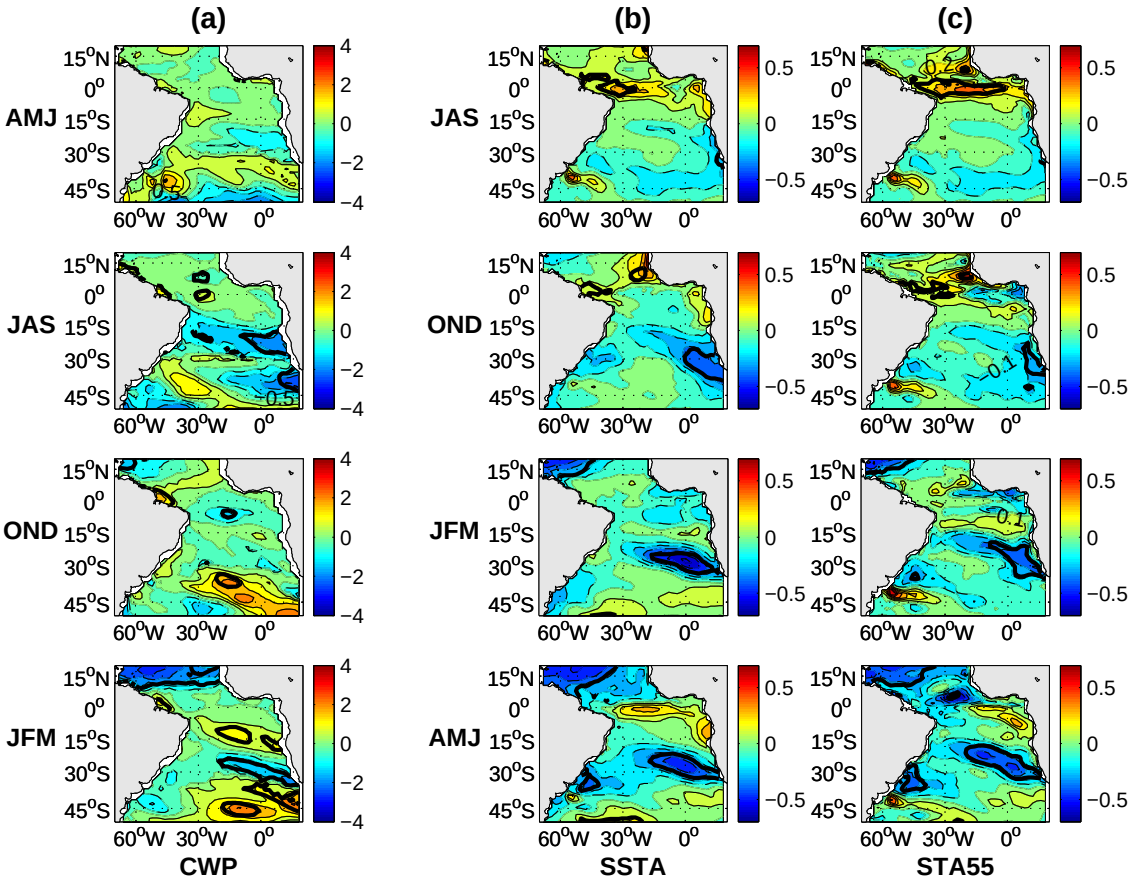

Figure 28: As for Figure 25 but for the La Niña phase.

during AMJ, OND and JFM in the midlatitudes, and during AMJ, JAS and JFM in the subtropics. Positive anomalies are apparent mostly in the tropical region in AMJ, JAS and JFM. The negative anomalies in the midlatitudes (subtropics) reduce (enhance) the climatological northward (southward) Ekman heat transport. They are therefore consistent with the dissipation of the JAS cool anomaly near 40°S by JFM and the maintaining of the cool anomalies in the subtropics. The positive MEHT anomalies in the tropics during AMJ, JAS and JFM favour warming over the tropical and eastern tropical South Atlantic a season later.

The heat flux anomalies for AMJ and the calculated temperature changes (Figures 29b, 29c) show some similarities in pattern over the South Atlantic (except the southwest and equatorial regions) with the observed model temperature anomalies one season later (JAS). Better agreement is seen between the JAS heat flux anomalies/ temperature tendencies and the OND temperature anomalies (Figures 29b and 29c, 28b and 28c) over most of the South Atlantic. This improvement continues for OND and JFM when the calculated temperature changes are consistent with most of the model upper ocean temperature characteristics. However, as for the El Niño case, the calculated temperatures are typically too low in magnitude when compared to the actual model temperature anomalies.

Summary

During La Niña, the upper ocean temperatures are generally colder than average over most of the basin except the tropical southeast Atlantic and the midlatitudes in AMJ. As in the El Niño case, the anomalies show a northward movement with the northern tropical response appearing to lag that in the southern tropics by about a season. The midlatitude westerly belt over the South Atlantic is generally weaker and, to lesser extent, the subtropical anticyclone is stronger during La Niña, enhancing the trades and thus favouring cooling. These winds lead to changes in the net surface heat fluxes which are in broad agreement with the model temperature anomalies. Changes in the meridional Ekman heat transport are also seen to contribute to the SST and ST55 anomalies, particularly in the tropical southeast Atlantic and the midlatitudes.

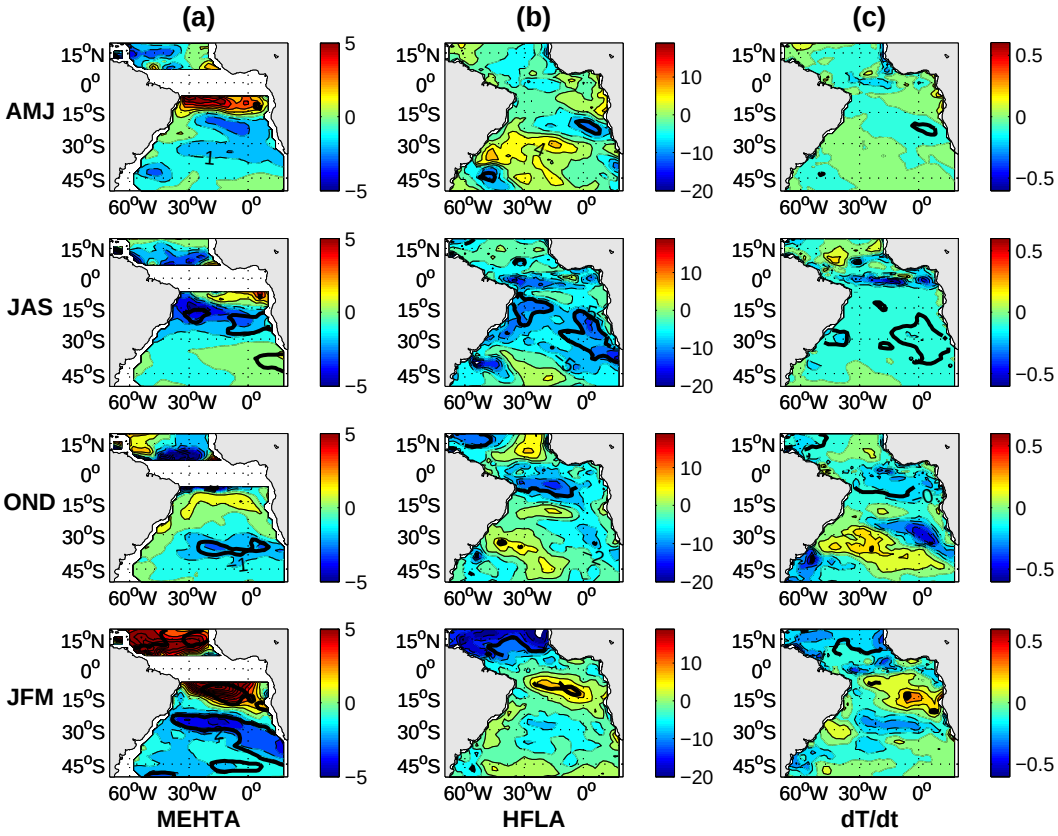

Figure 29: As for Figure 27 but for the La Niña phase.

5.3 Subsurface temperature anomalies (STA215)

Patterns

Temperature patterns at 215 m depth (STA215) associated with ENSO were also examined and found to not vary much with the season. Therefore, annual mean ENSO composites are shown for the El Niño -1, 0, +1 years (Figure 30) and La Niña -1, 0, +1 years (Figure 31). During the El Niño -1 to +1 year (Figure 30), two positive anomalies are apparent, one situated near the centre of the subtropical gyre (15°S-30°S), and the other stretching southeastwards from the midlatitude South American coast to south of Africa. The equatorward and poleward margins of the subtropical gyre tend to show cold anomalies as does the far southwest. During La Niña (Figure 31), the pattern reverses sign to some extent, although cool anomalies tend to dominate, again implying nonlinearity between the El Niño and La Niña response. A subsurface signal in the South Atlantic related to El Niño and La Niña is evident in Figures 30 and 31 suggest that there is. Although the pattern remains quite stable in shape and intensity, there is variability; the warm anomaly in the centre of the basin increases during the El Niño-1 to the El Niño+1 year as does the corresponding cold anomaly during the La Niña-1 to the La Niña+1 year. The tropical cold anomaly increases during the El Niño year but decreases after that.

Mechanisms

Since the STA215 patterns do not change a great deal during the -1 to +1 years in both the El Niño and La Niña case, the forcing for these patterns is likely to be steady on at least annual time scales. If the potential forcing shows any evidence of altering the STA215 from year to year, then it would be apparent in their annual means. Thus, the following analyses are based on annual means. Changes in thermocline depth are known to have an impact on temperature in the upper and lower ocean levels. An increasing (decreasing) thermocline depth can lead to a warmer (cooler) ocean at shallower levels. Up - and downwelling and associated divergence and convergence also modify upper and lower level temperatures. The thermocline itself may be altered by wind-driven up- or downwelling but also by heat loss to the

atmosphere, which implies convection. Ekman pumping patterns and thermocline depth anomalies (Figure 30) show some features that can help explain the STA215. The upwelling cells in the El Niño and El Niño +1 year near 10° S correspond well with the tropical cold anomaly in the STA215, although some advection by the equatorial currents is apparent. South and north of that, downwelling is evident which coincides with the observed warm anomaly near 20°S and, in El Niño-1, also at 0-5°S. The warm anomaly at 35°S-40°S corresponds reasonably well with downwelling cells existing during the three years. The cold anomaly at 20°S-30°S may be linked to some extent with upwelling cells in the west. The thermocline depth (Figure 30) gives further support for the cold STA215 near 10°S since it shows regions of decreased thermocline depth in all three years in the tropical western Atlantic. During the El Niño and to lesser extent El Niño+1 year, this region of decreased depth spreads over most of the tropics and subtropics consistent with the mainly cool anomalies evident. An exception is the warming near 15°S-20°S; which displays some areas with small increases in thermocline depth at its western and eastern margins during the El Niño and El Niño+1 years. A mainly shallower thermocline in the centre of this latitude zone is apparent, suggesting that this region is mainly responding to the strong downwelling from the upper layers. The area of increased thermocline depth near 30°S- 35°S moves southeast in the El Niño year and further east in the El Niño+1 year consistent with the band of midlatitude warming in these years. The southwestern cold anomaly near 40°S-45°S coincides with a shallower thermocline during each year.

During La Niña, many of the previously described features are the same, but with reversed signs. Thermocline depth and Ekman pumping anomalies (Figure 31) both imply warm STA215 near 10°S throughout the La Niña years. Large areas of shallower thermocline and upwelling are apparent over the subtropics in the -1 and 0 years, leading to reduced STA215. In the +1 year, the region of cooling is more obvious in the western and central subtropics, mainly consistent with the other fields. In the midlatitudes near 35°S-40°S, there are areas of Ekman suction and shallower thermocline (particularly in the -1 and +1 years), that correspond with parts of the

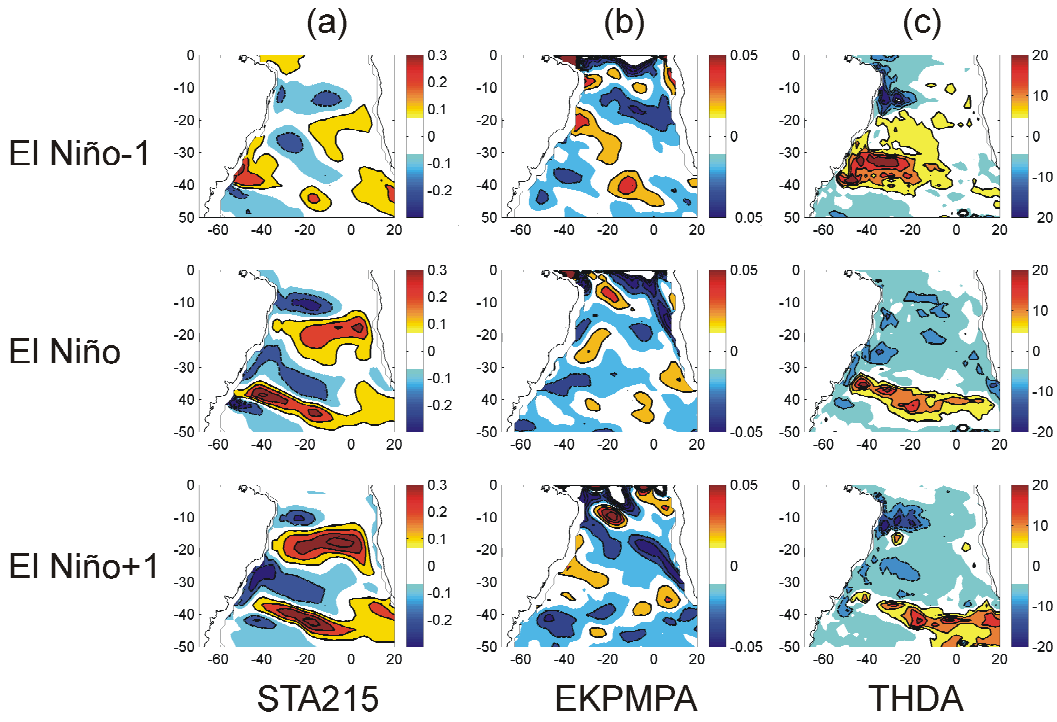

Figure 30: Annual means of: (a) STA215, (b) Ekman pumping anomalies where negative (positive) values indicate down- (upwelling), and (c) thermocline depth anomalies where negative (positive) values indicate a shallower (deeper) thermocline for the El Niño-1 to El Niño+1 years. Dashed (solid) contours denote negative (positive) values. The contour intervals are (a) $0.1\,^{\circ}C$, (b) $0.02\,m\,s^{-1}$, and (c) $5\,m$. The zero contour line is omitted.

band of cool STA215. This correlation is also seen between the warm STA215 in the southwest and the increased thermocline depth for the La Niña 0 and +1 years. In all cases, however, there is not an exact match between the STA215 anomalies and those in the thermocline depth or Ekman pumping due to advection by the mean currents. Examples of such advection can be seen in the Brazil/ Malvinas Current confluence region in the southwest and the South Atlantic Current region across the basin near 40°S.

The results suggest that Ekman pumping may significantly influence the thermocline depth, and hence subsurface temperatures, in the South Atlantic. In turn, these Ekman pumping anomalies arise from the wind stress anomalies, implying a time-filtered signal from the overlying atmosphere to the subsurface South Atlantic Ocean is apparent. Previous work (e.g. *Reason et al.*, 1987) suggests that there is a robust annual period Rossby wave signal in this basin, particularly in the South East Atlantic. Rossby waves may also play a role in influencing the subsurface temperatures and, to investigate this, Hovmöller plots (both meridional and zonal with time - not shown) were constructed of anomalies in thermocline depth, subsurface temperature, and sea surface height for the 1949-1999 period. Although Rossby wave signals are apparent during this period, no obvious modulation of these features by ENSO was evident. This lack of a coherent signal may occur because the changes in the SLP and winds during ENSO (Figure 26), are rather complex in pattern suggesting that a coherent and obvious Rossby wave modulation will not be easy to detect.

5.4 Summary and discussion

This section investigates the South Atlantic response to ENSO induced climate variability by means of an OGCM (ORCA2). Seasonal composites of upper ocean temperature, SLP, windstress, meridional Ekman heat transport and net surface heat flux anomalies suggest that during ENSO, upper ocean temperatures in the South Atlantic are significantly influenced by the ENSO-induced windstress anoma-

lies. Figure 32 shows a schematic picture of the processes that lead to temperature changes during El Niño events in the South Atlantic.

During the El Niño onset, the global SLP teleconnection pattern implies a negative SLP anomaly in the South Atlantic. Its main effects are the weakening of the southeasterly trades (mainly during AMJ and JAS of the onset year) and a strengthening of the midlatitude westerlies, thereby reducing (enhancing) the southward tropical (northward midlatitude) Ekman heat transport. This in turn favours warming over the South Atlantic from the equator to the subtropics and cooling in the midlatitudes. Upper ocean warming (cooling) is also supported by anomalous net heat flux, which is broadly consistent with the observed temperature anomalies. Examination of the NCEP latent heat fluxes suggest that evaporation is the major contributor to the net surface heat flux, consistent with findings of *Sterl and Hazeleger* (2003). During La Niña, the upper ocean temperature changes and the associated mechanisms are roughly the reverse of those evident during El Niño.

The spatial extent and evolution of ENSO induced temperature anomalies in the subtropical South Atlantic resemble the second rotated EOF displayed in Section 4 (Figure 3) and thus confirm the suggested connection between this mode and the SOI. Furthermore, anomalous windstress and heat flux pattern are also in broad agreement with those found for the second leading mode. Changes in the westerlies and associated Ekman heat flux anomalies for the eastern midlatitudes during ENSO agree well with the forcing mechanisms of the third rotated EOF, therefore explaining the significant correlation between Ekman velocities and the SOI (Section 4, Section 4.1.3).

Annual means of Ekman pumping anomalies and thermocline depth anomalies are broadly consistent with the observed near thermocline ocean temperature anomalies with some advection of the response by the mean currents. They imply subsurface temperature changes due to atmospheric forcing since the Ekman pumping anomalies are derived from the windstress anomalies. It is possible that Rossby wave generation via these windstress anomalies could contribute; however, an investigation showed that, although such waves are prominent during the 52 years of

model output, no obvious modulation of their characteristics during ENSO could be found.

The results of this section imply that there is a coherent and significant ENSO impact on the South Atlantic. It is evident that mainly during ENSO onset significant upper ocean temperature anomalies appear in the South East Atlantic. They partly cover the Benguela upwelling system and the tropics (more clearly so for positive phases of ENSO). This implies possible changes in the intensity and position of the ABFZ during ENSO events. However, due to the rather coarse resolution of the ORCA2 model a detailed examination of such influence is not possible. In order to investigate ENSO induced variability in these regions a higher resolution ocean model needs to be employed. The following section provides such a model. It is forced with monthly climatologies at the upper ocean and as such must be seen as a first step towards a better understanding of variability in this region. A 32 year integrated model run and several experiments with idealised windstress forcing provide the basis for (a) a provisional comparison between ENSO induced and internal variability and (b) a rough estimation of a possible ENSO influence in this region.

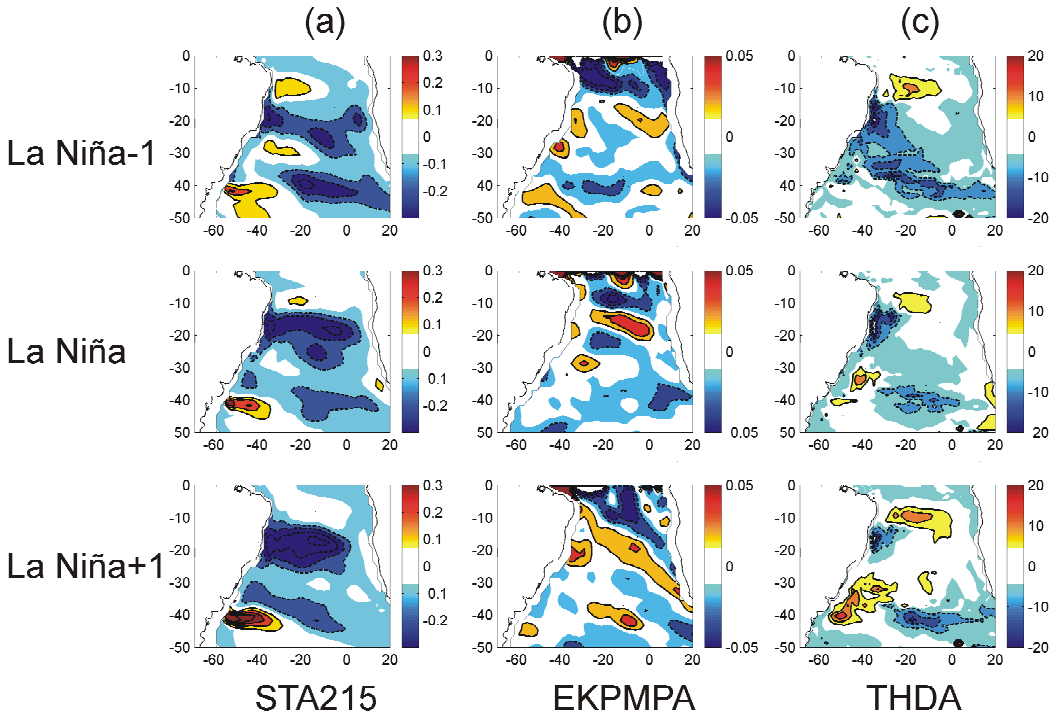

Figure 31: As for Figure 30 but for La Niña composites.

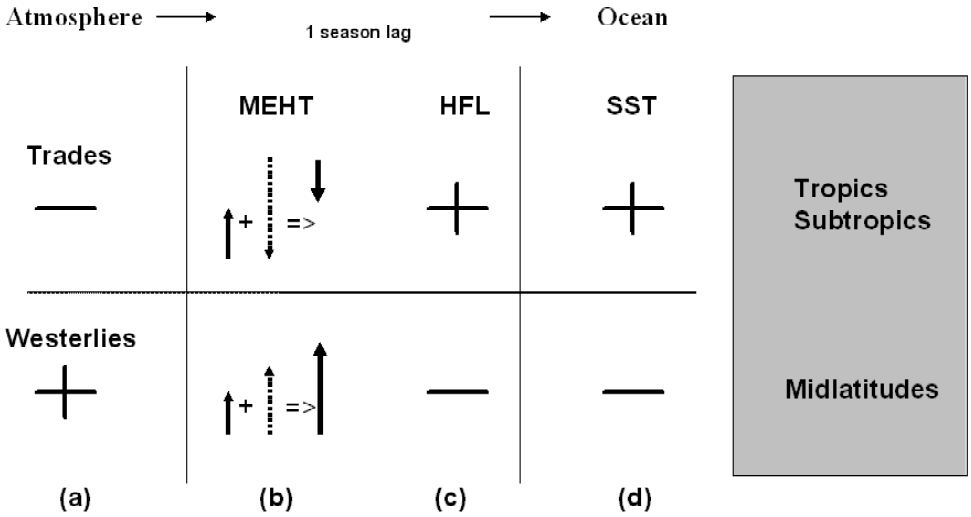

Figure 32: Schematic picture of the South Atlantic response to El Niño. (a) Weaker trades (stronger westerlies) lead to (b) reduced tropical southward (enhanced midlatitude northward) meridional Ekman heat transports (thin arrow denotes the anomaly, dotted arrow denotes the climatology, thick arrow denotes the resulting Ekman heat transport) and (c) positive (negative) net surface heat fluxes. These anomalies favour (d) upper ocean warming (cooling) in the tropics to subtropics (midlatitudes).

6 A Model for the South East Atlantic Ocean

This section explores the variability in the South East Atlantic with a special focus on the Angola Benguela Frontal Zone (ABFZ). The importance of the front as a system boundary has been highlighted in Section 2 and partly in the Introduction. The aim of this section is to (a) investigate possible wind induced mechanisms that may play a role in altering the position and strength of the ABFZ, and (b) discuss the intra-seasonal to interannual variability apparent in the frontal area. The section begins with a general model validation, in which eddy kinetic energy and ocean temperatures are compared with observational data. The model's ability to represent the ABFZ is highlighted and the general mean atmospheric and oceanic state with respect to the ABFZ are discussed.

6.1 The reference experiment

6.1.1 Comparison with observations

As described in Section 3, a regional model (ROMS) has been applied to the South East Atlantic region. The climatological windstress has been calculated from QuikSCAT, heat fluxes have been taken from the NCEP/ NCAR reanalysis, and monthly climatologies of temperature, salinity and velocities have been taken from the output of an OGCM model (ORCA2). Several experiments have been conducted in order to investigate the structure and sensitivity of the front. In this section the reference experiment will be defined as the one with original windstress as derived from the QuikSCAT and the results of this experiment will be validated in this section.

Eddy Kinetic Energy

Figures 33a and 33b show the model annual mean eddy kinetic energy (EKE) and the EKE as derived from the AVISO dataset (*Ducet et al.*, 2000), respectively. The model generally underestimates the EKE by at least 50%, which is to be expected as the model resolution is relatively coarse (1/3°) (see also *Penven et al.*, 2005b). However, the position of the main centres of high EKE, near the tropics

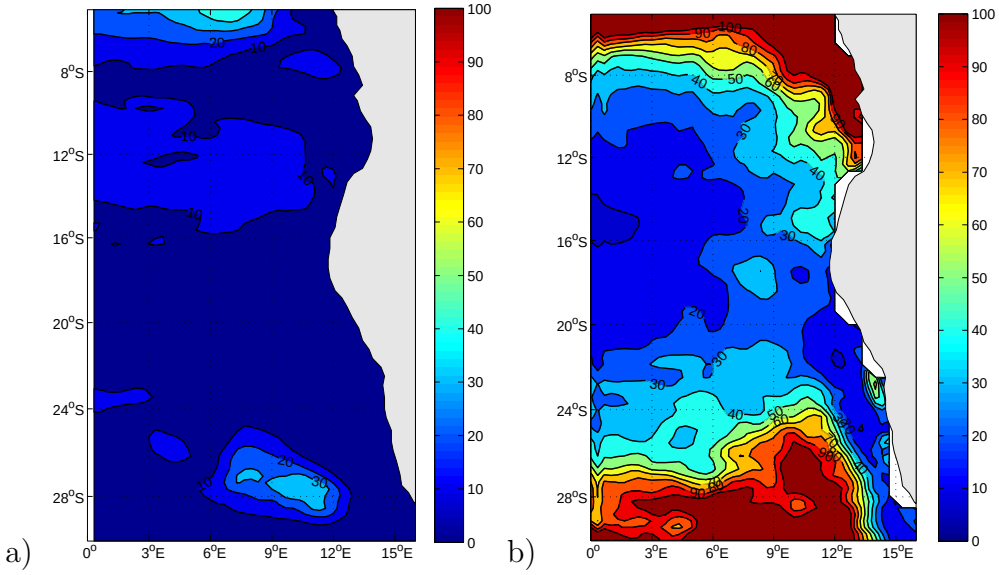

Figure 33: (a) Mean surface eddy kinetic energy for the model output, (b) Mean surface eddy kinetic energy derived from the AVISO sea surface height. The contour interval is $10\,cm^2\,s^{-2}$.

and towards the west of the upwelling system, compare reasonably well with the observations. The area of high AVISO EKE stretching southward from the tropics along the Angolan coast (Figure 33b) is only partially indicated by the modelled EKE. Qualitatively it seems as if the model performs better in the southern half of the domain (southward of 15°S). The model EKE suggests the existence of a patch of high EKE near 12°S and 10°E, stretching towards the west, which is not apparent in the AVISO EKE.

Temperatures

The seasonal climatologies of model and World Ocean Atlas (WOA, *Conkright et al.*, 2002) temperatures at a depth of $10m$ are shown in Figure 34 (a difference plot is shown in Appendix 73). There is overall agreement in terms of spatial distribution and magnitude between the model temperature and the WOA fields. However, the WOA temperatures are somewhat cooler south of 15°S, and the isotherms are orientated differently. It appears that the upwelling related cooling in the Benguela system is more localised and confined nearer to the coast in the model output than

in the WOA climatology. This result is expected as the WOA dataset does not explicitly resolve the upwelling areas and hence tends to produce a more offshore extent of cooler water. North of 15°S the model output compares well with the WOA data during JFM and OND, but during the other two seasons (AMJ, JAS), the model seems to be warmer near the coast. The model temperatures agree better with the NCEP/ NCAR ones (Appendix 72) consistent with the model forced by NCEP heat fluxes.

Larger differences between the model temperatures and the WOA ones are apparent at greater depth. Figure 35 shows the seasonal climatologies for the temperature at $75m$ depth. Similar to the EKE, the model and WOA temperatures compare fairly well in the southern part of the region, while in the northern part larger differences are evident. The most striking difference is the much deeper permanent cold tongue in the model. In the WOA data, the cold tongue becomes clearly visible below a depth of $30m$. Vertical sections at 5°E of the annual mean of WOA and model temperatures (Figure 36) confirm this result and furthermore suggest that stronger vertical stratification exists north of 15°S for the WOA temperatures. Both model and observations show the doming of the thermocline between 5°S-20°S.

In order to investigate whether differences between model and WOA temperatures are sensitive to the forcing, various experiments with different boundary conditions taken from the Simple Ocean Data Assimilation dataset (SODA1.2, *Carton et al.*, 2005) and upper ocean forcing from the NCEP/ NCAR reanalysis and the Comprehensive Ocean-Atmosphere Data Set (COADS, *Da Silva et al.*, 1994) have been conducted.

The experiments revealed that differences in upper ocean forcing have a rather weak impact on ocean temperatures and stratification in the northern half of the domain, hence the deeper lying cold tongue is apparent for all experiments (Appendix 76). However, the doming of the thermocline between 5°S-20°S (Appendix 77) is sensitive to upper ocean forcing, particularly to the the applied windstress. Best agreement between the model and WOA temperatures occur when ROMS is forced with QuickSCAT or COADS winds.

Furthermore, other regional models such as CLIPPER or TOTEM (both of which are configurations of the OPA) show the same warmer upper ocean compared to WOA (see e.g. *Veitch*, 2004). Other model experiments with ROMS that cover the whole tropical Atlantic and hence do not rely on modelled velocities for the boundary condition in the tropics, show the same problem (Queiroz, T. and Florenchie, P., personal communication). The model phenomenon of a too deep cold tongue may be related to the dynamics of the equatorial current system and the associated heat transport into the South East Atlantic. Experiments that do not involve the equatorial dynamics, i.e. have a northern boundary south of the equator, compare somewhat better with the WOA data. A north-south velocity section (Appendix 74) suggests that the modelled South Equatorial Under Current may be too shallow compared with observations (e.g. *Molinari et al.*, 1981, and others). Furthermore, the maximum flow of the modelled South Equatorial Under Current occurs during austral summer compared to austral spring in the observations. Both of these results support the idea that the model may have difficulties in representing the equatorial current system accurately and thereby altering the heat transport into the South East Atlantic. A similar problem in representing of the equatorial current system has been observed in the CLIPPER model (*Veitch*, 2004).

However, a general problem in the South East Atlantic is the rather sparse data coverage. Few cruises have been conducted in these regions, which clearly affects the quality of the WOA dataset here. The total number of observations that have been considered for the WOA is less than 50 for larger parts of the South Atlantic Ocean and the area of the permanent cold tongue (Appendix 78). Furthermore, reliable radiation and turbulent heat fluxes are difficult to derive in this area, as strong and persistent cloud cover make satellite observations inaccurate. As a result, uncertainties in the NCEP flux data are inevitable and may contribute to model deficiencies. Given these uncertainties and the similarity of the ROMS temperatures to other models, it appears reasonable to proceed with the analysis using the model configuration given above.

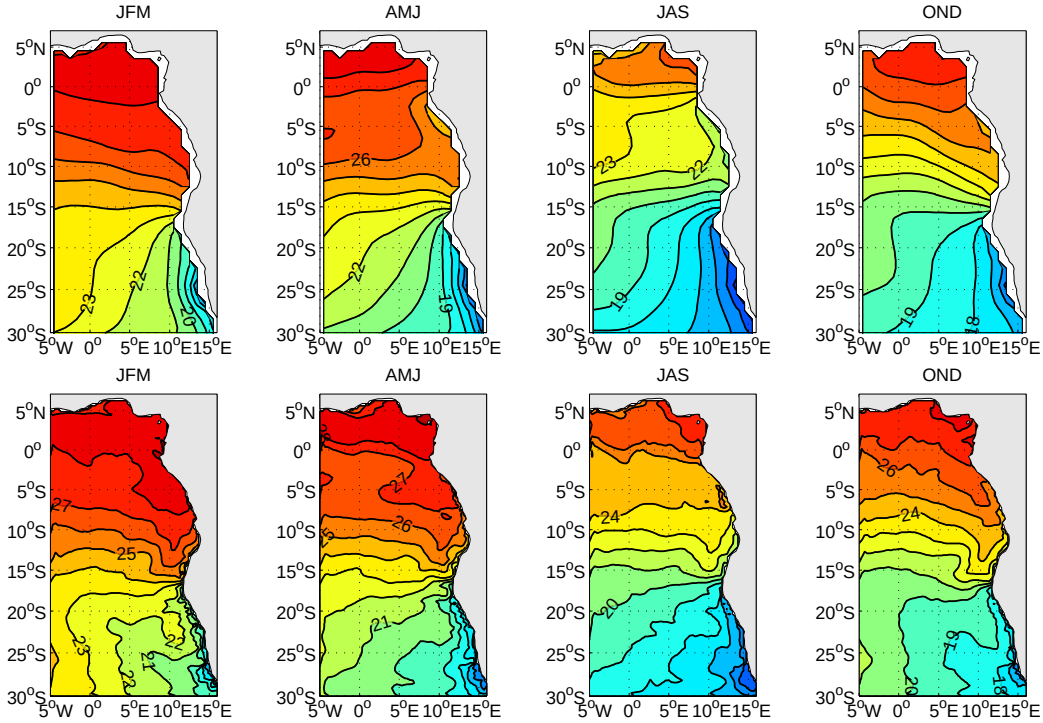

Figure 34: Seasonal climatology of ocean temperature at $z = -10m$. Upper: For the WOA dataset. Lower: For the ROMS model. The contour interval is $1°C$.

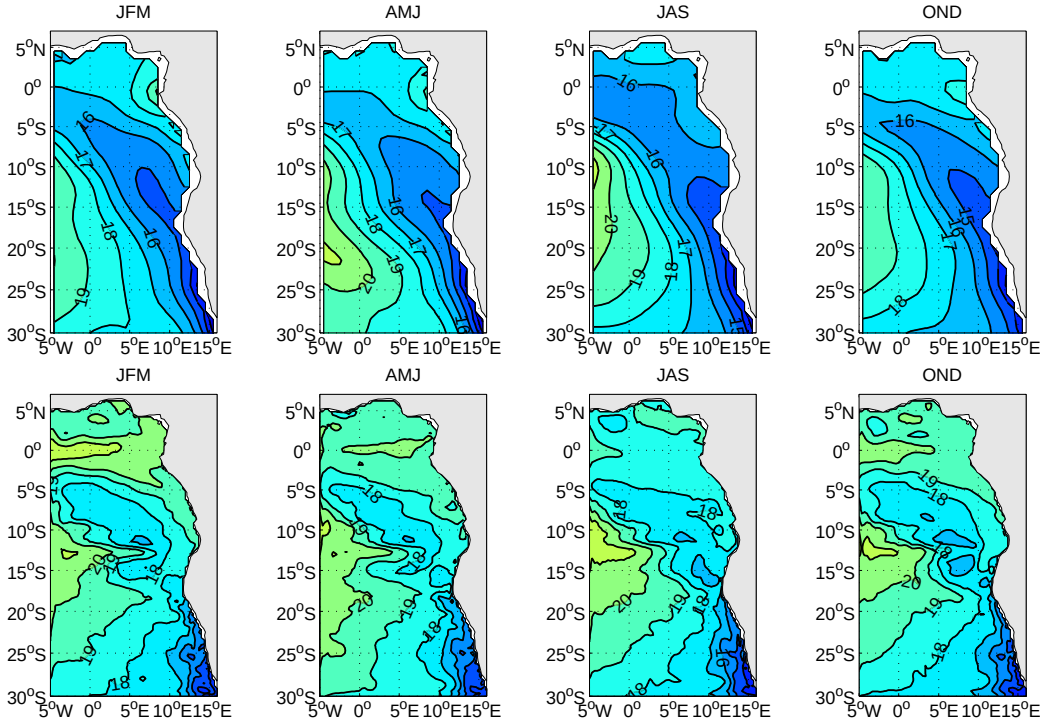

Figure 35: As Figure 34 but for $z = -75m$.

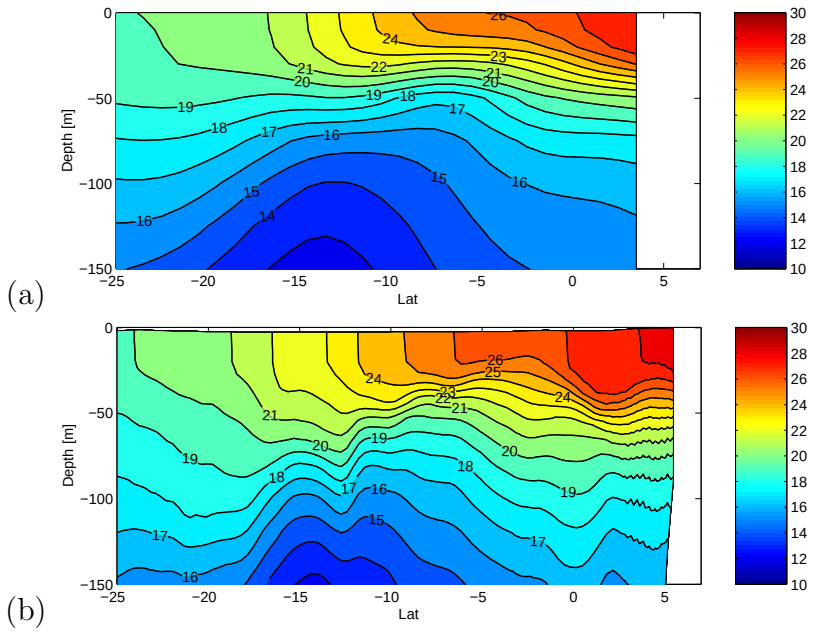

Figure 36: Annual mean temperature section at 5°E, (a) for the WOA dataset and (b) for the ROMS model. The contour interval is $1°C$.

6.1.2 The ABFZ and the atmospheric and oceanic mean state

Meridional Temperature Gradient and Upper Ocean Temperature

Since the aim of this section is to investigate variability within the ABFZ, it is important to note how well (or not) the front is modelled. In the following it will be assumed that the front can be identified from the meridional gradient of upper ocean temperature.

Figure 37a shows the annual mean meridional temperature gradient in the frontal area at a depth of $20m$. Multiple fronts are evident between 12°S and 19°S. The strongest front (the middle front) is situated between 16°S and 17°S, and is in good agreement with observations of the typical position of the ABFZ from ship measurements and satellite imagery (e.g *Shannon and Nelson*, 1996; *Kostianoy et al.*, 1999; *Lass et al.*, 2000; *Veitch et al.*, 2005). The front is clearly defined up to 10°E, but can be traced farther westwards to at least 6°E. The frontal orientation appears to be in an east-west direction, consistent with satellite maps of SST for the period 1982 to 1985 (*Meeuwis and Lutjeharms*, 1990).

From the vertical north-south section at 11°E shown in Figure 37b it is evident that the middle front is well defined within the upper $50m$, similar to the findings of *Shannon et al.* (1987), who examined vertical temperature and salinity profiles off southern Angola during 1968. However, the southernmost front, located between 18°S and 19°S, appears to extend to depths below $150m$.

The meridional movement and intensity of the middle front during the annual cycle is more clearly shown in the Hovmöller diagram (Figure 37c) derived at a depth of $20m$. In agreement with observations (*Shannon et al.*, 1987; *Meeuwis and Lutjeharms*, 1990) the front is weakest and positioned farthest north in July. The southernmost position appears to be in early spring (October) and in January, which only partly agrees with observations, as most authors suggest that the front is furthest south during summer (*Shannon and Nelson*, 1996; *Meeuwis and Lutjeharms*, 1990). The difference between the southernmost position of the front in October and January is small. The front is strongest in late summer/ early autumn (March

to April), which marks the beginning of the upwelling season off Namibia and is in good agreement with observations (e.g. *Meeuwis and Lutjeharms*, 1990; *Shannon and Nelson*, 1996; *Kostianoy et al.*, 1999). Furthermore, Figure 37c suggests the occurrence of northward and southward lying fronts positioned at approximately 14°S and 18°S, respectively. Both of these fronts are most distinct during late summer/ early autumn, and hence coincide with strongest gradients of the middle front. Maximum values of the middle front suggest a temperature difference of more than $4°C$ per 1° of latitude and hence agree well with ship measurements and satellite data (*Shannon et al.*, 1987; *Meeuwis and Lutjeharms*, 1990).

A Hovmöller plot for the upper ocean temperature is shown in Figure 38. The annual cycle, characterised by warmer upper ocean temperatures in summer and colder ones in winter is clearly evident. It is interesting to note that the northernmost position of the ABFZ in July does not agree with the coldest temperatures apparent in August. The 19°C isotherm may be indicative of the frontal position in winter, while the 22°C isotherm seems to approximate the frontal position in summer. Hence, during the annual cycle the mean temperature for the mid-frontal position in the model changes from 21-22°C in summer to 18-19°C in winter, spanning a temperature range of about 3°, which compares well with satellite data examined by *Veitch et al.* (2005).

Windstress, Curl and Volume Transport

The annual mean windstress derived from QuikSCAT for the ABFZ area is shown in Figure 39a. It reveals similar characteristics as described for example by *Shannon and Nelson* (1996); *Lass et al.* (2000). It is controlled mainly by the South Atlantic Anticyclone and hence is southeasterly for most of the domain, with the strongest windstress near the ABFZ. Towards the north, the wind weakens and turns towards a more southerly/ southwesterly direction suggesting cyclonic windstress *curl* may be present (discussed below). Figure 39b depicts the Hovmöller plot for the meridional component of the windstress averaged between 11°E to 14°E. Maximum windstress occurs between 17°S and 18°S, with a semi-annual signal evident, leading to strongest northward directed windstress between April and June and a somewhat

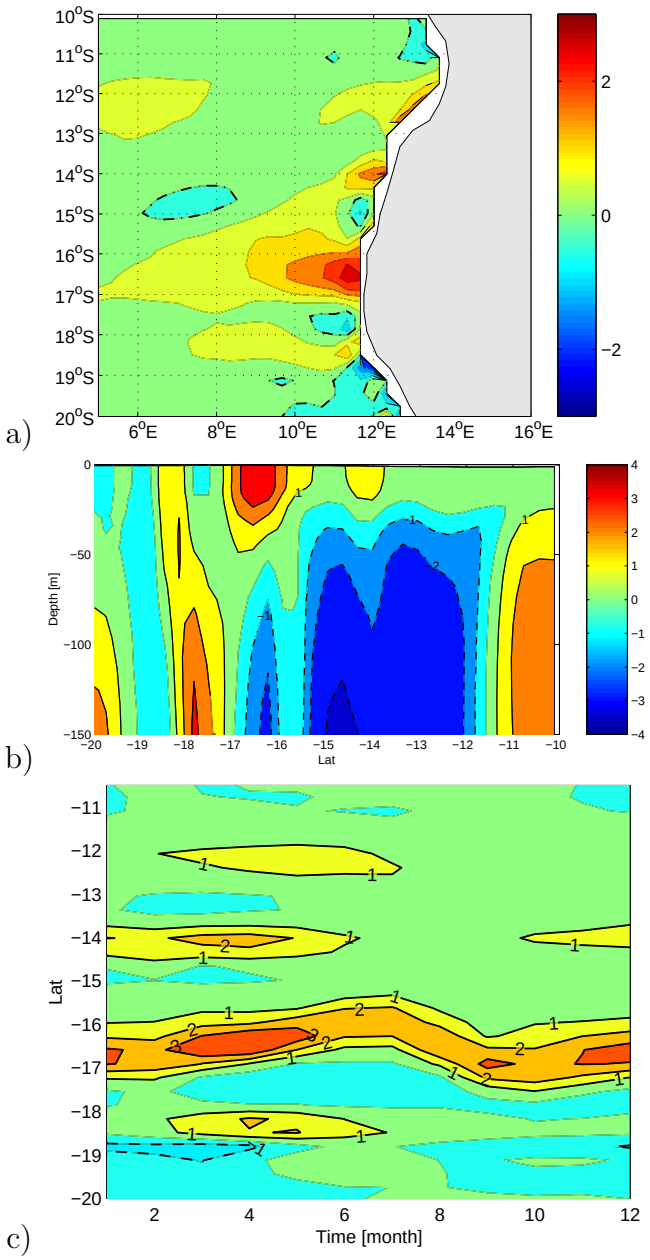

Figure 37: Annual mean of the model meridional temperature gradient (dT/dy) at $20m$. (a) Horizontal plot, (b) vertical section at 11°E, and (c) Hovmöller plot at $20m$ depth, averaged between 11°E-14°E. Positive (negative) contour lines are solid (dashed) for (b) and (c), omitted for (a). The zero contour line is dashed - dotted for (a), omitted for (b) and (c). The contour interval is $1°C/100km$.

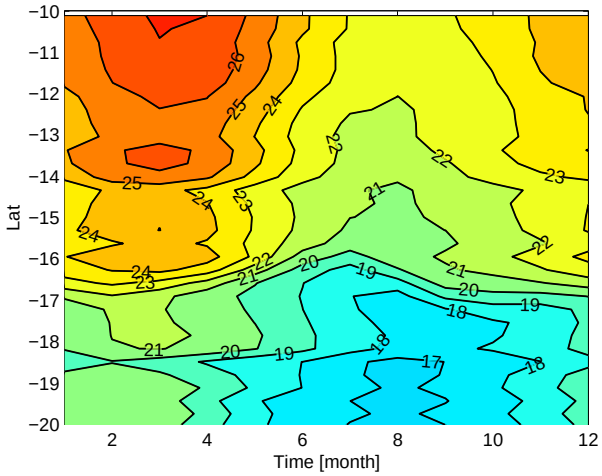

Figure 38: Hovmöller plot for the annual cycle of the ocean temperature at $20m$ depth, averaged between 11°E-14°E. The contour interval is $1°C$.

weaker maximum between July and November. This result is in good agreement with the alongshore windstress $40miles$ offshore derived by *Boyd* (1987), who uses data from longterm records of ship's weather reports that have been kept on file at the Fleet Numerical Centre at Monterey, California. Maximum windstress in April and June agrees well with the northernmost position of the South Atlantic Anticyclone (see e.g. *Tyson*, 1986). The second maximum corresponds with the timing of the westernmost position of the South Atlantic Anticyclone. Furthermore, the maximum windstress in April and June agrees well with the strongest temperature gradients apparent within the ABFZ (Figure 37), suggesting possible connection between the front and the local wind forcing.

The annual mean windstress *curl* for the ABFZ region is shown in Figure 40a and it compares well with observations (e.g *Shannon and Nelson*, 1996; *Lass et al.*, 2000). Strongest negative *curl* is apparent at 17°S close to the coast. It stretches northwestward and is clearly visible up to at least 14°S. Negative *curl* favours Ekman pumping, which may reduce the sea surface height (SSH) in that area. The associated model SSH (Figure 39c) appears to possess a strong gradient in the region of strongest negative windstress *curl*, suggesting a possible connection between

the applied windstress and the sea surface elevation and hence the position of the ABFZ. The Hovmöller plot for the *curl* of the windstress is shown in Figure 40b. Similar to the windstress (Figure 39b), the *curl* shows a prominent semi-annual signal and is strongest between April and May and July and September. However, compared to the windstress, the strength of these two maxima are swapped, the *curl* of the windstress is weaker during the first half of the year and stronger thereafter. Furthermore, the band of maximum *curl* is located farther north compared to the windstress, since it is positioned between 16°S and 17°S.

The Sverdrup balance due to the windstress *curl* has been derived using Equation 17. Figure 41a shows the meridional volume transport due to the windstress *curl*. A net southward transport is apparent in the areas corresponding to cyclonic windstress *curl*. Southward transport stretches in a roughly 4° wide band all the way along the coast from 30°S towards the ABFZ. This result implies that the poleward undercurrent beneath the Benguela Coastal Current (*Shannon and Nelson*, 1996) exists not only due to the dynamics of the upwelling system (e.g. *McCreary et al.*, 1987; *Clarke*, 1989) but is also partly due to a Sverdrup response to the large scale atmospheric circulation. Strongest transport occurs near the well-known upwelling cell at 27°S (near Lüderitz) but also close to the ABFZ, implying strongest southward transport due to the windstress *curl* between 16°S and 17°S. Equatorward Sverdrup transport is generally weaker and mostly exists in the southeast, west of the coastal upwelling zone, where it contributes towards the northward flow of the Benguela Ocean Current.

The volume transport for the upper $500m$ is shown in Figure 41b. Within two degrees off the coast and north of 15°S the transport is generally southward, agreeing with the Sverdrup transport (Figure 41a) in both magnitude and spatial extent. However, strongest southward transport near the ABFZ is centred somewhat further north. Further offshore and south of 15°S, the transport is not as clearly defined and meridional transport alternates between northward and southward. A tendency towards positive, i.e. northward transports is visible, which is in agreement with the Sverdrup relation.

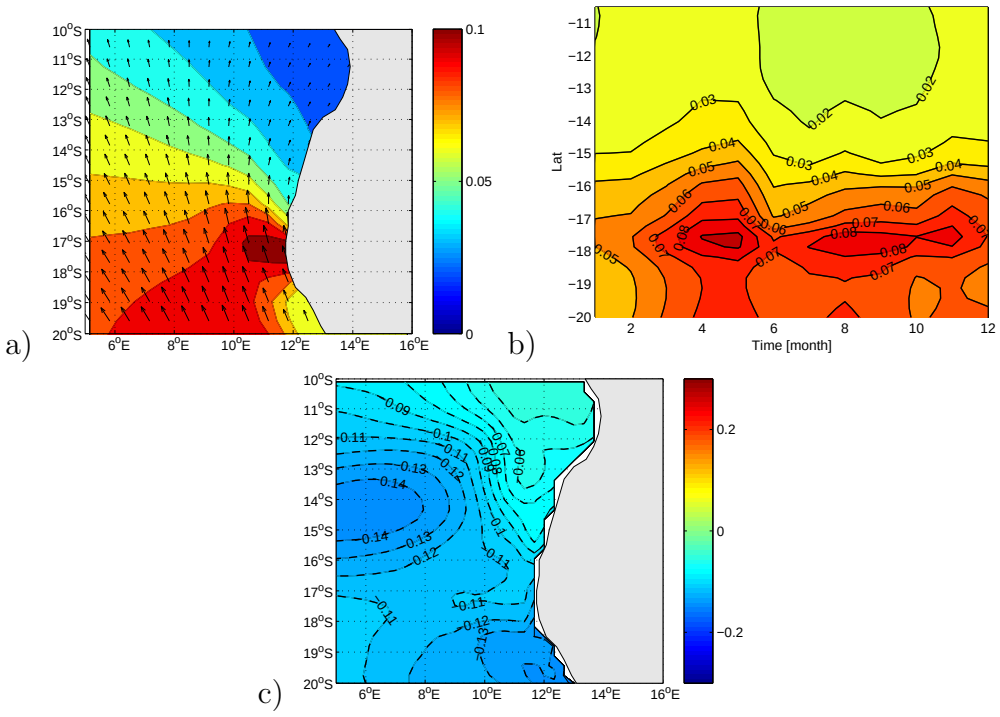

Figure 39: (a) Annual mean of the windstress, (b) Hovmöller plot for the annual cycle of the windstress close to coast, and (c) Annual mean of the sea surface height. The contour interval is $0.01 Nm^{-2}$ for (a) and (b) and $0.01m$ for (c) .

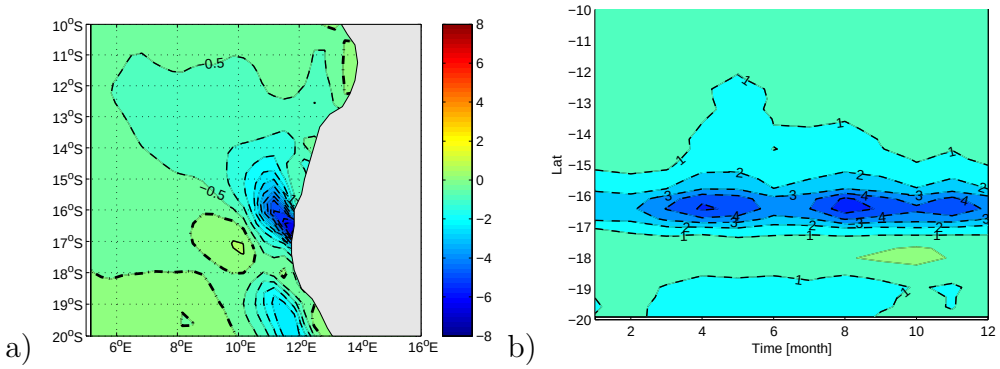

Figure 40: (a) Annual mean of the windstress *curl*, (b) Hovmöller plot for the annual cycle of the windstress *curl* close to coast. Positive (negative) contour lines are solid (dashed). The zero contour line is dashed - dotted. The contour interval is for (a) $0.5 \times 10^{-7} Nm^{-3}$ and (b) $10^{-7} Nm^{-3}$.

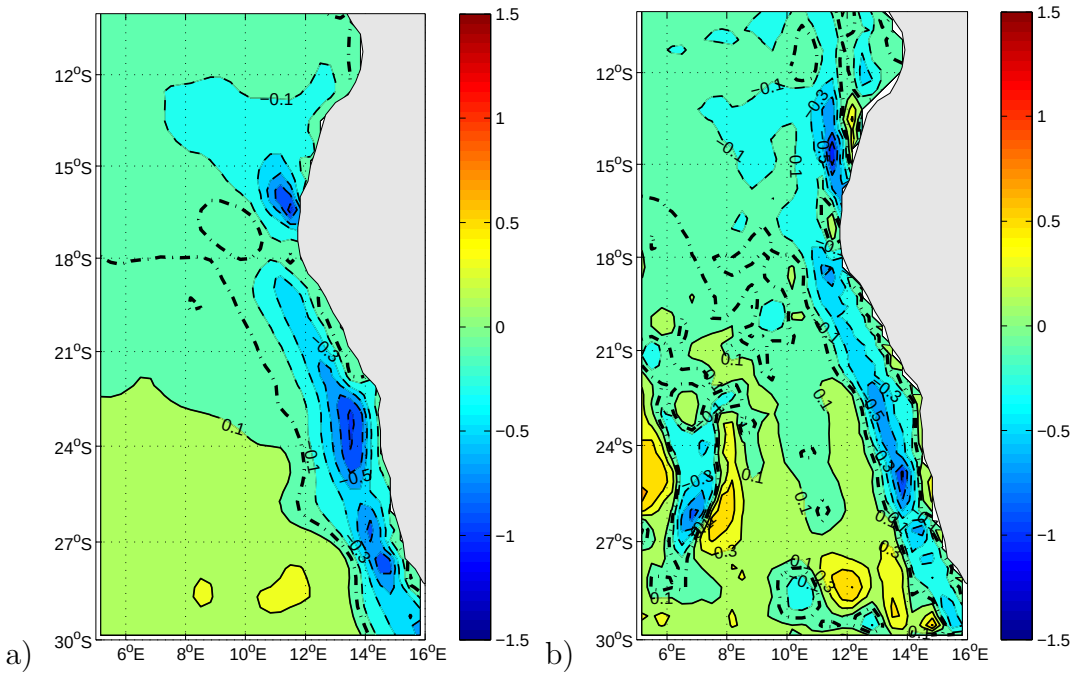

Figure 41: (a) Annual mean of the meridional Sverdrup transport, (b) integrated volume transport over the upper $500m$ as derived from the model output. Positive (negative) contour lines are solid (dashed). The zero contour line is dashed - dotted. The contour interval is $0.2Sv$. ($1Sv = 10^6 m^3/s$).

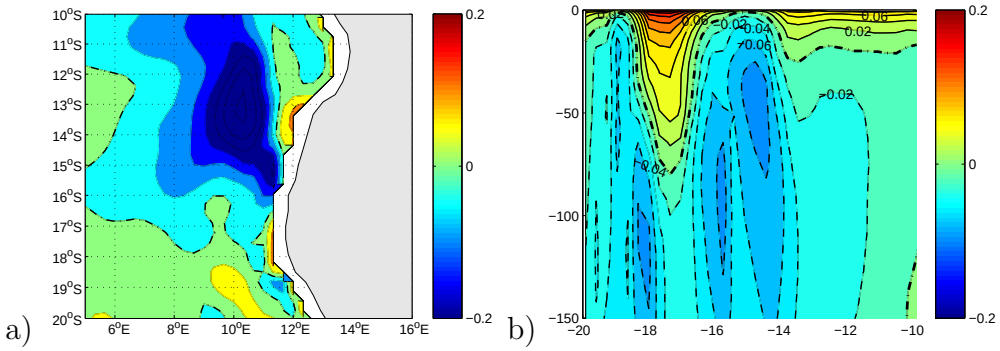

Figure 42: (a) Annual mean of the meridional geostrophic velocity, (b) vertical section of the meridional velocity, averaged between 11°E-14°E. Positive (negative) contour lines are solid (dashed). The zero contour line is dashed - dotted. The contour interval is $0.04ms^{-1}$ for (a) and $0.02ms^{-1}$ for (b)

Velocities

The annual mean meridional geostrophic velocity associated with the sea surface elevation is shown in Figure 42a. Close to the coast, a northward directed jet-like current is visible, encountering a somewhat stronger southward current between 16°S and 17°S (the approximate position of the ABFZ). The northward directed jet is likely caused by upwelling close to the coast (see e.g. *Philander and Yoon*, 1982; *McCreary et al.*, 1987), which reduces the sea surface elevation there, leading to an onshore pressure gradient, which in turn drives a geostrophic balanced coastal jet. This picture is in agreement with the observations of e.g. *Shannon et al.* (1987). The upwelling mechanism does not necessarily depend on the *curl* of the windstress but rather on the alongshore winds apparent between 17°S and 18°S (Figure 39). These winds drive an offshore Ekman flow (Appendix 79), which leads to divergence near the coast and requires upwelling due to mass conservation. A vertical temperature section (Appendix 79) between 16°S and 17°S indeed shows signs of upwelling in that area supporting this idea.

Farther offshore, southward flow dominates between 10°E and 11°E (Figure 42a), giving rise to the Angola tongue (e.g *Shannon et al.*, 1987). Westwards of 11°E, north and southward directed flows again oppose each other. These opposing flows are in

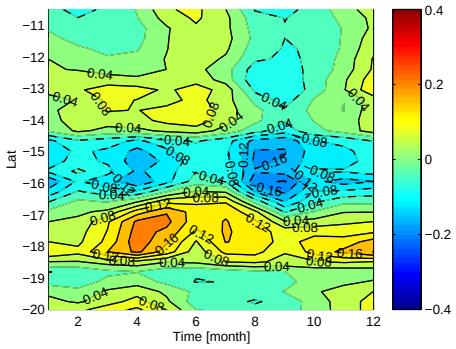

Figure 43: Hovmöller plot for the annual cycle of the meridional geostrophic velocity, averaged between 11°E-14°E. Positive (negative) contour lines are solid (dashed). The zero contour line is omitted. The contour interval is $0.04ms^{-1}$

agreement with the Sverdrup balance (Figure 41a). Therefore, within the frontal area, northward flow may be associated with (a) local upwelling close to the coast and (b) a large scale response further off shore due to the positive windstress *curl*. Similarly, the southward flow may be related to cyclonic windstress *curl*, which is prevalent north of about 15°S. However, closer to the coast, strongest southward flow exists just north of the maximum negative windstress *curl*, which may favour a lowered sea surface height due to upwelling, and hence may act to steer the prevailing currents.

A vertical section of meridional velocity close to the coast (Figure 42b) indicates that the northward flow is prominent up to a depth of $50m$, in agreement with the vertical extent of the middle front (Figure 37b), highlighting the possible connection between the flow and the existence of the front.

The Hovmöller plot of the meridional geostrophic velocity close to the coast is shown in Figure 43 and displays alternating bands of northward and southward flow. Strongest northward flow within the middle front area (15°S-18°S) occurs during April, which coincides with strongest alongshore windstress and strong windstress *curl* (Figure 40b and 39b), suggesting that enhanced upwelling and thus a stronger onshore pressure gradient may be responsible for the maximum northward flow. Maximum southward flow is also evident during April and again between August

and November, similar to that observed for the maximum windstress *curl*, hence suggesting a possible connection. The meridional movement of the opposing flow that characterises the annual cycle is in close agreement with the annual migration of the ABFZ. Furthermore, the northward flows, between 14°S-13°S and 20°S-19°S, are absent in early spring and winter, agreeing with the partial disappearance of the southern and northern front (Figure 37), respectively.

6.1.3 Summary and discussion

An analysis of the annual cycle of windstress and the model temperature, velocity and transport for the reference experiment has been discussed. The ABFZ is evident and it undergoes a seasonal variation in which it varies in strength and position, and such as, is in general agreement with observations (*Shannon et al.*, 1987; *Meeuwis and Lutjeharms*, 1990). Apart from the middle front, the model develops a northern and southern front during late summer and early winter, as has been observed by *Kostianoy et al.* (1999). *Meeuwis and Lutjeharms* (1990) reported the occurrence of double fronts as a prominent feature mainly in summer. The middle front position of about 16.5°S is in good agreement with e.g. *Veitch et al.* (2005), although it should be noted that other authors (e.g. *Meeuwis and Lutjeharms*, 1990) suggested mean positions of the front further north at around 16°S. Possible reasons for this difference will be discussed in more detail in the next section.

The analysis suggests that the windstress and the windstress *curl* may potentially influence the position and strength of the ABFZ. The position of maximum windstress and windstress *curl* differ by about 1°, with the maximum windstress being located further towards the south, between 17°S and 18°S. Strongest temperature gradients occur in late summer/ early autumn (April), in conjunction with strongest southerly windstress. However, the northernmost position of the ABFZ occurs in winter (June, July), which is the time of rather weak windstress and windstress *curl*.

The corresponding model geostrophic velocities imply that the position of the front may be determined as the confluence zone of opposing north and southward flow. The flow fields may be controlled by the overlying windstress and its *curl*.

Close to the coast, meridional winds appear to drive coastal upwelling and hence a geostrophic balanced equatorward jet, while further north the windstress *curl* may enhance the southward flow as suggested by the Sverdrup relation (see also *Lass et al.*, 2000). Furthermore, Ekman pumping may alter the sea surface elevation and thus steering the geostrophic flow in a southeasterly direction. Strongest and weakest southward flow in the model agree with the northernmost and southernmost position of the ABFZ, respectively, while the strongest northward flow is in conjunction with the most intense temperature gradients.

The annual intensification of the middle front during autumn (April) is in agreement with strong alongshore windstress and enhanced northward flow, which indicates enhanced upwelling. Thus, cooler temperatures occur to the south of the ABFZ, leading to an increased meridional temperature gradient.

The above analysis suggests that the atmospheric circulation may be important in altering the position and strength of the ABFZ due to coastal upwelling and Ekman pumping. These results suggest that both windstress and windstress *curl* may be equally important in affecting the ABFZ. In the following section, this hypothesis will be explored further.

6.2 Sensitivity of the position and intensity of the ABFZ to changes in windstress

The previous section has shown that the model ABFZ is evident in the reference experiment and that it undergoes an annual cycle in which it varies in strength and position. The mean frontal position lies at $16.5°S$. The following section tests the sensitivity of the strength and position of the ABFZ to changes in windstress forcing. Three sets of experiments with anomalous windstress have been conducted.

6.2.1 Description of the experiments

Set 1 consists of two experiments in which the magnitude of the windstress has been modified such as to simulate a stronger and weaker trade wind system, re-

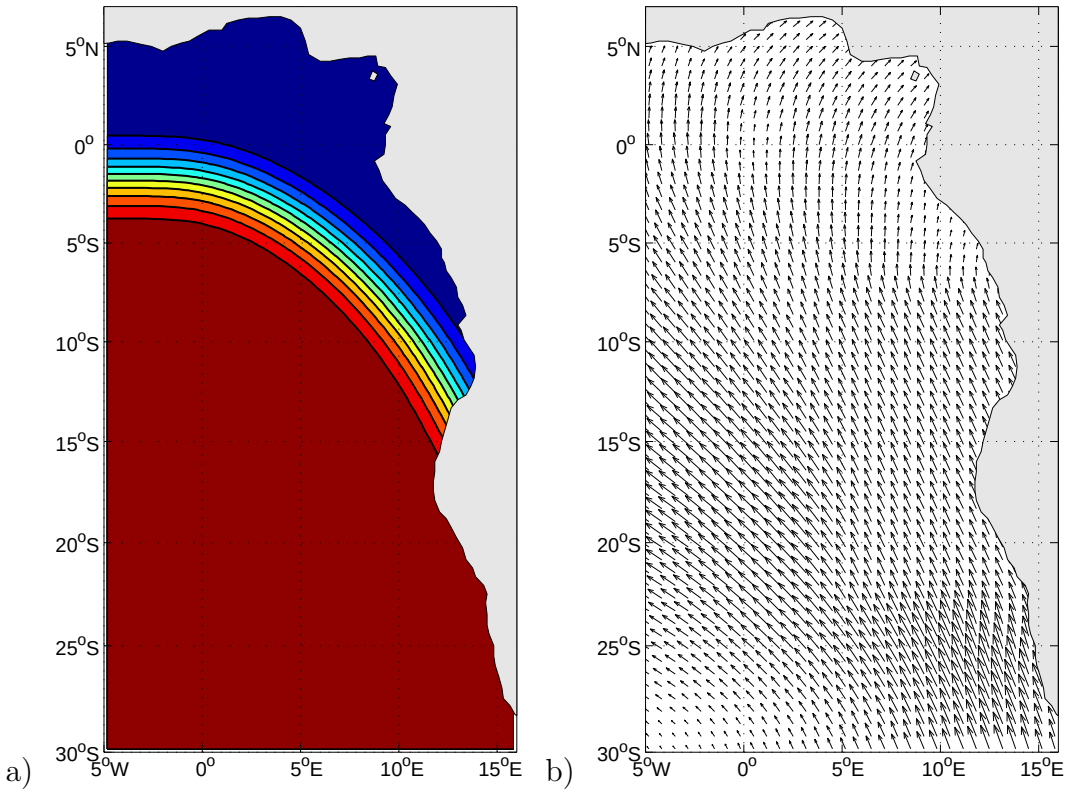

Figure 44: (a) Mask for the windstress anomaly used for the experiments of Set 1. Blue (red) areas indicate original windstress values (original windstress values that are enhanced or reduced by 50%), and (b) modified windstress for Experiment 1 of Set 3.

spectively. To do so, an ellipsoid-like shaped windstress anomaly (shown in Figure 44a) has been superimposed on the monthly climatological windstress. To avoid strong gradients, which may lead to unwanted divergence, the transition zone between the anomaly and the original windstress has been smoothed. The resulting values of the windstress and superimposed anomaly are 50% stronger (weaker) for experiment 1 (2). A stronger and weaker trade wind system has been observed for negative (positive) phases of ENSO (*Reason et al.*, 2000; *Colberg et al.*, 2004) and for the second South Atlantic leading mode. Thus, although the values chosen for the windstress anomaly may be unrealistically large, the results of the experiments could be interpreted as extreme cases of these events.

Set 2 also consists of two experiments, which aim to simulate an anomalous northward or southward position of the South Atlantic Anticyclone (SAA). To do this, the windstress has been shifted meridionally by 1.5° to the north and south of its mean position, respectively.

In the previous section, a possible connection between the windstress *curl* and the position and strength of the ABFZ has been suggested. It appeared that the negative *curl* may alter the sea surface height due to Ekman pumping thereby allowing the SECC to turn southeastwards and thus affect the confluence zone. However, from the reference run alone it is not possible to distinguish cause and effect. Therefore, these additional experiments are necessary in order to investigate the underlying mechanisms. If the proposed wind forcing mechanism is correct than a shift in the mean winds should force a clear response within the ABFZ.

Set 3 consists of only one experiment. In order to assess the relative importance of the windstress *curl*, the winds have been modified in an area from 10°S to 22°S and 5°E to the coast in such a way that the resulting *curl* is close to zero (Figure 44b). The transition zone between the original windstress and the anomaly has been smoothed. It is important to extract the effect of the windstress *curl* and to test if a front can be establish without it. If a front occurs then this would clearly indicate that apart from the above proposed mechanism, other factors such as coastline orientation, alongshore windstress or bottom topography also contribute to the formation of the ABFZ.

6.2.2 Results

Temperature Gradient

Figures 45b to 45f display the resulting Hovmöller plots of the frontal position for the experiments described above and in the following section will be compared to the reference experiment (Figure 45a). The strengthening of the trade winds, as simulated in Experiment 1 of Set 1, results in a firmly established front (Figure 45b), which is positioned at around the same latitude as the front simulated by the reference experiment. However, the gradient is slightly stronger during the first half

of the year, in agreement with *Kim et al.* (2003), who suggested that an enhanced trade wind system may lead to an intensification of the ABFZ, due to the combined effect of an enhanced heat transport into the tropical South Atlantic via the SEC and stronger upwelling. However, in the model, the gradient increases only marginally, because the idealised wind system does not affect the SEC due to the model setup. Figure 45b indicates a reduced meridional movement of the front throughout the year, with a smaller northward shift in June, but a slightly enhanced southward shift of the front in October. The position of the southern front does not change a great deal, but is slightly weaker than that of the reference experiment.

The reduction of the trade winds (the second experiment of Set 1), leads to an almost absent front between 18°S and 15°S (Figure 45c), due to reduced upwelling and is in agreement with *Kim et al.* (2003). The weakish front is most pronounced during late summer through to late spring with associated temperature gradients about three times smaller than in the reference experiment.

The front resulting from Experiment 1 of Set 2 (northward shifted mean winds, Figure 45d) is positioned between 15°S and 16°S. It is thus shifted northwards by slightly more than 1° compared to the reference experiment. Hence, it has responded almost linearly to the meridional shift in windstress of 1.5°. It it not as wide as the front of the reference experiment and is more intense throughout the year. Thus the front is more distinct. The southern front between 18°S and 19°S is evident throughout the year, but it has not changed its position in response to the anomalous windstress forcing. Maximum gradients in the front are apparent in late summer/ early autumn and it shows a meridional migration similar to the middle front. A weak northern front is also apparent throughout the year except for late winter/ early spring. A connection between large scale changes in windstress in the South East Atlantic and the ABFZ has been proposed by *Shannon et al.* (1987), who compared the position of the SAA using synoptic weather charts of the South African Weather Bureau, with daily surveys of the areas 15°S-17°S and 15°S-18°S during a week in July 1973 and January 1974. It was found that a more southerly position of the SAA corresponds to a period when the Angola tongue was

progressing southwards and vice versa for a more northerly position of the SAA.

The southward shifted SAA (the second experiment of Set 2, Figure 45e), results in one visible weaker front that is positioned between 18°S and 20°S. The front responds to a southward shift of the SAA and is strongest during late summer/ early autumn (March-May). It attains its southernmost position during spring.

The frontal system corresponding to the last experiment (no windstress *curl*) resembles that of Experiment 1 of Set 2 (northward shifted SAA). A southern and a middle front are obvious throughout the year, while an intermittent front in the north is apparent during late summer and autumn. However, the middle front is weaker than the one for Experiment 1 of Set 2 and positioned somewhat further north between 14°S and 15°S. The meridional migration is stronger, with northern (southern) most positions in December/ January (February) and June (October). Hence, a semi-annual signal is apparent. The southern front lies between 18°S and 19°S and attains its maximum intensity in summer and lags the seasonal migration of the middle front by one month.

In order to assess the mechanisms potentially associated with the modelled fronts, the geostrophic velocities of windstress *curl* in each cases are discussed next.

Geostrophic Velocities and Windstress curl

Possible relationships between the upper ocean geostrophic currents and the overlying windstress *curl* for the experiments are indicated in Figures 46a to 46f. The flow pattern in the northern part of the region is similar for each experiment, except for the last one (no windstress *curl*). Thus, in the first 4 experiments the eastward flowing South Equatorial Counter Current (SECC) is apparent somewhat north of 15°S, and turns into a southward direction between 8°E and 11°E, similar to the geostrophic currents derived from CDT measurements during 20 April and 13 May 1997 shown by *Lass et al.* (2000). The southward flow splits into an eastern and a western branch just to the north of maximum windstress *curl*. The western branch is steered into a southeastward direction following the maximum windstress *curl* towards the coast (Figures 46a to 46e).

South of the maximum windstress *curl*, eastward flow becomes apparent between

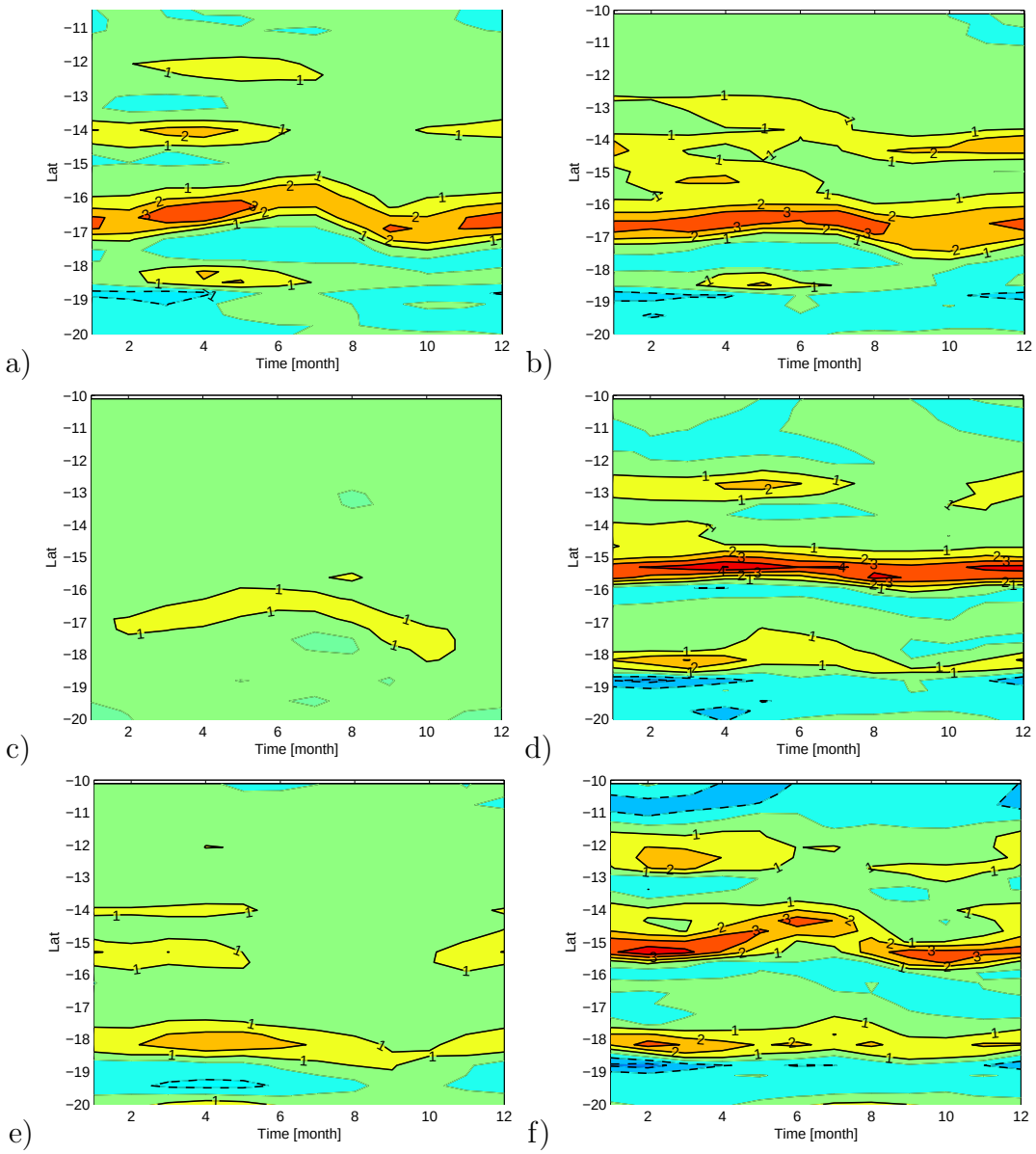

Figure 45: Hovmöller plot for the annual cycle of dT/dy, averaged between 11°E-14°E. For (a) Reference experiment (b) Experiment 1 of Set 1 (enhanced trade winds), (c) Experiment 2 of Set 1 (reduced trade winds), (d) Experiment 1 of Set 2 (northward shifted SAA), (e) Experiment 2 of Set 2 (southward shifted SAA), and (f) Experiment 1 of Set 3 (no windstress *curl*). Positive (negative) contour lines are solid (dashed). The zero contour line is omitted. The contour interval is $1°C/100km$.

10°E and 12°E for all experiments (Figures 46a to 46c and 46e to 46f), except for Experiment 2 of Set 2 (southward shifted SAA, Figure 46d). The eastward flow turns northward for Experiment 1 Set 1 (enhanced trades, Figure 46b), Experiment 1 Set 2 (northward shifted SAA, Figure 46d) and the last experiment (no windstress *curl*, Figure 46f), which is indicative of the presence of the equatorward coastal jet already discussed in the previous section. It thus opposes the southeastward directed flow described above. For Experiment 2 of Set 1 (Figure 46c), the eastward current turns poleward near the coast.

It appears that the enhanced trade winds of Experiment 1 of Set 1 and the northward shift of the SAA of Experiment 1 of Set 2 (figures 46b and 46d) favour the development of a jet-like current structure with strong meridional flow. Reduced trades and a southward shifted SAA on the other hand (Figures 46c and 46e) seem to lead to the development of a much broader flow field, hence the velocities are more evenly distributed and the flow direction appears to be in a more southeastward direction.

The flow pattern for the last experiment (Figure 46f), differs from the other ones in that no southward flow is evident. Near the coast, a strong northward flow dominates, while an eastward flow is apparent farther offshore, implying that the SECC does not turn southward. In fact, it transforms into an equatorward current near 12°E. Since the imposed windstress favours upwelling all along the coast and is also much stronger in magnitude in the northern part of the shown region compared to the other experiments, the existence of the dominant northward directed flow pattern is not surprising. The enhanced northward flow implies that enhanced upwelling near the coast may lead to equatorward flow due to geostrophic adjustment as previously suggested. Due to the absence of any windstress *curl* in this experiment, no southward flow can be established, similarly to that shown for the California Current upwelling system (*McCreary et al.*, 1987). However, the dominating northward flow also leads to apparent convergence near areas where the coastline changes direction, mainly near 15°S and 13°S, suggesting that these convergences may enable the development of a frontal system as observed for this

experiment (Figure 45f).

Geostrophic Volume Transport for the upper 50m

Time and zonally averages of the geostrophic volume transport for the upper $50m$, averaged between 11°E and 14°E, have been derived (Figures 47a and 47b) in order to investigate possible relations with the position of the ABFZ. Figure 47a shows the time and zonally averaged transports for the reference experiment, Experiment 1 of Set 1 (stronger trade winds) and Experiment 1 of Set 2 (northward shifted SAA), while Figure 47b shows the other experiments. It is evident that zero transport in Figure 47a always coincides with the mean position of the frontal zone as indicated in Figures 45a to 45f. Another feature is a local minimum in transport between 18°S and 19°S in all three experiments, indicating the mean position of the southern front. No such clear indication of the northern front is visible.

Figure 47b shows that for Experiment 2 of Set 1 (reduced trade winds) and Experiment 2 of Set 2 (southward shifted SAA) transports are much weaker and are close to zero north of 15°S. However, even for these experiment the zero transport south of 15°S may be indicative of the frontal areas, although the ABFZ is only weakly established. In contrast, the pattern for the last experiment (no windstress *curl*) differs remarkably from the others, suggesting that the dynamics have changed substantially. On the time average, no southward transport is apparent, instead the northward transport is almost doubled compared to the other experiments. The first local minimum north of 16°S appears to coincide with the middle front position, while the southern front is similar to the other experiments (the first minimum south of 16°S).

6.2.3 Summary and discussion

The sensitivity of the position and strength of the ABFZ has been investigated. Three sets of experiments with idealised windstress have been conducted. The first set aims to model a stronger/ weaker trade wind system, while the second set simulates anomalous north and southward positions of the SAA. The third set

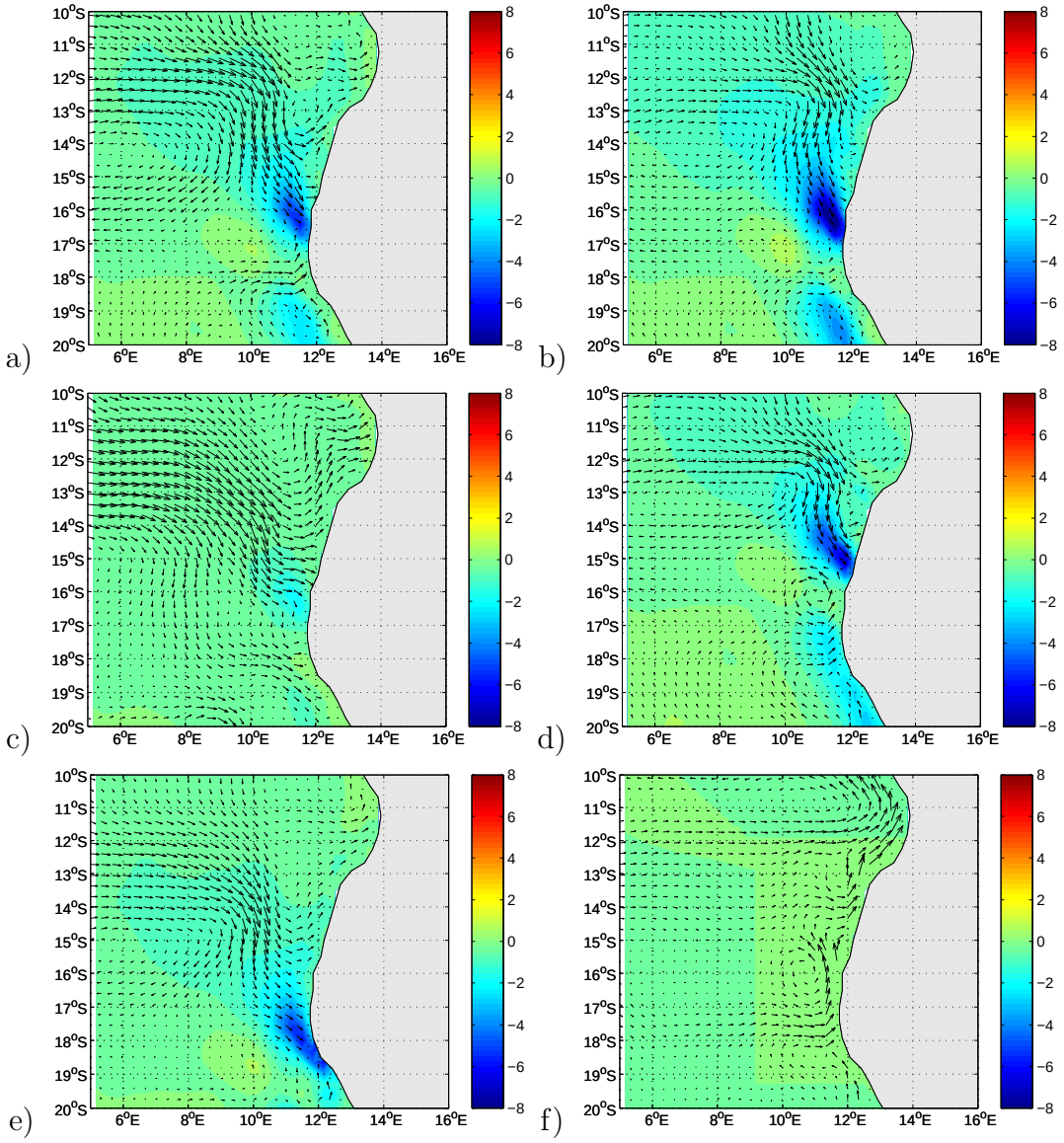

Figure 46: Annual mean of windstress *curl* with geostrophic velocities (arrows) superimposed. For (a) Reference experiment (b) Experiment 1 of Set 1 (enhanced trade winds), (c) Experiment 2 of Set 1 (reduced trade winds), (d) Experiment 1 of Set 2 (northward shifted SAA), (e) Experiment 2 of Set 2 (southward shifted SAA), and (f) Experiment 1 of Set 3 (no windstress *curl*). A colour scale in $10^{-7}Nm^{-3}$ is given to the right of each plot.

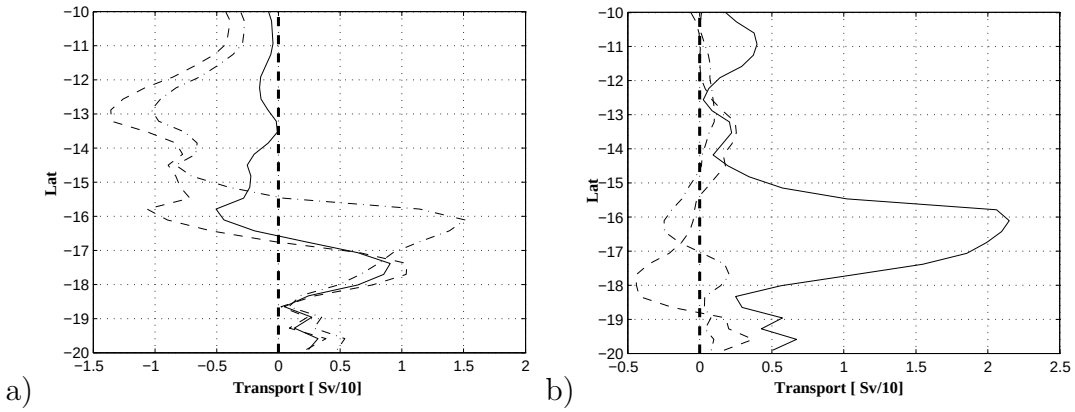

Figure 47: Time and zonally averaged transports for the conducted experiments. (a) Reference experiment (solid line), Experiment 1 of Set 1 (dashed line) and Experiment 1 of Set 2 (dashed - dotted line), and (b) Experiment 2 of Set 1 (dashed - dotted line), Experiment 2 of Set 2 (dashed line) and Experiment 1 of Set 3 (solid line).

(consisting of only one experiment) investigates the regional ocean's response to windstress forcing with zero *curl* near the ABFZ.

In the model, the intensity of the trade wind system has a negligible effect on the position of the front. However, in agreement with *Kim et al.* (2003), an increased frontal intensity is apparent for stronger winds, while reduced trade winds lead to a much weaker and almost absent frontal system. The increase (decrease) of the strength of the front is not linearly related to the anomalous intensity of the trade winds, implying that changes in the tropical current system due to anomalous windstress, which is not modelled here, may be important.

The position of the ABFZ responds to a meridional shift of the South Atlantic Anticyclone as suggested by *Shannon et al.* (1987). A northward (southward) shifted South Atlantic Anticyclone results in a correspondingly northward (southward) shift of the ABFZ. The intensity of the ABFZ also changes according to the anomalously shifted windstress with stronger (weaker) frontal gradients resulting from a northward (southward) shift of the SAA.

The absence of windstress *curl* influences both the position and intensity of the

ABFZ. The resulting middle front position is shifted northwards so that it coincides with an eastward change in the coastline orientation.

The model results suggests that the ABFZ is only well defined when there is equatorward geostrophic flow or geostrophic transport in the upper $50m$. In the case of the experiment without any windstress *curl*, the frontal position is then given by the first local minimum of the flow (or transport) as shown in Figure 47b. This position agrees with an eastward bend of the coastline. A possible explanation may be that changes in upwelling due to the curvature of the coastline lead to convergence/ divergence of the northward flow field (as indicated in Figure 46f), and hence to changes in the associated heat transport, which may then favour a greater range of temperatures within a smaller area. For the other experiments, the frontal position is accurately defined as the confluence zone of opposing northward and southward flow (transport) near the coastline (Figures 47a and 47b). This result is also valid for the seasonal migration of the front, which follows the nodal line between the opposing flows.

The mechanisms responsible for the opposing geostrophic flow between near the coast depend on the windstress and windstress *curl*. Cyclonic windstress *curl* is associated with (a) Ekman pumping, that may alter the sea surface height, and (b) southward flow as suggested by the Sverdrup balance. Northward geostrophic flow on the other hand may be the result of the meridional windstress component, which causes upwelling near the coast, and hence changes the sea surface height. This requires a geostrophically adjusted equatorward flow.

The role of the windstress *curl* cannot be overemphasised. It plays the dominant role in steering the model SECC southward and southeastwards towards the coast, and thereby alters the position of the ABFZ. Therefore, no southward flow is apparent for the experiment with zero windstress *curl* and hence the position of the front may be derived from the relation between windstress and the coastline orientation. This result may help explain why larger changes in the frontal position only occur for experiments with (a) a north/ southward shifted South Atlantic Anticyclone and (b) zero windstress *curl*.

The experiments with a reduced trade wind system and southward shifted South Atlantic Anticyclone, only develop a weak front. This front is related to the absence of or only weakish equatorward flow, which in the case of the reduced trade wind system is clearly related to reduced upwelling. In the case of the southward shifted South Atlantic Anticyclone, upwelling is in fact favoured by the alongshore windstress, but cyclonic windstress *curl* and associated southward flow is stronger due to the southward shift and therefore reduces the northward coastal jet.

6.3 Variability in the ABFZ

The aim of this section is to explore possible variability on intra-annual to interannual time scales within the ABFZ. Figure 48 shows a Hovmöller plot of the meridional temperature gradient for the reference run. The front is defined as in section 6.1.2, and its annual migration in location and variation in strength are clearly visible. Figure 48 also shows variability within the front on different time scales. Anomalous northward (southward) positions are apparent in the years 14, 22 (16, 19). The northernmost (southernmost) positions of the front are 15.5°S (17.5°S). The intensity of the front also varies, but this is not so clearly seen. Strongest (weakest) temperature gradients for the middle front appear for example in year 23 (7) of the integration. Maximum intensities of the front are about $5°C$ per $100km$. In order to investigate the variability in more detail it is useful to define indices that are able to (a) describe the meridional shift of the ABFZ and (b) give an estimation of the intensity of the temperature gradient within the front.

6.3.1 Two indices for the ABFZ

Index 1

For simplicity an index describing the meridional shift of the middle front has been defined as the difference between the temperature gradient at 15.5°S and 17.5°S, encompassing the middle front. A northward (southward) shift of the middle front subsequently enhances (reduces) *Index 1*. The mean annual cycle of this

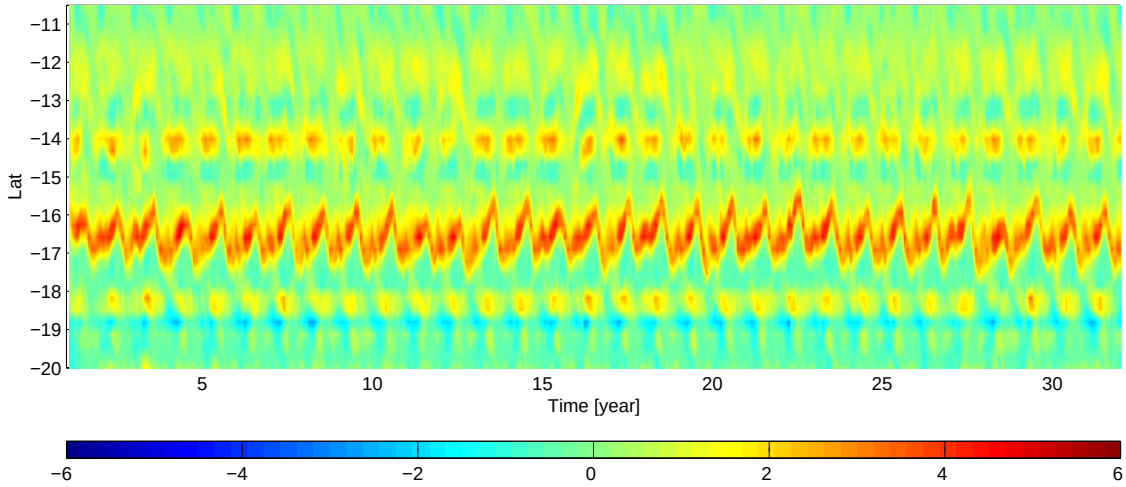

Figure 48: Hovmöller plot of the meridional temperature gradient for the integrated reference run. Isolines are omitted. A colour scale in $°C/100km$ is given below.

index is shown in Figure 49a. Positive (negative) values correspond to a northward (southward) shifted ABFZ relative to its mean position. The index attains its positive (negative) maximum in July (October), in good agreement with the annual cycle of the front (Figure 37c). Other characteristics, such as the slow northward movement during the first half of the year and the rather abrupt southward shift of the ABFZ thereafter are also well captured.

The time series of this index and its wavelet analysis are shown in Figure 50. From visual inspection, it is evident that the maximum and minimum values of the index compare well with extreme northward and southward positions of the middle front (Figure 48). For example, compare the northernmost (southernmost) positions of the front during the years 10, 14 and 27 (12, 19 and 28). Thus the index may be useful to further investigate the nature of the variability of the middle front. The wavelet transform (Figure 50b) indicates that the annual cycle accounts for most of the displayed variability. A weaker, but sometimes intermittent, semi-annual signal is also apparent. Both the annual and semi-annual signals appear to become stronger with time with maximum intensities occurring after 16 years of integration.

The semi-annual and annual signals also fluctuate on shorter time scales on a rather irregular basis. However, it is apparent that the semi-annual signal disappears at those times when the annual signal is weak, e.g. in the years 12, 16 and 25.

In order to capture the irregularities more clearly, deviations from the monthly mean values have been derived for *Index 1*. The resulting time series is shown together with the wavelet spectrum in Figure 51. The wavelet analysis suggests that variability on various time scales is present within the ABFZ. The strongest signal is apparent on the intra-annual (3 to 5 month) time scale and represents high frequency variations in the prominent semi-annual and annual signals seen in the annual cycle of the frontal movement (Figure 37c). Sources of variability on these time scales are coastal Kelvin waves, generated due to upwelling and periodic wind forcing (*Philander and Yoon*, 1982). The connection with the tropical Atlantic also includes the possibility of equatorial Kelvin waves (generated by trade wind modulation) contributing towards the variability of the ABFZ, as e.g. suggested by *Florenchie et al.* (2004).

An interannual signal with a period of between 1 and 2 years is also visible throughout most of the integration. This signal seems to weaken and strengthen about every 8 years. Times of maximum power correspond with times of weakest annual signal (Figure 50b), suggesting this signal may represent modulations of the annual cycle. A weaker signal on the interannual time scale with a period of about 4 years appears after 10 years of integration and intensifies thereafter. *Philander and Yoon* (1982) investigated the ocean's response to seasonal varying winds in a shallow water model with vertical walls and a flat bottom. One primary result is that time-dependent winds parallel to the coast, even if their *curl* is zero, create a source of vorticity in the surface layers of the ocean near the coast. Rossby waves excited in this manner give rise to a complex circulation system and their period is dependent on the period of the wind forcing. Hence, Rossby waves are likely to contribute towards the observed variability in the ABFZ.

Index 2

The second index defined here is a measure of the intensity of the ABFZ. It is

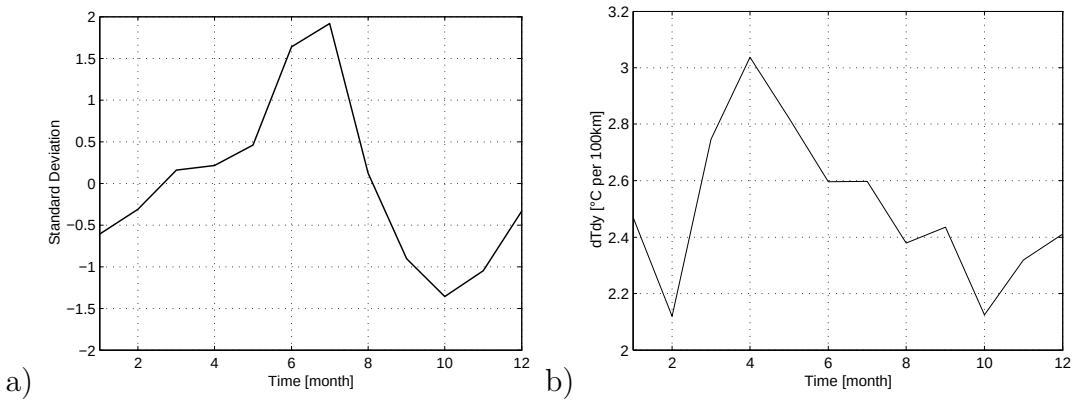

Figure 49: (a) The standardized and detrended annual mean of *Index 1*, and (b) the annual mean of *Index 2*.

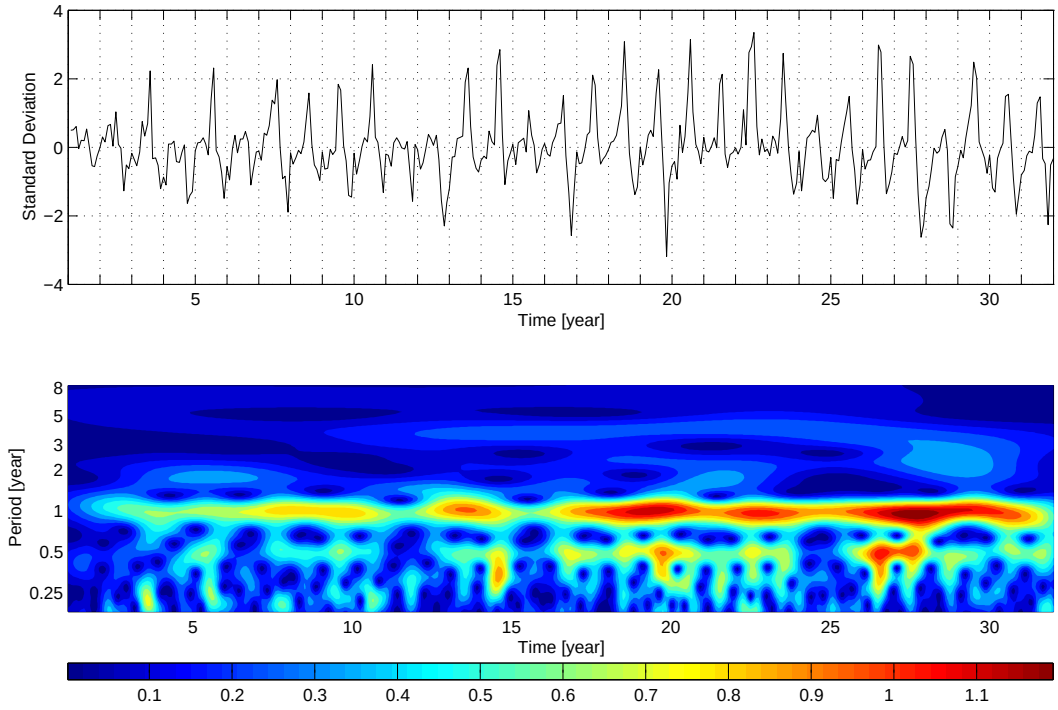

Figure 50: Upper: The standardized and detrended time series of *Index 1* for the reference run. Lower: The corresponding Morlet wavelet transform. Isolines are omitted. A colour scale is given below.

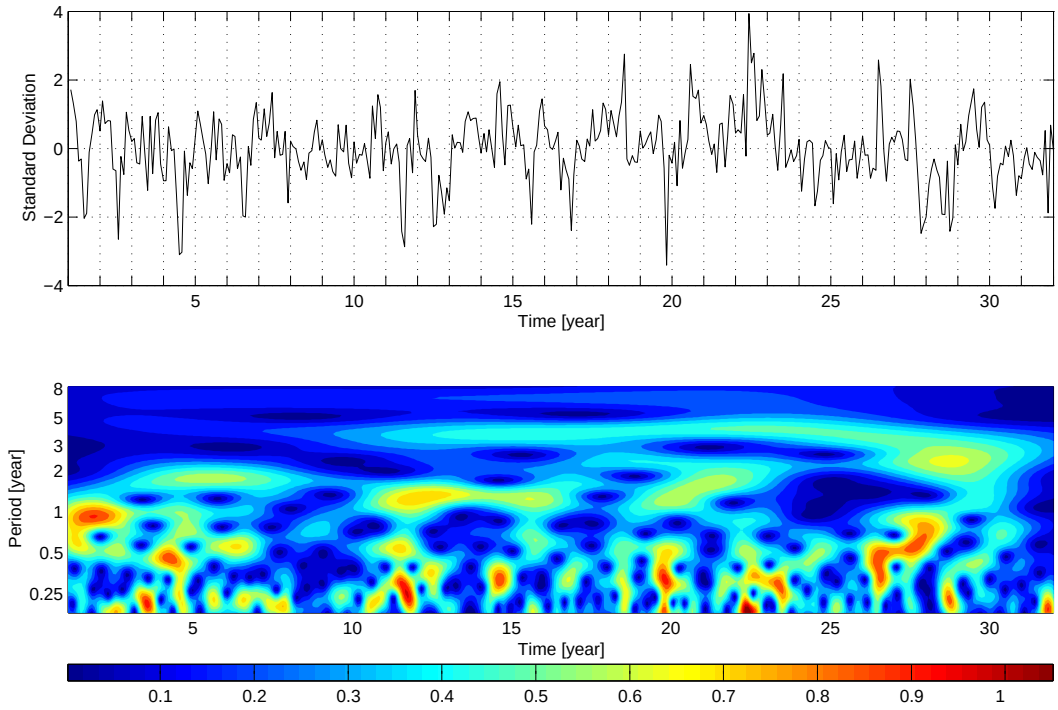

Figure 51: Upper: The standardized and detrended time series of the anomalous *Index 1* for the reference run. Lower: The corresponding Morlet wavelet transform. Isolines are omitted. A colour scale is given below.

calculated by taking the mean temperature gradient over that part of the the front where it exceeds values of $1°C$ per $100km$. Figure 49b depicts the annual mean of this index. *Index 2* attains its maximum value of approximately $3°C$ per $100km$ in April. Other local maxima exist in September and December to January and are in agreement with the annual cycle of the ABFZ (Figure 37c). The front is least well defined in February and October with typical gradients of less than $2.2°C$ per $100km$. Hence, on the annual average, *Index 2* suggests differences of the mean temperature gradient of about $1°C$ per $100km$.

The index for the 32 years of model integration and its wavelet analysis are shown in Figure 52. Maximum (minimum) values occur in years 16 and 23 (13 and 7) and are in agreement with the Hovmöller plot of Figure 48. The wavelet analysis suggests that maximum energy is apparent at 12 months. Similar to the wavelet spectrum of the first index (Figure 50), *Index 2* becomes stronger after the first 15 years of integration. Minimum energy occurs in years 14, 21 and 31, hence decadal fluctuation of the annual signal is evident. The semi-annual signal is less well defined. In fact, most of the power, apart from the annual signal is concentrated on time scales of less than 6 months (3-4 months), reflecting variability of the two local minima apparent in the annual cycle (Figure 49b).

The anomalous index and its wavelet spectrum are shown in Figure 53. Maximum (minimum) anomalies are about $1°C(0.5°C)$ per $100km$. The energy is concentrated on intra-annual to annual time scales, with the major amount of energy for periods less than 6 months. In contrast to *Index 1*, no significant modulation of the annual signal is apparent, since the intra-annual signal is very strong. The high frequency signals strengthen and weaken on a rather irregular basis. However, after 20 years of integration, fluctuations seem to appear more regular with an approximate period of 2 years.

6.3.2 Mechanisms of variability in the ABFZ

To further investigate the nature of anomalous frontal positions and intensities of the middle front, correlation analyses have been performed. The analyses start off

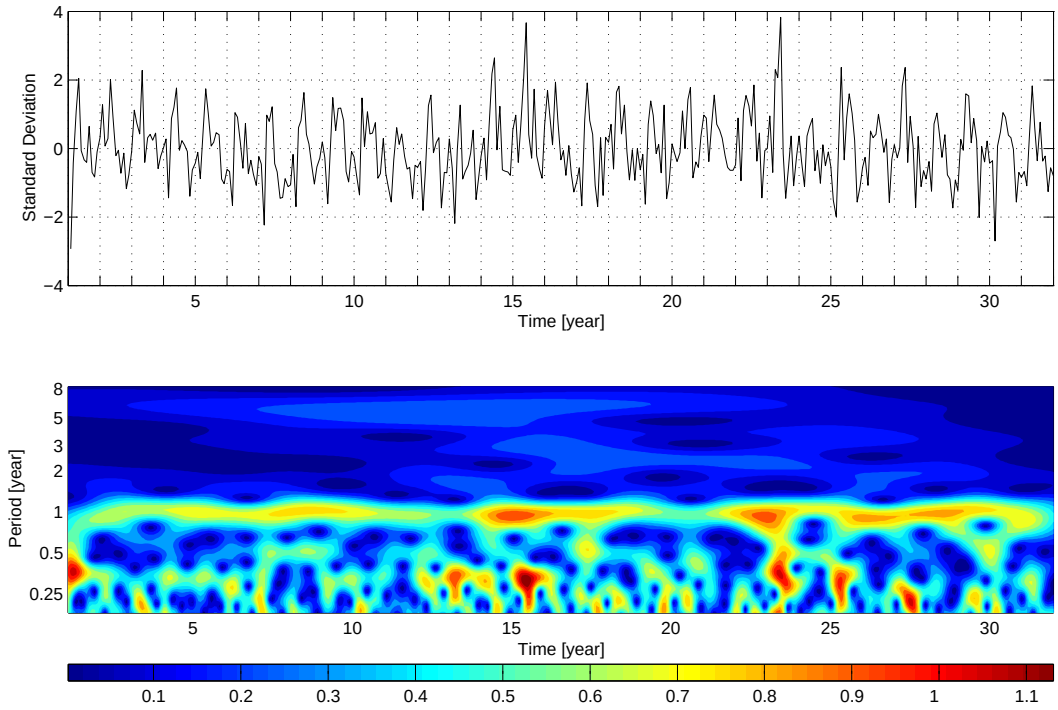

Figure 52: Upper: The standardized and detrended time series of *Index 2* for the reference run. Lower: The corresponding Morlet wavelet transform. Isolines are omitted. A colour scale is given below.

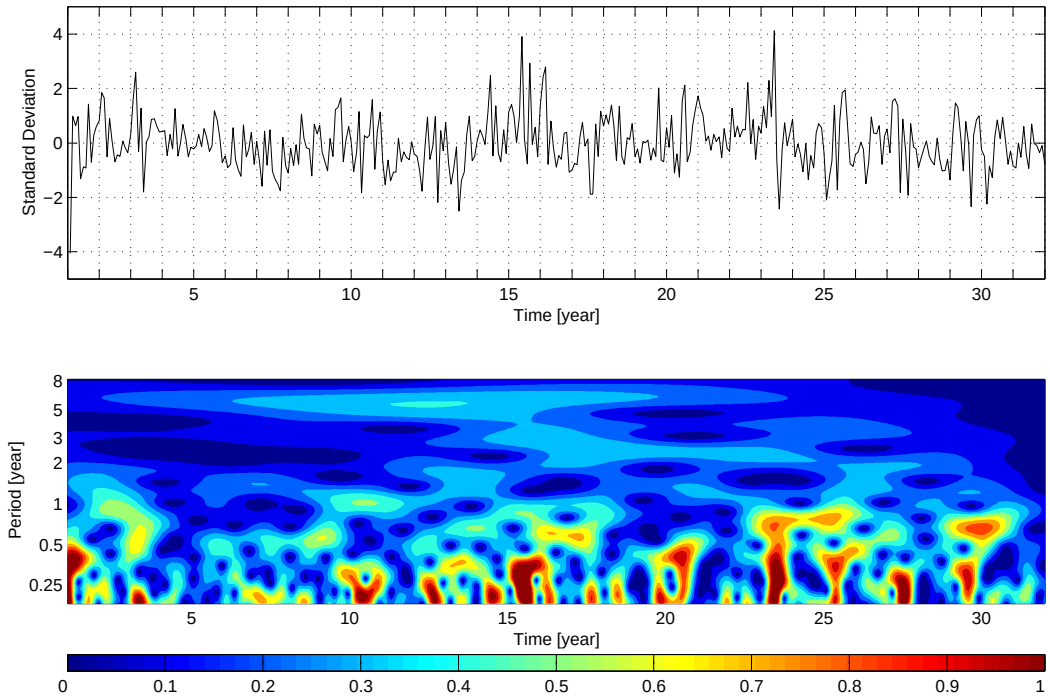

Figure 53: Upper: The standardized and detrended anomalous *Index 2* for the reference run. Lower: The corresponding Morlet wavelet transform. Isolines are omitted. A colour scale is given below.

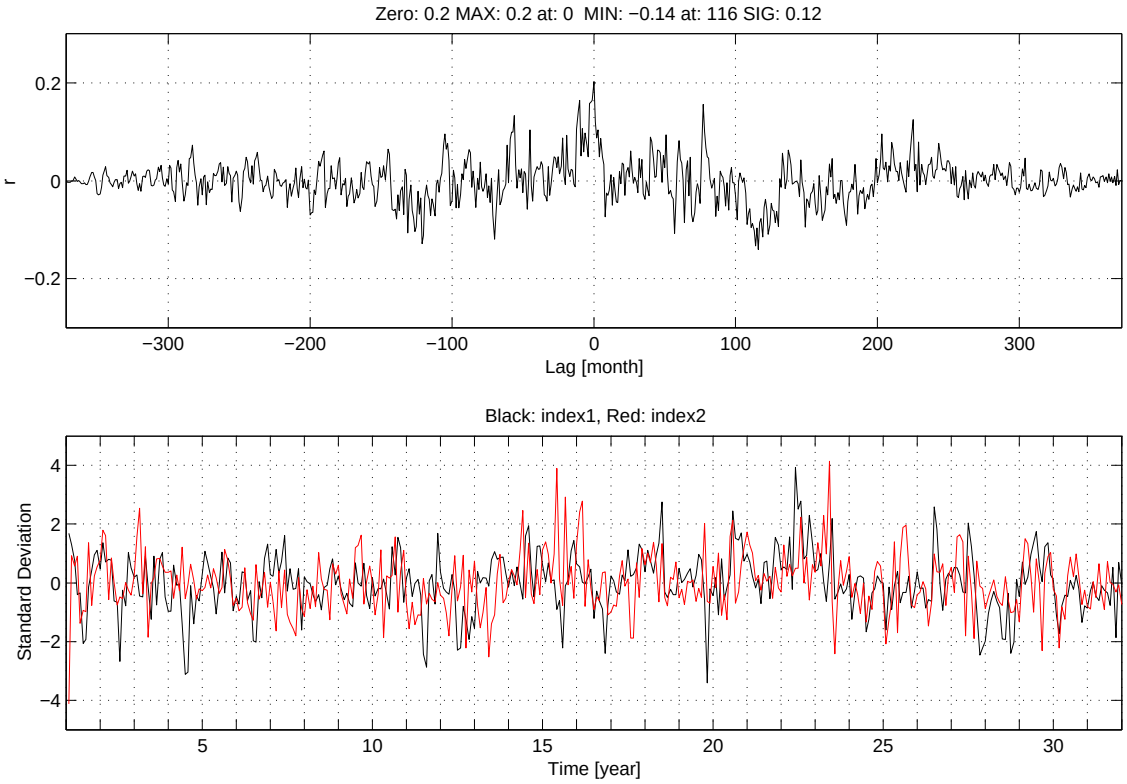

Figure 54: Upper: Correlation analysis between *Index 1* and *Index 2*. Lower: The corresponding time series of the indices.

with an investigation of the relationship between the two indices in order to explore whether northernmost (southernmost) frontal positions are related to anomalous intensities of the front. After that, other variables such as velocities and temperature are considered. The following correlation analyses have been performed with the anomalous indices only, thus *Index 1/ 2* always denotes the anomalous indices (Figures 51 and 53).

The cross correlation between the two indices is shown in Figure 54. Maximum correlation occurs at zero lag, with $r = 0.2$. The correlation is significant at the 95% level but rather small. However, this picture changes drastically when considering correlations for the different seasons. Maximum correlation values are shown in the bar diagram of Figure 55. During spring (OND) and summer (JFM) correlations are strong, with maximum values of $r \approx 0.50$ and $r \approx 0.42$, for *Index 1* leading *Index 2*

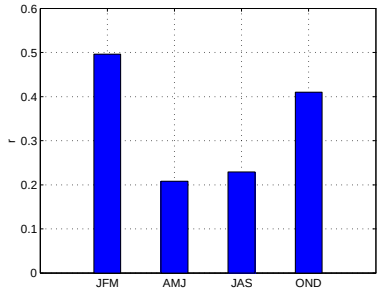

Figure 55: Maximum correlation values for the seasonal correlation between the two indices.

by one month. Weaker correlations occur during autumn (AMJ) and winter (JAS).

Thus, the relation between the two indices is seasonally dependent. Anomalous northward (southward) frontal positions and enhanced (reduced) frontal intensities are phase locked to spring and summer. Since, correlation values are not greater than $r \approx 0.5$ a significant amount of the variability displayed by each index is independent of the other.

Velocity and Temperature

The correlation analysis between *Index 1* and the meridional velocity anomaly at $20m$ is shown in Figure 56a. Highest significant correlations occur in the ABFZ area with a maximum positive correlation of $r = 0.68$. The spatial extent of high ($r > 0.4$) correlation values is closely tied to the region of opposing northward and southward flow, (as discussed previously), which are thus enhanced (reduced) and reduced (enhanced) during phases of anomalous northward (southward) shift of the ABFZ. Weaker negative correlation is apparent towards the west, between 16°S-18°S and 9°W-11°E, suggesting enhanced southward flow there during positive phases of *Index 1*. Figure 56b shows the correlation time series in the area of high r. Apart from the peak at zero lag, the time series fluctuates with an approximate period of 1 to 3 years, which indicates the presence of interannual variability, which will be discussed further in the next section.

The correlation analysis between *Index 1* and zonal velocity (not shown) suggests anomalous westward (eastward) flow centred in the middle front area (between 17°S-

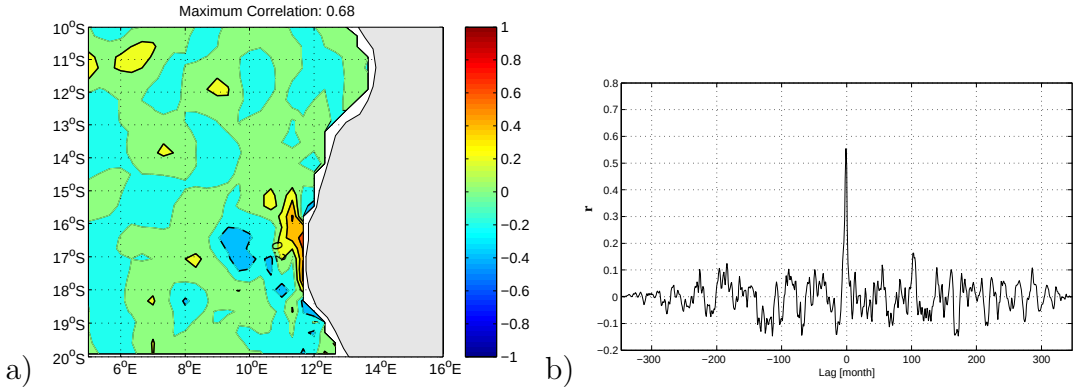

Figure 56: (a) Correlation between the meridional velocity at $20m$ and *Index 1* at zero lag, (b) the correlation time series in a region of high correlation. Positive (negative) contour lines are solid (dashed). The zero contour line is omitted. The contour interval is 0.2.

18°S) during positive phases of *Index 1*. It thus appears that the circulation pattern associated with anomalous northward (southward) positions of the middle front is of anticyclonic (cyclonic) nature near the ABFZ. The correlation plot for the velocity vector is shown in Figure 57a. The anticyclonic circulation pattern in the vicinity of the middle front is clearly visible.

Associated with this circulation pattern are changes in the upper ocean temperatures (Figure 57b). Cooler temperatures are evident in areas of enhanced northward and westward flow, between 17°S to 16°S, while warmer temperatures agree with areas of enhanced eastward flow and are centred around 18°S. Possible reasons for changes in the upper ocean temperature are discussed just below.

The same correlation analyses have been performed for *Index 2*. The horizontal correlation plot of meridional velocity and *Index 2* is shown in Figure 58. Correlation values are lower than for *Index 1*. Maximum values of $r = 0.36$ exist in a very small region of the frontal area near the coast. The analysis therefore suggests that anomalous meridional velocity does not affect *Index 2* in such an obvious way as *Index 1*. This picture changes when considering seasonal correlations (Figure 59). Strongest positive correlation with $r_{max} = 0.74$ at zero lag occurs during summer

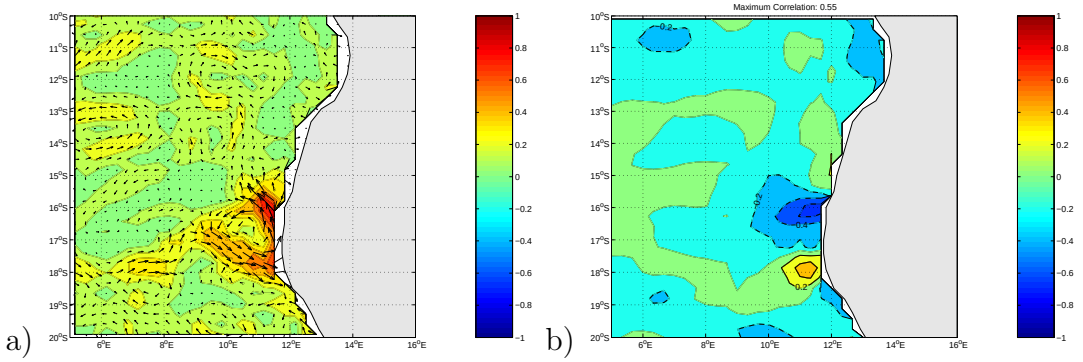

Figure 57: Correlation analysis between *Index 1* and (a) the velocity vector at $20m$, (b) temperature at $20m$. Positive (negative) contour lines are solid (dashed). The zero contour line is omitted. The contour interval is $0.1°C$.

(JFM) in the vicinity of the opposing Angola and Benguela Currents. Weaker correlations are apparent in AMJ and OND. In winter (JAS), r becomes stronger and exceeds $r > 0.5$, with highest values to the north of the mean middle front position, between 15°S and 14°S.

The correlation analyses between upper ocean temperatures and *Index 2* (not shown) are similarly seasonally dependent. Hence, strongest correlation occurs during the summer, with $r_{max} = 0.74$ and spring, with $r_{max} = 0.54$. Weak correlation is evident for winter and autumn.

These results suggest that anomalous positions of the middle front are accompanied by anomalous velocities. Repeating the analyses with geostrophic velocities reveal similar results (not shown). This implies that changes in the ageostrophic circulation are less important. However, during anomalous northward (southward) positions of the middle front, the coastal jet is enhanced (reduced) and the poleward current near the coast is reduced (enhanced). This results in a northward (southward) shift of the confluence zone and hence the ABFZ. The anomalous coastal currents during positive phases of *Index 1* form the eastern limb of an anticyclonic circulation pattern centred at around 17°S and 11°E. Associated with this pattern is convergence and divergence near the coast, which alter the coastal upwelling and thereby lead to dipole-like anomalies in the temperature field (Figure 57b), with

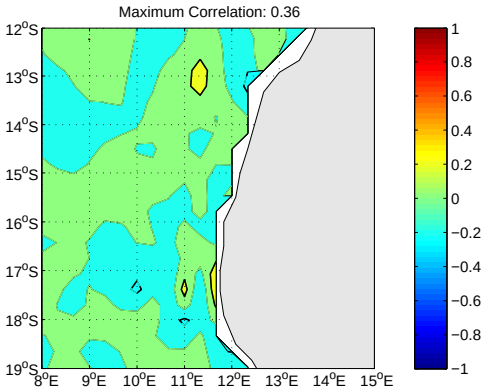

Figure 58: Correlation analysis at zero lag between *Index 2* and the meridional velocity at $20m$. Positive (negative) contour lines are solid (dashed). The zero contour line is omitted. The contour interval is 0.2.

cooler temperatures towards the north of the front. Since the enhanced northward coastal jet also implies enhanced upwelling (*McCreary et al.*, 1987), cool temperature anomalies are more pronounced.

Furthermore, since the frontal position is shifted towards the north, cooler upwelled water occurs mainly to the south of the front and to a lesser extent within the front. Thus, the anomalous temperature field leads to a net increase in the meridional temperature gradient within the front. This explains why there is positive correlation between the two indices. However, this mechanism appears to be most efficient during summer and spring, when upper ocean temperatures are warmer (Figure 38) since climatological upwelling is reduced due to reduced windstress (Figure 39). Figure 60 summarises this mechanism in schematic form.

6.3.3 Interannual variability and large scale circulation features

So far, only variability in the close vicinity of the ABFZ has been analysed. The correlation analyses above suggest that changes in the position and intensity of the front are mainly caused by dynamic effects.

The wavelet analysis of *Index 1* (Section 6.3.1, Figure 50) and also the correlation plot between *Index 1* and the meridional velocity revealed variability on interannual

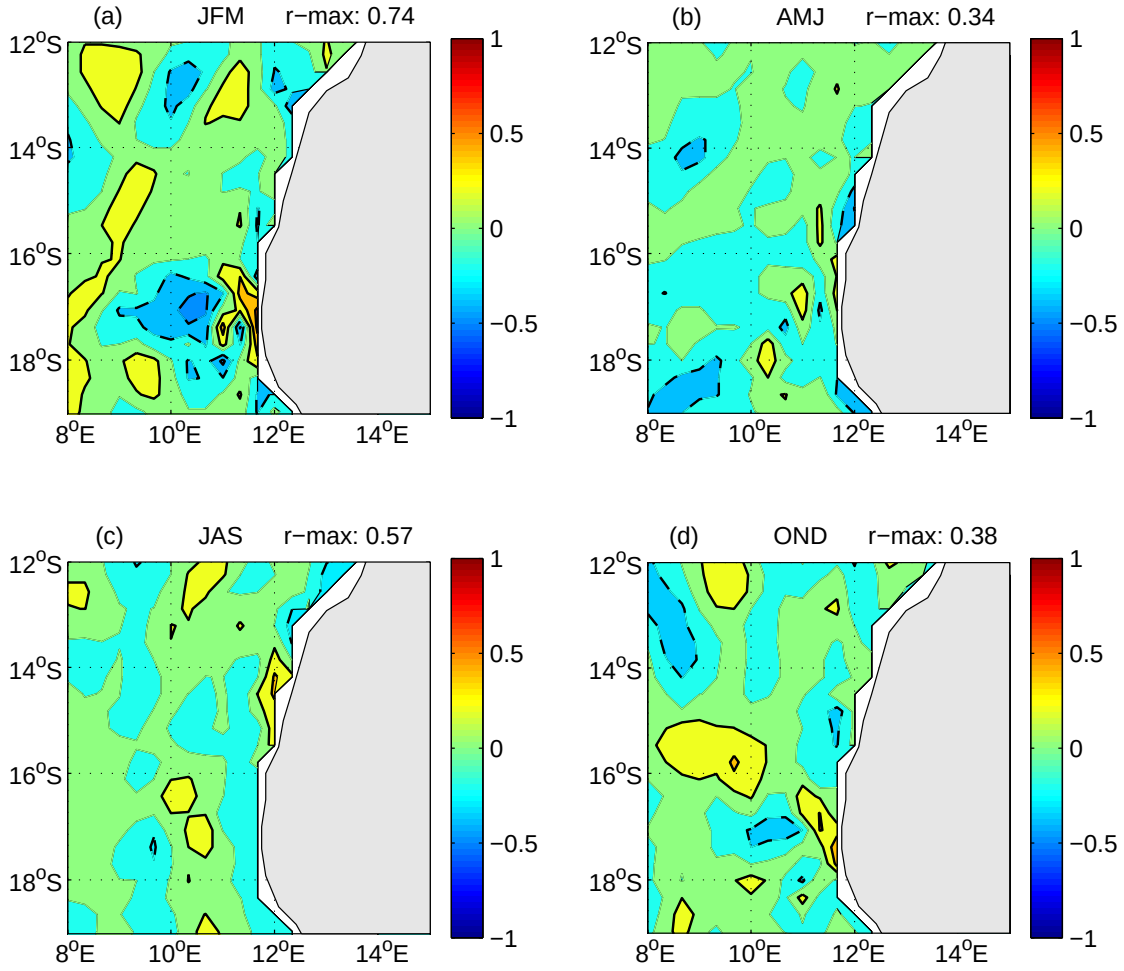

Figure 59: Seasonal correlation analysis between *Index 2* and the meridional velocity at $20m$. Positive (negative) contour lines are solid (dashed). The zero contour line is omitted. The contour interval is 0.2.

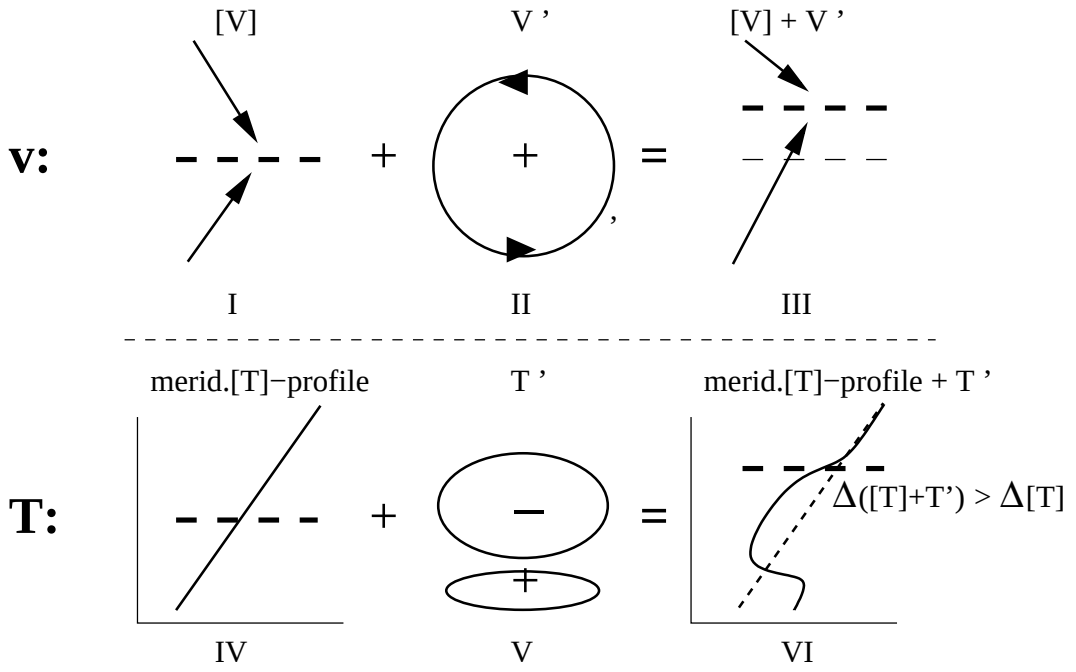

Figure 60: Schematic diagram of the dynamics responsible for anomalous northward positions of the ABFZ (thick dashed line). (I) The mean circulation $[V]$ estimates the mean position of the ABFZ. (II) An anomalous anticyclonic circulation V' is superimposed onto the mean flow, and (III) shifts the symmetry of the system towards the north. V' also induces changes in the mean temperature field (IV), as it leads to convergence (divergence) to the south (north). This results in a dipole like temperature anomaly T' (V) due to anomalous upwelling, with cooler temperatures towards the north, beneath the northward shifted front. The resulting temperature field (VI) thus enhances the meridional temperature gradient within the ABFZ.

time scales, with fluctuations of 1 to 3 years. This section aims to investigate possible relationships evident on the larger scale (within the model domain) and these frequencies. The indices and other variables are smoothed with a 12 month running mean when necessary, so that any possible relationships are more clearly revealed.

Figure 61 shows the filtered indices and their cross correlation. Clearly, the maximum correlation value is higher than for the original time series (Figure 54), due to filtering and subsequent reduction of the degrees of freedom. Maximum values of $r = 0.56$ occur when *Index 1* leads *Index 2* by three months. From visual inspection of the smoothed indices, it is evident that they are less coherent during the first 10 years, but agree well thereafter, with maximum correlation values of $r \approx 0.7$. It is interesting to note that increased correlation between the indices coincides with increased power evident for the annual and semi-annual signals discussed previously (Section 6.3.1). Furthermore, it is evident that both indices fluctuate with an approximate period of 2 to 3 years.

It was found that correlation analyses of the indices with velocities are quite noisy even after smoothing and are difficult to interpret. Therefore the following analysis focusses on SSH anomalies. This may also be helpful for the detection of wave-like motion that may be associated with interannual variability.

Sea Surface Height (SSH)

Figure 62 shows correlation sequences between *Index 1* and SSH anomalies over the whole model domain. The sequence starts at $lag = -90\,months$ and shows correlation maps every 6 months up to zero lag.

Qualitatively, the correlation values are more homogeneous and smaller north of 12°S than south of that latitude. The correlation values near the frontal region are generally weak except at zero lag (last Figure). Subsequently they are indicative of the geostrophic currents discussed above. For other lags, the region near the ABFZ does not show higher correlations than other regions. In fact, it often seems as if correlation values are lower. It is interesting to note that at zero lag high correlation values occur between 9°S-12°S, suggesting that changes in the SECC are

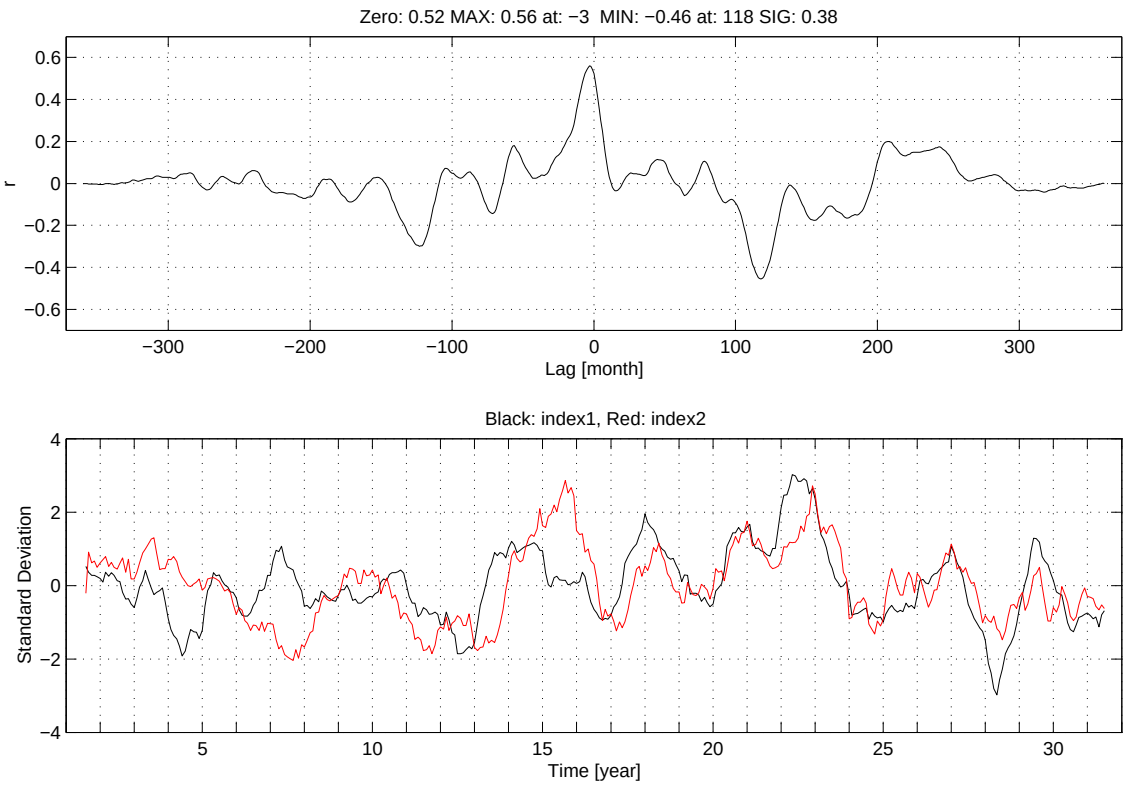

Figure 61: Upper: Correlation analysis between the two indices smoothed with a 12 month running mean. Lower: The corresponding time series.

related to anomalous frontal positions (as suggested by *Shannon et al.*, 1987; *Lass et al.*, 2000). However, the most prominent feature of the correlation sequence is a general westward movement of SSH correlation anomalies, apparent between 9°S and 30°S, but most pronounced between 12°S and 18°S and around 27°S.

The westward propagating anomalies between 12°S and 18°S occur mainly in the area of opposing geostrophic flow and seem to originate between 8°E-10°E. Positive and negative SSH correlation anomalies occur periodically, suggesting that wave-like motion may be present. A positive-negative anomaly cycle is completed after 4 to 5 years. The anomalies appear to undergo two phases, both of which take about a year. During the first phase the anomalies start to evolve anywhere between 8°E-10°E and 9°S-12°S or further south between 15°S-18°S. The anomalies then travel westward and reach the western model boundary within another year, thus travelling with an approximate velocity of $0.05ms^{-1}$. This is somewhat smaller than the mean westward directed geostrophic flow apparent south of 15°S. The speed of a westward travelling Rossby wave at 20°S is approximately $0.09ms^{-1}$ and at lower latitudes this speed increases. Hence, the westward propagating anomalies are too slow to account for Rossby wave motion and it is likely that these anomalies are eddies generated by oceanic instabilities and are advected within the mean geostrophic currents. The westward movement of SSH anomalies is also evident in the original SSH data. Figure 63 shows a Hovmöller plot for the SSH anomalies, averaged between 12°S and 18°S (note the SSH anomalies are not filtered).

Similar westward propagating SSH anomalies have been observed in a model study for the California upwelling system (*Marchesiello et al.*, 2001), and the Peruan upwelling system (*Penven et al.*, 2005b). *Marchesiello et al.* (2001) suggested that the speed of these anomalies ($0.02ms^{-1}$) is expected from baroclinic Rossby waves at around 40°N. They further note that the propagating signal appears more as propagating eddies than as wavefronts, similar to what is observed here.

The anomalies of the correlation sequence appear to become more elongated towards the north, indicating the presence of geostrophic turbulence as suggested by *Theiss* (2004). *Theiss* (2004) derived a formalism in the quasi-geostrophic frame-

work that accounts for a variable Rossby radius of deformation. It appears that the degree of Rossby wave induced anisotropy is depended on latitude. Above a certain critical latitude, the flow becomes isotropic featuring coherent vortices, whereas below this latitude, anisotropy increases with decreasing latitude.

Further to the south near 27°S, the anomalies are less coherent and travel faster and thus are more likely to be related to Rossby wave modulation as suggested by *Marchesiello et al.* (2001). They seem to originate in a region of high eddy kinetic energy (Figure 33a), which indicates that instability processes may provide a possible and coherent source of variability there. *Reason et al.* (1987) used a simple linear reduced gravity model applied to the South Atlantic Ocean and forced with observed climatological winds to analyse the propagation of first mode annual period baroclinic Rossby waves. Strong winds near the Namibian coast (25°S) were found to generate these waves, whose energy propagates northwestwards between 23°S and 15°S. It is possible that similar waves are generated in this model and that nonlinear interaction between waves of different wavelength could account for the quasi-periodic oscillation between 1 to 3 years.

These results show that there is a constant and remote signal apparent on interannual time scales within the South East Atlantic. This variability appears to be related to either internal instability processes of the oceanic currents and/ or to modulated Rossby waves. The periodic nature of this signal intuitively suggests that wave motion is important. This signal is at times highly correlated with *Index 1*, suggesting that it may be related to anomalous positions of the ABFZ and may be the source for the interannual variability found within the frontal movement. Correlation analyses with *Index 2* (Appendix 80) reveal similar results.

6.3.4 Summary and discussion

In this section, variability in the ABFZ has been discussed. In order to quantify variations of the location and motion and intensity of the ABZF, two indices have been introduced. It appears that they are able to describe variations in the positions and intensities of the front adequately and are thus used to further investigate the

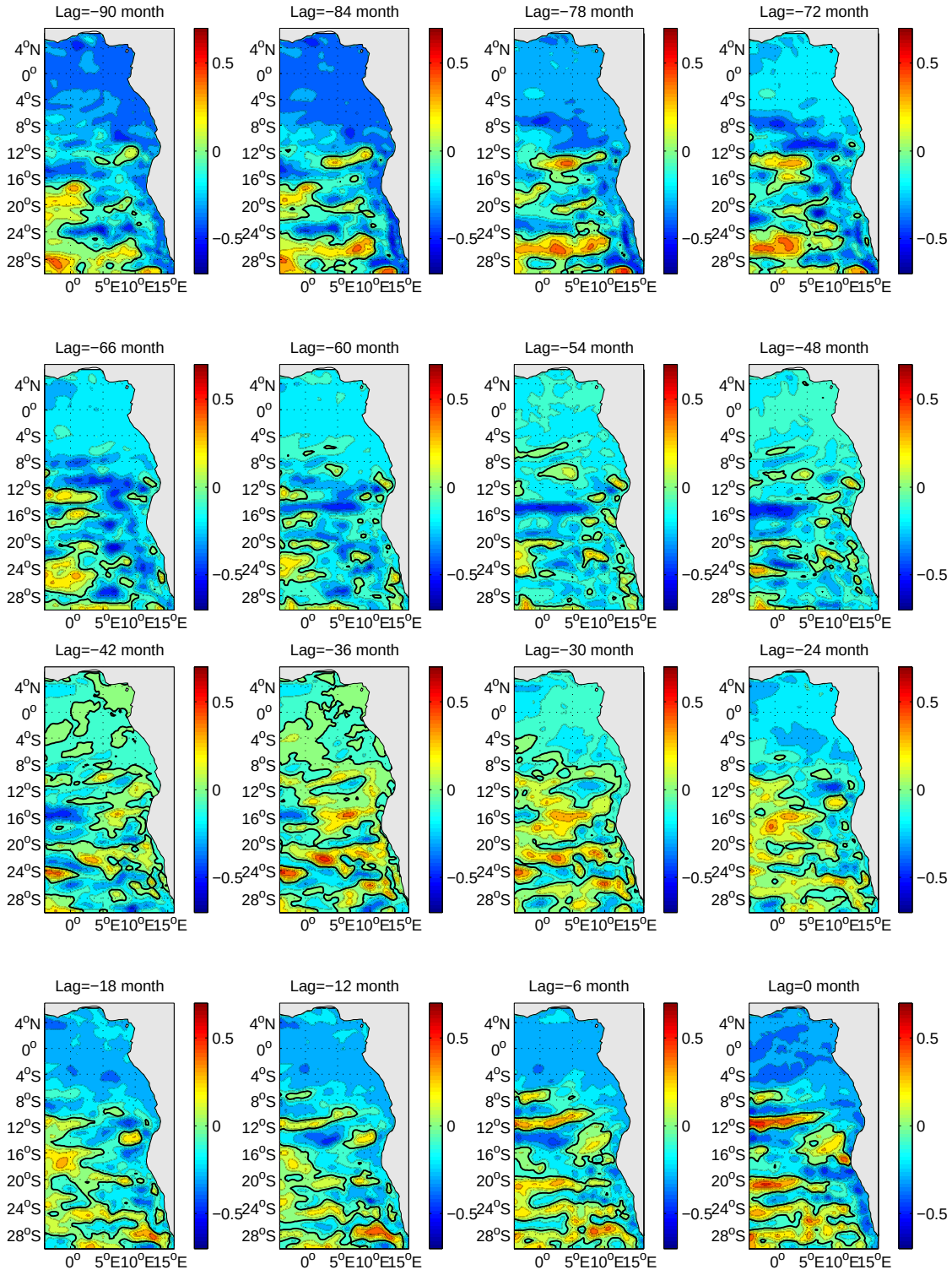

Figure 62: Correlation sequence between the filtered *Index 1* and the sea surface height (SSH) anomaly. Positive (negative) contour lines are omitted. The zero contour line is solid. A colour scale is given to the right of each plot.

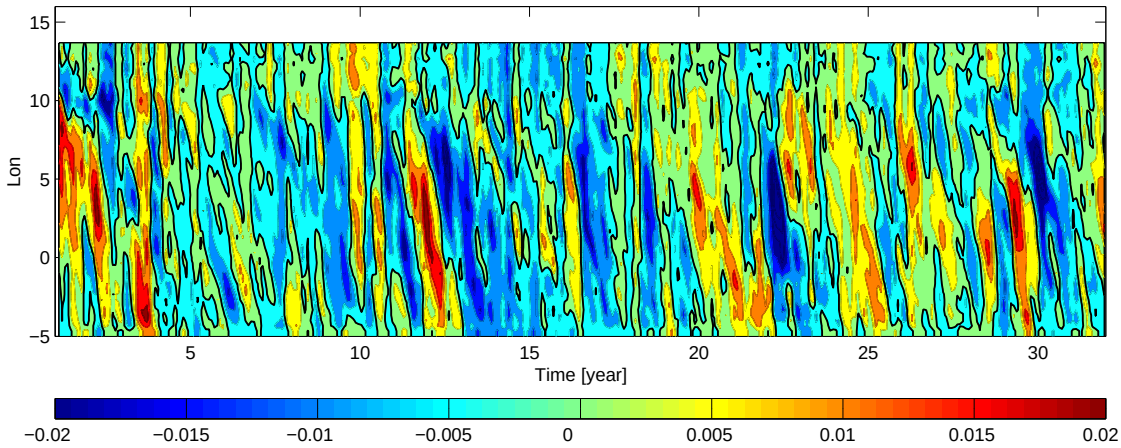

Figure 63: Hovmöller plot of the sea surface height (SSH) anomaly for the integrated reference run. The SSH anomalies are averaged over 12°S-18°S. Positive and negative isolines are omitted. Zero isoline is shown. A colour scale in m is given below.

nature of variability in the ABFZ. The wavelet analyses of the indices suggest that variability on various time scales is present, but the annual cycle accounts for most of the variability displayed. Intra-annual variability is also evident, with maximum power at 6 months (*Index 1*) and less than 6 months (*Index 2*). The anomalous indices reveal fluctuations of these prominent signals. Sources of variability on shorter time scales and high frequencies encompass Kelvin wave generation due to upwelling and seasonal varying wind forcing (*Philander and Yoon*, 1982).

Correlation analyses suggest that anomalous migrations of the middle front are connected to changes in the meridional temperature gradient. However, this relation is seasonally dependent and is phase locked particularly to spring and summer. In the model, changes in upwelling are most effective during these months since upper ocean temperatures are usually warmer and climatological upwelling is reduced then. A mechanism that relates anomalous positions and intensities of the front to the dynamics of the region has been suggested. Figure 60 schematically demonstrates this mechanism for anomalous northward position of the ABFZ. The mean circulation pattern of opposing flow (I) reveals the mean position of the ABFZ. An anomalous

anticyclonic circulation (II) is superimposed onto the mean flow and shifts the symmetry of the system towards the north (III), thereby altering the position of the ABFZ. The anomalous circulation also induces changes in the mean temperature field (IV), since it leads to convergence (divergence) to the south (north). This results in a dipole-like temperature anomaly due to anomalous upwelling (V), with cooler temperatures towards the north beneath the northward shifted front. The resulting temperature field (VI) thus enhances the meridional temperature gradient within the ABFZ.

However, this mechanism as described here is highly idealised. In nature, one would expect a much more complex behaviour of upper ocean currents and sea surface temperatures in the ABFZ (*Shannon et al.*, 1987). *Veitch et al.* (2005) examined seasonal and interannual fluctuations of the ABFZ using 18 years of $4.5km$ resolution satellite data and discussed the behaviour of the ABFZ during warm events such as Benguela Niños. Results of *Veitch et al.* (2005) suggest that the mean frontal position during such warm events remains relatively stable and that the intensity is reduced. However, strong gradients occur further south at 22°S and intensify during warm events. Hence, *Veitch et al.* (2005) concluded that the ABFZ shifts southward in response to anomalous warm events. In this study, no such gradients towards the south have been observed and in fact the meridional shift of the front is strongly confined between 18°S and 15°S.

Interannual variability with a period of 1 to 3 years has been shown to exist within the South East Atlantic and may potentially affect variability in the ABFZ. Sea surface height anomalies travel westwards with velocities of about $0.05ms^{-1}$, similar to what has been observed in other eastern boundary current systems (*Marchesiello et al.*, 2001; *Penven et al.*, 2005b). Possible sources of variability on longer time scales are oceanic instabilities and Rossby wave modulations due to time varying winds (*Philander and Yoon*, 1982; *Reason et al.*, 1987; *Marchesiello et al.*, 2001).

It is interesting to view the results of this section in context with other sources of variability in the South Atlantic. The temperature anomalies associated with anomalous shifts and intensities of the ABFZ are assessed by computing seasonal

composites for the anomalous years (Table 3). The derived composites (shown for positive phases of *Index 1* in Figure 64) reveal maximum temperature anomalies of up to 1°C (0.6°C) near the ABFZ for anomalous northward (southward) positions of the ABFZ. This order of magnitude is comparable to ENSO induced temperature anomalies in the South Atlantic (as discussed in Section 5). During Benguela Niños temperature anomalies reach values up to 5°C in the ABFZ area (e.g *Florenchie et al.*, 2003). Thus, modelled internal variability alone could account for up to 20% of the observed temperature anomalies during these events. This is a not negligible amount. Thus, a better understanding of internal variability in the South East Atlantic should be of high priority. In fact, the composite analysis reveals that maximum temperature anomalies associated with an anomalous northward shifted ABFZ occur during AMJ (Figure 64). Benguela Niños project onto the South East Atlantic mainly during late summer and autumn. It is tantalising to suggest that the seasonal dependence of Benguela Niños is influenced to some extent by internal variability.

$Index\,1 > 0$	$Index\,1 < 0$
7	4
14	12
17	16
22	28
29	30

Table 3: Positive (negative) years for *Index 1*, as chosen for the composite analyses.

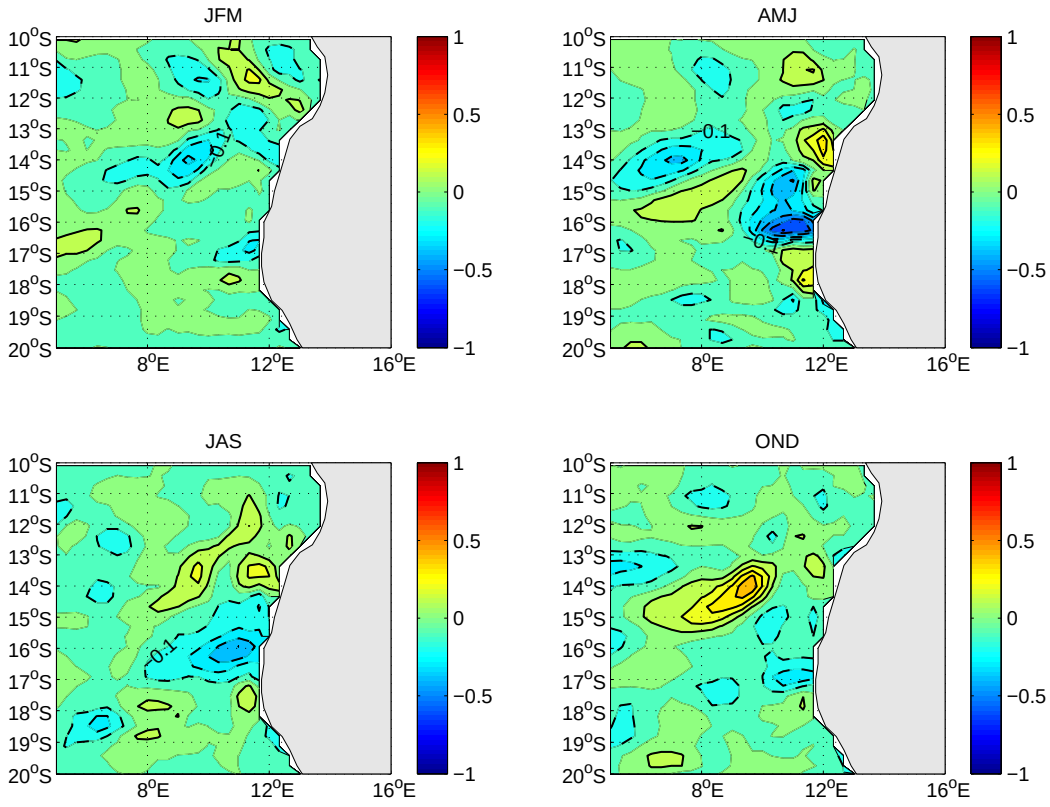

Figure 64: Seasonal composites of anomalous temperature for years where *Index 1* > 0. Positive (negative) contour lines are solid (dashed). The zero contour line is omitted. The contour interval is $0.1°C$.

6.4 Summary

In this section, a regional model (ROMS) has been applied to the South East Atlantic region. It is forced with monthly climatologies of QuikSCAT winds and NCEP/ NCAR reanalysis heat fluxes. The boundary conditions of monthly climatology for temperature, salinity and velocity climatologies are derived from an OGCM (ORCA2).

This section consists of three parts. The first one discussed the model's performance with respect to the ABFZ, the second one tested the sensitivity of the ABFZ towards changes in windstress, while the last part investigated the variability within the ABFZ on intra-annual to interannual time scales.

The first part revealed that the model successfully simulates a sharp thermal front, situated at 16.5°S, which is identified as the ABFZ. The characteristics of the front are in general agreement with observations (e.g. *Shannon et al.*, 1987). Maximum temperature gradients within the front are $4°C$ per $100km$. The front shifts meridionally, with the northern (southern) most position during July (October). The front is most intense during austral spring (April) and least defined during austral winter (August).

The position of ABFZ appears to be given by the confluence zone between opposing northward and southward geostrophic flow from 11°E towards the coast. Equatorward geostrophic flow to the south of the ABFZ appears to be related to alongshore windstress, which is strongest between 16°S and 17°S. The alongshore windstress favours upwelling and thereby alters the sea surface elevation near the coast allowing for an equatorward jet to evolve. Southward geostrophic flow to the north of the ABFZ on the other hand may be related to the windstress *curl*, which attains maximum negative values between 17°S and 18°S. Associated with the negative windstress *curl* is (a) upwelling that alters the sea surface height, and (b) a net southward volume transport due to the Sverdrup relation. Both effects may be responsible for the observed southward flow and thereby actively determine the confluence zone of opposing flows. The seasonal migration of the ABFZ is mainly

related to changes in the southward flow during the annual cycle.

The windstress and windstress *curl* display a semi-annual signal superimposed onto the annual cycle. Maximum values occur from April to May and August to October. Maximum values during the first half of the year thus coincide with maximum intensities of the ABFZ, implying a possible relationship as follows. Enhanced alongshore windstress leads to enhanced coastal upwelling and cooler water temperatures towards the south of the ABFZ, thereby effectively enhancing the temperature gradient within the ABFZ. However, the second, weaker, windstress maximum apparent during the second half of the year does not force such a clear response within the ABFZ.

The implied relationship between the front's position and intensity is further investigated in the second part of this section. In order to assess the influence of the applied windstress, several experiments with varying windstress have been conducted. The experiments explore the role of the strength of the trade wind system, the position of the South Atlantic Anticyclone and the windstress *curl* within the ABFZ area.

Results of the sensitivity study confirm that the position of the ABFZ is mainly determined by opposing northward and southward geostrophic flow near the coast. Furthermore, it appears that the intensity of the trade wind system has a rather negligible effect on the front's position but it does influence the intensity of the front. However, the response of the front towards weaker or stronger trade winds is not linear, since weaker winds lead to an almost absent front, while stronger winds only marginally increase the intensity. It is suggested that this result is partly caused by the model setup, which does not account for an adjustment of the equatorial currents towards changes in the winds.

The position of the ABFZ is sensitive to a meridional shift in the windstress, since the maximum windstress *curl* near the ABFZ tends to steer the SECC southeastwards and actively determines the zone of opposing geostrophic flow, which then gives rise to the ABFZ. It is evident that a northward (southward) shift of the South Atlantic Anticyclone enhances (weakens) the ABFZ, which is explained by the en-

hanced (absent or weak) equatorward flow due to enhanced (reduced) upwelling.

The last part of this section investigated variability within the ABFZ. Two indices that measure (a) the position, and (b) the intensity of the ABFZ are introduced. The indices reveal variability on mainly intra-annual to interannual time scales. The strongest power is apparent for the annual cycle. Intra-annual variability is evident for both time series with maximum power at (a) 6 month and (b) less than 6 month. The anomalous indices reveal fluctuations of these prominent signals.

Anomalous northward positions of the ABFZ are associated with an anticyclonic circulation near the frontal area, which enhances the equatorward coastal jet and reduces the southward flowing Angola Current, thereby shifting the symmetry of the system towards the north. The anomalous circulation also induces changes in the mean temperature field, as it leads to convergence (divergence) to the south (north). This results in a dipole-like temperature anomaly due to anomalous upwelling and effectively enhances the meridional temperature gradient across the ABFZ.

The filtered indices reveal interannual variability within the South East Atlantic and the ABFZ. Correlation analyses suggest that associated with the interannual signal are SSH anomalies that propagate westward in a periodic fashion. A cycle is completed after 4 to 5 years. It is suggested that mainly oceanic instabilities, between 12°S-15°S and/ or Rossby wave modulations, further south, are responsible for the interannual signal. Similar westward propagating anomalies have been observed for the California and Peru Current systems (*Marchesiello et al.*, 2001; *Penven et al.*, 2005b).

7 Conclusions

The work carried out in this study has examined climate variability in the South Atlantic. To account for variability on large and regional scales two ocean models were employed. An OGCM (ORCA2), forced with the NCEP/ NCAR reanalysis for the 1948-1999 period was used to investigate the South Atlantic leading modes, associated ocean-atmosphere couplings and changes in heat and volume flux. Furthermore, the possible response to ENSO induced variability has been explored. A regional ocean model (ROMS) was used to further investigate possible variability in the South East Atlantic, with the special focus on variability within the ABFZ.

A better understanding of interannual to decadal variability in the South Atlantic region is important due to its possible impact on large and regional climate (*Gordon*, 1986; *Schmitz*, 1995; *Reason et al.*, 2002; *Rouault et al.*, 2003; *Robertson et al.*, 2003). Model studies are necessary as they allow the examination of the deeper ocean structure, the movement of the mixed layer depth, and enable the derivation of both Ekman and geostrophic velocities thus revealing additional information on advective processes and baroclinic structures of the upper ocean. Hence, results give a more complete picture of the oceanic circulation. With this in mind, the South Atlantic leading modes were calculated for the ocean mixed layer temperature in Section 4.

It is apparent that the resulting modes mainly fluctuate on interannual to interdecadal time scales. The four rotated EOFs, explaining the most of the variability, appear to divide the South Atlantic into four subdomains with typical spatial and temporal scales.

The first mode is situated in the tropics with a connection to the northern Benguela and fluctuates on primarily interannual time scales. Reduced trade winds over the central to eastern tropics lead to upper ocean warming due to changes in surface latent heat flux and heat advection. However, anomalous windstress does not favour warming in the eastern tropics and northern Benguela, suggesting possible non-local atmospheric influences, such as equatorial Kelvin wave propagation being

the cause for the apparent warming (as e.g. suggested by *Carton and Huang*, 1994; *Florenchie et al.*, 2003, 2004). The analysis of the temperature tendency equation suggests that upwelling is reduced in these areas due to reduced entrainment and turbulent mixing. The model results suggest that the anomalous atmospheric circulation induces changes in the depth of the mixed layer, which is shallower (deeper) in the western (eastern) tropics. The timing of this mode also suggests connections to the Benguela Niños, since for example strongest warming was apparent in 1963. Other warm events are also captured by the time series of this mode but are not as extreme as the one in 1963. It has been shown by *Rouault et al.* (2003) that warm events in the tropical South East Atlantic can lead to changes in rainfall variability over the adjacent landmasses. This mode provides further evidence that anomalous warm events are associated with interannual variability in the tropical South East Atlantic and thus could prove valuable to better understand their occurrences and intensities.

The second leading mode is situated in the eastern subtropical South Atlantic and shows coherent variability between interannual to decadal time scales. Changes in the windstress over the subtropics lead to changes in latent heat flux and hence upper ocean warming and cooling. The timing and spatial structure of this mode suggests a connection to ENSO, in agreement with *Venegas et al.* (1997) and *Sterl and Hazeleger* (2003). In addition, it has been shown that trade wind modulations significantly alter the Ekman related meridional volume and heat transport, which in turn lead to changes in the gyre circulation and thus geostrophic related volume and heat transports. The anomalous transports are strongest in the Benguela ocean current region and reach depths of up to $200m$. This mode thus provides evidence that upper ocean temperature anomalies in coastal regions, for example, the Benguela, are strongly affected by the large scale modes. This implies variability on interannual to inter-decadal time scales there and has implications for understanding of the occurrences of extreme warm/ cool events in this region. Variability in the northward directed heat transport may have significant implications for the global heat balance and thus the thermohaline circulation.

For the third mode, the midlatitude westerlies are weakened and this results in a reduced northward directed Ekman heat transport, which leads to warming in the central to eastern midlatitudes. Anomalous Ekman velocities in the region are significantly correlated with ENSO, in agreement with the findings of Section 5 (discussed below) and *Colberg et al.* (2004). Decadal to inter-decadal variability is also evident and is associated with geostrophic advection of heat in the western to central midlatitudes. Changes in the northward (southward) flowing Falklands/ Malvinas (Brazil) current are associated with these velocities bringing cooler (warmer) water into the area. This mode shows similarities to the inter-decadal SST signal found by *Wainer and Venegas* (2001).

The last mode fluctuates on interannual to decadal time scales in the first 10 to 15 years of integration and on shorter interannual (less than 3 years) time scales thereafter. Upper ocean temperature anomalies for this mode respond to changes in the net heat flux, which is increased (reduced) during warm (cold) phases. Changes in the short wave flux favour the observed ocean temperature in some parts over the ocean, but counteracting them in others. Reduced short wave flux may also be indicative of enhanced cloud cover and thus increased reflected long wave radiation, which could account for the observed warming. Only the the modelled net heat and short wave flux were available, therefore examination of the ORCA2 long wave flux was not possible. Since the MLT anomaly is centred near the South Atlantic Convergence Zone, a region associated with convection and strong cloud cover, changes in long wave flux may become important and substantially affect upper ocean temperatures here. Also associated with this mode are changes in the strength of the South Atlantic Anticyclone, which mainly acts to enhance (reduce) entrainment during positive (negative) phases and thus dissipates the observed temperature anomalies.

A possible ENSO influence on the South Atlantic is implied by the analyses of the second and third South Atlantic leading modes. ENSO impacts on the South Atlantic are also suggested by e.g. *Venegas et al.* (1997) and *Reason et al.* (2000). It is thus appropriate to further investigate the evolution and impact of ENSO over the South Atlantic. This has been done in Section 5. The Niño 3.4 index has been

derived from ORCA2 upper ocean temperature in order to define positive (negative) phases of ENSO. Seasonal composites of upper ocean temperature, SLP, windstress, meridional Ekman heat transport and net surface heat flux anomalies for El Niño and La Niña years have been investigated. It has been shown that during ENSO, upper ocean temperatures in the South Atlantic are significantly influenced by the ENSO-induced windstress anomalies.

During the El Niño onset, the global SLP teleconnection pattern implies a negative SLP anomaly in the South Atlantic region via the Pacific South America pattern (*Mo and Paegle*, 2001). The main effects of the SLP anomaly are the weakening of the southeasterly trades (mainly during AMJ and JAS of the onset year) and a strengthening of the midlatitude westerlies (particularly from JAS to the following JFM mature phase). As a result, the southward tropical (northward midlatitude) Ekman heat transport is reduced (enhanced), thus favouring warming over the South Atlantic from the equator to about 25°S and cooling in the midlatitudes, with a lag of about one season. The wind anomalies lead to changes in the net surface heat fluxes that are generally consistent with the observed changes in the model upper ocean temperatures one season later. During La Niña, the upper ocean temperature changes and the associated mechanisms are roughly the reverse of those evident during El Niño. The patterns are not exactly opposite, suggesting some nonlinearity to the response. The mechanisms leading to temperature changes during El Niño (La Niña) in the tropical South Atlantic are comparable to those that cause warming (cooling) in the northern tropics, i.e. a weakening (strengthening) of the trades and associated changes in surface heat fluxes (*Huang et al.*, 2002; *Giannini et al.*, 2001). Furthermore, the results from the ORCA2 model suggest that the warm (cold) ENSO signal reaches the South Atlantic region via an atmospheric teleconnection pattern, one season in advance (i.e. in OND), in comparison with the North Atlantic.

The investigation also suggests an ENSO impact on subsurface temperatures. Annual means of Ekman pumping and thermocline depth anomalies appear to be consistent with the modelled near thermocline ocean temperature anomalies, sug-

gesting subsurface temperature changes are responding towards the prevailing atmospheric conditions during ENSO events.

The results of Section 5 imply that there is a coherent and significant ENSO impact on the South Atlantic, extending from low to midlatitudes. Modulations of the South Atlantic anticyclone and associated tradewinds and westerlies, suggested here as part of the PSA pattern, are important for the evolution of the anomalies. Modulations of the anticyclone are also very important for the leading South Atlantic climate mode (e.g. *Venegas et al.*, 1996) as well as Benguela warm and cool events (*Florenchie et al.*, 2003).

The region of interest is narrowed down to the South East Atlantic in Section 6. Variability in this region is strongly affected by the occurrences of Benguela Niños (e.g. *Shannon et al.*, 1986; *Florenchie et al.*, 2003) and, as suggested by the previous discussion, ENSO also impacts on the region with apparent warmer (cooler) ocean temperatures towards the south (north) of the ABFZ (see also e.g. *Reason*, 2000). The ABFZ separates the tropical dynamics from the Benguela upwelling system and hence is an important system boundary, whose fluctuation potentially affect fisheries and rainfall variability. An improved understanding of the dynamics, mechanisms and variability of the ABFZ is therefore necessary. Hence, a regional ocean model (ROMS) has been applied to the South East Atlantic region. The model is forced with climatological windstress (QuikSCAT) and NCEP/ NCAR heat fluxes. Other boundary conditions such as temperature, salinity and velocity are derived from an OGCM (ORCA2) model. The reference run has been integrated for 32 years.

The model successfully simulates the occurrence of a sharp thermal front situated at approximately 16.5°S, which is identified as the ABFZ. The characteristics of the front are in general agreement with observations (e.g. *Shannon et al.*, 1987; *Lass et al.*, 2000; *Veitch et al.*, 2005). The front migrates annually, with the northern and southern most position during austral winter (July) and spring (October). The intensity of the front also varies, with strongest (weakest) gradients during autumn (April) and winter.

Several experiments have been conducted in order to assess the sensitivity and

intensity of the ABFZ in the presence of changing windstress. In summary, the model results suggest that the position of the front is closely tied to opposing north and southward geostrophic flow within 1-2 degrees off the coast. The opposing flows are generated by the overlying atmospheric circulation, strong anticyclonic windstress *curl* in the frontal area acts to steer the South Equatorial Counter Current (SECC) southeastwards towards the Angolan coast, while alongshore windstress further to the south enables coastal upwelling, which triggers the equatorward coastal jet. Changes in the meridional position of the windstress *curl*, thus leads to changes in the position of the ABFZ.

The intensity of the ABFZ is found to be mainly related to the generation of upwelled water towards the south of the ABFZ. Thus, changes in the intensity of the ABFZ respond to enhanced (reduced) tradewinds. The model results agree partially with *Kim et al.* (2003), who suggested that changes in trade winds alter the intensity of the ABFZ, due to the combined effect of enhanced upwelling and changes in heat transport into the tropical South East Atlantic. However, in this study it is found that the response of the ABFZ towards increased (reduced) winds is not linear. Enhanced winds only marginally increase the temperature gradient, while reduced winds lead to an almost absent front. Differences between the model results and *Kim et al.* (2003) are likely due to fact that the model setup does not account for an adjustment of the equatorial currents towards changes in the trade wind system.

Variability in the ABFZ has been investigated by introducing two indices that measure (a) the position and (b) the intensity of the ABFZ, respectively. It appears that the annual signal accounts for most of the variability displayed. Intra-annual variability is also evident for both time series with maximum power at (a) 6 month and (b) less than 6 month. The anomalous indices reveal fluctuations of these prominent signals.

Anomalous northward frontal positions are associated with an anticyclonic circulation near the frontal area, which enhances the equatorward coastal jet and reduces the southward flowing Angola Current, thereby shifting the symmetry of the system

towards the north. Associated with this pattern are anomalous temperatures due to changes in upwelling. These give rise towards cooler temperatures beneath the frontal position and thus effectively enhance the meridional temperature gradient. This mechanism is most effective in the model during spring and summer, when climatological upwelling is reduced.

Lastly, interannual variability is investigated. The filtered indices reveal coherent variability between 1 to 3 years, that is associated with changes in the sea surface height. Anomalous SSH propagates westward in a periodic fashion, with an approximate speed of the surrounding geostrophic velocities. A cycle is completed after 4 to 5 years. It is suggested that internal instability processes are responsible for the anomalous propagation. The SSH anomalies are elongated towards the north suggesting the presence of geostrophic turbulence due to changes in the Rossby radius of deformation (*Theiss*, 2004).

The model analysis has implications for the understanding of variability in the ABFZ. Several authors (e.g. *Shannon et al.*, 1987) have suggested that windstress may play an important role in determine the position of the ABFZ. Results of the work presented here prove that the *curl* of the windstress is (when existent) the most important factor in determine the frontal position. However, the model results also suggest that windstress *curl* only modifies the position of the front and is not necessarily the cause, implying that alongshore winds, coastline orientation and bottom topography are also important and future work should focus on their influence on the ABFZ.

The results presented in Section 6 reinforce results given in the previous section, since for example enhanced (reduced) trade winds, as modelled, are comparable to negative (positive) phases of ENSO. Thus, the investigation implies a reduced (enhanced) ABFZ during El Niño (La Niña). The seasonal composites shown in Section 5, reveal warmer (colder) upper ocean temperatures towards the south (north) of the front during the onset of El Niño (JAS, OND), which is in agreement with a reduced temperature gradient across the front.

According to *Shannon et al.* (1987), an excess of tropical water is shifted south-

wards during Benguela Niños. Results of the study presented here suggest that the ABFZ would respond with a corresponding southward shift and, consequentially, this results in a reduced meridional temperature gradient. This effect would be strongest in summer and spring. A recent study of *Veitch et al.* (2005) indeed suggests that the ABFZ between 15°S and 17°S weakens during major warm events in the South East Atlantic, confirming the results presented here.

Quantitatively, it appears that in certain areas near the ABFZ, temperature anomalies due to internal variability can reach an order of magnitude comparable to those induced by ENSO (Section 5). Internal variability alone could account for up to 20% of the observed temperature anomalies during Benguela Niños. This is a not negligible amount. Thus, internal variability in the South East Atlantic needs to be considered as a source for variability and an improved understanding of it should be of high priority. Possible positive feedbacks in the coupled ocean atmosphere system need to be investigated, as these can amplify and organize upper ocean temperatures (*Jochum and Murtugudde*, 2004). In addition temperature anomalies in this area are known to affect rainfall variability and possible interactions between internal and external modes of variability could effectively enhance (reduce) the severity of South East Atlantic warm or cold events.

In this thesis two ocean models have been used in order to diagnose variability in the South Atlantic. The performance of ocean models has been improved during recent years, but is still dependent and limited by the given boundary conditions. The results shown here must be seen in that respect. In the Southern Hemisphere data coverage is sparse compared to the Northern Hemisphere, underlining the need of modelling studies as this one but also the importance of observational projects such as ARGO or PIRATA, which should receive ongoing high attention. More observations are necessary in order to improve the quality of data assimilation projects and to verify model output.

Ongoing studies should focus in more detail on the interaction between large scale modes and local forcings. Further investigations especially model simulations are therefore necessary. The model study presented here is an important first step in

understanding variability in the South East Atlantic and would allow for easier interpretation of variability resulting from more complex forcings. Results of this study and others (e.g. *Venegas et al.*, 1997; *Sterl and Hazeleger*, 2003) suggest, that South Atlantic upper ocean temperatures respond mainly to the overlying atmospheric circulation. Therefore a better monitoring of the South Atlantic Anticyclone should be of high priority. Investigations of possible impacts of other sources of variability on its strength and position are necessary in order to better understand South Atlantic climate variability.

References

Barreiro, M., P. Chang, and R. Saravanan (2000), Variability of the South Atlantic convergence zone simulated by an atmospheric general circulation model, *J. Climate*, *15*, 745–763.

Berger, W. H., and G. Wefer (1996), *The South Atlantic: Present and Past Circulation*, chap. Central Themes of South Atlantic Circulation, pp. 1–11, Springer-Verlag, Berlin Heidelberg.

Binet, D., B. Gobert, and L. Maloucki (2001), El Niño-like warm events in the Eastern Atlantic (6 N, 20 S) and fish availability from Congo to Angola (1964-1999), *Aquat. Living Resour.*, *14*, 99–113.

Björnsson, H., and S. A. Venegas (1997), *A manual for EOF and SVD Analyses of Climatic Data*, Centre for Climate and Global Change Research, McGill University.

Blanke, B., and P. Delecluse (1993), Variability of the Tropical Atlantic Ocean simulated by a general circulation model with two different mixed layer physics, *J. Phys. Oceanogr.*, *23*, 1363–1388.

Boyd, A. J. (1987), The oceanography of the Namibian shelf, *Ph.D. thesis*, University of Cape Town.

Boyd, A. J., J. Salat, and M. Maso (1987), *The Benguela and Comparable Ecosystems*, vol. 12, chap. The seasonal intrusion of relatively saline water on the shelf off northern and central Namibia, pp. 107–120, *S. Afr. J. Mar. Sci.*

Bretherton, C. S., M. Widman, V. P. Dymnikov, J. M. Wallace, and I. Blade (1999), The effective number of spatial degress of freedom of a time-varying field, *J. Climate*, *12*, 1990–2009.

Bryan, K. (1962), Measurements of Meridional Heat Transport by Ocean Currents, *J. Geophys. Res.*, *67*(9), 3403–3414.

Carton, J. A., and B. Huang (1994), Warm events in the Tropical Atlantic, *J. Phys. Oceanogr.*, *24*, 888–903.

Carton, J. A., X. Cao, B. S. Giese, and A. M. da Silva (1996), Decadal and interannual SST variability in the Tropical Atlantic Ocean, *J. Phys. Oceanogr.*, *26*, 1165–1175.

Carton, J. A., B. S. Giese, and S. A. Grodsky (2005), Sea level rise and the warming of the oceans in the Simple Ocean Data Assimilation (SODA) ocean reanalysis, *J. Geophys. Res.*, *110*.

Clark, A. J., and S. Van Gorder (1994), On ENSO coastal currents and sea level, *J. Phys. Oceanogr.*, *25*, 661–679.

Clarke, A. J. (1989), *Poleward Flows along Eastern Ocean Boundries* , chap. Theoretical understanding of eastern ocean boundary poleward undercurrents , pp. 110–130, Springer-Verlag, Berlin.

Colberg, F., C. J. C. Reason, and K. Rodgers (2004), South Atlantic Response to El Niño-Southern Oscillation induced Climate Variability in an OGCM, *J. Geophys. Res.*, *109*, C12015, doi:10.1029/2004JC002301.

Conkright, M. E., R. A. Locarnini, H. E. Garcia, T. D. O'Brien, T. P. Boyer, C. Stephens, and J. I. Antonov (2002), World ocean atlas 2001: Objective analyses, data statistics, and figures, cd-rom documentation, *Tech. rep.*, National Oceanographic Data Center, Silver Spring, MD.

Da Silva, A. M., C. C. Young, and S. Levitus (1994), Atlas of surface marine data 1994, vol. 1, algorithms and procedures, *Tech. rep.*, U. S. Department of Commerce, NOAA.

Daubechies, I. (1992), *Ten Lectures on Wavelets*, *CBMS-NSF Regional Conference Series in Applied Mathematics*, vol. 16, 357 pp., Society for Industrial and Applied Mathematics Press.

Davis, R. E., B. P. Hayden, D. A. Gay, W. L. Phillips, and G. V. Jones (1997), The North Atlantic Subtropical Anticyclone, *J. Climate*, *10*, 728–744.

de Ruijter, W. P., A. Biastoch, S. S. Drijfhout, J. R. E. Lutjeharms, R. P. Matano, T. Pichevien, P. J. van Leeuwen, and W. Weijer (1999), Indian-Antlantic interocean exchange: dynamics, estimation and impact, *J. Geophys. Res.*, *104*(C9), 20.885–20.910.

Dengler, A. T. (1985), Relationship between physical and biological processes at an upwelling front off Peru, *Deep-Sea Res.*, *32*(11A), 1301–1315.

Ducet, N., P. Y. Le Traon, and G. Reverdin (2000), Global high-resolution mapping of ocean circulation from TOPEX/Poseidon and ERS-1 and -2, *J. Geophys. Res.*, *105*, 19,477–19,498.

Dunbar, R. S. (2000), *QuikSCAT Science Data Product User's Manual, Version 1.0*, JPL Document D-18053, Jet Propulsion Laboratory, Pasadena, CA.

Emery, W. J., and R. E. Thomson (1998), *Data Analysis Methods in Physical Oceanography*, 500 pp., Pergamon, Oxford.

Enfield, D. B., and D. A. Mayer (1997), Tropical Atlantic SST variability and its relation to El Niño-Southern Oscillation, *J. Geophys. Res.*, *102*, 929–945.

Fichefet, T., and M. A. Morales (1997), Sensitivity of a global sea ice model to the treatment of ice thermodynamics and dynamics, *J. Geophys. Res.*, *91*, 5037–5046.

Florenchie, P., J. R. E. Lutjeharms, C. J. C. Reason, S. Masson, and M. Rouault (2003), The source of the Benguela Niños in the South Atlantic Ocean, *Geophys. Res. Lett.*, *30*(10), 1505, doi:10.1029/2003GLO17172.

Florenchie, P., C. J. C. Reason, J. R. E. Lutjeharms, M. Rouault, and C. Roy (2004), Evolution of internnual warm and cold events in the south-east Atlantic Ocean, *J. Climate*, *17*, 2318–2334.

Folland, C. K., T. N. Palmer, and D. E. Parker (1986), Sahel rainfall and world-wide sea temperatures, *Nature*, *320*, 602–607.

Gammelsrod, T., C. H. Bartholomae, D. C. Boyer, V. L. L. Philipe, and M. J. O. Toole (1998), Intrusion of warm surface layer along the Angolan- Namibian coast on February- March: the 1995 Benguela Niño, *S. Afr. J. Mar. Sci.*, *19*, 41–56.

Gent, P. R., and J. C. McWilliams (1990), Isopycnal mixing in ocean circulation models, *J. Phys. Oceanogr.*, *20*, 150–156.

Giannini, A., C. H. John, M. A. Cane, Y. Kushnir, and R. Saeger (2001), The ENSO Teleconnection to the Tropical Atlantic Ocean: Contributions of the Remote and Local SST to Rainfall Variability in the Tropical Americas, *J. Climate*, *14*, 4530–4544.

Giannini, A., R. Saravanan, and P. Chang (2004), The preconditioning role of Tropical Atlantic Variability in the development of the ENSO teleconnection: implications for the prediction of Nordeste rainfall, *Climate Dynamics*, *22*, doi: 10.1007/s00382-004-0420-2.

Gordon, A. L. (1985), Indian-Atlantic transfer of thermocline water at the Agulhas retroflection, *Science*, *227*(4690), 1030–1033.

Gordon, A. L. (1986), Inter-Ocean exchange of thermocline water, *J. Geophys. Res.*, *91*, 5037–5046.

Gordon, A. L. (1996), *The South Atlantic: Present and Past Circulation*, chap. Comment on the South Atlantic's role in the Global Circulation, pp. 121–124, Springer-Verlag, Berlin Heidelberg.

Gordon, A. L., R. F. Weiss, W. M. Smethjie Jr., and M. J. Warner (1992), Thermocline and intermediate water communication between the South Atlantic and Indian Oceans, *J. Geophys. Res.*, *97*(C5), 7223–7240.

Haarsma, R. J., E. J. D. Campos, W. Hazeleger, C. Severijns, A. R. Piola, and F. Molteni (2005), Dominant modes of variability in the South Atlantic: A study with a hierachy of ocean-atmosphere models, *J. Climate*, *Revised*.

Hannachi, A. (2004), *A Primer for EOF Analyses of Climate Data*, Department of Meteorolgy, University of Reading, Reading RG6 6BB, U.K.

Hart, T. J., and R. I. Currie (1960), The Benguela Current, *Discovery Rep.*, *31*, 123–297.

Hastenrath, S. (1990), Decadal-scale changes of the circulation in the tropical Atlantic sector associated with Sahel drought, *Int. J. Climatol.*, *10*, 459–472.

Hastenrath, S., and L. Heller (1977), Dynamics of climate hazards in Northeast Brazil, *Roy. Met. Soc.*, *103*, 77–92.

Hazeleger, W., P. de Vries, and Y. Friocourt (2002), Sources of the Equatorial Undercurrent in the Atlantic in a High-Resolution Ocean Model, *J. Phys. Oceanogr.*, *33*, 677–693.

He, R., Y. Liu, and R. H. Weisberg (2004), Coastal ocean wind fields gauged against the performance of an ocan circulation model, *Geophys. Res. Lett.*, *31*, LI4303, doi:10.1029/2003GL019261.

Hermes, J. C., and C. J. C. Reason (2005), Ocean Model Diagnosis of Interannual Coevolving SST Variability in the South Indian and South Atlantic Ocean, *J. Climate*, *18*, 1–19.

Horel, J. D., and J. M. Wallace (1981), Planetary scale atmospheric phenomena associated with the interannual variability of sea surface temperature in the equatorial Pacific, *Mon. Wea. Rev.*, *109*, 813–829.

Horel, J. D., V. E. Kousky, and M. T. Kagano (1986), Atmospheric conditions in the Atlantic sector during 1983 and 1984, *Nature*.

Huang, B., P. S. Schopf, and Z. Pan (2002), The ENSO effect on the tropical Atlantic variability: A regionally coupled model study, *Geophys. Res. Lett.*, *29*(21), doi: 10.1029/2002GL014872.

Huddleston, J. N., and B. W. Stiles (2000), *Multidimensional Histogram (MUDH) Rain Flag Product Description, Version 2.1*, Jet Propulsion Laboratory, Pasadena, CA.

Jerlov, N. G. (1968), *Optical Oceanography*, 194 pp., Elsevier.

Jochum, M., and R. Murtugudde (2004), Internal variability in the tropical Pacific ocean, *Geophys. Res. Lett.*, *31*, L14309, doi:10.1029/2004GL020488.

Johns, W. E., T. N. Lee, R. C. Beardsley, J. Candela, R. Limeburner, and B. Castro (1998), Annual cycle and variability of the North Brazil Current, *J. Phys. Oceanogr.*, *28*, 103–128.

Kaiser, H. F. (1958), The varimax criterion for analytic rotation in factor analysis, *Psychometrika*, *23*, 187–200.

Kalnay, E., N. Kanamitsu, R. Kistler, W. Collins, D. Deaven, L. Gandin, M. Iredell, S. Saha, G. White, J. Wooljen, Y. Zhu, M. Chelliah, W. Ebisuzaki, W. Higgins, J. Janowiak, K. C. Mo, C. Ropelewski, J. Wang, A. Leetsmaa, R. Reynolds, R. Jenne, and D. Joseph (1996), The NCEP/NCAR, 40-Year Reanalysis Project, *Bull. Am. Meteorol. Soc.*, *77*(3), 437–471.

Kim, J. H., R. R. Schneider, S. Mulitza, and P. J. Müller (2003), Reconstruction of SE trade-wind intensity based on sea-surface temperature gradients in the Southeast Atlantic over the last 25 Kyr, *Geophys. Res. Lett.*, *30*(22), 2144, doi:10.1029/2003GL017557.

Kostianoy, A. G., and J. R. E. Lutjeharms (1999), Atmospheric Effects in the Angola Benguela Frontal Zone, *J. Geophys. Res.*, *104*(9), 20,963–20,970.

Lamb, P. J., and R. A. Peppler (1992), Further case studies of tropical Atlantic surface atmospheric and oceanic patterns associated with sub-Saharan drought, *J. Climate*, *5*, 476–488.

Large, W. G., J. C. McWilliams, and S. C. Doney (1994), Oceanic vertical mixing: A review and a model with a nonlocal boundary layer parameterization, *Rev. Geophys.*, *32*, 363–403.

Lass, H. U., M. Schmidt, V. Mohrholz, and G. Nausch (2000), Hydrographic and Current Measurements in the Area of the Angola-Benguela Front, *J. Phys. Oceanogr.*, *30*, 2589–2609.

Lau, K. M., and H. Y. Weng (1996), Climate signal detection using wavelet transform: How to make a time series sing, *Bull. Amer. Meteor.*, *76*(12), 61–78.

Lentini, C. A. D., G. G. Podesta, E. J. D. Campos, and D. B. Olson (2000), Sea surface temperature anomalies in the western South Atlantic from 1982 to 1994, *Continental Shelf Res.*, *21*, 89–112.

Levitus, S. (1987), Zonally integrated meridional Ekman heat fluxes for the world Ocean and individual ocean basins, *J. Phys. Oceanogr.*, *17*, 1484–1492.

Levitus, S. (1998), World Ocean Atlas 1998, *Tech. rep.*, US Department of Commerce.

Liu, W. T., W. Tang, and P. S. Polito (1998), Nasa scatteromter provides global ocean-surface wind fields with more structures than numerical weather prediction, *Geophys. Res. Lett.*, *25*, 761–764.

Lutjeharms, J. R. E. (1996), *The South Atlantic: Present and Past Circulation*, chap. The exchange of Water Between the South Indian and South Atlantic Oceans, pp. 121–124, Springer-Verlag, Berlin Heidelberg.

Madec, G., P. Delecluse, M. Imbard, and C. Levy (1998), OPA 8.1 Ocean General Circulation Model reference manual, *Institut Pierre Simon Laplace*, *11*, 91.

Marchesiello, P., J. C. McWilliams, and A. Shchepetkin (2001), Open boundary conditions for long-term integration of regional oceanic models, *Ocean Modelling*, *3*, 1–20.

McCreary, J. P., P. K. Kundu, and S.-Y. Chao (1987), On the dynamics of the California Current system, *J. Mar. Res.*, *45*, 1–32.

McGee, O. S., and S. L. Hastenrath (1966), Harmonic analysis of the rainfall over South Africa, *Notos*, *15*, 79–90.

Meeuwis, J. M., and J. R. E. Lutjeharms (1990), Surface thermal characteristics of the Angola Benguela front, *S. Afr. J. Mar. Sci*, *9*, 261–279.

Mehta, V. M. (1998), Variability of the tropical ocean surface temperatures at decadal-multidecadal time scales. Part I: The Atlantic Ocean, *J. Climate*, *11*, 2351–2375.

Melice, J. L., and J. Servain (2003), The tropical Atlantic meridional SST gradient index and its relationship with the SOI, NAO and Southern Ocean, *Climate Dyn.*, *20*, 447–467.

Melice, J. L., A. Coron, and A. Berger (2001), Amplitude and frequency modulation of the Earth's obliquity for the last million years, *J. Climate*, *14*, 1043–1054.

Mo, K. C., and J. N. Paegle (2001), The Pacific-South American Modes and their downstream effects, *Int. J. Climatol.*, *21*, 1211–1229.

Molinari, R. L., B. Voituriez, and R. P. Bubnov (1981), Observations in the subthermocline undercurrent of the equtorial South Atlantic Ocean: 1978-1980, *Oceano. Acta.*, *4*, 451–456.

Morlet, J. (1983), *Issues in Accoustic Signal/ Image processing and Recognition*, *NATO ASI Series*, vol. 1, chap. Sampling theory and wave propagation, pp. 233–261, Springer.

Moura, A., and J. Shukla (1981), On the dynamics of droughts in northeast Brazil: Observations theory and numerical experiments with a general circulation model, *J. Atmos. Sci.*, *38*, 2653–2675.

Mulenga, H. M., M. Rouault, and C. J. C. Reason (2003), Dry summers over northeastern South Africa and associated circulation anomalies, *Climate Res.*, *25*, 29–41.

Nobre, P., and J. Shukla (1996), Variations of sea surface temperature, wind stress, and rainfall over the tropical Atlantic and South America, *J. Climate*, *9*, 2464–2479.

Palastanga, V., C. S. Vera, and A. R. Piola (2002), On the leading modes of sea surface temperature variability on the South Atlantic ocean, *CLIVAR Exchanges*, *7*(3-4), 12–15.

Palastanga, V., C. S. Vera, and A. R. Piola (2005), South Atlantic Sea surface temperature variability from seasonal to interdecadal time scales, *Submitted*.

Paulson, C. A., and J. J. Simpson (1977), Irradiance Measurements in the Upper Ocean, *J. Phys. Oceanogr.*, *7*, 952–956.

Penven, P., L. Debreu, P. Marchesiello, and J. C. McWilliams (2005a), Evaluation and application of the ROMS 1-way embedding procedure to the central california upwelling system, *Ocean Modelling*, *In Press*.

Penven, P., V. Echevin, J. Pasapera, F. Colas, and J. Tamx (2005b), Average circulation, seasonal cycle, and mesoscale dynamics of the Peru Current System: A modeling approach, *J. Geophys. Res.*, *110*, C10021, doi:10.1029/2005JC002945.

Peterson, R. G., and L. Stramma (1991), Upper-level circulation in the South Atlantic Ocean, *Prog. Oceanogr.*, *26*, 1–73.

Philander, S. G. H., and J.-H. Yoon (1982), Eastern Boundary Currents and Coastal Upwelling, *J. Phys. Oceanogr.*, *12*, 862–879.

Picaut, J. (1985), Major dynamics affecting the eastern tropical Atlantic and Pacific oceans, CalCOFI Rep., Vol. XXVI.

Pizarro, O., A. J. Clark, and S. Van Gorder (2001), El Niño sea level and currents along the South American coast: comparisons of observations with theory, *J. Phys. Oceanogr.*, *31*, 1891–1903.

Preston-Whyte, R. A., and P. D. Tyson (1988), *The Atmosphere and Weather of Southern Africa*, Oxford University Press, Cape Town.

Rajagopalan, B., Y. Kushnir, and Y. Tourre (1998), Observed decadal midlatitude and tropical Atlantic climate variability, *Geophys. Res. Lett.*, *25*, 3967–3970.

Rayner, N. A., E. B. Horton, D. E. Parker, C. K. Folland, and R. B. Hackett (1996), Version 3.0 of the Global Sea-Ice and Sea Surface Temperature Data Set, *UK Met. Office, Bracknett*, clim. Res. Tech. Note. 74.

Reason, C. J. C. (2000), Multidecadal climate variability in the subtropics/ mid-latitudes of the southern hemisphere oceans, *Tellus*, *52A*, 203–223.

Reason, C. J. C., and D. Jagadheesha (2005), Relationships between South Atlantic SST Variability and Atmospheric Circulation over the South African Region during Autral Winter, *J. Climate*, *18*, 3339–3355.

Reason, C. J. C., and M. R. Jury (1990), On the generation and propagation of the southern African coastal low, *Quart. J. Roy. Meteorol. Soc.*, *116*, 1133–1151.

Reason, C. J. C., L. A. Mysak, and P. F. Cummins (1987), Generation of annual period Rossby waves in the South Atlantic Ocean by the wind stress curl, *J. Phys. Oceanogr.*, *17*, 2030–2043.

Reason, C. J. C., R. J. Allan, J. A. Lindesay, and T. J. Ansell (2000), ENSO and climatic signals across the Indian Ocean basin in the global context: Part I, interannual composite patterns, *Int. J. Climatol.*, *20*, 1285–1327.

Reason, C. J. C., M. Rouault, J. L. Melice, and D. Jagadheesha (2002), Winter rainfall variability in SW South Africa and large scale-ocean-atmosphere interactions, *Meteorol. Atm. Phys.*, *80*(1-4), 19–29.

Reason, C. J. C., J. R. E. Lutjeharms, J. C. Hermes, A. Biastoch, and R. E. Roman (2003), Inter-ocean Fluxes south of Africa in an eddy permitting model, *Deep-Sea Res. II*, *50*, 281–298.

Reynolds, R. W., and T. M. Smith (1994), Improved global sea surface temperature analyses using optimum interpolation, *J. Climate*, *7*, 929–948.

Richman, M. B. (1986), Rotation of Principal Components, *J. Climatol.*, *6*, 293.335.

Risien, C. M., C. J. C. Reason, and F. A. Shillington (2004), Variability in satellite winds over the Benguela upwelling system during 1999-2000, *J. Geophys. Res.*, *109*, C03010, doi:10.1029/2003JC001880.

Robertson, A. W., J. D. Farrara, and C. R. Mechoso (2003), Simulations of the Atmospheric Response to South Atlantic Sea Surface Temperature Anomalies, *J. Climate*, *16*, 2540–2551.

Rouault, M., P. Florenchie, N. Fauchereau, and C. J. C. Reason (2003), South East tropical Atlantic warm events and southern African rainfall, *Geophys. Res. Lett.*, *30*(5), 8009, doi:10.1029/2002GLO14840.

Roy, C., and C. J. C. Reason (2001), ENSO related modulation of coastal upwelling in the eastern Atlantic, *Progr. Oceanogr.*, *49*, 245–255.

Ruiz-Barradas, A., J. A. Carton, and S. Nigam (2000), Structure of interannual to decadal climate variability in the tropical Atlantic sector, *J. Climate*, *13*, 3285–3297.

Schmitz, W. J. (1995), On the interbasin scale thermohaline circulation, *Rev. Geophys.*, *33*, 151–173.

Seager, R., B. Blumenthal, and Y. Kushnir (1995), An Advective Atmospheric Mixed Layer Model for Ocean Modelling Purposes: Global Simulation of Surface Heat Fluxes, *J. Climate*, *8*, 1951–1964.

Seager, R., R. Murtugudde, N. Naik, A. Clement, N. Gordon, and J. Miller (2003), Air-sea interaction and the seasonal cycle of the subtropical anticyclones, *J. Climate*, *16*, 1948–1966.

Servain, J. (1991), Simple climate indices for the tropical Atlantic Ocean and some applications, *J. Geophys. Res.*, pp. 15,137–15,146.

Shannon, L. V., and J. J. Agenbag (1990), A large-scale perspective on interannual variability in the environment in the South-East Atlantic, *S. Afr. J. Mar. Sci.*, *9*, 161–168.

Shannon, L. V., and G. Nelson (1996), *The South Atlantic: Present and Past Circulation*, chap. The Benguela: Large Scale Features and Processes and System Variability, pp. 163–210, Springer-Verlag, Berlin Heidelberg.

Shannon, L. V., A. J. Boyd, G. Brundrit, and J. Faunton-Clark (1986), On the existence of an El Niño type phenomenon in the Benguela system, *J. Mar. Res*, *44*, 495–520.

Shannon, L. V., J. J. Agenbag, and M. E. L. Buys (1987), Large and Mesoscale Features of the Angola-Benguela front, *S. Afr. J. Mar. Sci.*, *5*, 11–34.

Shchepetkin, A., and J. C. McWilliams (1998), Quasi-monotone advection schemes based on explicit locally adaptive dissipation, *Mon. Wea. Rev.*, *126*, 1271–1286.

Singleton, A. T., and C. J. C. Reason (2006), Numerical simulations of a severe rainfall event over the Eastern Cape coast of South Africa: sensitivity to sea surface temperature and topography, *Tellus*, *58A*, 355–367.

Sloyan, B. M., and S. R. Rintoul (2001), Circulation, renewal and modification of Antarctic Mode and Intermediate Water, *J. Phys. Oceanogr.*, *31*, 1005–1030.

Smith, W. H. F., and D. T. Sandwell (1997), Global Sea Floor Topography from Satellite Altimetry and Ship Depth Soundings, *Science*, *277*(5334), 1956–1962.

Stammer, D., R. Tokmakian, A. Semtner, and C. Wunsch (1996), How well does a 1/4° global circulation model simulate large-scale oceanic observations ?, *J. Geophys. Res.*, *101*(10), 25,779–25,811.

Stander, G. H., and A. H. B. De Decker (1969), Some physical and biological aspects of an oceanographic anomaly off South West Africa in 1963, *Invest. Rep. Div. Sea Fish. S. Afr.*, *81*, 46 pp.

Sterl, A. (2001), On the impact of gap-filling algorithms on variability patterns of reconstructed oceanic surface fields , *Geophys. Res. Lett.*, *28*, 2473–2476.

Sterl, A., and W. Hazeleger (2003), Coupled variability and air-sea interaction in the South Atlantic Ocean, *Climate Dyn.*, *21*, 559–571.

Stramma, L. (1989), The Brazil Current transport south of 23°S, *Deep-Sea Res.*, *36*(4A), 639–646.

Stramma, L. (1991), Geostrophic transport of the South Equatorial Current in the Atlantic, *J. Mar. Res.*, *49*(2), 281–294.

Stramma, L., and R. G. Peterson (1989), Geostrophic transport in the Benguela Current region, *J. Phys. Oceanogr.*, *19*, 1440–1448.

Stramma, L., and R. G. Peterson (1990), The South Atlantic Current, *J. Phys. Oceanogr.*, *20*, 846–859.

Stramma, L., Y. Ikeda, and R. G. Peterson (1990), Geostrophic transport in the Brazil Current region north of 20°S, *Deep-Sea Res.*, *37*(12A), 1975–1886.

Tanimoto, Y., and S. P. Xie (1999), Ocean-atmosphere variability over the Pan-Atlantic basin, *J. Meteor. Soc. Japan*, *77*, 31–46.

Taunton-Clark, J., and L. V. Shannon (1988), Annual and Interannual Variability in the South-East Atlantic during the 20th Century, *S. Afr. J. Mar. Sci.*, *6*, 97–106.

Tennant, W. (2004), Considerations when using pre-1979 NCEP/ NCAR reanalyses in the southern hemisphere, *Geophys. Res. Lett.*, *31*, L11112, doi: 10.1029/2004GL019751.

Theiss, J. (2004), Equatorward Energy Cascade, Critical Latitude, and the Predominance of Cyclonic Vortices in Geostrophic Turbulence, *J. Phys. Oceanogr.*, *34*, 1663–1678.

Todd, M. C., and R. Washington (2004), Climate variability in Central Equatorial Africa: Influence from the Atlantic sector, *Geophys. Res. Lett.*, *31*(23), L23202, doi:10.1029/2004GL020975.

Torrence, C., and G. P. Compo (1998), A practical guide to wavelet analysis, *Bull. Amer. Meteor. Soc.*, *79*(1), 61–78.

Tyson, P. D. (1986), *Climate Change and Variability in Southern Africa*, Oxford University Press., Cape Town.

Tyson, P. D., and R. A. Preston-Whyte (2000), *The Weather and Climate of Southern Africa*, Oxford Univ. Press, New York.

van Loon, H., and R. L. Jenne (1972), The zonal harmonic standing waves in the southern hemisphere, *J. Geophys. Res.*, *77*, 992–1003.

Veitch, J. A. (2004), Numerical model investigation of near surface circulation features of the Angola Basin, *Master's thesis*, University of Cape Town.

Veitch, J. A., P. Florenchie, and F. A. Shillington (2005), Seasonal and interannual fluctuations of the Angola-Benguela Frontal Zone (ABFZ) using 4.5 km resolution satellite imagery from 1982 to 1999, *Int. J. Rem. Sens.*, *Accepted*.

Venegas, S. A., L. A. Mysak, and D. N. Straub (1996), Evidence for interannual and interdecadeal climate variability in the South Atlantic, *Geophys. Res. Lett.*, *23*(19), 2673–2676.

Venegas, S. A., L. A. Mysak, and D. N. Straub (1997), Atmosphere-ocean coupled variability in the South Atlantic, *J. Climate*, *10*, 2904–2920.

Venegas, S. A., L. A. Mysak, and D. N. Straub (1998), An interdecadal climate cycle in the South Atlantic and its links to other ocean basins, *J. Geophys. Res.*, *103*(C11), 24,723–24,736.

von Storch, H. (1995), *Analysis of Climate Variability: Application of Statistical Techniques*, chap. Spatial patterns: EOFs and CCA, pp. 227–257, Springer Verlag.

Wainer, I., and S. A. Venegas (2001), South Atlantic Multidecadal Variability in the Climate System Model, *J. Climate*, *15*, 1408–1420.

Walker, N. D. (1987), Interannual Sea Surface Temperature variability and associated Atmospheric forcing within the Benguela System, *S. Afr. J. Mar. Sci.*, *5*, 121–132.

Weare, B. C. (1977), Empirical orthogonal analysis of Atlantic Ocean surface temperatures, *Quart. J. Roy. Meteorol. Soc.*, *103*, 467–478.

Xie, S., and Y. Tanimoto (1998), A Pan-Atlantic decadal climate oscillation, *Geophys. Res. Lett.*, *25*, 2185–2188.

Zebiak, S. E. (1993), Air-sea interaction in the equatorial atlantic region, *J. Climate*, *6*, 1567–1580.

A Additional figures for Section 4

B Additional figures for Section 6

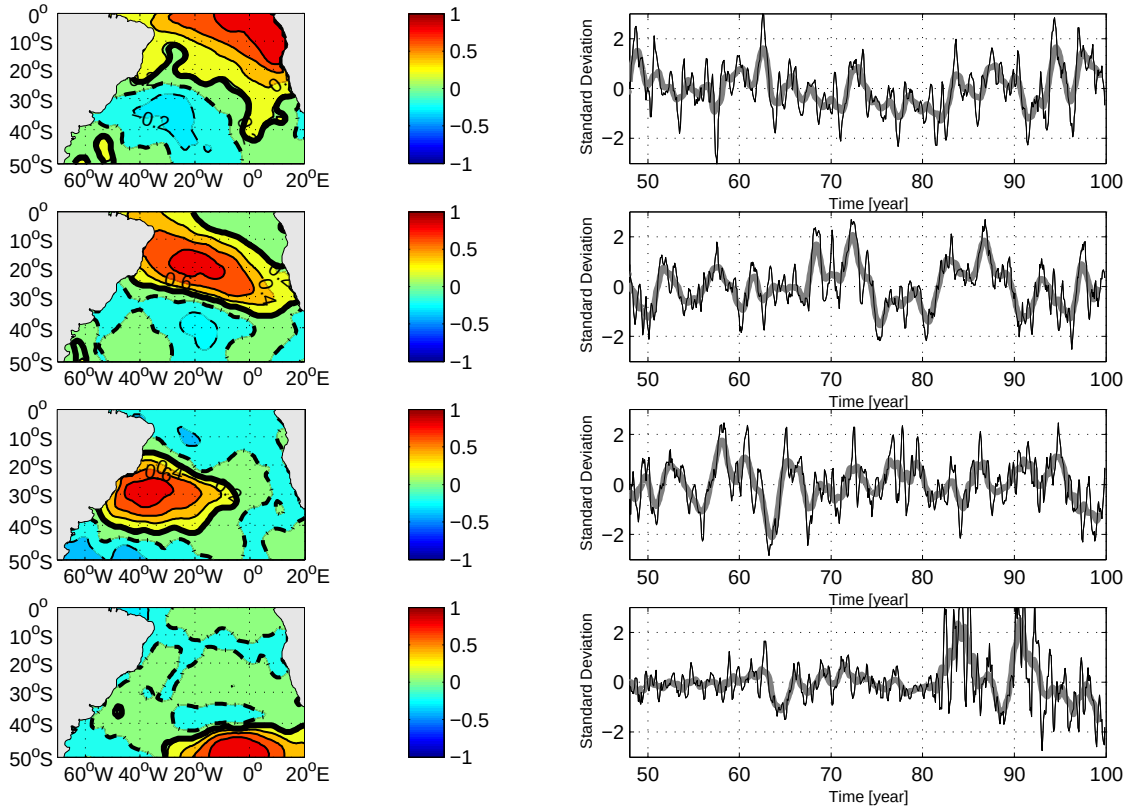

Figure 65: Section 4.1.1: From top to bottom: First four rotated EOFs of GISST3.0 SST. Left: Spatial pattern as correlation maps. The explained variances are: 23%, 16%, 15% and 11%, respectively. Positive (negative) contour lines are solid (dashed). The zero contour line is dashed - dotted, the contour interval is 0.2. The regions of significant correlation at the 95% level are within the thick lines. Right: Corresponding time series normalized by their standard deviation. The raw time series is shown in black. The grey line represent the time series smoothed with a one year running mean.

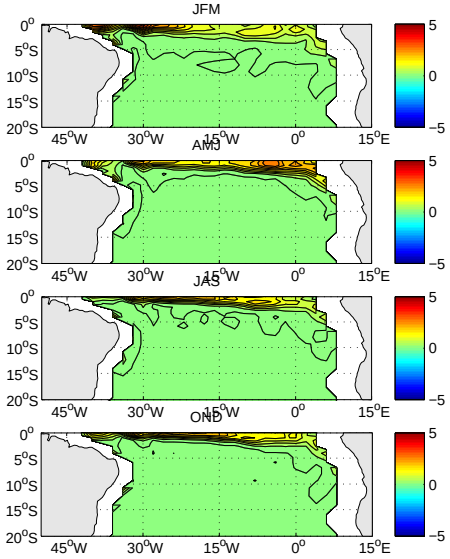

Figure 66: Section 4.1.3: Seasonal cycle of the vertical entrainment term. Positive (negative) contour lines are solid (dashed). The zero contour line is omitted. The contour interval is $0.3 \times 10^{-6} K s^{-1}$.

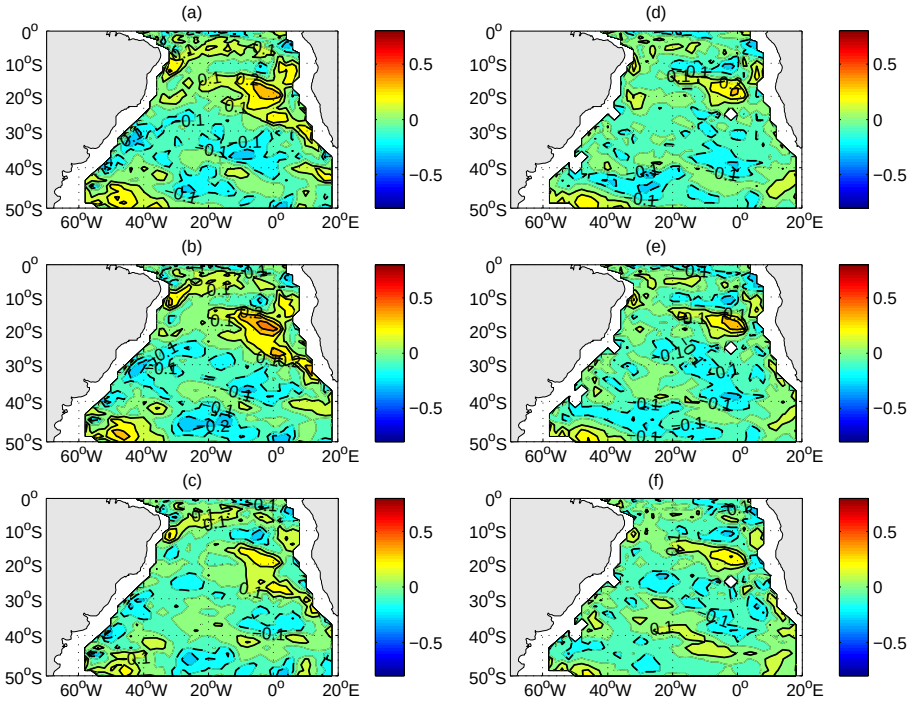

Figure 67: Section 4.1.3: Sequence of the lagged correlation between the second REOF(MLT) and $-\frac{\overline{w'T'}}{h}$ (left) and $-\frac{\Delta T}{h}w_h$ (right). With $lag = -3$ (upper), $lag = 0$ (middle) and $lag = 3$ (lower). Lag in *months*. Negative (positive) lag means leading (lagging) forcing field. Positive (negative) contour lines are solid (dashed). The zero contour line is omitted. The contour interval is 0.1

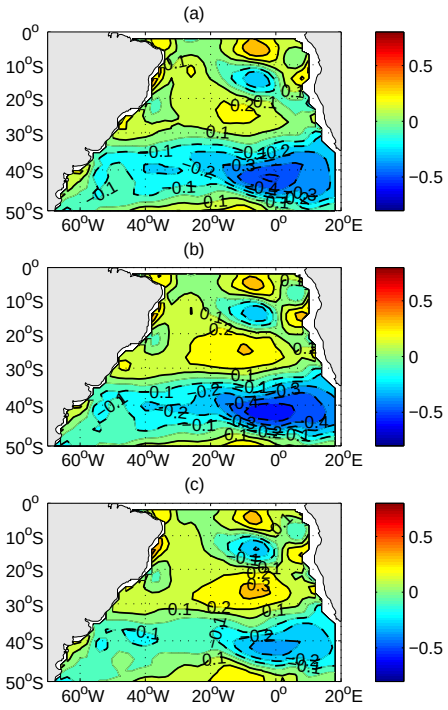

Figure 68: Section 4.1.3: Sequence of the lagged correlation between the third REOF(MLT) and meridional Ekman heat flux anomalies. With $lag = -3$ (upper), $lag = 0$ (middle) and $lag = 3$ (lower). Lag in *months*. Negative (positive) lag means leading (lagging) forcing field. Positive (negative) contour lines are solid (dashed). The zero contour line is omitted. The contour interval is 0.1

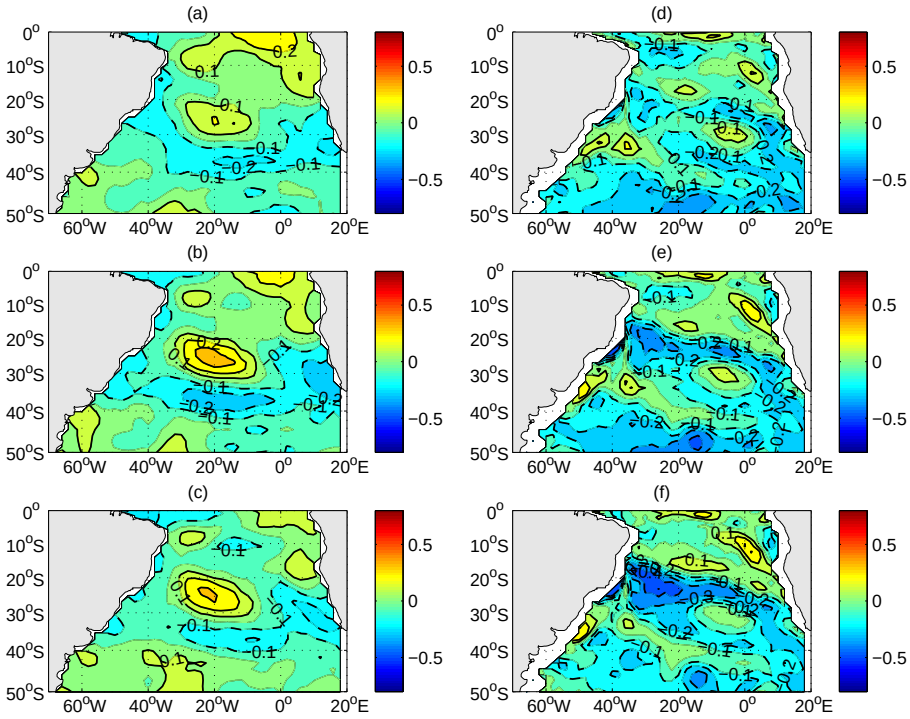

Figure 69: Section 4.1.3: Sequence of the lagged correlation between the fourth REOF(MLT) and shortwave flux (left) and $-v\nabla T$ (right). With $lag = -3$ (upper), $lag = 0$ (middle) and $lag = 3$ (lower). Lag in *months*. Negative (positive) lag means leading (lagging) forcing field. Positive (negative) contour lines are solid (dashed). The zero contour line is omitted. The contour interval is 0.1

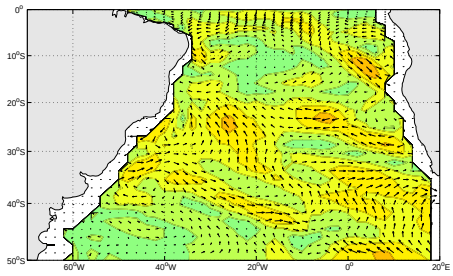

Figure 70: Section 4.1.3: Correlation between the fourth REOF(MLT) and mixed layer velocities for $lag = 3\,month$. The contour interval is 0.1

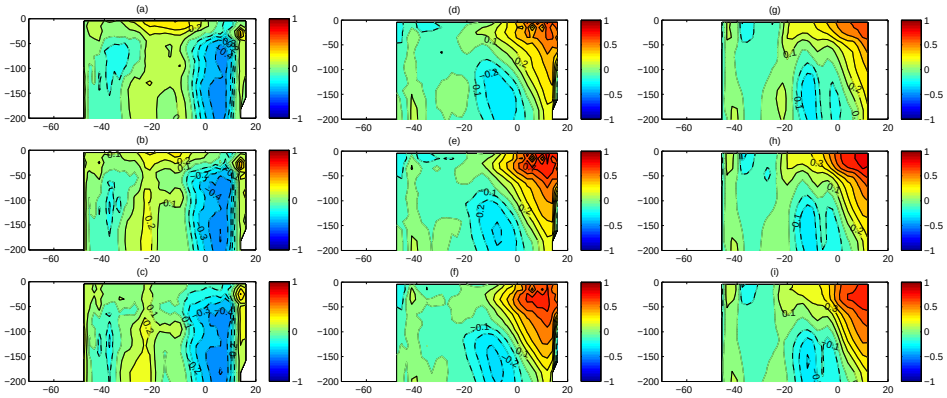

Figure 71: Section 4.1.4: Sequence of vertical section of correlation between the second REOF(MLT) and heat transport anomalies through 30°S. Left: $v'T$, middle: vT', and right: v_gT'. With $lag = -3$ (upper), $lag = 0$ (middle) and $lag = 3$ (lower). Lag in *months*. Negative (positive) lag means leading (lagging) transport field. Positive (negative) contour lines are solid (dashed). The zero contour line is omitted. The contour interval is 0.1.

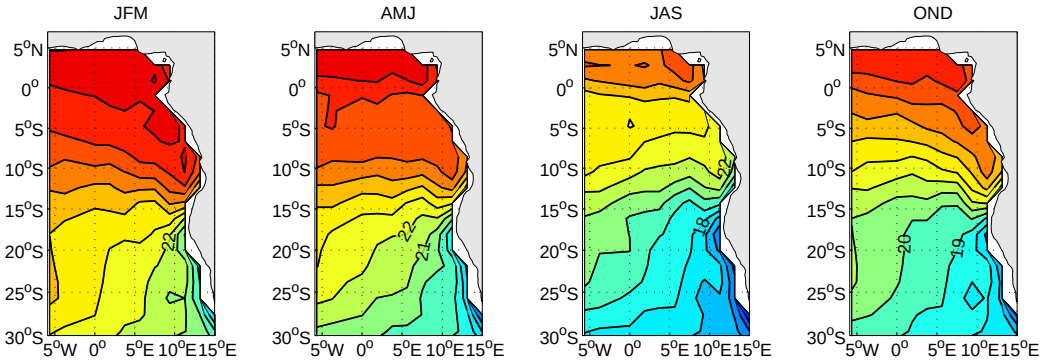

Figure 72: Section 6.1.1: Seasonal climatology of NCEP/ NCAR SST. The contour interval is $1°C$.

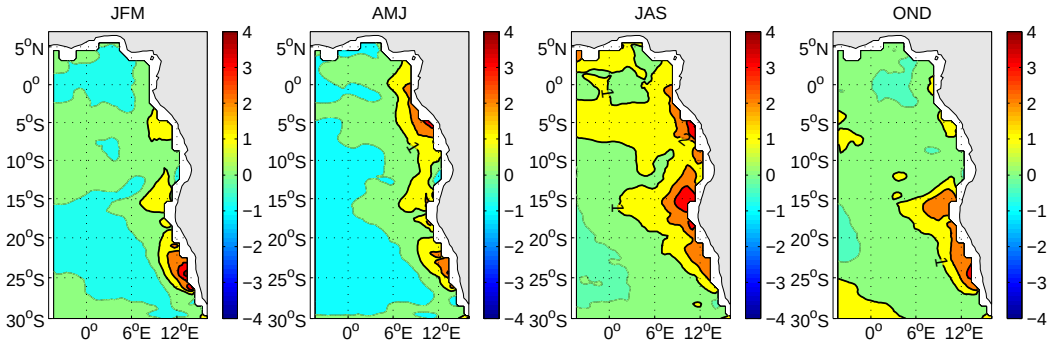

Figure 73: Section 6.1.1: Seasonal climatology of the temperature difference between WOA temperatures and modelled temperatures at a depth $z = 10m$. The contour interval is $0.5°C$.

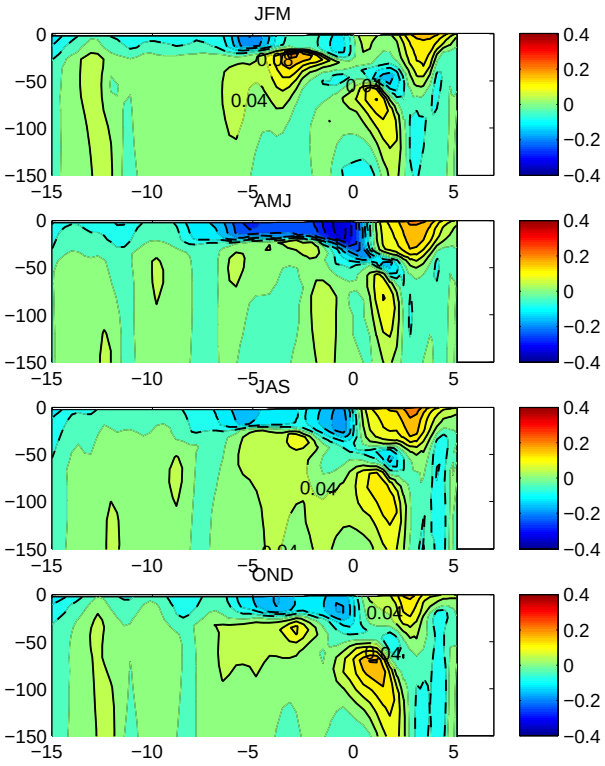

Figure 74: Section 6.1.1: North-south section of the seasonal climatology of the model zonal velocity. The contour interval is $0.04ms^{-1}$.

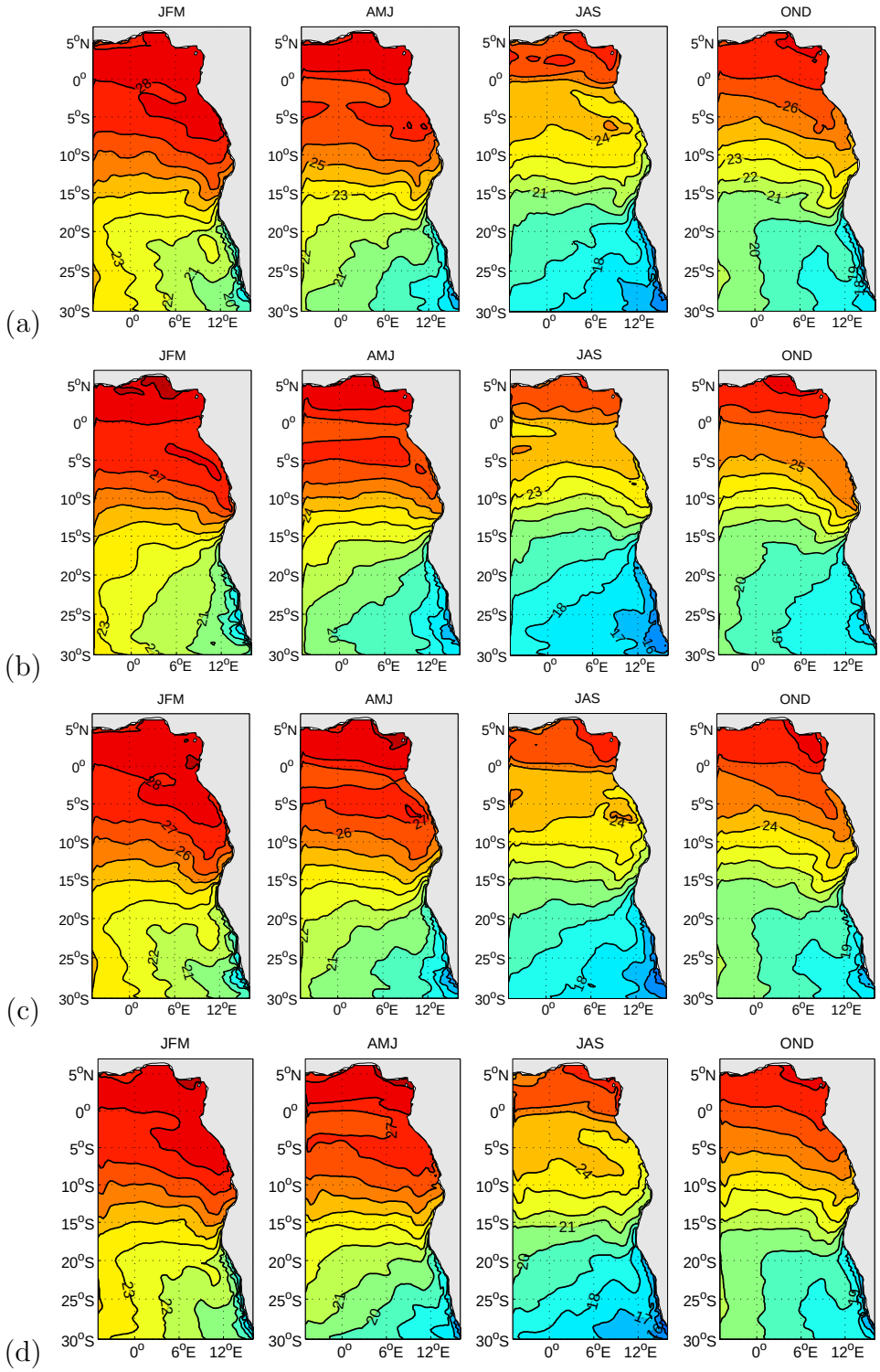

Figure 75: Section 6.1.1: Seasonal climatology of ROMS temperature at $10m$ forced with (a) NCEP/ NCAR windstress and fluxes, (b) COADS windstress and fluxes, (c) COADS windstress and NCEP/ NCAR fluxes, and (d) SODA1.2 boundary conditions and NCEP/ NCAR windstress and fluxes. The contour interval is $1°C$.

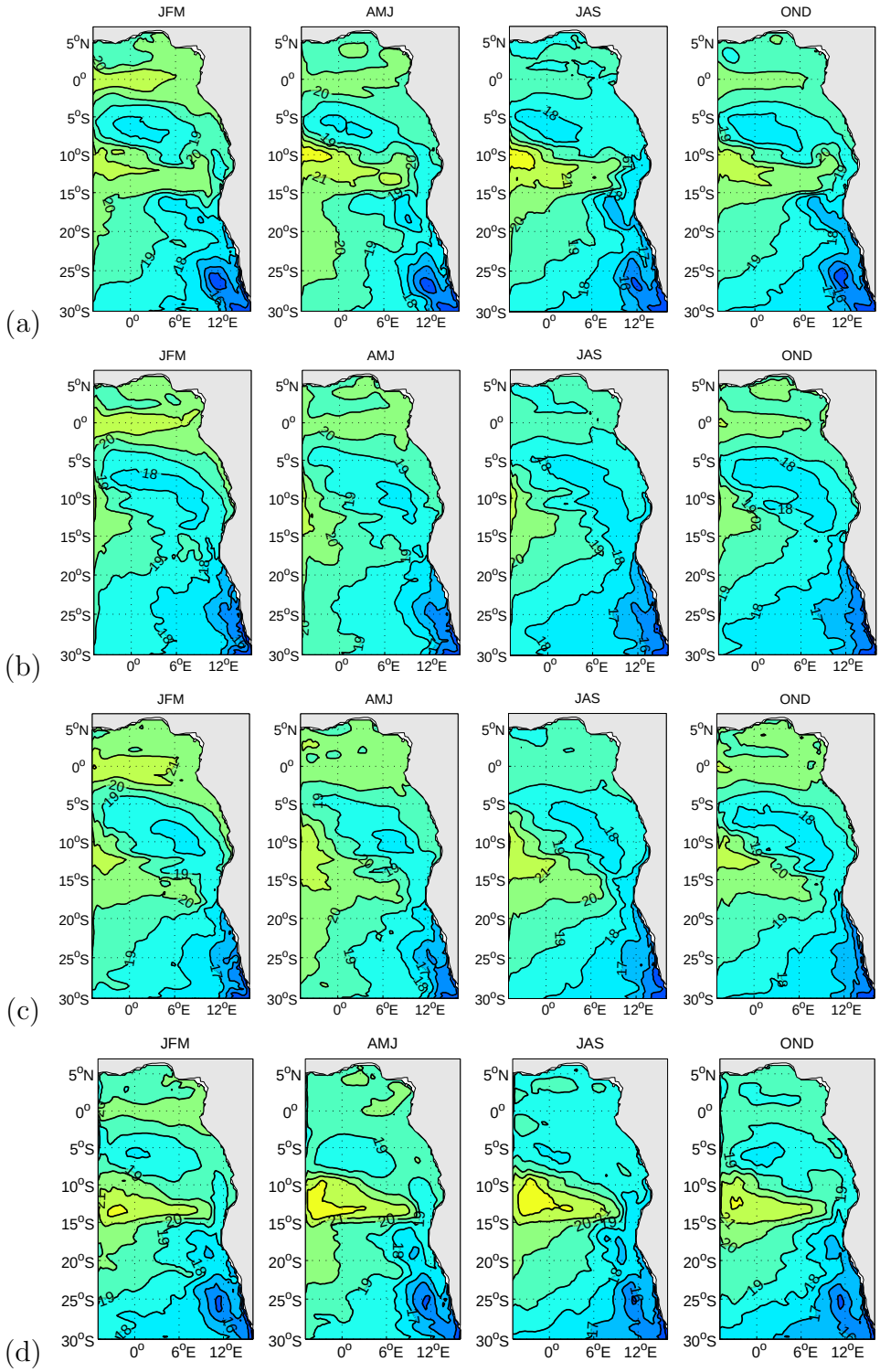

Figure 76: Section 6.1.1: Seasonal climatology of ROMS temperature at $75m$ forced with (a) NCEP/ NCAR windstress and fluxes, (b) COADS windstress and fluxes, (c) NCEP/ NCAR fluxes and COADS windstress, and (d) SODA1.2 boundary conditions and NCEP/ NCAR windstress and fluxes. The contour interval is $1°C$.

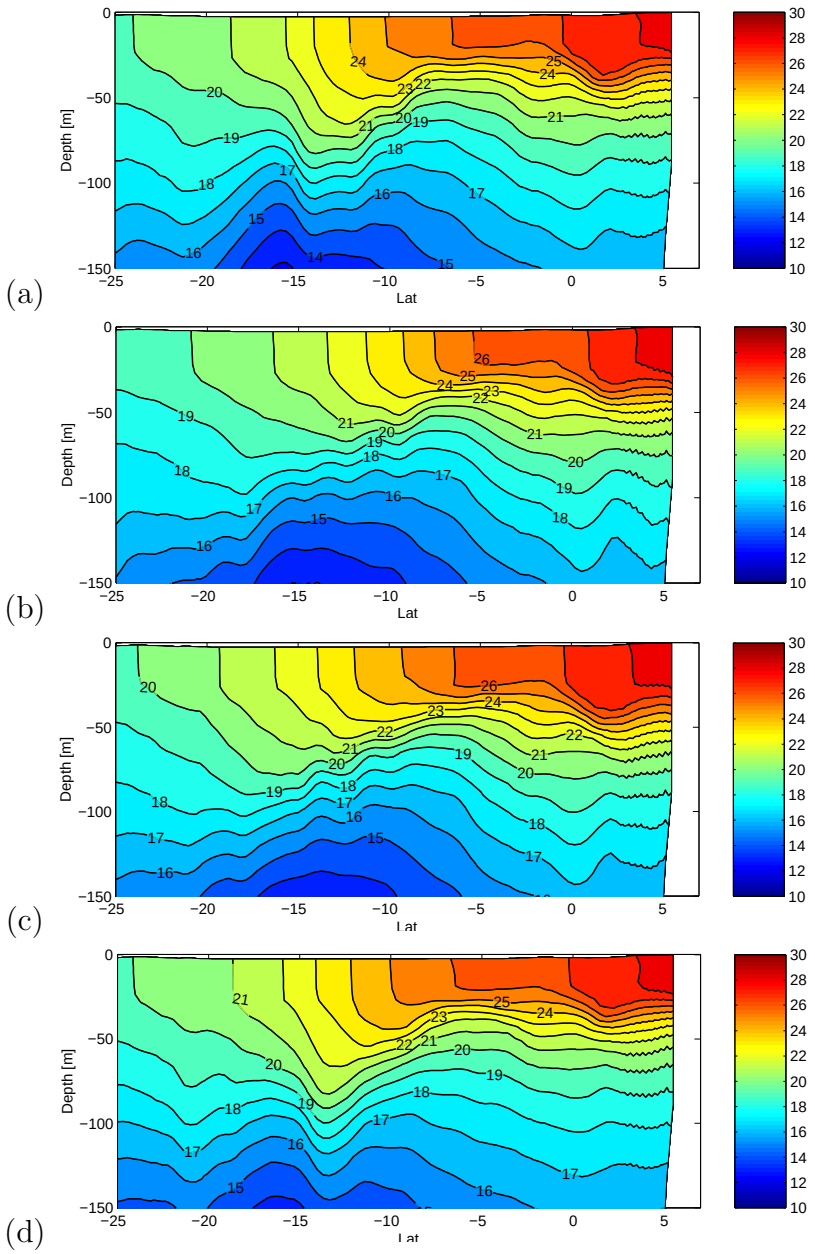

Figure 77: Section 6.1.1: Vertical section of ROMS temperature at 5°E forced with (a) NCEP/ NCAR windstress and fluxes, (b) COADS windstress and fluxes, (c) NCEP/ NCAR fluxes and COADS windstress, and (d) SODA1.2 boundary conditions, NCEP/ NCAR windstress and fluxes. The contour interval is $1°C$.

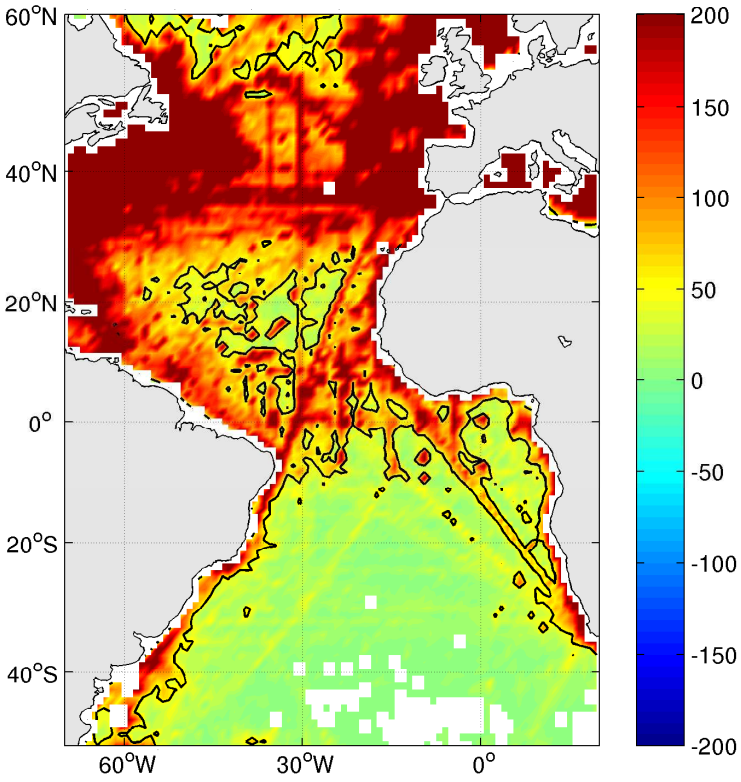

Figure 78: Section 6.1.1: Total number of observations for the upper ocean temperatures that have been considered for the World Ocean Atlas (*Conkright et al.*, 2002). The shown isoline indicates 50 observations.

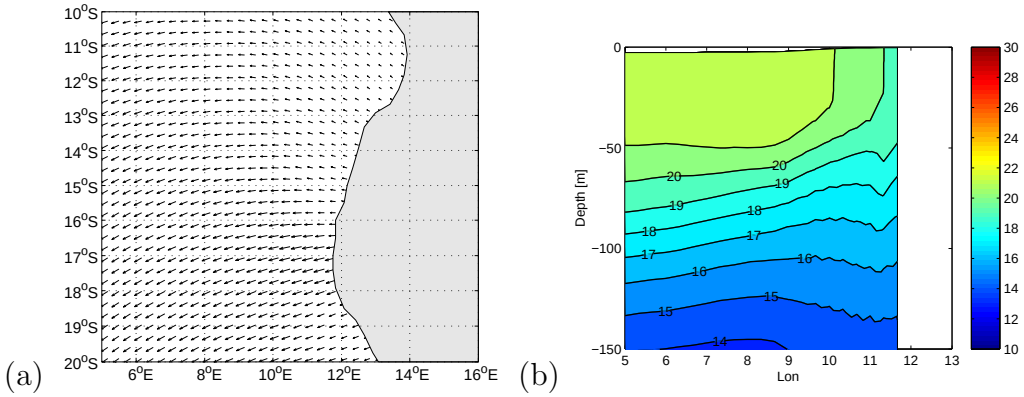

Figure 79: Section 6.1.2: (a) Annual mean of the Ekman flow in the ABFZ area and (b) annual mean of a vertical temperature section between 16°S and 17°S. The contour interval is 1°C.

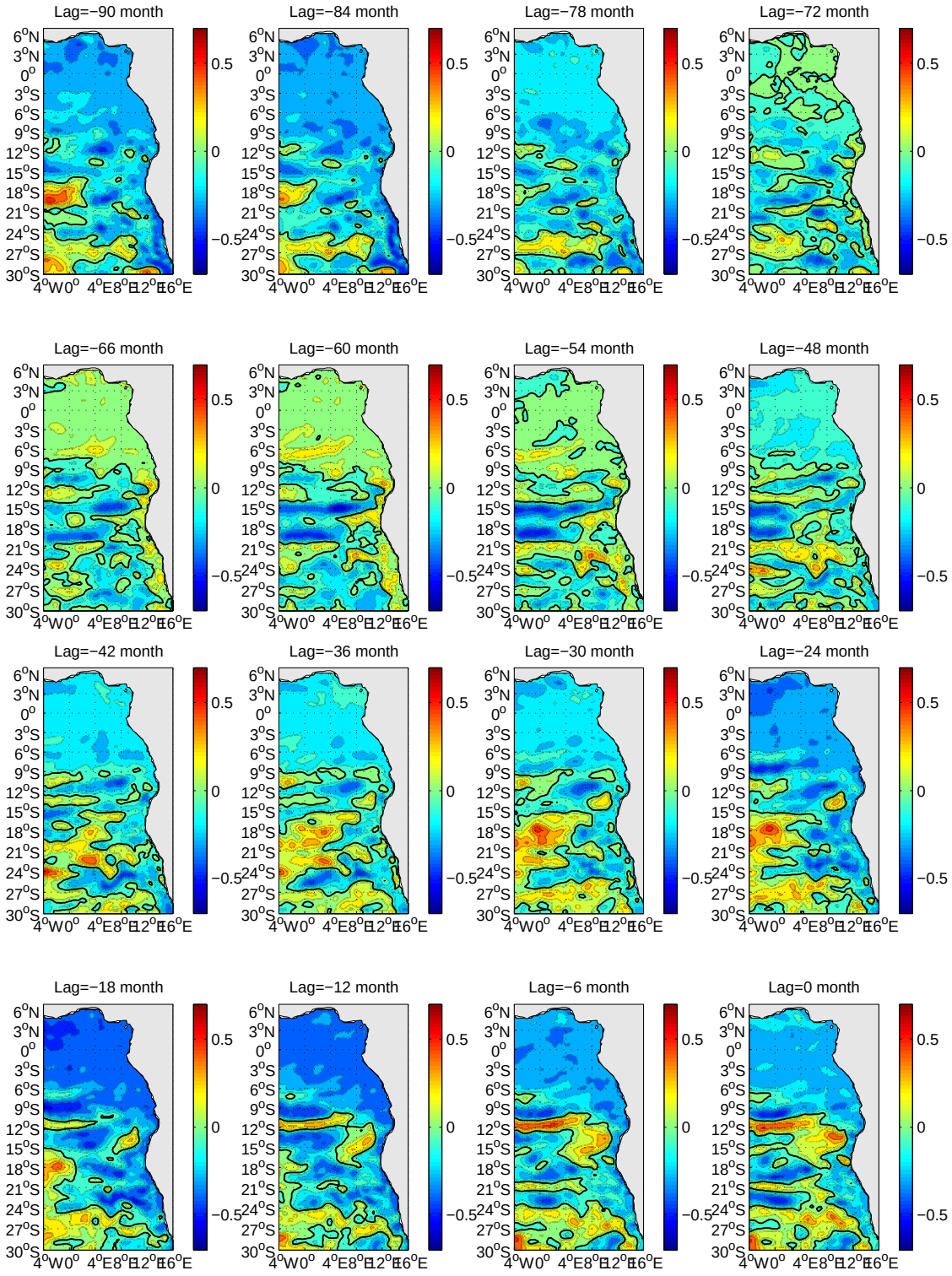

Figure 80: Section 6.3.3: Correlation sequence between the filtered *Index 2* and the sea surface height (SSH) anomaly. Positive (negative) contour lines are omitted. The zero contour line is solid. A colour scale is given to the right of each plot.